DESIGN PARAMETERS AND PHYSIOLOGIC FACTORS GOVERNING MITRAL VALVE ANNULAR LOADING FOLLOWING DEVICE IMPLANTATION

A Dissertation
Presented to
The Academic Faculty

by

Eric L. Pierce

In Partial Fulfillment
of the Requirements for the Degree
Doctor of Philosophy in the
Department of Biomedical Engineering

Georgia Institute of Technology and Emory University
August 2018

DESIGN PARAMETERS AND PHYSIOLOGIC FACTORS GOVERNING MITRAL VALVE ANNULAR LOADING FOLLOWING DEVICE IMPLANTATION

Approved by:

Dr. Ajit P. Yoganathan, Advisor
Department of Biomedical Engineering
Georgia Institute of Technology and Emory University

Dr. Joseph H. Gorman
School of Medicine
University of Pennsylvania

Dr. Wei Sun
Department of Biomedical Engineering
Georgia Institute of Technology and Emory University

Dr. Changfu Wu
Center for Devices & Radiologic Health
U.S. Food and Drug Administration

Dr. Robert E. Guldberg
Department of Biomedical Engineering
Georgia Institute of Technology and Emory University

Date Approved: April 03, 2018

Dedicated to my father

ACKNOWLEDGEMENTS

To my advisor, Dr. Yoganathan: you took a chance by investing in a confused molecular biologist, and we've come a long way since then. I am grateful for the trust you put in me. Your top-level strategic thinking and your refusal to lose sight of the fundamentals are examples I will work to emulate throughout my career.

To my thesis committee: I have enjoyed productive, intellectual conversations with each of you, and your efforts have meaningfully strengthened this dissertation. I recognize the time and energy you have devoted to this work. Dr. Gorman, special thanks for your mentorship and partnership over the course of >50 shared large animal studies completed in your lab. I am proud of what we accomplished together.

To Sarah, Deborah, Ajay, Siddhi, and Fiona: You each contributed meaningfully to the completion of this thesis. It was a pleasure working alongside you, struggling, learning, and achieving together. I am grateful for the dedication you each showed, and I hope that you found our time together in the CFML rewarding. The future is very bright for every one of you.

To my friends and colleagues who have shared their time and expertise over the years: I wholeheartedly acknowledge I would never have reached this point without you. Among so many of you, I must acknowledge in particular Charlie, Andrew, Ikay, Vrishank, and Prem. The standards you each set continue to inspire me. Ikay, thank you for being my rabbit, I don't believe I'll ever catch you. Charlie, it was circumstance that prompted us to begin working together in 2013, but it was our mutual dedication to our research and

support for one another's goals that kept our work so productive and fun thereafter. Your generosity is unparalleled. You have taught me so much, and I cannot articulate the depth of my gratitude.

To my family: I've tapped into your unconditional support more than I ever intended. Mike, Becca, and Mom, thank you for lifting me up in some very low moments. Dave, Nat, Dani and Chloe, simply put, you made Atlanta home. Leaning on you during these years has meant more than you know.

To Shanthi: the wisdom, compassion, and patience you have provided through so many challenges are immeasurable. Your love and generosity cannot be repaid, but I will keep trying anyway.

To Ada: Becoming a parent during the final year of a PhD is not easy, but I would not change a thing! Thanks for giving me so much to smile about every day. Let this thesis, in all its 400 pages of glory, be a lesson in the power of focus and perseverance, and in the importance of drawing support from those around you. I love you.

TABLE OF CONTENTS

LIST OF TABLES

LIST OF FIGURES

LIST OF SYMBOLS AND ABBREVIATIONS

ΔP	trans-mitral Pressure gradient
ANOVA	Analysis of Variance
APC	Anterior-Posterior Commissure (tricuspid valve)
AS	Aortic Stenosis
C	Circular
D	D-shaped
F_C	Cyclic contracile Force (suture)
F_{IC}	Inter-Commissural Force (during radial expansion)
F_P	Pullout Force (suture)
F_{SL}	Septal-Lateral Force (during radial expansion)
F_{TD}	Tie-down Force (suture)
FTR	Functional Tricuspid Regurgitation
GLM	General Linear Model
$HWHM_{norm}$	normalized Half-Width at Half-Maximum
HYP	Hydroxyproline mass fraction
IC	Inter-Commissural
IMR	Ischemic Mitral Regurgitation
LA	Left Atrium
LT	Left Trigone
LV	Left Ventricle
LVP	Left Ventricular Pressure

MR	Mitral Regurgitation
MS	Mitral Stenosis
MV	Mitral Valve
nMPI	normalized Mean Pixel Intensity
PSC	Posterior Septal Commissure (tricuspid valve)
PV	Pulmonary Valve
PVL	Paravalvular Leakage
PVL_{norm}	normalized Paravalvular Leakage
RA	Right Atrium
REFT	Radial Expansion Force Transducer
RS	Residual Strength (suture)
RT	Right Trigone
RV	Right Ventricle
SAC	Septal Anterior Commissure (tricuspid valve)
SL	Septal-Lateral
TAVR	Transcatheter Aortic Valve Replacement
TMV	Transcatheter Mitral Valve
TMVR	Transcatheter Mitral Valve Replacement
TR	Tricuspid Regurgitation
TV	Tricuspid Valve

SUMMARY

The range of implantable devices to correct mitral regurgitation (MR) is diverse and continually expanding. It consists mainly of annuloplasty rings, which restore native valve competency, and prosthetic valve replacements. Both attach to the mitral annulus via suture anchoring. Additionally, many transcatheter mitral valve (TMV) replacements, in which anchoring and sealing often rely on radial expansion against the mitral annulus, are now developing rapidly. The mechanical interactions of all such devices with the annulus remain poorly studied, yet are critical for device safety and performance.

In this work, custom measurement techniques were applied to study device-annulus interactions in clinically and industrially relevant *in vivo*, *ex vivo*, and *in vitro* models. First, the impacts of mitral annuloplasty ring shape, size, and stiffness on suture dehiscence likelihood were assessed across 37 ovine subjects and a series of benchtop tests. A critical role of ring flexibility was uncovered, which suggested a promising new design concept to improve suture retention without compromising effectiveness. Second, TMV radial expansion forces and paravalvular leakage dynamics were quantified in explanted porcine hearts, as functions of the device's profile. Findings quantitatively demonstrated key advantages of a non-circular TMV shape, implications of annular oversizing, and criteria for industrial TMV test system performance. Taken together, these studies yield significant new insights into best practices for MR device design, assessment, and usage.

CHAPTER 1. INTRODUCTION

The four heart valves open and close in response to cyclic contraction and relaxation of the heart. By ensuring efficient, unidirectional blood flow, they each serve a vital role in cardiovascular function. However, due to the mechanical demands they face, in combination with genetic and other factors, a heart valve may become incapable of effective opening (valvular stenosis) or effective closure (valvular regurgitation). Among the four valves, the mitral valve (MV) faces the harshest mechanical environment due to its positioning between the left atrium and left ventricle. Mitral regurgitation (MR) is the most common form of clinically significant valve disease: the incidence of moderate or severe regurgitation in the US is 1.7% and rising.[1]

The MV is a complex structure, consisting of two asymmetric leaflets, a branching network of chordae tendineae that insert across the leaflets' ventricular surfaces, and two papillary muscles that connect the chordae tendineae to the left ventricular wall. Further, the leaflets hinge from a ring of tissue referred to as the mitral annulus, whose non-circular and non-planar contour changes throughout the cardiac cycle. MR can result from any of a range of failures at the level of the leaflets, chordae tendineae, papillary muscles, annulus, or any combination thereof. This makes determining an optimal correction for a given MR phenotype a multi-faceted process.

The landscape of prostheses to correct MR is diverse and steadily expanding. It consists mainly of annuloplasty rings that reshape the native tissue and prosthetic heart valves that replace native MV function. Despite overall positive outcomes using these surgically implantable devices, MR correction suffers from two major problems today.

First, whether correction is achieved by MV repair or replacement, post-operative failures persist. These include, but are not limited to, device migration, paravalvular leak, hemolysis, thrombosis, embolization, structural failure of the device (e.g., fracture), left ventricular outflow tract obstruction, and adverse ventricular remodeling.[2-8] Second, an enormous sector of the MR patient population (with estimates ranging from 50-98%, depending upon the disease subtype[9-11]) is denied access to surgical correction altogether, largely due to operative risk. Inspired by the success of transcatheter aortic valve replacement (TAVR) in reaching otherwise-inoperable patients, development of novel devices for transcatheter mitral valve replacement (TMVR) is now an industry-wide goal.[12-16] With no TMVR devices yet to achieve regulatory approval, the eventual success of TMVR will be dictated its ability to avoid myriad potentially critical modes of failure.

Among the various modes of failure known to undermine surgical MR correction, as well as those anticipated to challenge TMVR, many are attributable to events occurring *at the device-annulus interface*. **In spite of a rich recent history of engineering research to understand MV mechanics and to optimize MR corrective techniques,[17, 18] two such failure modes that stand out as markedly understudied are (a) annuloplasty ring suture dehiscence and (b) paravalvular leak (PVL) post-TMVR.**

In annuloplasty ring suture dehiscence, failure occurs in the sutures tie the annuloplasty ring to the MV annulus. When the force acting on one or more of these sutures exceeds the tissue's suture holding strength, the suture tears out from the tissue. Studies of reoperation for failed annuloplasty-based MV repairs have reported the proportion of failures attributable to annular suture dehiscence to fall between 13-42%.[19-21] Despite its prevalence, the factors contributing to dehiscence remain largely unclear. Although clinical

reports may be easily attributed to surgical error, multiple groups have questioned the extent to which dehiscence likelihood is determined systematically.[22-24] Quantification of such systematic factors would offer two principal benefits. First, in a review of recent literature (with mean patient follow-up > 1 year), Khamooshian et al found insufficient evidence to establish any superior ring type, in terms of New York Heart Association class and ventricular function.[25] Amidst such uncertainty, differences in anchoring performance would constitute a basis to discriminate among existing rings. Second, mechanistic description of the factors contributing to suture dehiscence would be instrumental in the development of controls and/or novel device designs to reduce its occurrence.

Meanwhile, although the capacity for PVL post-TMVR has been demonstrated through early clinical experience,[26-30] its eventual incidence upon wider use of TMVR remains to be determined. However, it is clear that PVL is (a) lethal in the TAVR setting, even when mild,[31] (b) deadlier at the mitral than at the aortic position,[32] (c) likely far more challenging to prevent in the TMVR setting than the TAVR setting, due to numerous biomechanical disadvantages,[12-14] (d) difficult to diagnose, especially when mild or moderate,[33] and (e) especially difficult to treat in surgically inoperable patients.[34, 35] In light of the now-widespread use of TAVR and the rapid momentum of TMVR development,[15] a significant burden falls upon engineers, clinicians, standards bodies, and regulators to develop a rigorous understanding of TMVR PVL dynamics. Such understanding would support the continued development of existing and new TMVR systems toward optimal sealing against PVL.

Presently, very little engineering research exists regarding the influences of MV annular mechanics and annuloplasty ring design parameters on suture dynamics. Despite a

wealth of clinical experience, carefully defining the mechanisms governing suture dehiscence remains a critical step before next-generation ring designs and usage techniques to prevent its occurrence can be developed. Similarly, very little engineering research exists regarding the influences of MV annular mechanics and TMV design parameters on PVL. Learning from surgical experience, TMVR outcomes may be improved *prospectively* by first characterizing the requirements for an optimal TMV-annulus seal. These are the goals of this thesis, as described herein.

CHAPTER 2. BACKGROUND

2.1 The Circulatory System and the Heart

2.1.1 *The Circulatory System*

The circulatory system is a complex, pump-driven network of vessels that carry blood to and from the cells of the human body. Sustained flow of blood throughout the body is central to numerous fundamental aspects of physiology. The foremost of these is gas exchange between cells throughout the body and red blood cells suspended in the blood. Gas exchange entails collection of oxygen from (and delivery of carbon dioxide to) the alveoli within the lungs, and delivery of oxygen to (and collection of carbon dioxide from) all other tissues. Oxygen is a critical metabolic reagent (i.e. used in energy production within cells), and carbon dioxide is a metabolic waste. Other critical functions of the circulatory system include transport and delivery of immune cells, nutrients, and hormones across the body, as well as regulation of body temperature, pH, and water content. All cells in the body require oxygen as a fundamental reagent in the chemical processes that generate usable energy.

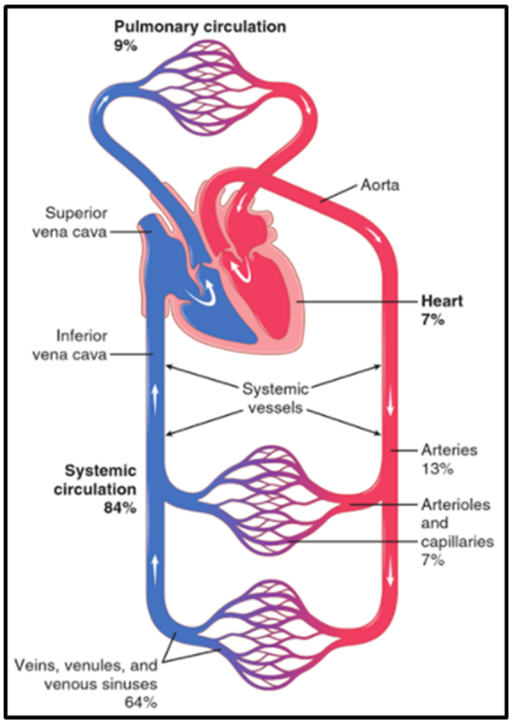

Figure 2-1 Overview of the circulatory system, highlighting the percentage of total blood in each part of the system (modified from Hall[36])

At the center of the circulatory system sits the heart, a four-chambered pump that generates pressure to drive blood through the vasculature. It is described further in the following section. The right heart drives blood out through the pulmonary circulation: that is, through the pulmonary artery, into progressively smaller arteries and into capillary beds in the lungs, and back to the left heart via progressively larger veins ending with the pulmonary veins. The left heart drives blood to the systemic circulation: that is, through the aorta, into progressively smaller arteries and into capillary beds throughout the rest of the body, and back to the right heart via progressively larger veins ending with the vena cavae. The systemic circulation also includes the *coronary circulation*, a small network of vessels that branches from the aorta and delivers blood to the tissues of the heart itself.

2.1.2 The Heart

Circulatory function requires the unidirectional flow of blood through the vasculature. This is made possible by the heart, a pump that generates pressure via rhythmic contraction and relaxation of its muscle to drive blood flow. The heart is composed of four chambers: the left and right atrium (LA and RA), and the left and right ventricles (LV and RV). The left and right sides deliver blood to the pulmonary and systemic circuits, as described above.

The pumping of the heart is referred to as the cardiac cycle, and can be broken into two distinct phases. In diastole, the ventricles expand and fill with blood. In systole, the ventricles contract, ejecting blood into the vasculature. Ventricular pressures rise and fall over large magnitudes, which on its own can cause blood to flow both forward and backward. However, to prevent backward flow, the ventricles are gated at their entry and exit points with four heart valves.

The mitral and tricuspid valves (MV and TV) sit proximal to the left and right ventricle, respectively, and are also called the atrioventricular valves. The aortic and pulmonary valves (AV and PV) sit proximal to the aorta and pulmonary artery, respectively, and are also called the semilunar valves. All four heart valves open and close passively in response to oscillating pressure gradients across them. The atrioventricular valves open during diastole and close during systole; the opposite is true for the semilunar valves. The left heart's valves face the largest pressure gradients: at healthy resting conditions, 120 mmHg at peak systole for the mitral valve, and 80 mmHg at peak diastole for the aortic valve. Immediately downstream of the AV are the coronary ostia, two entry

points into the coronary vasculature, which provides blood flow to the cardiac tissue itself. The coronary circulation drains into the right atrium.

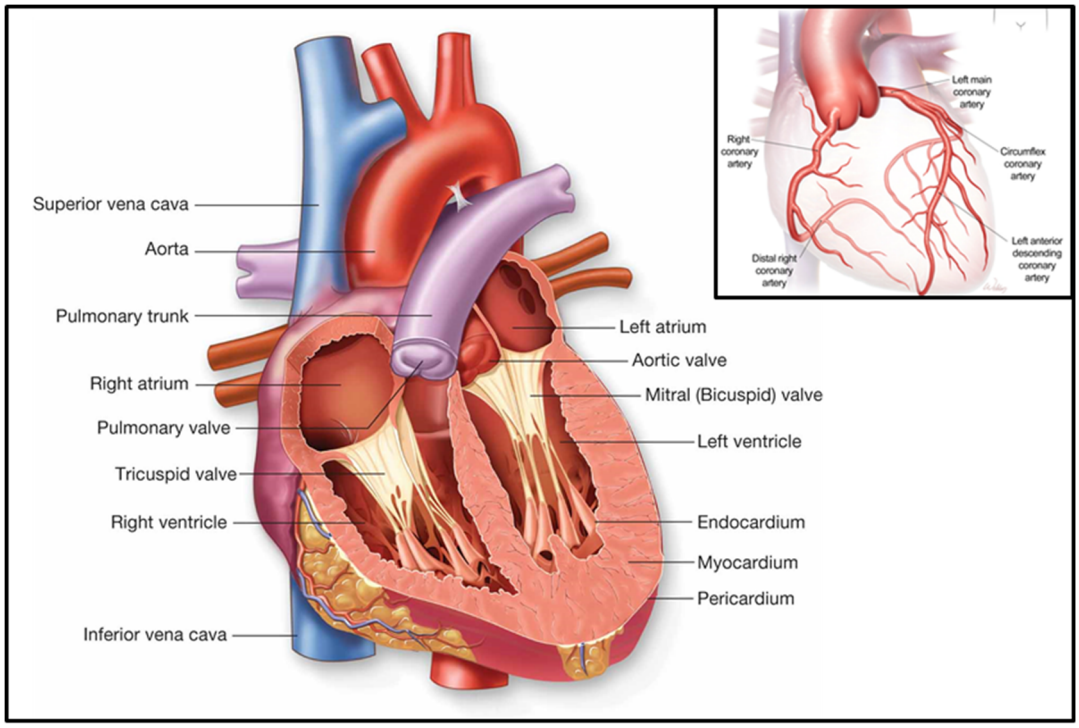

Figure 2-2 Long-axis view of the heart's chambers, valves, and large vessel connections (image: biology-forum.com). Inset: Coronary arteries branching from the aorta (image: Scott Weldon, via bcm.edu).

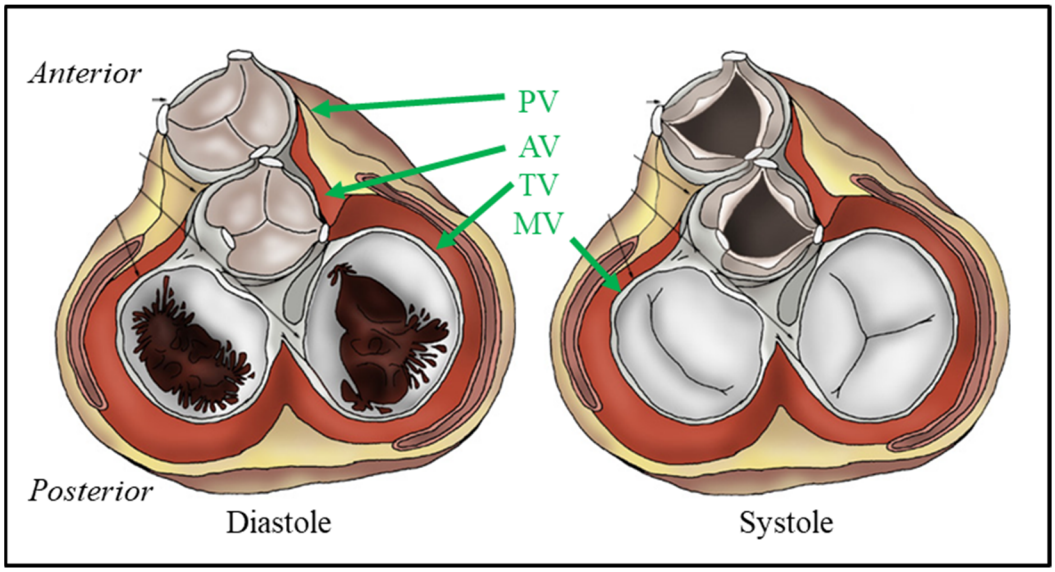

Figure 2-3 Short-axis views of the heart during diastole (ventricular relaxation) and systole (ventricular contraction), revealing the opening and closure of the four heart valves (modified from prenhall.com).

2.2 The Mitral Valve

2.2.1 The Mitral Leaflets

The *anterior and posterior leaflets* are the central components of the MV. Although the two leaflets differ in shape (with the posterior leaflet occupying the majority of the valve circumference, and the anterior leaflet being longer), their surface areas are similar.[37] In total, their combined surface area is approximately twice that of the MV orifice.[37] As such, MV closure during ventricular contraction exhibits redundant *coaptation* (leaflet-leaflet contact). This provides an effective seal against leakage from LV to LA (i.e. *mitral regurgitation*, MR). The anterior and posterior leaflets meet at two *commissures*. The

posterior leaflet is scalloped by two indentations, which divide it into the P1, P2, and P3 segments. The anterior leaflet is not scalloped (see Figure 2-8 below).

In cross-section, the MV is the thickest of the four heart valves.[38] The leaflets are roughly divided into three layers. In order from the atrial face (inflow) to the ventricular face (outflow), these are the *atrialis*, the *spongiosa*, and the *fibrosa*, with either side covered with endothelial cells.[17] The major structural components of the leaflets are extracellular, namely collagen fibers, elastin fibers, glycosaminoglycans, and proteoglycans. At very low stretch levels, elastin provides the primary load-bearing function; under higher stretch, collagen does so. The deposition and alignment of these fibers varies across the three layers, as shown in Figure 2-4.

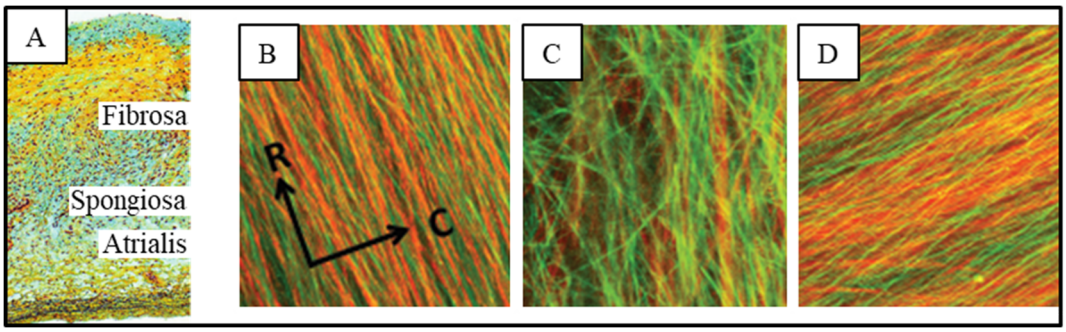

Figure 2-4 (A) Histologic, cross-sectional image of the MV leaflet, highlighting its distinct layers (modified from Brazile et al[38]). (B-D) From left to right, histologic images of the atrialis, spongiosa, and ventricularis, with the leaflet until bi-axial stretch. In (B-D), green fibers are collagen and red fibers are elastin. R: radial direction; C: circumferential direction (modified images, originally courtesy of Dr. Michael Sacks et al).

2.2.2 *The Sub-Valvular Apparatus*

The *sub-valvular apparatus* is comprised of two *papillary muscles* that extend inward from the LV wall, and the *chordae tendineae*, a complex, branching network of chords that emanate from either papillary muscle and insert at numerous points across the ventricular faces of the leaflets. The precise branching structure of the chordae varies among individuals; branch taxonomy and the distinct functions of specific taxa are the subjects of ongoing research.[39, 40] As a whole, the sub-valvular apparatus provides a critical function during systole. As left ventricular pressure (LVP) drives the MV leaflets basally (i.e. away from the heart's apex), the chordae tendineae, combined with the contracting papillary muscles, exert tension on the leaflets. This tension restrains the leaflets from prolapsing into the LA, thereby holding them in a coapted state.

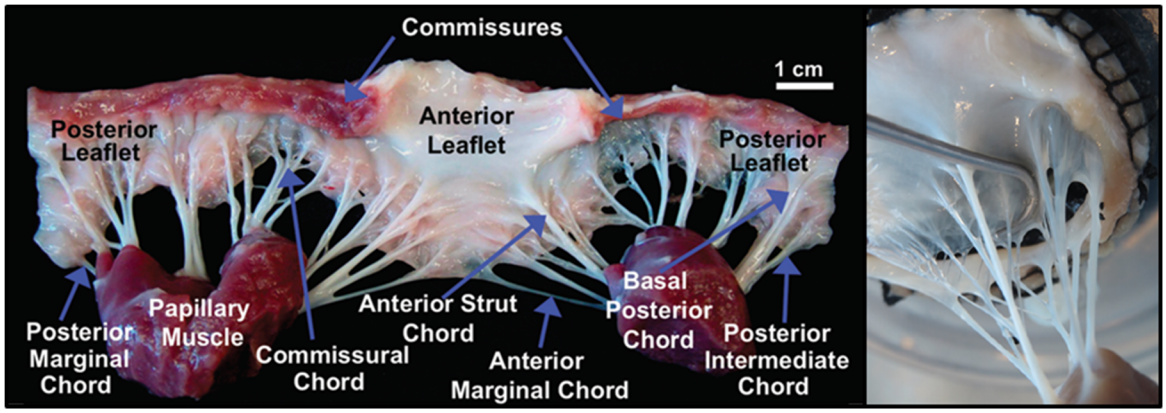

Figure 2-5 Porcine (left) and ovine (right) MVs, manipulated *in vitro* to highlight the different sub-types of chordae tendineae and their complex, three-dimensional branching patterns (left: modified from Rabbah et al[17]).

2.2.3 The Mitral Annulus

The leaflets hinge around the *mitral annulus*, a region of myocardium, collagen, and other tissue that separates LA from LV. The boundaries of the annulus are not well defined, and the mere existence of the annulus as a coherent structure is debated. One clue comes from Angelini et al, who in 1988 described the presence of a "cord-like ring" at the intersection of the atrium, ventricle, and mitral leaflets.[41] The completeness of, and the locations of gaps in, this ring were observed to vary widely among a cohort of 13 cadaveric hearts. More recently, Stephens et al illustrated that the distinct layers of the MV leaflets (especially the atrialis and fibrosa) may be considered to extend into the annulus.[42] Gunning et al, investigating collagen distribution in segments of the porcine mitral annulus, provided some evidence in favor of circumferential fiber alignment.[43] These findings are depicted in Figure 2-6 and Figure 2-7.

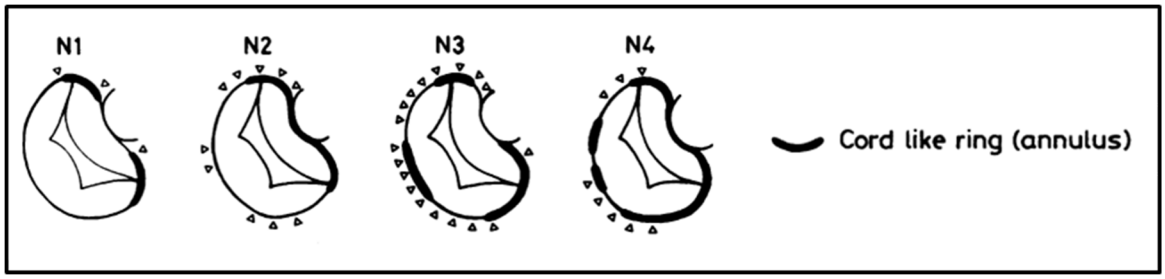

Figure 2-6 A 1988 illustration of the variability in the annular region among individual cadaveric hearts (modified from Angelini et al[41]).

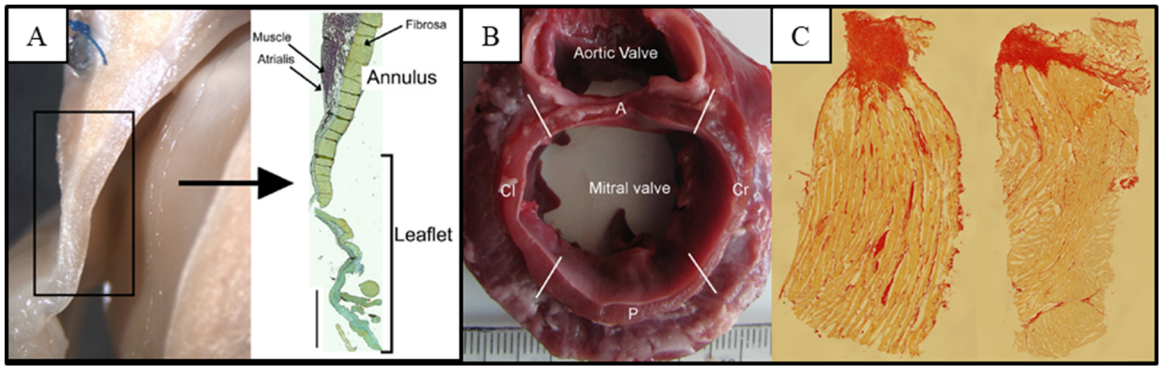

Figure 2-7 (A) Histologic illustration of the mitral leaflet and annulus, suggesting that the leaflet's layered structure may be considered to extend into the annulus (modified from Stephens et al[42]). (B-C) Segmental analysis of the porcine aortic annulus. Segments shown in (B) were stained for collagen; representative segments shown in (C) suggest collagen is aligned circumferentially around the MV (modified from Gunning et al.[43]

A few key characteristics of the MV annulus are functionally noteworthy. One arc of the annulus, centered at the mid-anterior annulus, sits in close proximity to the aortic valve. The region between the two valves is referred to as the *aortic mitral curtain*. At either end of the aortic mitral curtain, a few millimeters beneath the endocardial surface, are two dense fibrous structures, the *left and right trigones*. The right trigone is between the mitral, tricuspid, and aortic valves. Exterior from the trigones, the posterior annulus is surrounded by thick myocardium. Two major coronary vessels, the left circumflex artery and the coronary sinus, circumscribe the posterior annulus. Although Gunning et al reported that the anterior quadrant of the porcine annulus possessed over 8-fold greater collagen density than any other quadrant,[43] Stephens et al found approximately 1/3 collagen reduction in the posterior annulus versus every other quadrant.[42]

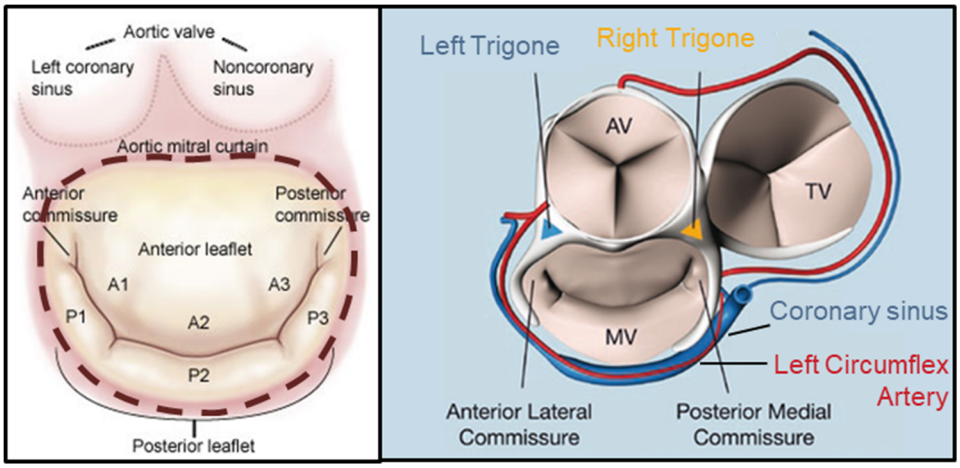

Figure 2-8 Left: Illustration of the closed MV as viewed from the LA (dotted line: mitral annulus; modified from Carpentier et al[37]). Right: Illustration of key structures surrounding the mitral valve (modified from cthsurgery.com).

The annulus is generally described as having a D-shaped projection, and a saddle shape when accounting for its three-dimensional shape.[44, 45] Yet, the annulus changes significantly in size and three-dimensional shape throughout the cardiac cycle. In a study of ovine annular dynamics by Rausch et al,[46] systolic contraction caused the septal portion of the annulus to increase in perimeter by 6%, while the lateral perimeter reduced by 7%. Annular area reduced by 15%, while eccentricity increased 14% (each based on its planar projection). Out-of-plane, the annular height increased by 65%. The accentuation of the saddle shape during systole is generally attributed to some combination of (a) lesser translation of the annulus toward the apex following to ventricular contraction in the inter-trigonal region, due to aortic root tethering,[47] and (b) expansion of the aortic root against this region due to the inflow of blood to the aorta.[48, 49]

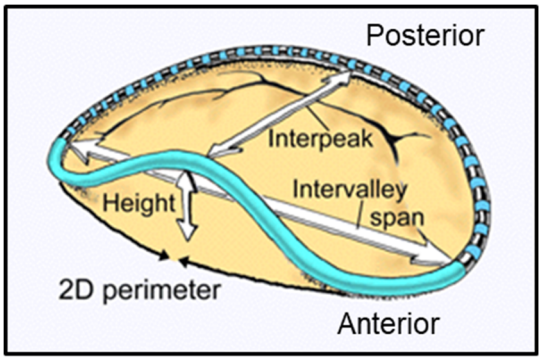

Figure 2-9 Three-dimensional saddle shape of the MV annulus (modified from depts.washington.edu/cvrtc).

2.3 Mitral Regurgitation

A major study by Nkomo et al. identified the MV as the most common heart valve to experience hemodynamically significant disease in the United States.[1] As with any heart valve, the two forms of dysfunction are *mitral regurgitation* (MR), in which it cannot close fully, and *mitral stenosis* (MS), in which it cannot open fully. MR is substantially more common than MS (estimated frequency among 2000 US adult population: 1.7% vs. 0.1%, respectively).[1] Due to the increased demand on the left heart, chronic MR leads to LA and/or LV enlargement (hypertrophy) as a compensatory mechanism. Over time, further enlargement may not adequately address these demands, leading to reduced ejection fraction. MR and LA enlargement may also induce secondary arrhythmia.[50] The resulting decompensated state may lead to patient fatigue, shortness of breath, and edema.

The two major classes of MR are *primary* (or *degenerative*) and *secondary* (or *functional*). Less common, particularly in developed countries, are congenital, inflammatory, and infective subtypes. In primary MR, the valve tissue itself undergoes

adverse remodeling. Morphologic changes may include connective tissue deficiency (such as in Fibroelastic Deficiency) or excess (with overall enlarged leaflets, such as in Barlow's disease).[51] Annular dilation and/or disorganization are common throughout primary MR,[52, 53] and at the time of surgery, rupture or elongation of one or more chordae is also usually observed.[52] Consequently, primary MR usually exhibits one or more sites of leaflet prolapse into the LA. In secondary MR, the MV leaflets and sub-valvular apparatus are generally regarded as biologically normal. Regurgitation occurs following an underlying annular and/or ventricular malfunction, which distorts leaflet geometry and inhibits coaptation. As such, secondary MR is often associated with significant comorbidities. In ischemic MR (IMR), ventricular remodeling follows from coronary disease, inducing papillary muscle displacement, annular dilatation, and restricted leaflet motion.[54]

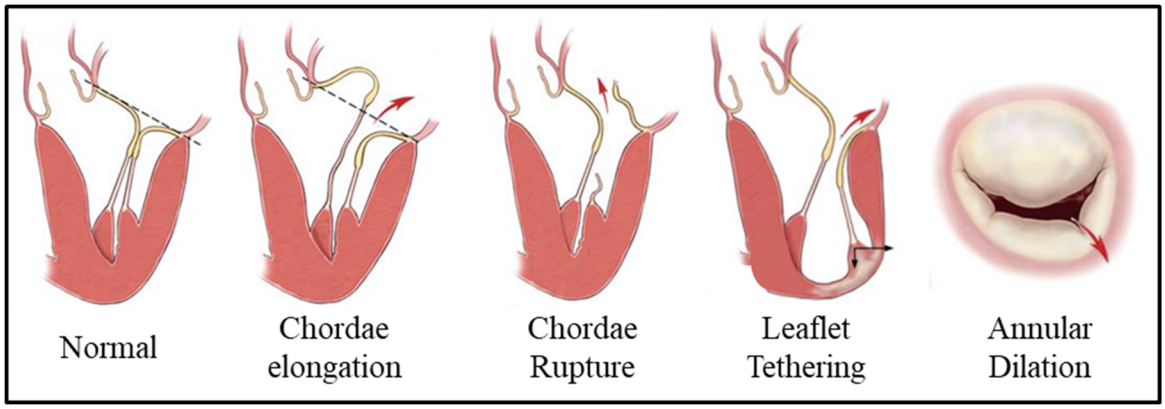

Figure 2-10 Examples of common mechanisms of MR (modified from Carpentier et al[37]).

MR severity is commonly graded as "none," "trace," "mild," "moderate," or "severe." Severity is also often referred to as "1+" (mild), "2+" (moderate), "3+" (moderate-to-severe), or "4+" (severe).[55, 56] Grading is multi-factorial, and can account for

structural and fluid descriptors.[57] One critical component of MR diagnosis is MR volume. Current American Heart Association guidelines classify primary MR or secondary MR as severe when regurgitant volume is ≥60 ml/stroke or ≥30 ml/stroke, respectively.[57] This discrepancy reflects the generally lower tolerance for regurgitation among secondary MR patients, on account of their increased comorbidities. Note, following implantation of a replacement mitral valve, MR may also take a third form, known as paravalvular leakage (PVL; i.e., leakage through one or more gaps along the annulus-device interface). PVL is further described in Section 2.5.2.

Overall, MR presents a sizeable clinical burden. MV prolapse can be surgically corrected, provided the patient is healthy enough for the operation. Yet, 45% of patients experience moderate or severe recurrent MR within ten years post-repair of degenerative MR.[52] Ischemic MR, which affects an estimated 2.2 million Americans,[58] has even poorer outcomes. Post-myocardial infarction patients have exhibited 1-year mortality rates of 11% with no MR, 22% with mild-to-moderate MR, and 52% with severe MR.[58] Surgical intervention may initially correct the condition, but survival remains poor, with 28% recurrence of severe ischemic MR within 6 months post-repair.[59]

2.4 Corrections for Mitral Regurgitation

2.4.1 Surgical Approaches to MR Correction

Surgical correction of MR centers around two paradigms: replacement and repair. In MV replacement, the native leaflets are removed, and a heart valve replacement implanted in

its place (the sub-valvular apparatus is often left intact[60]). Most surgical MV replacement devices feature three key components. First, leaflets replicate the function of the native leaflets. These are either bioprosthetic (i.e., derived from porcine or bovine leaflet or pericardium), or mechanical (commonly pyrolytic carbon). Second, a frame or housing secures the leaflets. Third, a suture cuff extending from the frame is tied directly to the native annulus. Whereas mechanical valves tend to outlast bioprosthetic valves, especially at the mitral position,[61, 62] their greater thromboembolic risk also necessitates anticoagulation therapy. The choice of replacement type is therefore a function of patient health and potential to withstand reoperation.

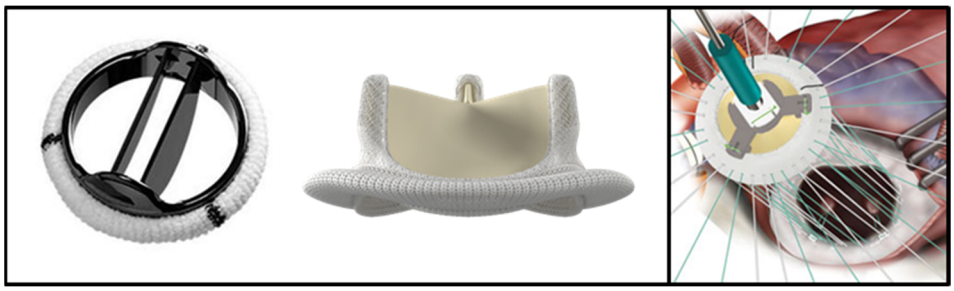

Figure 2-11 Left: The Regent™ (Abbott Laboratories, Chicago, IL) and PERIMOUNT (Edwards Lifesciences, Irvine, CA), examples of mechanical and bioprosthetic surgical heart valve replacement devices. Right: Suture-based implantation of the replacement valve into the native annulus.

In MV repair, the objective is to restore function to the native tissue, avoiding many of the potential complications of a complex artificial valve. Repair techniques are diverse, and may address the leaflets (e.g. by plication, augmentation or resection), chordae (e.g. by cutting problematic chordae or implantation of artificial "neo-chordae"), or papillary muscles (e.g. by approximation).[52, 58, 63-66] Nearly all of these techniques are used as

adjuncts to implantation of an *annuloplasty ring*. The ring generally consists of fabric wrapped around a solid core. Implantation is suture-based, similar to surgical valve replacement. Typically, a series of simple interrupted sutures is passed through the annulus and then the ring; the ring is then lowered down the sutures, and each suture is tied with multiple knot throws.

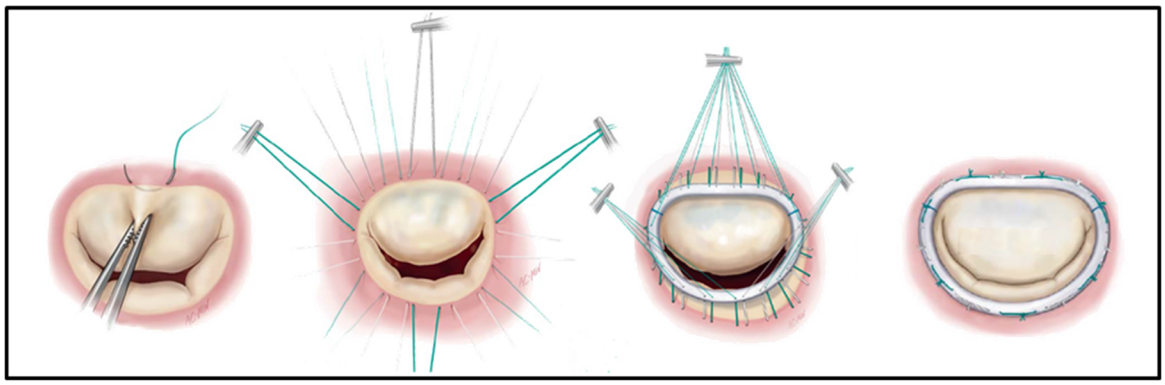

Figure 2-12 Mitral valve ring annuloplasty (modified from Carpentier et al[37])

Ring annuloplasty aims to restore proper annular shape and size, while simultaneously opposing further remodeling. Adams et al. have described annuloplasty as a mainstay of all primary MR repair procedures, "regardless of the leaflet and chordal techniques employed."[67] It is similarly recommended for both idiopathic and ischemic secondary MR.[63, 68] Numerous models are available commercially; specific device shapes, stiffnesses, materials, and sizes relative to the native annulus are frequently recommended for given MR etiologies.[69-72] For example, complete, undersized, rigid or semi-rigid rings are frequently recommended for ischemic MR.[63]

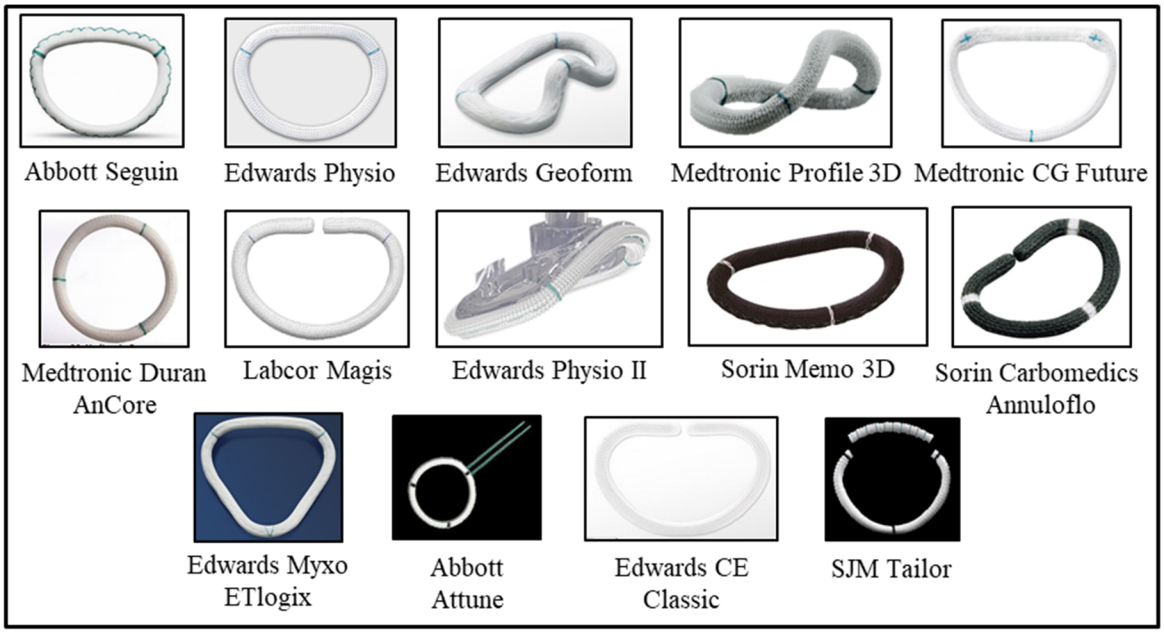

Figure 2-13 Common annuloplasty rings. In addition to the evident diversity in shape, rings also vary in stiffness, and are each available in a range of sizes.

2.4.2 Surgical Replacement vs. Repair – An Ongoing Debate

Provision of the optimal correction to every MR patient is a fundamental clinical goal. One challenge is that the superiority of MV repair versus replacement, particularly for ischemic MR, remains controversial.[5, 63, 73-75] Compounding this uncertainty, the likelihood of a surgeon electing MR repair has been shown to trend positively with the volume of operations they perform annually, likely due to the technical learning curve for repair.[73] This is a concerning statistic, given the median number of operations per surgeon per year is reportedly only five.[76] Clearly, a significant gap exists between current practice and the goal of optimal treatment.

2.4.3 Catheter-based Approaches to Correct MR

Furthering the gap between current practice and the goal of optimal treatment for all patients is the alarming fact that up to 50% of severe, symptomatic MR patients are denied surgery altogether, owing to high risk due to comorbidities.[11] For ischemic MR, it is estimated that less than 2% of 2.4 million patients receive surgical correction.[9, 10] To address this need, a wave of percutaneously delivered repair and replacement devices are currently in development.[12-16] These so-called *transcatheter* devices avoid the need for sternotomy and cardiopulmonary bypass. They offer significant potential to treat patients who are prohibitively high-risk for surgery, and perhaps even to provide advantage over surgery for lower-risk groups.

One repair device, MitraClip (Abbott Laboratories), was approved for United States use in degenerative MR in 2013. This device replicates the established surgical "edge-to-edge repair" technique.[77] The anterior and posterior MV leaflets are clipped together, easing their ability to coapt effectively. Presently, numerous important questions persist regarding MitraClip's usage, including its suitability for secondary MR, and best practices to avoid introduction of stenosis.[78, 79] It is also, in general, less effective than surgical techniques.[80] Revealingly, the EVEREST II clinical trial for MitraClip established a primary endpoint that included freedom from MR > 2+ at 12 months. Thus, moderate residual MR was considered successful treatment. Even so, MitraClip's primary endpoint rate (success rate) was significantly lower than that of surgical repair/replacement. A diverse range of other transcatheter MV repair devices are in development, aiming to replicate ring annuloplasty,[81] annulus plication, neo-chordae implantation, and others.[16]

Meanwhile, numerous transcatheter mitral valve replacement (TMVR) devices are also under development. TMVR takes inspiration from the recent success of transcatheter aortic valve replacement (TAVR). Transcatheter aortic valve replacement (TAVR) was developed for use in a calcified, stenotic aortic valve. It was first attempted in humans in 2002; 16 years later, multiple TAVR devices have received approval for sale in the United States and Europe. As of 2013, 27,000 new aortic stenosis (AS) patients were estimated to become TAVR candidates in North America and Europe annually.[82] Since that time, TAVR has been further approved for use in intermediate-risk patients.[83]

With substantially more patients suffering from MR than AS,[1] so many of whom are unfit for surgery,[11] the development of effective transcatheter mitral valves (TMVs) would have potentially transformative impact. Already, the TMVR procedure has found some early success for niche cases of mitral annular calcification (a subset of mitral stenosis)[84] and reoperation for recurrent MR post-annuloplasty (termed valve-in-ring).[85, 86] In these settings, off-label use of a TAVR device has proven viable, due to the relatively well-defined and smaller annular landing zone. However, for the majority of MR patients, TMVR must overcome challenges for which TAVR devices were not designed. These include higher pressure gradients, a larger, D-shaped annulus, and much more flexible (i.e., non-calcified) annular tissue, with a lower profile as compared to the aortic sinus.[12-14] Nevertheless, recognizing the substantial opportunity, many novel, dedicated TMVR systems are under development. At least 10 have reached clinical trials, and at least 20 others are in preclinical testing.[15] None has yet achieved regulatory approval.

Many common attributes exist among all TMV designs. In every case, a collapsible stent is fitted with bioprosthetic leaflets. The TMV is guided to the mitral annulus in

collapsed form via a catheter, and either self-expands or is expanded by a balloon. The deployed TMV anchors and seals without sutures, frequently relying on oversizing to generate radial force against the native annulus and some portion of the leaflets, along with some combination of additional features (flanges, cages, tethers, hooks, etc.).[14] The annular region of the stent is often circular, however, various iterations of oval or D-shaped stents have also been developed, to improve congruence with the native annulus shape.

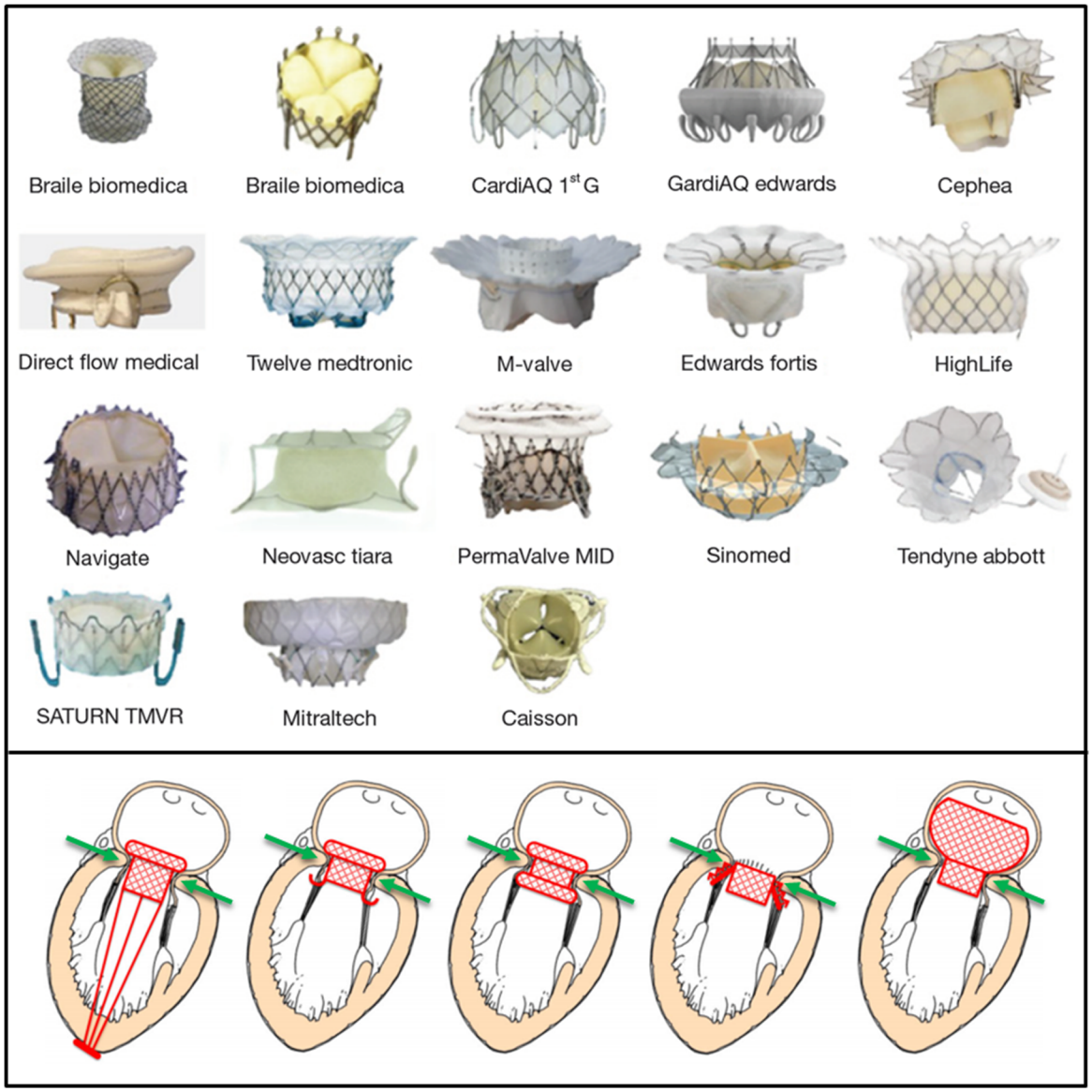

Figure 2-14 Top: Examples of publicly disclosed TMVs (modified from Carrel[15]). Bottom: Schematic depictions of some common modes of TMV anchoring/sealing. Green arrows indicate the annulus-contacting region, which is common to most designs (modified from Preston-Maher et al[14]).

2.5 Sub-Optimal Patient Outcomes

Despite the sizable benefit of both annuloplasty rings and prosthetic valves (and the anticipated benefit of TMVR), a number of modes of device failure present ongoing challenges to clinicians and device designers. These include, but are not limited to, device migration, paravalvular leak, hemolysis, thrombosis, embolization, structural failure, left ventricular outflow tract obstruction (particularly after TMVR), and adverse ventricular remodeling.[2-8] An important step in addressing these challenges is to characterize the underlying mechanisms at work. Improved understanding of the parameters governing such failures can inform advancements in device designs, standards, regulations, and usage techniques.

A common theme among many modes of MV device failure is adverse mechanical loading between the device and the native annulus. Although the biomechanics of the annulus have been increasingly studied in recent years,[43, 46, 87, 88] many aspects of device/annulus interaction remain poorly understood. For the purposes of this thesis, two issues are of particular interest: (a) suture dehiscence from the annulus after ring annuloplasty, and (b) paravalvular leak after TMVR. These are described in the following sections.

2.5.1 Annuloplasty Ring Suture Dehiscence

In the event that excessive force is applied on the sutures used to tie the annuloplasty ring to the MV annulus (Figure 2-12), *suture dehiscence*, or detachment from the annulus, can

result. Although the incidence of ring dehiscence is not known, evidence of its prevalence as a mode of critical device failure is growing in the literature. Partial and complete dehiscence have been demonstrated with varying devices and patient groups. Various studies of reoperation for failed annuloplasty-based MV repairs have reported the proportion of failures attributable to annular suture dehiscence to fall between 13-42%.[19-21] Looking specifically at degenerative MR, Dumont et al reported an overall suture dehiscence rate below 1%,[21] while Chitwood et al reported a rate of 2.3% among one center's first 300 robotic repairs.[89] _ENREF_83Kronzon et al reported 18 additional dehiscence cases across etiologies, encompassing 8 rings and 10 prosthetic valves.[90] Demonstrating that this risk extends to secondary MR repair, a large number of case studies have additionally been reported.[7, 91-94]

While these data collectively highlight the potential for dehiscence even at high-volume centers, its incidence may be greater at low-volume centers. Bolling et al reported that, among 1088 surgeons at 639 hospitals in the Society of Thoracic Surgeons Adult Cardiac Surgery Database, the median number of isolated MV operations per year was 5.[76] Further, it is likely that suture dehiscence is altogether underreported, given the common perception that it is purely a consequence of surgical error.

Literature demonstrates that the consequences of dehiscence are severe, emergent, and often fatal.[7, 89-99] However, little is known about what specific factors, if any, predispose to suture dehiscence. Interestingly, **it is apparent that sutures most commonly dehisce from the posterior annulus** (Figure 2-15 D-H). A mechanistic explanation for this observation could constitute a first step toward the reduction in its occurrence.

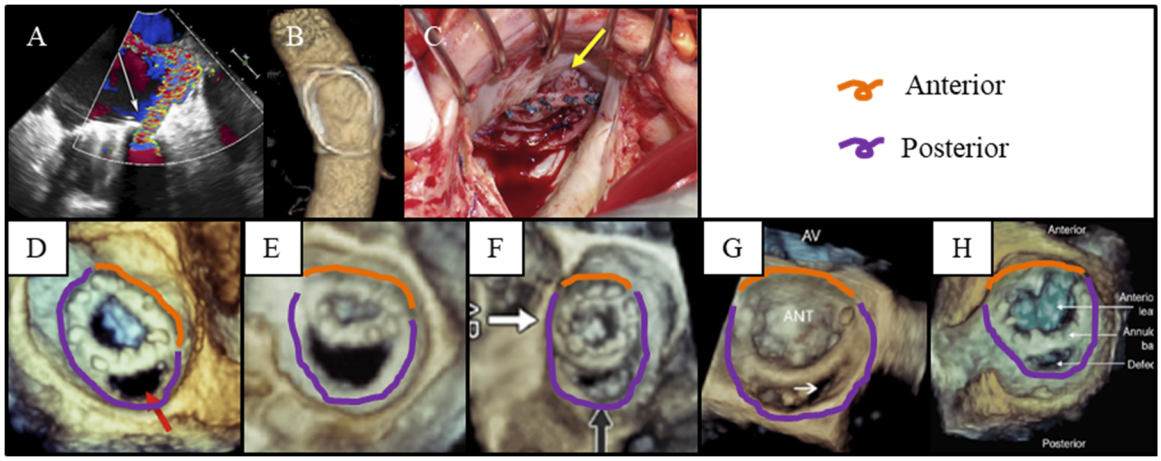

Figure 2-15 (A) Severe recurrent MR after ring dehiscence (modified from Jones-Haywood et al[7]). (B) Fully-dehisced and embolized ring, lodged in the descending aorta (modified from Tsang et al[94]). (C) Dehisced ring, photographed intraoperatively during re-repair (modified from Derkx et al[100]). (D-H) Cases of dehiscence from the posterior annulus (modified from Derkx et al,[100] Piatkowski et al,[95] Levack et al[93], Aggarwal et al[96], and Ghadimi et al[98]).

2.5.2 Paravalvular Leakage Post-TMVR

Whether valve replacement is performed surgically or percutaneously, its effectiveness is predicated on a competent seal between its exterior edge/face and the native tissue. Failure of this seal leads to regurgitation around the device periphery, known as *paravalvular leak* (PVL). Much like regurgitation through a faulty native MV, PVL hinders effective cardiac output. Further, another frequent consequence of PVL is *hemolysis* (red blood cell damage),[32, 101] likely owing to high-velocity regurgitant jets flowing past non-native materials. PVL is a significant problem for surgical MV replacement. In general, visualization and quantification is challenging, especially at mild or moderate levels.[33] Mitral PVL has proven highly lethal, with Cho et al reporting an event-free survival rate of approximately 40% at two years post-surgical MV replacement.[32] When PVL produces

symptoms of heart failure and/or hemolysis, correction is necessary.[102] Indeed, PVL is one of the leading causes of reoperation after surgical valve replacement.[6] For patients unfit for a second invasive surgery, PVL correction is challenging. Although percutaneous PVL closure is an emerging and promising field, it currently suffers from low reproducibility and from success rates reportedly as low as 60%.[34, 35]

In the TAVR setting, PVL has also proven a difficult challenge that is a function of both annulus-device congruence and of procedure.[103-105] Kodali et al demonstrated that PVL after TAVR significantly increases patient mortality, even when mild.[31] PVL is widely predicted to present an even greater challenge post-TMVR than post-TAVR. One reason for this is biomechanical:[49, 51, 97] the regurgitant mitral annulus is larger, less circular, more dynamic, and less rigid than the calcified, stenotic aortic annulus. The MV faces higher pressure gradients than the AV and the stent landing zone has a lower profile. Collectively, these factors challenge the TMV to generate sufficient radial force to seal against the native tissue around its full circumference. Another reason is experiential: mitral PVL is significantly more lethal than aortic PVL after surgical replacement.[32]

In limited publicly available information following animal and carefully selected human trials, early evidence of PVL post-TMVR has validated these concerns. In one instance, Ma et al reported significant PVL due to device-annulus mismatch.[27, 28] Sondergaard et al reported that the CardiAQ valve (Edwards Lifesciences) underwent design modifications from first- to second-generation to reduce PVL, which culminated in mild PVL in a first-in-man trans-femoral implantation.[29, 30] The Tendyne valve (Abbott Laboratories), following incidents of PVL in its first-generation design testing, introduced second-generation modifications that included imitation of the native annulus' D-shape.[26,

[27] Still, with no TMV yet to achieve regulatory approval, the eventual incidence of PVL upon wider TMVR usage remains to be determined. It is clear that a rigorous understanding of TMVR PVL dynamics will be necessary for device designers, regulators, and clinicians to effectively minimize its occurrence. Presently, very little engineering research exists regarding the influences of fundamental TMV design parameters on resultant PVL.

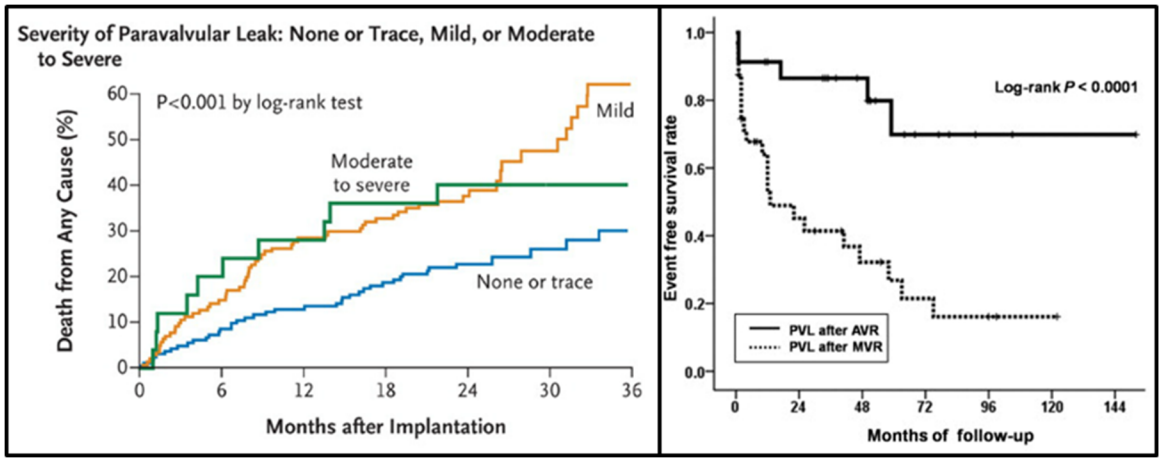

Figure 2-16 Left: Post-TAVR, even mild PVL significant increases mortality (from Kodali et al[31]). Right: Post-surgical valve replacement, PVL is significantly more lethal at the mitral position (from Cho et al[32]).

2.6 Investigations of MV Mechanics to Improve MR Treatment

2.6.1 Precedent

Large animal models and benchtop testers are well-established tools for the characterization of MV mechanics.[17, 18] Assessment of valve performance across well-controlled parameter spaces of interest (e.g. valve geometry, hemodynamic conditions, or repair type) is a fundamental approach toward the development and optimization of treatments for MR. One benefit of animal testing is the ability to employ high-fidelity

measurement tools that are too invasive, destructive, or high-risk for use in humans. Examples include trackable positional markers, radiographic imaging systems, pressure monitors, or force transducers. When the research question permits greater simplification, explanted mitral valves or whole hearts are may be mounted in benchtop cardiovascular simulators. These anatomic structures are integrated with various hardware components, including pumps, idealized anatomic replicas, and "lumped" resistance and compliance elements. Advantages of this testing format typically include an increased range of measurement equipment, rapid iteration among test conditions, and cost efficiency. Relevant studies of valve mechanics using these approaches include:

- Description of MV annular motion during the cardiac cycle, using trackable, radiopaque markers in normal ovine subjects.[46]

- Measurement of the MV annulus' radial contractile forces in normal and IMR ovine subjects.[106, 107]

- *In vitro* simulations of MV function following repairs or geometric alterations of interest, using explanted ovine or porcine valves mounted within an adjustable mock annulus/left heart. Optimization of leaflet augmentation patch dimensions to repair IMR,[108] or quantification of leaflet chordal forces according to the annulus' saddle height,[45] are two successful examples.

- *Ex vivo* recreations of passively beating, whole porcine hearts, with boroscopic or sonomicrometric tracking of leaflet kinematics.[109, 110] Use of the whole heart may be critical for research questions that depend upon accurate representation of the

complex material behaviour of the structures *surrounding* the valve itself (e.g. the annulus or aortic root).

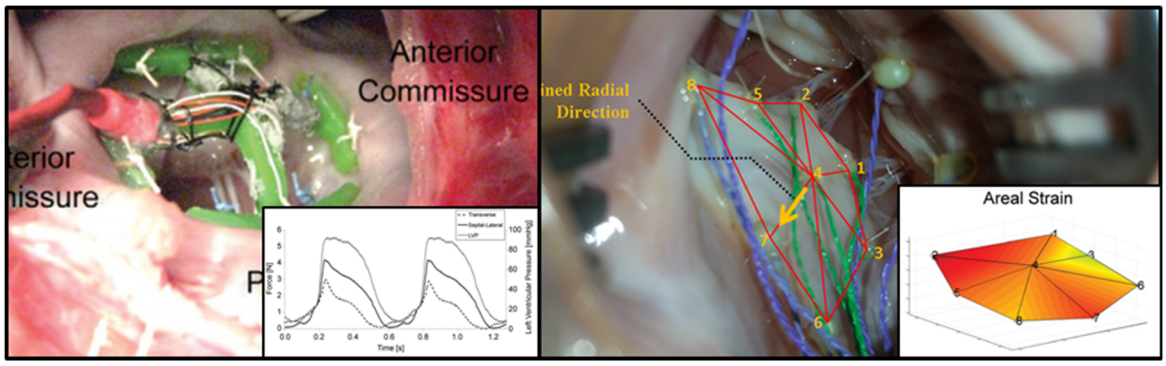

Figure 2-17 Left: *In vivo* assessment of MV annular contractile forces in ovine subjects (modified from Siefert et al[107]). Right: *Ex vivo* assessment of tricuspid valve leaflet strain in an explanted, passively beating porcine heart (modified from Khoiy et al[109]).

2.6.2 Potential for Impactful New Investigations

As described in Section 2.5, it is clear that numerous failure modes following MR correction are attributable to events occurring *at the device-annulus interface*. Despite a rich recent history of engineering research to understand MV mechanics and to optimize MR corrective techniques, suture dehiscence post-annuloplasty and PVL post-TMVR stand out as two such failure modes that remain markedly understudied. Systematic descriptions of annuloplasty suture force dynamics and of TMVR PVL dynamics are expected to yield meaningful insights toward improved strategies for device design, standardization, regulation, and usage. In the present work, these dynamics are explored as functions of both the MV annulus' material behavior and of fundamental device design parameters. The specific aims are described in the following chapter.

CHAPTER 3. HYPOTHESIS AND SPECIFIC AIMS

The incidence of moderate-to-severe mitral valve (MV) regurgitation in the US is 1.7% and rising.[1] The landscape of prostheses to correct mitral regurgitation (MR) is diverse and steadily expanding. These consist mainly of annuloplasty rings that reconstruct the native tissue, and prosthetic surgical heart valves that replace native MV function. Conventionally, these devices are implanted with interrupted sutures, which anchor the device to the MV annulus. Alternatively, a new wave of percutaneously implanted devices, which do not require sutures, are now in development, aiming to reach market throughout the next decade.[111] Of these, a cohort of *transcatheter mitral valve replacement* (TMVR) devices are implanted by means of radial expansion against the native MV.[13, 14] Among both surgical and transcatheter devices, nearly all rely on anchoring and/or sealing to the MV annulus, a D-shaped region of structurally and kinematically heterogeneous tissue. The mutual loading between annulus and device is a complex interplay between device design and tissue mechanics.

Ideally, this loading allows for stable, durable anchoring/sealing, and helps to ensure freedom from recurrent MR. In contrast, either excessive suture force post-surgical implantation or insufficient radial force after transcatheter mitral valve (TMV) deployment can have disastrous consequences. These have included paravalvular leak (PVL), hemolysis, and device embolization,[7, 90, 94, 99] all of which significantly increase morbidity/mortality rates. Trending with more frequent clinical reports of suture dehiscence,[7, 89-96, 99] and with the growing clinical potential for TMVR, increased attention is being paid to these performance concerns by manufacturers, regulators, and the

International Standards Organization.[112-114] Yet, limited publicly available work to date has systematically explored the impact of device design or physiology on the adequacy of annular anchoring/sealing, either for surgical (suture-based) or percutaneous devices.

To aid the development of next-generation suture-based devices and implantation techniques to prevent dehiscence, defining the mechanisms governing its occurrence is critical. Learning from surgical experience, TMVR outcomes may be improved *prospectively* by similarly characterizing the requirements for an optimal TMV-annulus seal. This thesis hypothesized that **improved understanding of the mechanical loading between the mitral valve device and the native annulus can reduce the risk of failure failure at their interface.** This was be tested through the following Specific Aims:

Specific Aim 1: Identify strategies to improve annuloplasty ring suture retention by describing the sensitivity of suture forces to ring design and annular biomechanics. First, the basic mechanism of annuloplasty ring suture dehiscence was characterized. Annular suture holding strength was measured in an *ex vivo* test system. Strength dynamics were linked to underlying tissue microstructure using two-photon excitation flouroscopy. Tensile forces acting on individual annuloplasty sutures in the beating heart were measured using custom, strain gage-based sensors.[24] Transducers were manufactured, calibrated, and attached to a common commercial annuloplasty ring. The instrumented ring was implanted in healthy ovine subjects and cyclic contractile forces (F_C) were recorded. Next, using this data as a reference, a parametric assessment of the impact of ring design on F_C was conducted. Ring shape, ring sizing, and ring stiffness were systematically varied, and the

resulting F_C distributions were analyzed. This effort relied on a novel system for the fabrication of rings of desired material properties. These results provide insight into the clinical potential for ring selection/sizing to affect suture tension around the annulus. Further, they motivate the development of putatively optimized ring design strategies to reduce suture dehiscence likelihood. One such novel ring was prototyped, and its F_C dynamics preliminarily assessed *in vivo*.

Specific Aim 2: Quantify the impact of TMV size and shape on PVL and radial expansion force. The importance of radial loading to prevent PVL post-transcatheter *aortic* valve replacement is well documented.[103, 104, 115] At the MV position, the annulus' complexity presents an added challenge to optimizing TMVR radial loading. The risk of PVL post-TMVR will depend on the mechanical interaction between stent and annulus (multiple stent shapes have been proposed, and sizing is poorly understood). A novel, whole-heart, steady flow simulator was developed. Using rigored porcine hearts, mock D-shaped and circular TMV "plugs" (simulating closed TMVs) were implanted over a range of sizes. PVL was quantified under fixed pressures by ultrasonic flow probes.[112] Further, a custom, strain gage-based force sensing system was developed and employed in porcine hearts, to provide direct assessment of the force required to radially expand each TMV design to the same oversizing levels studied in PVL testing. Comparison of TMV shapes and sizes in terms of PVL and radial expansion force will aid the development of optimized TMV geometries, to improve sealing performance and/or allow for lower-profile delivery.

The completion of this work has yielded extensive insights into (a) the hazards surrounding MV annulus-device interaction, and (b) associated design, testing, and usage strategies to improve device performance.

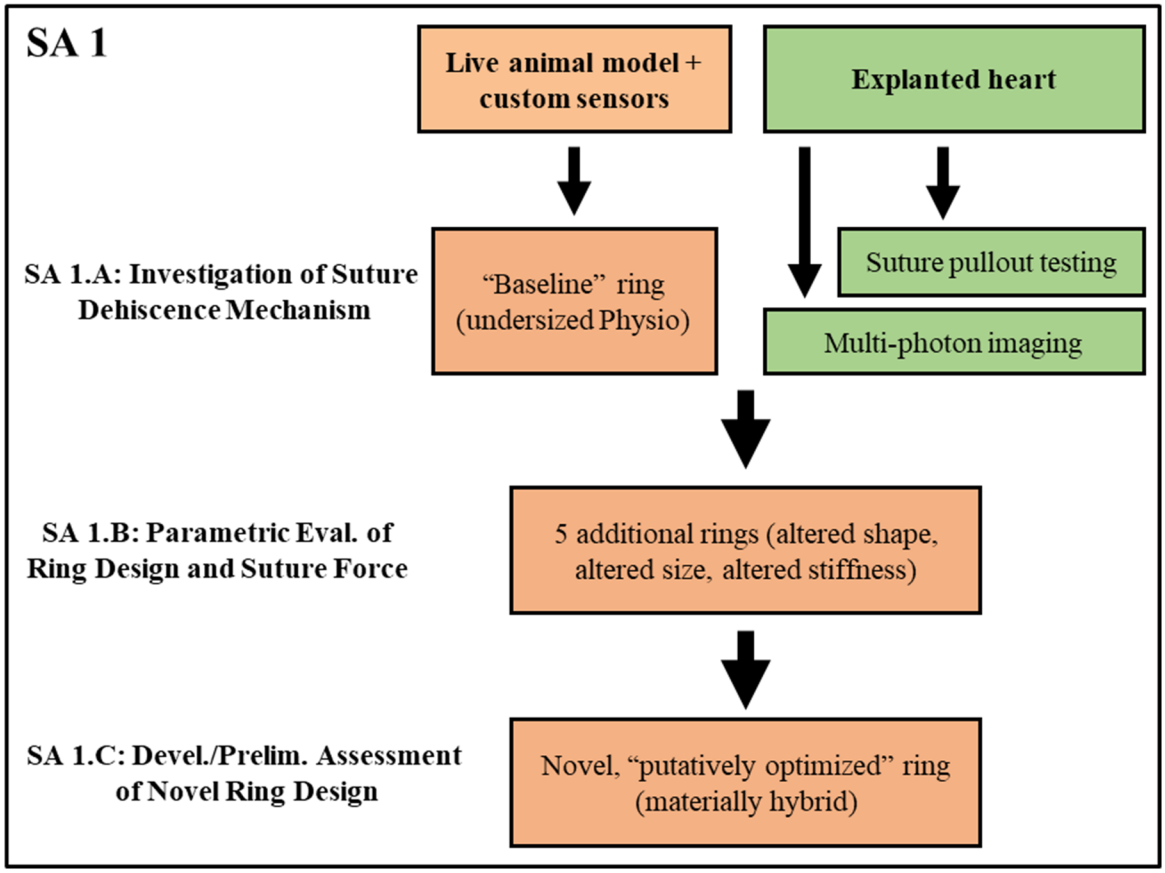

Figure 3-1 Schematic for SA 1 experiments.

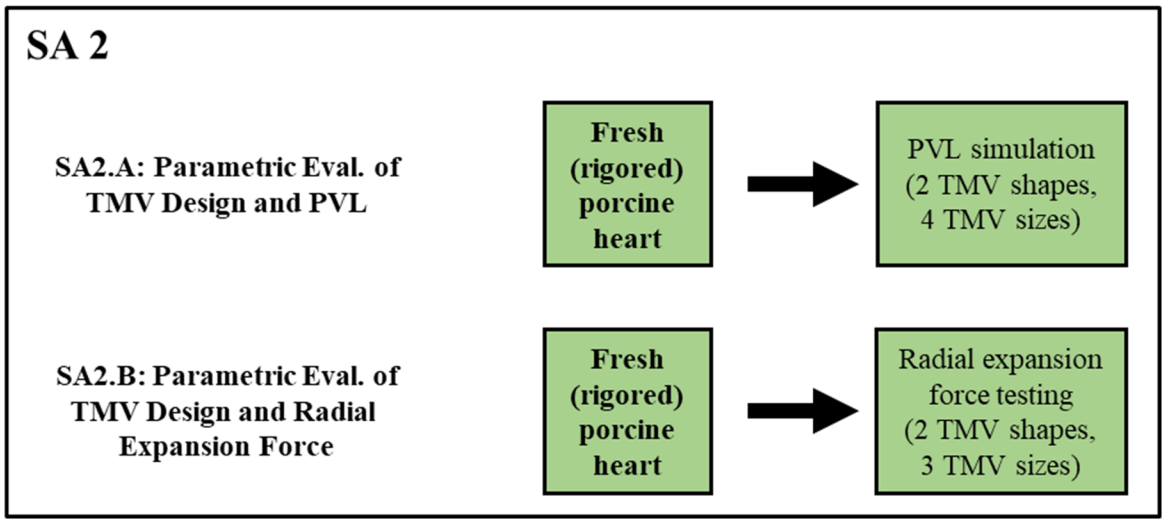

Figure 3-2 Schematic for SA 2 experiments.

CHAPTER 4. MATERIALS

Note that many custom components were used in this thesis. All computer aided design was performed in SolidWorks (Dassault Systemes, Waltham, MA). Computer aided design files have been uploaded to the Georgia Tech repository as a supplement to this thesis. Files for both individual parts and multi-component assemblies are included. For more information, refer to the supplement and/or APPENDIX H. This appendix also describes material and method used for fabrication.

4.1 Specific Aim 1 Materials

4.1.1 Test Subjects

4.1.1.1 Ovine subjects used in *in vivo* testing

In SA 1.A, 1.B, and 1.C, annuloplasty suture force dynamics were studied in the beating hearts of normal Dorsett hybrid sheep (a well-established model for heart valve research).[116] These studies were conducted at the University of Pennsylvania, in collaboration with the Gorman Cardiovascular Research Group. The animals used in this work received care in compliance with protocols approved by the Institutional Animal Care and Use Committee at the University of Pennsylvania, in accordance with guidelines for humane care (National Institutes of Health Publication 85-23, revised 1996).

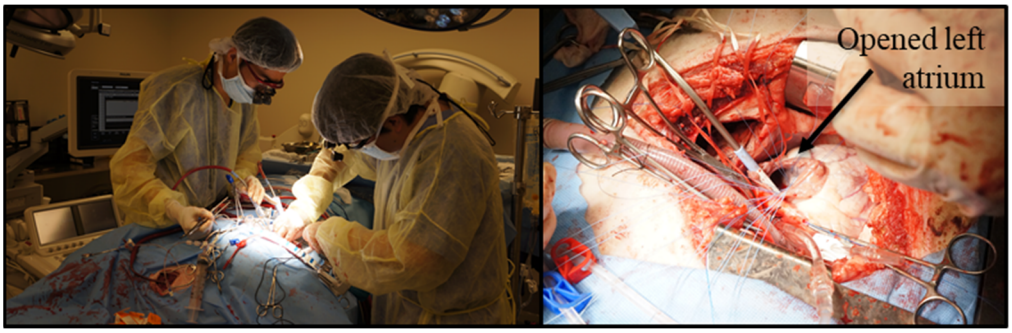

Figure 4-1 Left: Peri-operative image of surgical suite. Right: Ovine subject post-thoracotomy and left atriotomy.

4.1.1.2 Ovine annular tissue used in *in vitro* testing

In SA 1.A, suture pullout and collagen quantification tests were conducted on mitral annuli, explanted from normal ovine hearts. These hearts, procured from a local market via Superior Farms (Sacramento, CA), were previously frozen; prior studies have established previously frozen MVs and annuli as suitable structural models for living tissue.[117, 118]

4.1.2 Annuloplasty Rings

4.1.2.1 Commercial Rings

In vivo testing in SA 1 used five different annuloplasty rings, two of which were commercial products. These were the flat, semi-rigid Physio (Edwards LifeSciences, Irvine, CA) and the saddle-shaped, rigid Profile 3D (Medtronic, Dublin, Ireland). Sizes 24, 26, and 28 of each ring type were used.

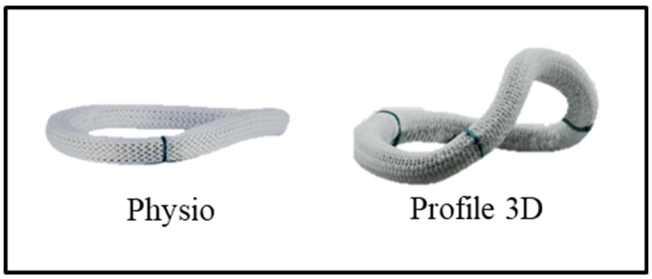

Figure 4-2 Commercially available annuloplasty rings used in this work.

4.1.2.2 Prototype Rings

Three annuloplasty rings (used in SA 1.B and 1.C) were prototypes, based on the Physio or Profile 3D geometries. Each such ring was manufactured in sizes 24, 26, and 28. The methods by which these were produced and analysed are discussed in Section 5.1.2.

The fully-rigid prototype ring was 3D printed from polycarbonate (Stratasys, Eden Prairie, MN) at Georgia Tech College of Architecture. The fully-flexible prototype ring was cast in-house from quick-curing, durometer 40A silicone putty (Quick-Sil, Castaldo, Franklin, MA). The hybrid ring consisted of two core segments of 3D printed Ti-6AL-4V titanium (Protolabs, Maple Plain, MN) overmolded with the same silicone used for the fully-flexible rings. Both the fully-flexible and hybrid rings were cast using specialized molds. These molds were 3D printed from VeroWhite (Stratsys) or GPCL02 (FormLabs, Somerville, MA), at the Georgia Tech Manufacturing Institute or at 3D Printing Tech (Atlanta, GA), respectively. These materials were selected because they could be printed at high resolution (each part was printed at 50 μm or better).

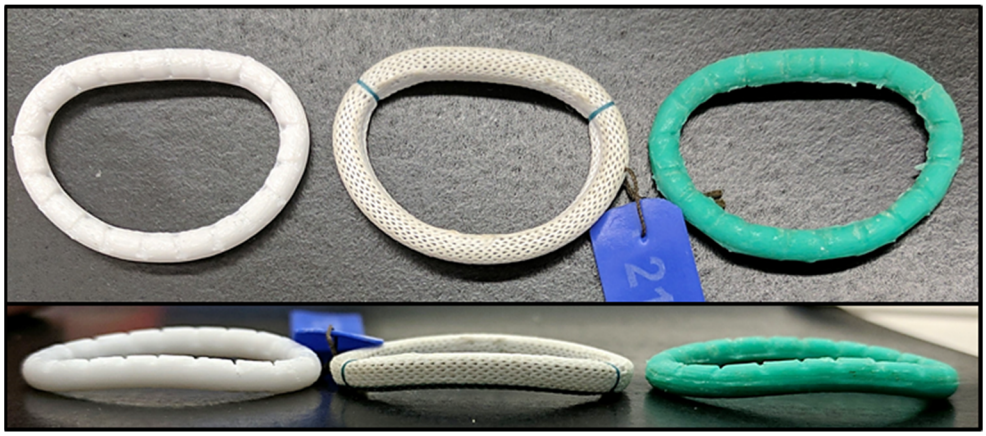

Figure 4-3 Top and side views of rigid (left) and flexible (right) prototype rings. Semi-rigid commercial Physio ring is shown in center to illustrate matched geometry.

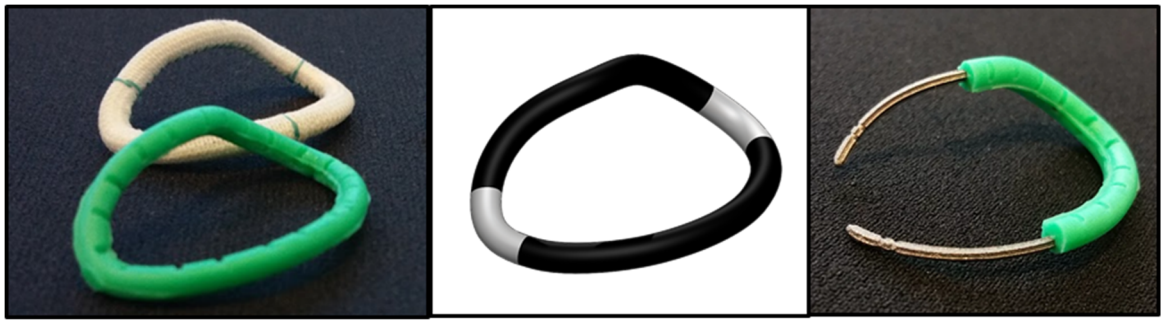

Figure 4-4 Left: Hybrid prototype ring, with Profile 3D shown in background to illustrate matched geometry. Center: schematic CAD rendering of segmental material properties (black: rigid; white: flexible). Right: hybrid ring with portion of silicone overmolding cut away, illustrating the embedded titanium segments.

4.1.3 Suture Force Transducers

4.1.3.1 Suture Force Transducer Materials

Suture force measurements used previously designed and demonstrated transducers.[24] These were manufactured in-house, using the components listed in Table 4-1 and detailed further in Section 5.1.1.

Table 4-1 Materials used for manufacturing Suture Force Transducers.

	Supplier	Item	Supplier Serial Number
1	Protolabs (Maple Plain, MN)	3D printed spring element (316L stainless steel)	N/A
2		Rosin flux	7799A11
3		Loctite E-120HP epoxy	6430A24
4		Heat shrink tubing	7856K33
5		Electrical pins	69295K111
6		Electrical sleeves	69295K115
7	McMaster Carr	Electrical pin housing (12 pole)	69295K99
8	(Atlanta, GA)	Electrical sleeve housing (12 pole)	69295K8
9		M-Prep Conditioner A	MCA-1
10		M-Prep Neutralizer 5A	MN5A-1
11		Sandpaper	SCP-3
12		Surface wipes (gauze)	GSP-1
13		Strain gage installation tape	PCT-2M
14		Half-bridge strain gages	EA-13-062TZ-350/E
15		M-Bond 200 adhesive and catalyst	F006678
16		M-Line Rosin Solvent	RSK-1
17		Waterproofing sealant (nitrile rubber)	F006688
18	Micro-Measurements	Eutectic solder	361A-20R-25
19	(Wendell, NC)	36 gage, etched PTFE-coated, three-stranded wire	336-FTE

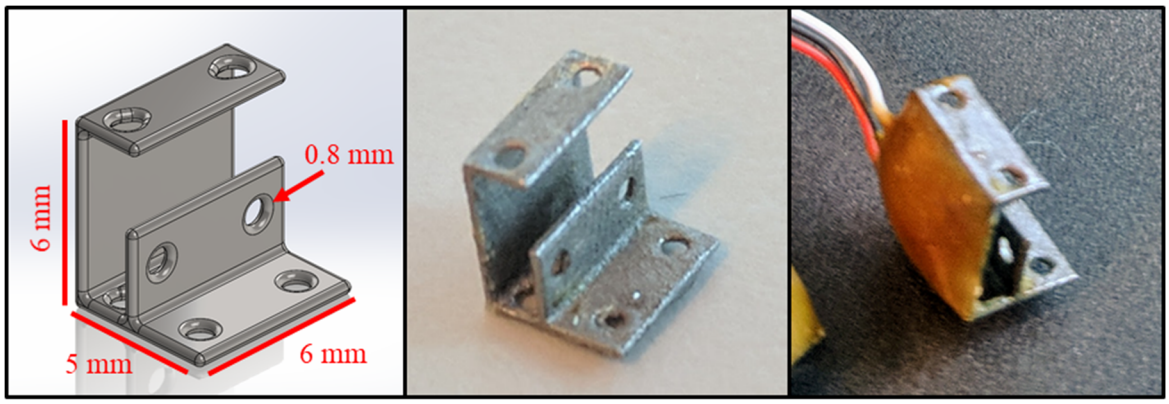

Figure 4-5 Left: CAD rendering of spring element. Middle: Printed spring element, prior to strain gage instrumentation. Right: Fully instrumented Suture Force Transducer.

4.1.3.2 Suture Force Transducer Data Acquisition System

Two identical data acquisition systems were used for all Suture Force Transducer-related testing (i.e. one each at Georgia Tech and at University of Pennsylvania). All system components and software were from National Instruments (Austin, TX). This system utilized a modular compact Data Acquisition System (cDAQ-9174), equipped with three strain gage input modules (NI-9237 DSUB) for strain gage signal recording, and, when applicable, one analog voltage input module (NI-9215) for left ventricular pressure (LVP) recording. LVP was measured using a high-fidelity pressure transducer (SPR-3505; Millar Instruments, Houston, TX). Data was monitored and recorded using a custom LabVIEW program.

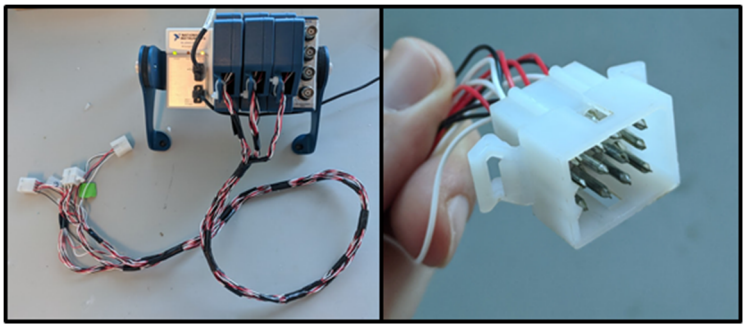

Figure 4-6 Left: Data Acquisition Hardware, including cDAQ chassis, input modules, and wiring. Right: Close-up view of a handsome man's hand holding the plugs for connection to the strain gage-based transducers.

4.1.4 Suture Pullout Testing

In order to pull sutures from mitral annuli in Specific Aim 1.A, each annulus was first excised and mounted to a multi-layer test plate. The plate's top layer was a sheet of rubber, to which the annulus was attached, as described in Section 5.1.3. The rubber was glued to a rigid acrylic plate, which in turn was fixtured to the upper-most of three aluminium layers. The aluminium layers were free to slide along one another in two orthogonal directions; the desired position could be fixed with lateral set screws. Testing was performed with an ElectroForce 3200 uniaxial tester (Bose Corporation, Eden Prairie, MN), equipped with a 25 N in-line load cell (SMT1-22; Interface, Scottsdale, AZ).

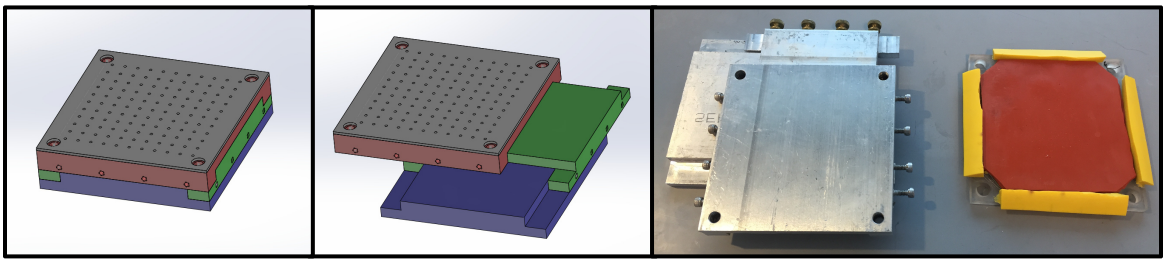

Figure 4-7 Suture pullout testing plate. Left, Center: CAD renderings of aluminum and acrylic layers, demonstrating the two degrees of lateral freedom the top layer achieves relative to the bottom. Right: As-manufactured test plate, with acrylic/rubber layer detached. Lateral set screws enabled locking to a desired position.

4.1.5 Collagen Quantification

Collagen quantification in Specific Aim 1.A used the native autofluorescence properties of the tissue under two-photon excitation. After slides were prepared for each sample (using 30 μm thick slices of annulus tissue), they were imaged under a 10X objective (1.66 x 1.66 μm resolution) using a laser scanning microscope (LSM 710 NLO; Zeiss, Oberkochen, Germany).

4.2 Specific Aim 2 Materials

4.2.1 Test Subjects

All SA 2 experiments were conducted using porcine hearts, acquired the same day from a local slaughterhouse (Holifield Farms, Covington, GA), and tested 5-12 hours post-mortem. Importantly, these hearts were in rigor mortis, a natural stiffening of muscle that

occurs after death due to the depletion of the molecule adenosine triphosphate.[119] In the absence of adenosine triphosphate, strong actin-myosin bonds lock the muscle. Rigor may begin in under one hour and persist until tissue degradation induces a more relaxed state once again. Myocardial contraction during rigor mortis is reportedly 60-100% of normal systolic contraction in the beating heart.[120, 121] Therefore, these hearts were intended to model a snapshot of a beating heart's material properties during systole.

Hearts were selected according to target dimensions of the MV annulus perimeter, as described in **5.2.1**. Two key measurements of the mitral annulus were used as selection criteria: inter-trigonal distance and total annular perimeter.

Following a preliminary assessment of the available hearts in terms of (a) the range of sizes commonly available, and (b) the correlation between annular perimeter and inter-trigonal distance, specifications of inter-trigonal distance = 30 mm and annular perimeter ≈ 108.4 mm were set. This assessment is detailed in Section 5.2.1. Inter-trigonal distance was measured using a Physio annuloplasty ring sizer set (Edwards LifeSciences).

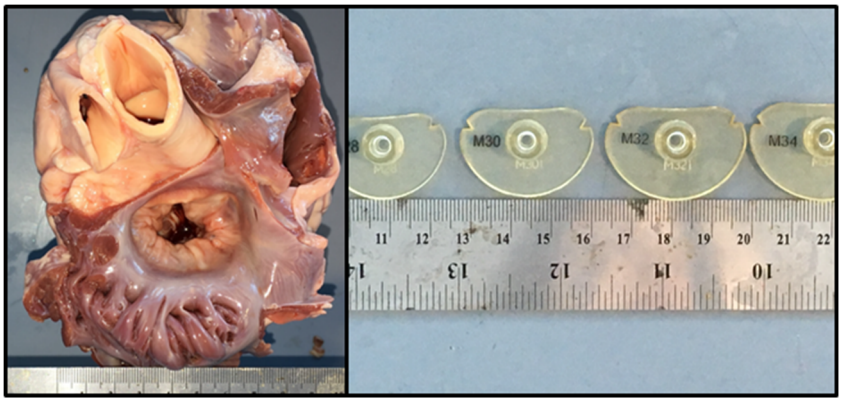

Figure 4-8 Left: Porcine heart trimmed to expose mitral annulus for sizing. Right: Annuloplasty sizer set used for inter-trigonal distance measurement.

4.2.2 Mock TMV Plugs (SA 2.A)

In SA 2.A, TMVR paravalvular leak was investigated using "mock TMV plugs," as opposed to commercial or pre-market TMV devices. These plugs, which were made in house, served to occlude the mitral orifice under trans-mitral pressure gradient (ΔP) between 50-210 mmHg, in a manner analogous to a TMV with perfectly sealed leaflets. After deploying a plug, any leakage across the mitral orifice was paravalvular (paravalvular leak, PVL).

Each plug was rapid-prototyped from ABS plastic (Stratasys) and acetone vapor-polished. The region that contacted the mitral annulus was wrapped with a polyester fabric that is intended for use in cardiovascular implants (007831; C.R. Bard, Inc., Murray Hill, NJ).

Eight plugs in total were used, including D-shaped and circular devices, each in four perimeter-matched sizes (termed +0, +2, +4, and +6). Their specific dimensions of

were selected based on a preliminary assessment of (a) the range of sizes commonly available from the slaughterhouse, and (b) the correlation between annular perimeter and inter-trigonal distance in these hearts. The details of this assessment, including the final dimensions, are provided in Section 5.2.1. Further details of plug design/function are provided in Section 5.2.2. An image of the plugs, and the handling funnel used to position and collect flow past them, is given in Figure 4-9.

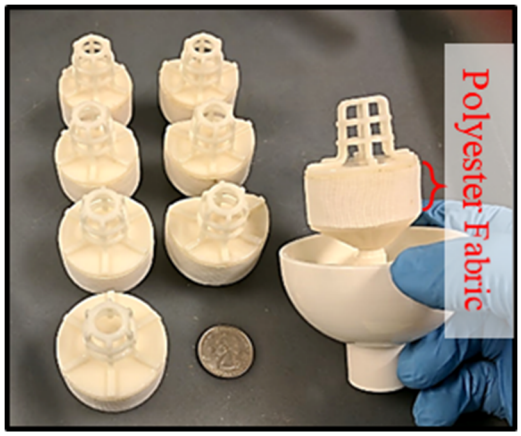

Figure 4-9 Eight mock TMV plugs used for PVL testing. At right, one plug is mounted to the handling funnel. Further details are provided in Section 5.2.2.

4.2.3 Steady Back-Pressure Test System (SA 2.A)

4.2.3.1 Flow Loop Materials

PVL measurements used porcine hearts mounted in a novel flow loop, in which steady ΔPs of interest were generated. ΔP and trans-mitral leakage flow rate were monitored. The flow loop consisted of the components listed below.

Table 4-2 Materials used for the assembly of flow loop.

	Supplier	Item	Supplier Serial Number
1	Holifield Farms (Covington, GA)	Porcine heart	N/A
2	QC Supply (Schuyler, NE)	Small umbilical clamps	140899
3	Dayton Electric Manufacturing, Co. (Lake Forest, IL)	Steady flow pump	12U596
4	Powerstat (Bristol, CT)	Variac transformer	3PN126
5	Utah Medical Products (Midvale, UT)	Pressure transducer	6199
6	Transonic (Ithaca, NY)	In-line flow meter	ME25PXN
7	VWR (Radnor, PA)	Thermometer	89369-136
8	McMaster Carr (Atlanta, GA)	Ball valves	4757K19
9		Tubing and connectors	various
10	Made in-house	Apical port	N/A
11		Drill bit for apical port	N/A

The apical port was a two-part device, which was 3D printed from ABS plastic (Stratasys), acetone vapor-polished, and threaded. The inner component (shown in red in Figure 4-10) was passed through the mitral orifice and then its narrow tubular region was passed through a hole in the apex (ID = 0.3”, OD = 0.5”). The outer component (shown in blue in Figure 4-10) was then screwed onto it until tight, such that apical tissue was sandwiched in between the flanges to create a robust seal. The apical hole was made using a custom hole-cutting drill bit, lathed from aluminium (ID = 0.21”, OD = 0.25”, filed to a sharp edge).

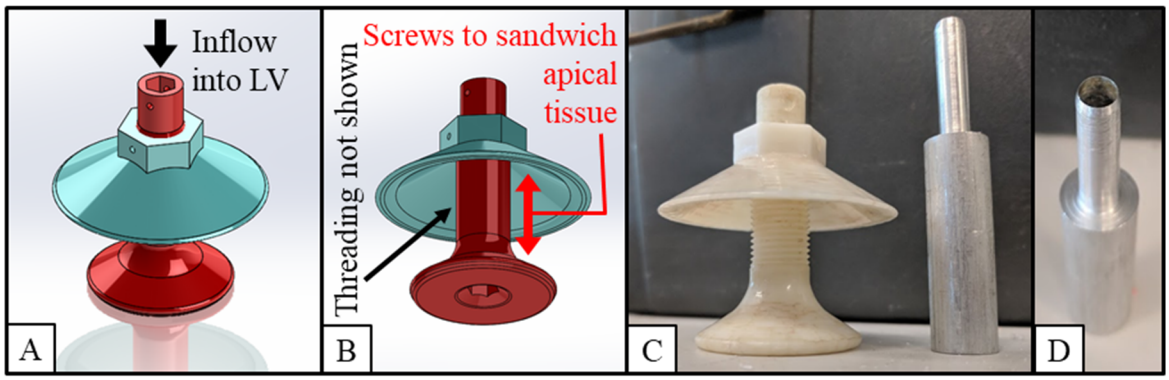

Figure 4-10 (A-B) CAD renderings of apical port. Threading was added manually to each part after vapor polishing and is not shown. (C-D) Images of finished apical port and apical port drill bit.

4.2.3.2 Flow Loop Data Acquisition System

The data acquisition system used for PVL studies was the same as that used in SA 1 (see Section 4.1.3.2). However, in this case, strain modules (NI 9237) were not used; only the BNC analog voltage input module (NI 9215) was used for pressure and flow monitoring.

4.2.4 Radial Expansion Force Transducer (SA 2.B)

4.2.4.1 Transducer Materials

TMV radial expansion force measurements used either of two variants of a novel force transducer, referred to as the Radial Expansion Force Transducer (REFT). These variants were the Circular REFT (C-REFT) and D-shaped REFT (D-REFT). Either transducer was deployed within the mitral annulus and expanded radially; the radially-inward force with which the tissue opposed this expansion was measured along the septal-lateral (SL) and inter-commissural (IC) axes via a network of strain gages. REFTs were manufactured in-house, using the materials listed in

Table 4-3 and described in detail in Section 5.2.4.

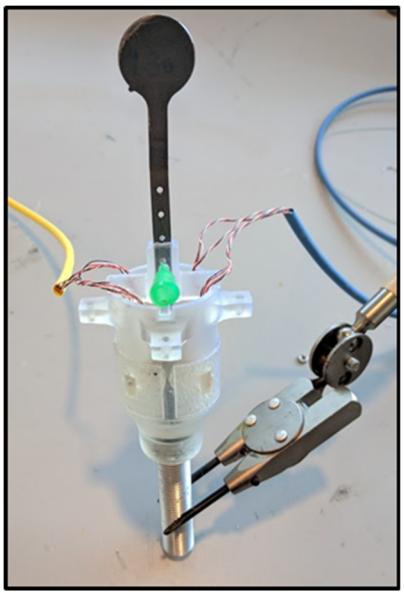

Figure 4-11 Circular Radial Expansion Force Transducer (C-REFT).

Table 4-3 Materials used for manufacturing Radial Expansion Force Transducers.

	Supplier	Item	Supplier Serial Number
1	3D Printing Tech (Atlanta, GA)	3D printed hubs (Form Labs Clear Resin)	N/A
2		3D printed arms (Form Labs Clear Resin)	N/A
3		3D printed wedges (Form Labs Clear Resin)	N/A
4		3D printed caps (Form Labs Clear Resin)	N/A
5	McMaster Carr (Atlanta, GA)	Loctite 4014 Adhesive	1818A43
6		1/2"-20 Aluminum Threaded Rod, for machining	94435A533
7		Low-carbon steel sheet, for machining	2102T27
8		Rosin flux	7799A11
9		Loctite 3321 UV Curable Adhesive	6430A24
10		Heat shrink tubing	7856K33
11		Electrical pins	69295K111
12		Electrical sleeves	69295K115
13		Electrical pin housing (12 pole)	69295K99
14		Electrical sleeve housing (12 pole)	69295K8
15	Micro-Measurements (Wendell, NC)	M-Prep Conditioner A	MCA-1
16		M-Prep Neutralizer 5A	MN5A-1
17		Sandpaper	SCP-3
18		Surface wipes (gauze)	GSP-1
19		Strain gage installation tape	PCT-2M
20		Half-bridge strain gages	EA-13-062TZ-350/E
21		M-Bond 200 adhesive and catalyst	F006678
22		Eutectic solder	361A-20R-25
23		36 gage, etched PTFE-coated, three-stranded wire	336-FTE

4.2.4.2 Transducer Calibration System

To facilitate calibration of each REFT, a well-defined calibration apparatus was developed (Figure 4-12). Each apparatus had the ability to impose SL and IC forces, either independently or in tandem. Mechanical loading of each REFT arm within the apparatus was accomplished through a screw-piston-spring-pusher assembly, shown in detail in Figure 4-13. The springs (36066GS, Gardner Spring, Tulsa, OK) had spring constant of 177.5 N/in. Each full turn of the screw (#6-40) compressed the spring by 0.025", thereby applying 4.44 N compressive force to the transducer along the REFT arm's major axis.

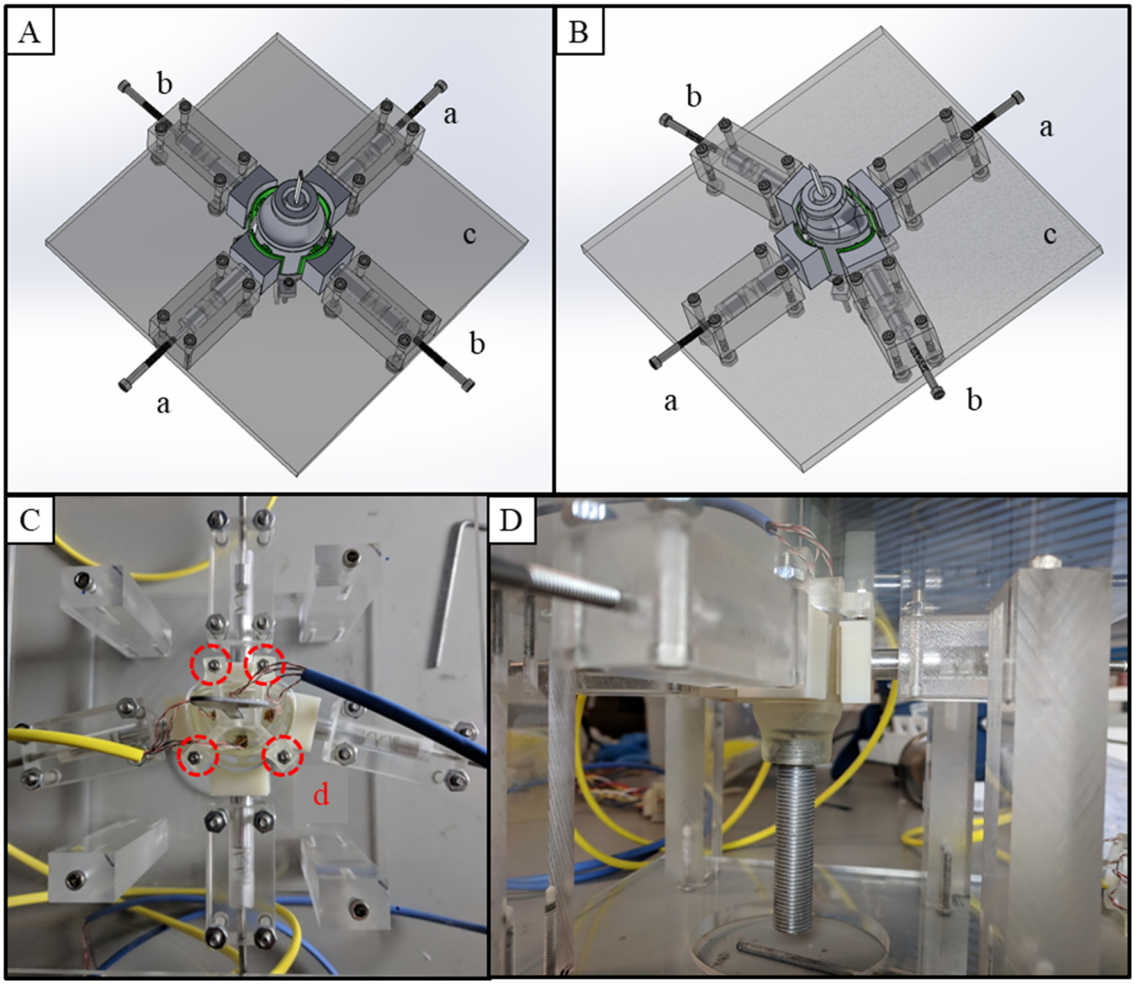

Figure 4-12 (A-B) CAD renderings of the C-REFT and D-REFT mounted within their calibration apparatuses (the hub's screw extender is not shown). (C-D) Top-view and side-view of the actual D-REFT mounted within its calibration apparatus. Screw extender is visible in (D). (a) Septal-lateral loading mechanisms, (b) inter-commissural loading mechanisms, (c) base plate, (d) screws mounting REFT to base plate.

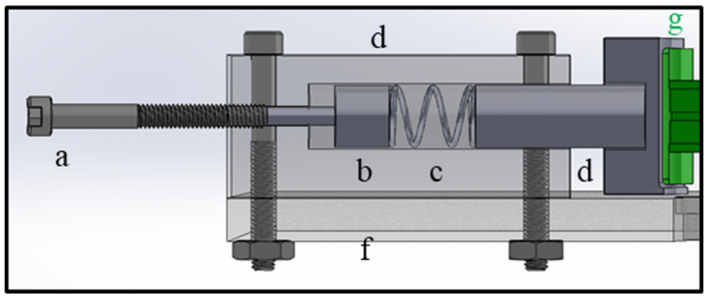

Figure 4-13 Loading mechanism for calibration apparatus. (a) Screw, (b) piston, (c) precision spring, (d) pusher that contacts the REFT arm, (e) housing, (f) base plate, (g) REFT arm.

4.2.4.3 Data Acquisition System

The data acquisition system used for REFT studies was the same as that used in SA 1 (see Section 4.1.3.2). However, in this case, only one strain module (NI 9237, for four force measurement channels) and one BNC analog voltage input module (NI 9215, for pressure monitoring) were used. Data were monitored and recorded using a custom LabVIEW program.

4.2.4.4 Additional Experimental Materials

SA 2.B experiments required various additional materials beyond the REFT devices and calibration apparatuses. The REFT was passed through the MV of a fresh porcine heart and out a hole cut through the ventricle, then secured to a base plate. The plate was mounted on a stand and the setup was submerged in a heated water bath. The aorta was pressurized using a simple hydraulic setup. These additional materials are listed in Table 4-4 and further detailed in Section 5.2.4.

Table 4-4 Additional materials used for radial expansion force measurement studies.

	Supplier	**Item**	**Supplier Serial Number**
1	Holifield Farms (Covington, GA)	Porcine heart	N/A
2		1/4" acrylic base plate with central 1/2"-20 threaded hole	*machined from* 8560K354
3		Acrylic stand for base plate	*machined from* various
4		Acrylic water tank	*machined from* various
5	McMaster Carr (Atlanta, GA)	Ball valves	4757K19
6		Tubing and connectors	various
7	Grainger (Lake Forest, IL)	Super Lube Synthetic Grease	44N719
8	QC Supply (Schuyler, NE)	Small umbilical clamps	140899
9	Dayton Electric Manufacturing, Co. (Lake Forest, IL)	Steady flow pump	12U596
10	Powerstat (Bristol, CT)	Variac transformer	3PN126
11	Utah Medical Products (Midvale, UT)	Pressure transducer	6199

CHAPTER 5. METHODS

Note that many custom components were used in this thesis. All computer aided design was performed in SolidWorks. Computer aided design files have been uploaded to the Georgia Tech repository as a supplement to this thesis. Files for both individual parts and multi-component assemblies are included. For more information, refer to the supplement and/or APPENDIX H. This appendix also describes material and method used for fabrication.

For MATLAB codes that were used for data processing and/or statistical analysis, refer to APPENDIX I.

5.1 Specific Aim 1 Methods

5.1.1 Suture Force Transducers: Concept, Production, and Characterization

5.1.1.1 Basic Strain Gage Principles

Fundamentally, a strain gage is an electrically conductive wire, configured in a specific shape to achieve desirable electrical properties. Strain gages are bonded to the surface of an object of interest to quantify the strain that the surface experiences, and/or the external force(s) that caused said strain. An example strain gage is shown below.

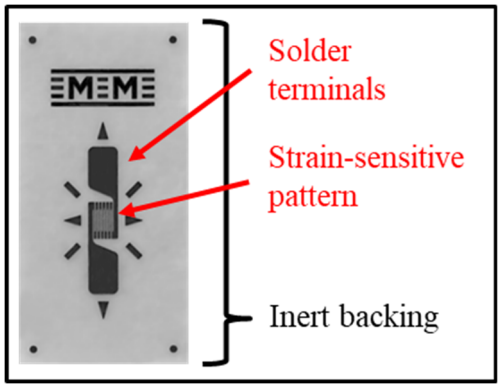

Figure 5-1 An example of a wire strain gage (015DJ) sold by Micro-Measurements (Wendell, NC).

The strain-sensitive pattern is a very fine metallic wire, which responds to being strained according to the fundamental equation for electrical resistance, R, of any physical object:

$$R = \frac{\rho L}{A} \tag{1}$$

Resistivity, ρ, is an intrinsic property of the material from which the wire is made. The wire's length, L, and cross-sectional area, A, are extrinsic, i.e. they can be controlled. These dimensions change in response to mechanical loading. When the strain-sensitive pattern is tensioned or compressed, the resultant geometric change (i.e., strain) will tend to increase or decrease, respectively, its electrical resistance.

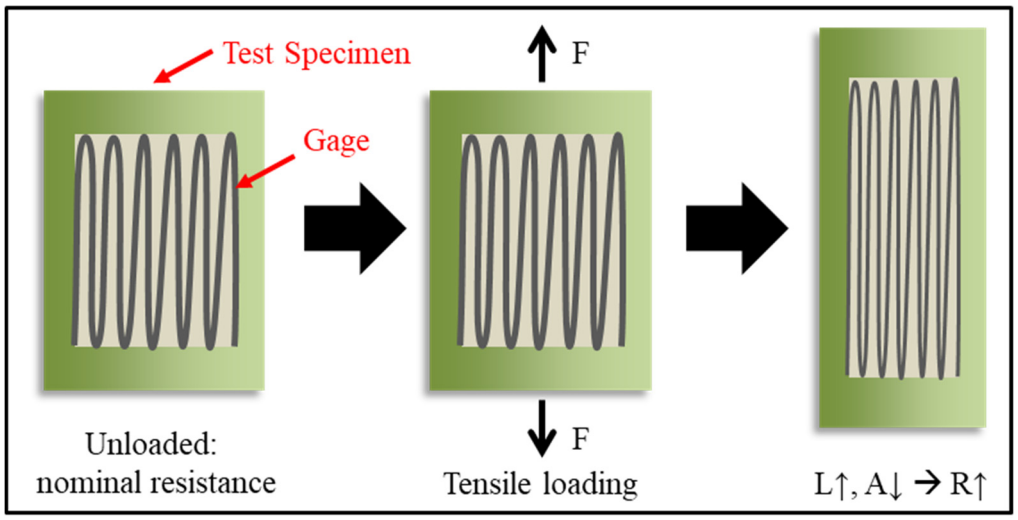

Figure 5-2 A strain gage bonded to a test specimen's surface responds to surface strain (and to the force that caused it) by changing its electrical resistance.

Thus, according to Ohm's Law, which states:

$$V = iR \tag{2}$$

under a constant supplied current, i, any force that strains the gage, and thus induces a change in its resistance, will induce a corresponding change in the voltage, V, across the gage. By exploiting this principle, combined with other well-established mathematical relationships, measuring this voltage change allows one to calculate the directional surface strains in a test specimen. Alternatively, a constant of proportionality can be empirically determined (using a well-designed calibration apparatus) to link this same voltage change to the applied force acting on the specimen. In this case, the component to which the gage is attached is referred to as the *spring element*. Collectively, the spring element and gage function as a *load cell* or *force transducer*.

Whether the experimental endpoint is strain or force, the gage is wired into a Wheatstone bridge circuit, whose most important effect is to improve measurement sensitivity to as low as 1 με. If desired, two or four gages can be integrated into one bridge circuit, to achieve benefits such as further sensitivity to strain, insensitivity to temperature change, or isolation of bending vs. axial strains. For further information on the various multiple-gage configurations, the reader is referred to National Instruments' white papers, especially 3642 (http://www.ni.com/white-paper/3642/en/#toc3).

5.1.1.2 Suture Force Transducer Design

In this work (and in SA 2.B), dedicated spring elements were designed, 3D printed, and instrumented with strain gages. The strains in these components were not, themselves, of interest. Instead, once instrumented with strain gages and calibrated, they served a critical function as force transducers, as described below.

The Suture Force Transducer's spring element is shown in Figure 4-5, and is further detailed in Figure 5-3 A below. The transducer utilized two strain gages, orthogonally aligned and wired in a half-bridge configuration (type I, as described in National Instruments white paper 3642; http://www.ni.com/white-paper/3642/en/#toc3). This configuration improved strain sensitivity and eliminated temperature sensitivity, as compared to a single gage in a quarter-bridge configuration). It featured an annuloplasty ring mounting bracket, such that it could be fixed directly to the ring by tying sutures through or around the ring and through the mounting holes. Transducers were attached to

ten positions per ring (Figure 5-3 B-C). Each transducer also featured a measurement arm, which was designed to replace the function of the ring's own suture cuff.

During implantation, simple interrupted sutures were passed through the valve annulus, through the implantation holes, and tied atop the measurement arm in the exact fashion used to secure sutures to a ring's suture cuff during a normal annuloplasty procedure. Thereafter, any force applied to the suture would transfer to the transducer, generating a detectable signal response (Figure 5-3 D).

As previously reported, these transducers exhibited a minimum measurable force of 0.05 N, and mean error between true and measured forces of less than 1%.[24]

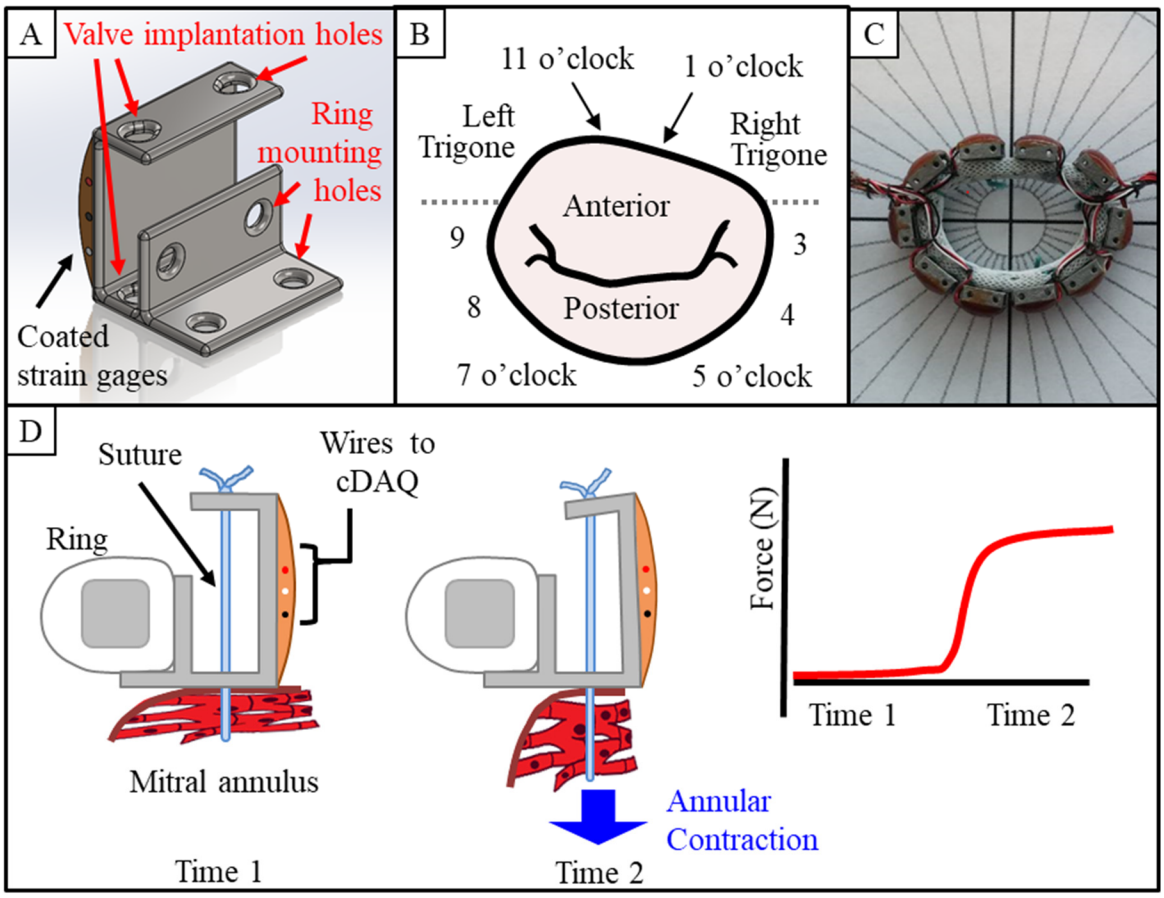

Figure 5-3 A) CAD rendering of transducer, highlighting key functional features. B) Ten locations around the annular circumference in which Suture Force Transducers were placed (dotted line distinguishes anterior from posterior regions). C) Example of fully instrumented ring. D) Schematic of implanted ring with suture force inducing transducer deformation and detectable signal.

5.1.1.3 Suture Force Transducer Fabrication

Note, the strain gage manufacturer, Micro-Measurements (Wendell, NC), provides extensive documentation on strain gage installation best practices. The interested reader is referred to their website (http://www.vishaypg.com/micro-measurements/stress-analysis-

strain-gages/appnotes-list/). The step-by-step installation process, as it was performed in this specific application, and using the materials listed in Table 4-1, is as follows.

Step 1: Strain gage preparation. A clean acrylic surface was prepared by wiping with a few drops of M-Prep Conditioner A, then wiping with a few drops of M-Prep Neutralizer 5A, then dried. Strain gages were extracted from their packaging with tweezers and laid on the clean surface. Excess gage backing material that extended beyond the bounds of the wiring was removed with a fresh razor blade. A piece of PCT-2M Gage Installation tape was laid over each gage (aligning the major axis of the gage with that of the tape) until further use.

Step 2: Spring element surface preparation. The surface of the spring element was wetted with M-Prep Conditioner A, sanded with 400 grit sandpaper, and wiped dry with gauze. A few drops of M-Prep Neutralizer 5A were then added to the surface, and dried thoroughly with fresh gauze. Further physical handling of the spring element was avoided.

Step 3: Strain gage alignment. The gage was lifted from the acrylic surface by delicately peeling the tape back from one edge. Next, the tape and gage were centered over the bonding area of the spring element, and the tape was "hinged" along the bottom edge of the spring element, such that the gage could be repeatably peeled back and returned to its proper position with ease. For each set of 10 transducers, five each were made with the

solder terminals oriented to the left and to the right. This supported easier harnessing of the wires in preparation for attachment to the ring (described further in Step 9 and in Section 5.1.1.4).

Step 4: Strain gage adhesion. The tape was peeled back such that it remained hinged along the spring element's edge, and the bonding surfaces of both spring element and gage were exposed. M-Bond 200 catalyst was lightly brushed in one continuous layer across the underside of the gage (after wiping the brush 8-10 times along the edge of the bottle to remove most of the liquid). After allowing ~30 seconds for the catalyst to air dry, one drop of M-Bond 200 adhesive was applied to the spring element's bonding surface. As quickly and precisely as possible, the gage was laid back down over the adhesive, taking care to maintain proper alignment. The glued surfaces were pressed together under firm finger pressure for 5 minutes and left at rest to cure further for another 20 minutes or more. Finally, the tape was peeled straight back along the spring element's surface, *shearing away* from the gage and leaving it bonded to the spring element.

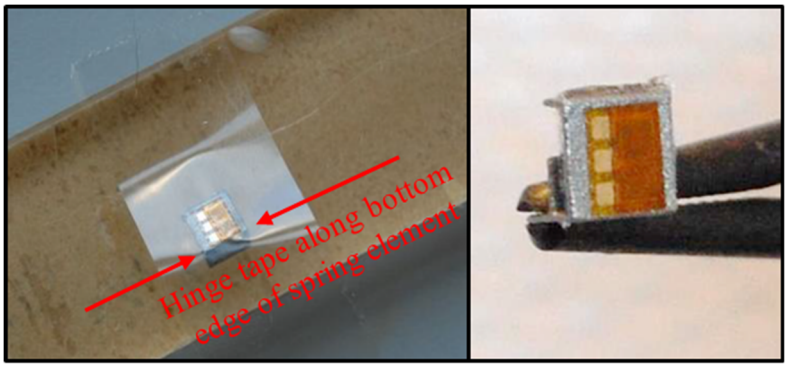

Figure 5-4 From left to right: post-Step 3, post-Step 4.

Step 5: Strain gage wiring. Each solder terminal was tinned, by first depositing a tiny drop of flux to the terminal, then depositing a round spot of solder. Next, a 5' length of three-stranded 336-FTE wire was slightly unwound and a miniscule length of outer Teflon coating was burned away to expose the metallic interior. One wire was bonded to each terminal.

Step 6: Rosin removal. M-Line Rosin Solvent was used to remove excess rosin from the soldered areas of each strain gage. The solvent was lightly brushed across each gage was blotted dry.

Step 7: Application of strain gage mechanical protectant. A thin layer (<0.5 mm) of Loctite E-120HP epoxy was applied over the entire spring element bonding face, covering gage, solder terminals, and a short span of each wire. Cure time was at least 36 hours.

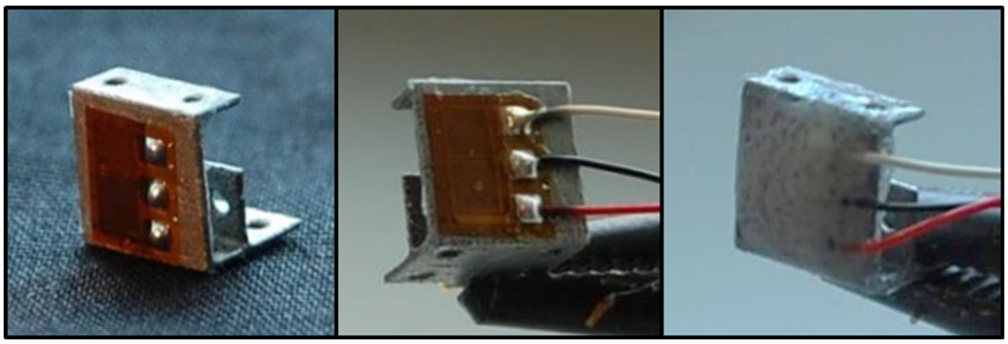

Figure 5-5 From left to right: Post-tinning (part of Step 5), post-Step 6, post-Step 7.

Step 8: Application of strain gage moisture protectant. A thin layer of nitrile rubber sealant was applied directly atop the mechanical protectant layer. After 2 hours of curing, if any visible gaps were detected, a second coat was applied, with another cure time of 2 hours.

Step 9: Final treatments for wiring. For each annuloplasty ring to be instrumented, two groups of five transducers were bundled within heat-shrink tubing. Each group's 15 wires were drawn through a length of tubing, by transiently tying them with thin suture to a 0.5 mm diameter braided metal wire, and carefully guiding the wire through the tubing. Note that, per Step 3, each transducer had wires extending to either its left or its right. Thus, one

group contained two left-facing and three right-facing transducers (or vice versa), and the other group contained the opposite.

Next, the free ends of the wires were burned to expose ~2-3 mm of their metallic cores, and each wire was soldered into a pin or sleeve (corresponding to the gender of the plug to which it would ultimately be mated). Groups of pins or sleeves were inserted into their respective housings. Tubing was shrunk with a standard heat gun. The tubing end proximal to the gages was occluded with nitrile rubber, to prevent filling with blood during *in vivo* use. The backs of the electrical connector housings were covered with silicone to provide some mechanical cushion against accidental tugging.

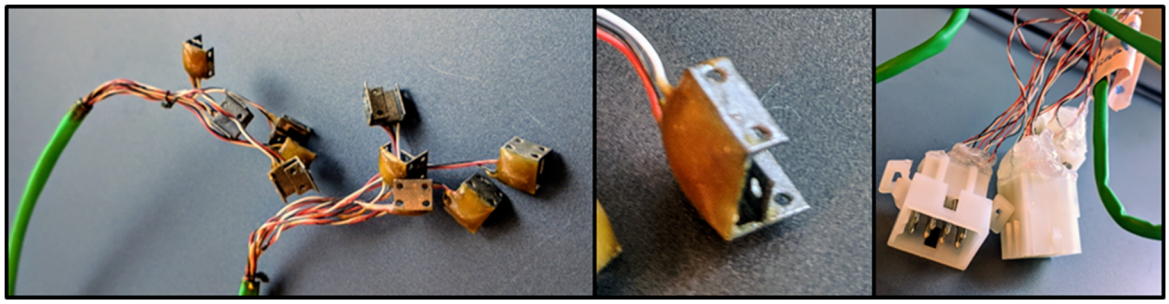

Figure 5-6 Left: Full set of 10 transducers after fabrication is complete. Center: Close-up of one transducer. Right: Electrical connectors for one set of transducers.

5.1.1.4 Suture Force Transducer Attachment to Rings

Ten Suture Force Transducers were attached to each annuloplasty ring of interest, at the positions shown in Figure 5-3 A) CAD rendering of transducer, highlighting key functional features. B) Ten locations around the annular circumference in which Suture Force Transducers were placed (dotted line distinguishes anterior from posterior regions). C)

Example of fully instrumented ring. D) Schematic of implanted ring with suture force inducing transducer deformation and detectable signal. B-C (i.e. 4 anterior, 6 posterior transducers). Using the method pictured in Figure 5-7, each transducer was tied around the ring's minor circumference using 2-0 suture. Its position was secured either by passing the suture *through* the ring's fabric suture cuff (for commercial rings) or by passing the suture *around* the ring and resting it in dedicated grooves, supported by a spot of cyanoacrylate glue to bond suture to ring (for prototype rings; see Section 0). Each mounting suture was tied with three knot throws, which were further secured with a spot of cyanoacrylate glue atop the knot.

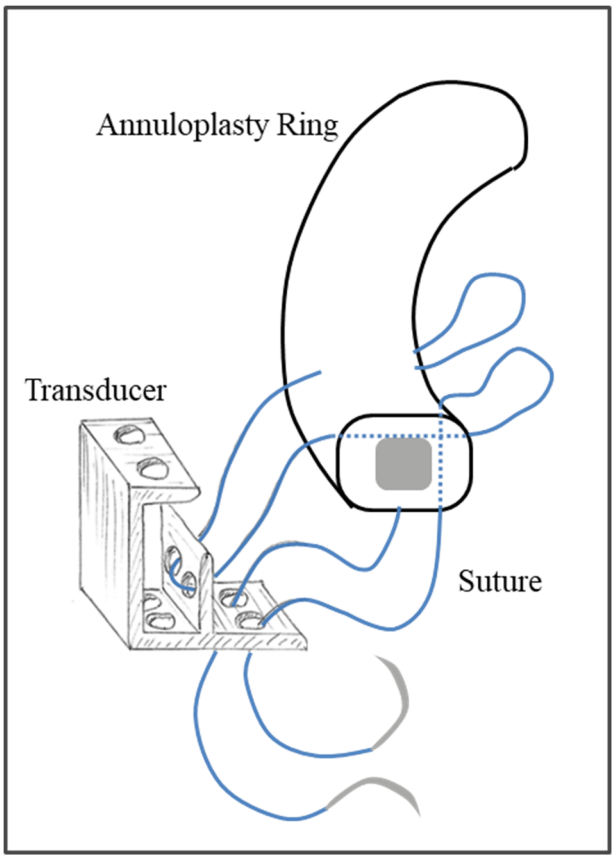

Figure 5-7 Method used to secure a Suture Force Transducer to Physio and Profile 3D annuloplasty rings. Sutures passed through the fabric suture cuff to prevent slippage. Not shown: for prototype rings, which did not include a suture cuff,

sutures were instead passed around the ring's minor circumference, along the same path shown. Sutures then rested in dedicated grooves to prevent slippage.

5.1.1.5 Suture Force Transducer Calibration

To calibrate the Suture Force Transducer, it was first detached from the annuloplasty ring. A loose loop of suture was passed through the transducer's measurement arm and through a table with two holes positioned to match the device's annular suture passages. The loop was knotted tightly to prevent any slippage. A small piece of tape secured the transducer's ring-mounting feature to the table. Five weights ranging from 0.5-10 N were each suspended from the suture loop beneath the table, three times apiece. The voltage vs. force curve was computed; R^2 was greater than 0.99 in all instances.

Note, transducers were calibrated before and after each *in vivo* use, to account for any changes in their sensitivity that may have occurred during use. When analyzing each *in vivo* data set, force values were generated according to the *averaged* calibration factors from before and after that experiment.

5.1.2 Prototype Annuloplasty Rings: Concept, Production, and Characterization

5.1.2.1 Reverse Engineering of Commercial Ring Geometry

Step 1: Commercial ring imaging. Physio and Profile 3D rings (each of sizes 24, 26, and 28) were subjected to micro-computed tomography imaging using a Siemens Inveon Scanner (Siemens Medical Solutions USA, Inc., Malvern, PA), tuned for metal

visualization (80 kV voltage, 500 mA, 500 msec integration time) at 43.29 μm isotropic voxel resolution. Raw output files were converted to DICOM format offline using Inveon Research Workplace (Siemens Medical Solutions).

Step 2: Commercial ring geometry segmentation, triangulation, and refinement. DICOMs were segmented to yield the volume corresponding to the ring's metallic core using InVesalius (São Paulo, Brazil). For the Physio ring, the multiple, closely packed Elgiloy strips were resolved as a single, closed tube. The resulting triangulated mesh was refined using Geomagic Studio 2014 (3D Systems, Cary, NC). Both global functions (Relax and Remove Spikes) and manual deletion of erroneous triangles were employed to generate a smooth ring surface. In preparation for Step 3, a short segment of the ring was deleted using the Trim With Sheet function, converting the surface from a closed tube to an open tube. The final geometry was saved as an .stl file.

Step 3: Commercial ring centerline extraction and refinement. Next, the centerline describing this .stl file was computed using the Vascular Modeling Toolkit, or VMTK, and its GUI interface PypePad (www.vmtk.org). This was achieved using the following line of code:

vmtksurfacereader -ifile *InputFilePath/InputFileName*.stl --pipe vmtkcenterlines -seedselector openprofiles -ofile *OutputFileName*.dat

After re-importing the output data to Geomagic, the centerline data was further smoothed using the Reduce Noise function. In preparation for ring design, a coordinate system was defined based on the centerline's transverse diameter and best-fit plane as shown below. At this point, the centerline was ready to be imported into SolidWorks for ring design.

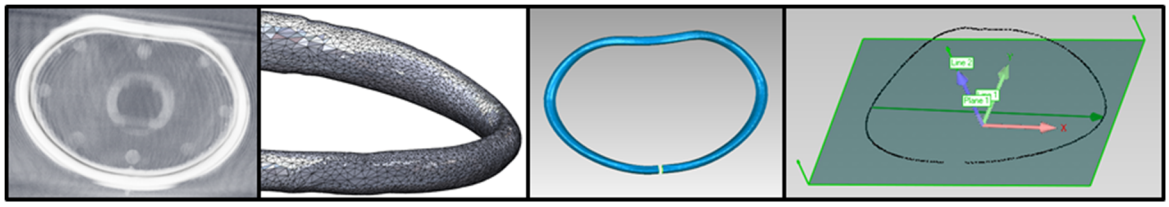

Figure 5-8 Reverse engineering of commercial ring geometry. From left to right: after micro-computed tomography scan; after surface triangulation; after surface refinement; after centerline extraction and refinement.

5.1.2.2 Fully Rigid and Fully Flexible Ring Design

To study the effect of ring stiffness on suture forces, fully rigid and fully flexible rings were produced in geometries exactly matching the Physio ring (sizes 24, 26, and 28). These were subsequently assessed in comparison to one another and to the semi-rigid commercial Physio ring.

Prototype ring geometry consisted of a 3mm diameter circular profile swept around the centerlines that were computed as detailed above. Note, the rings were composed of a single material (see Section 4.1.2.2), without the fabric suture cuff that is found in commercial rings. Consequently, it was not possible to secure the transducers to the ring by passing suture *through* the ring. Therefore, pairs of grooves (0.6 mm wide, 3.7 mm apart, and approximately 0.3 mm deep) were positioned at the sites where each Suture

Force Transducer would be attached. These grooves, which occupied only the atrial/inner quadrant of the ring's minor circumference, facilitated repeatable, secure transducer attachment, as described in Section 5.1.1.4.

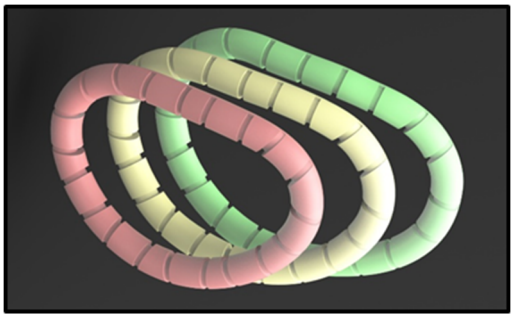

Figure 5-9 CAD Rendering of fully-rigid or fully-flexible ring prototypes fashioned in the Physio geometry. Sizes 24, 26, and 28 are shown. Suture grooves for transducer mounting are easily visible.

5.1.2.3 Fully Rigid and Fully Flexible Ring Fabrication

Rigid rings were 3D printed as described in Section 4.1.2.2. Flexible rings were cast from a fast-setting silicone with Shore hardness 40A (Quick-Sil; Castaldo; Franklin, MA), using the specialized molds described in Section 4.1.2.2. The mold's cavity matched the commercial ring geometry, with a few additional tracts incorporated to aid escape of excess silicone during mold closure.

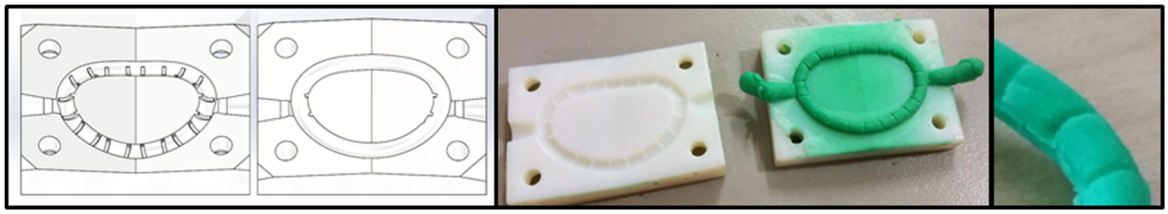

Figure 5-10 Left: CAD rendering of mold design. Center: Flexible ring immediately after opening mold, before flash removal. Right: Close-up of suture grooves in a finished flexible ring.

5.1.2.4 Fully Rigid and Fully Flexible Ring Characterization

The stiffness levels of rigid, semi-rigid (commercial), and flexible rings were characterized through mechanical compression in their septal-lateral directions. Compression testing was performed using an ElectroForce 3200 uniaxial tester (Bose Corporation) with 25 N in-line load cell (SMT1-22; Interface) with custom holders. Compression ended when the ring's most septal and lateral points moved to within 75% of one their nominal distance (5 mm total deflection) or when a load of 7.5 N was reached. Each of these limits are conservative representations of *in vivo* annular function.[46, 107]

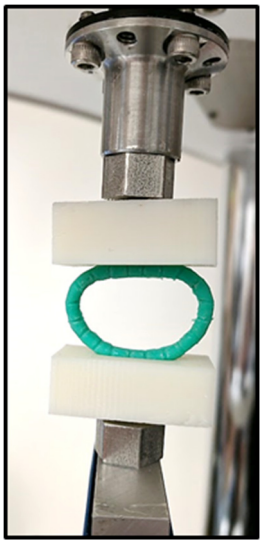

Figure 5-11 Mechanical characterization of prototype annuloplasty rings.

5.1.2.5 Hybrid Ring Design

Based on the findings of SA 1.A and 1.B, materially hybrid rings were designed to include rigid anterior and posterior segments, and flexible commissural segments. This putatively optimized design was intended to minimize suture dehiscence likelihood without compromise to repair efficacy. In light of the known and proposed benefits of saddle ring annuloplasty for repair efficacy,[45, 122-128] hybrid rings were modelled after the saddle-shaped Profile 3D geometry. Similar to the homogeneous prototype rings, these rings were constructed from a 3 mm circular profile sweep around a computed centerline, with the addition of suture grooves.

5.1.2.6 Hybrid Ring Fabrication

Hybrid rings were fabricated via a molding technique similar to that used for the fully flexible rings. However, in this case, the two 1 mm diameter titanium inserts were embedded within the silicone at the desired locations, as shown in Section 4.1.2.2.

5.1.3 Sample Preparation for In Vitro *Studies*

5.1.3.1 Suture Pullout Force Studies

Beginning with the ovine hearts described in Section 4.1.1.2, the left atrium was trimmed until approximately 1-2 cm of tissue superior to the leaflet hinge line remained. The left ventricle was removed; leaflets were left attached (with chords removed) to facilitate mounting to the test plate. To mount the annulus to the test plate, four simple interrupted sutures, followed by a running suture with Ford interlocking stitch, were first passed around its outer circumference and through the plate's rubber layer. Next, ten Y-31 2-0 Ti·Cron sutures (Medtronic) were passed through the same ten positions studied *in vivo* (see Figure 5-3 B). Placement adhered strictly to published annuloplasty guidelines (1-2 mm above hinge line, 10 mm bite width, minimum 10° between needle and tissue).[37] All sutures were placed by a single operator. Finally, another running suture with Ford interlocking stitch was passed around the inner circumference (i.e. mostly through the leaflet tissue) to further secure the annulus to the plate.

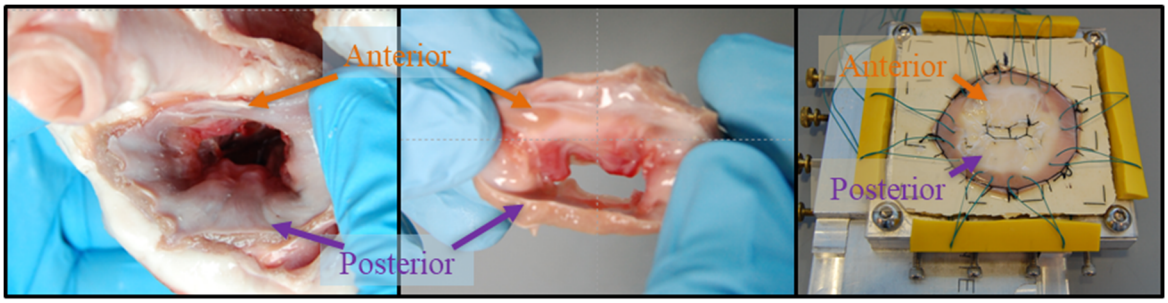

Figure 5-12 Left and Center: Mitral annulus, before and after explant from the heart. Right: Annulus mounted to test plate, after test suture passage (green sutures).

5.1.3.2 Collagen Quantification Studies

These tests again used the ovine hearts described in Section 4.1.1.2; note this was a distinct cohort of hearts than those used for suture pullout testing. Tissue sections were excised from the mitral annulus at each of four positions: LT, RT, 12 o'clock, and 6 o'clock. They were paraffinized, sectioned to 30µm (circumferential direction), and mounted on slides, all per standard protocol. Slices were roughly 5x3mm in the apical-basal and radial directions, respectively, such that the endocardial surface ran along one long edge of the sample.

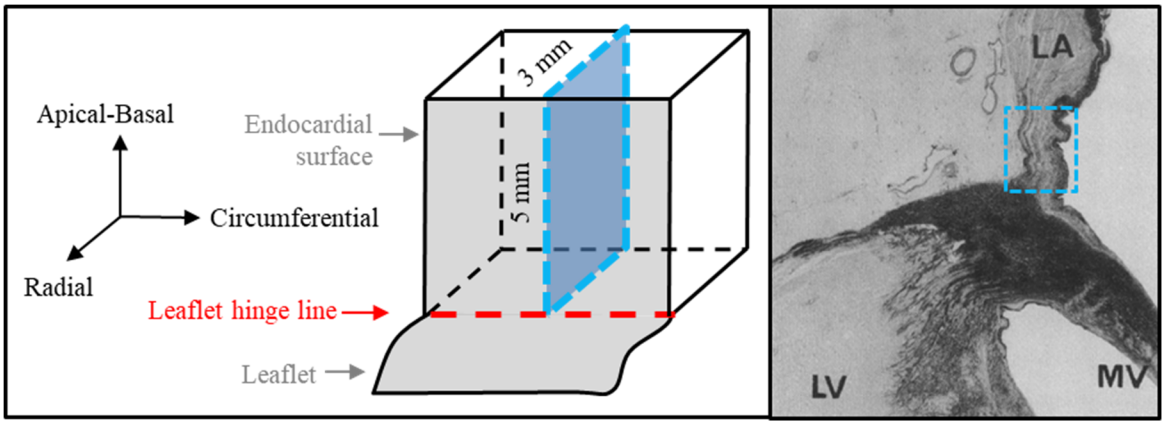

Figure 5-13 Region of the annulus subjected to collagen quantification testing. Left: 30 µm thick slices were prepared as shown (blue plane). Right: Blue box highlights the same annular region in a histologic image (adapted from Angelini et al[41]).

5.1.4 Experimental Protocols

5.1.4.1 Cyclic Suture Force (*In Vivo*) Studies

Normal Dorsett hybrid sheep were intubated, anesthetized, and ventilated with isofluorane (1.5-2%) and oxygen. Surface electrocardiogram and arterial blood pressure were monitored. 2D, 3D, 2D color Doppler, and pulsed-wave Doppler ultrasound imaging were used to assess mitral geometry and hemodynamics (iE33 ultrasound machine with x7-2 matrix-array probe; Philips Health Tech, Andover, MA). After establishing cardiopulmonary bypass, a left atriotomy was performed. The annulus was sized and a ring was selected (either true-sized or undersized by two full ring sizes). Ten Y-31 2-0 Ti·Cron sutures were passed through the annulus at the four anterior and six posterior positions shown in Figure 5-3 B (simple interrupted). Each suture was then passed through the implantation holes of the Suture Force Transducer at the appropriate position on the ring

of interest. Prior to tying the ring into the mitral annulus, all transducer signals were zeroed. Each suture was then tied, using six knot throws, in the following order: left trigone, right trigone, then clockwise from 11 o'clock.

Following left atrium closure and weaning from cardiopulmonary bypass, the pressure transducer was passed through the femoral artery to the left ventricle for continuous measurement of LVP. Surface electrocardiogram, LVP, and arterial pressure were monitored. All ultrasound image types were acquired upon re-establishment of baseline hemodynamics (100 mmHg peak LVP, 4.0 L/min cardiac output). To evaluate the effects of increasing afterload, peak LVP levels of 125 and 150 mmHg were subsequently achieved. Elevated peak LVP was achieved using a continuous infusion of neosynephrine and dobutamine. After data collection, the animal was euthanized via injection of 80 mEq KCl. The heart was explanted and examined to verify sutures were placed correctly and remained intact.

All suture force and LVP data was recorded at 1613 Hz. In the first 10 studies (SA 1.A and part of 1.B), data was recorded only during key events. Thereafter, the data acquisition software was modified, such that this data could be recorded continuously from before suture tie-down until after ring removal.

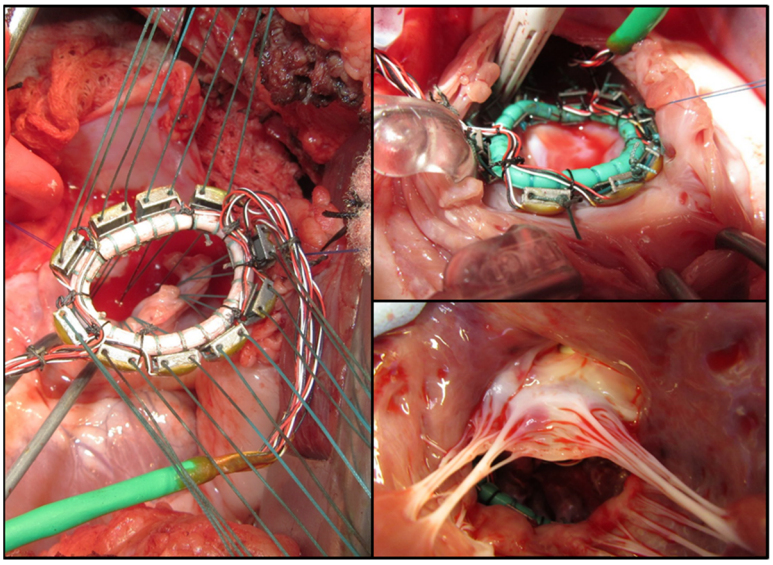

Figure 5-14 Left: Ring being lowered into atrium. Top right, Bottom right: LA view and LV view, respectively, during ring inspection after euthanasia.

5.1.4.2 Suture Pullout Force Studies

The valve, mounted on the test plate, was loaded onto the uniaxial testing system. The fixture was attached to the lower testing arm in line with the load. Each suture was sequentially tied to the upper arm and pulled at 1 mm/sec until it tore through the tissue or until the upper arm reached its maximum displacement (13 mm). The test plate's biaxial traverse enabled each suture to be positioned directly beneath the testing arm and pulled normal to the annulus. In terms of native MV geometry, this pulling was approximately radially inward, i.e. the approximate direction of suture tension following undersized annuloplasty *in vivo*. Throughout testing, MVs were kept topically hydrated with 0.75% saline spray.

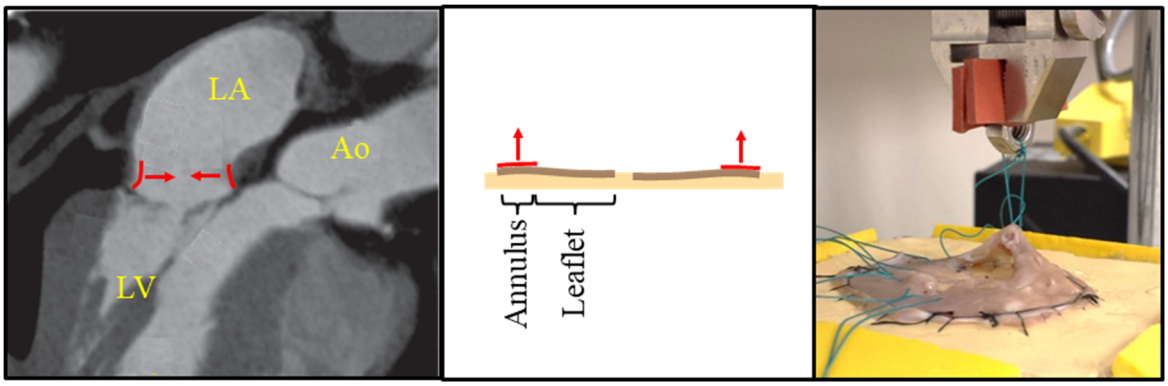

Figure 5-15 Left: Patient CT scan (adapted from Cuéllar et al[129]), highlighting the annular orientation and the radially inward direction that an undersized ring would pull the annulus (red arrows). Center: Sketch demonstrating that the geometric transform associated with valve mounting for suture pullout testing re-orients this force to the *upward* direction. Right: Suture pullout testing in action.

5.1.4.3 Collagen Quantification Studies

Each sample was imaged via two-photon excitation, at 10X, using an 800 nm excitation wavelength. Collagen was detected in one channel at 390-420 nm via second harmonic generation from the fibers,[130] while non-specific extracellular structures were detected in another channel at 485-700 nm. To maximize sensitivity and accuracy in assessing relative differences in microstructure, identical microscope acquisition settings (gain and offset) were used for each sample from a given MV. Among the four samples from each given MV, the sample with the strongest signal from either channel was identified. Settings were optimized for this sample, and held constant for the remaining three samples.

5.1.5 Data Processing and Experimental Endpoints

5.1.5.1 Cyclic Suture Force (*In Vivo*) Studies

Recorded data were processed offline using custom MATLAB scripts (MathWorks, Natick, MA). The primary endpoint was the *cyclic contractile force (F_C)* on each suture. F_C was computed as the difference between the minimum and maximum force recorded within a cardiac cycle (averaged over 10 consecutive cycles). Secondary endpoints across all studies included:

- *Trans-mitral pressure gradient increase:* Difference between gradient after ring implantation and gradient at baseline. This quantity was computed from Doppler ultrasound recordings for each experiment.

- *LVP_{max}:* Peak LVP. LVP_{max} was averaged over 10 cardiac cycles for every F_C data point.

- *Heart rate:* 1/T, where T was the cardiac cycle length as measured in the associated LVP waveform. Heart rates were averaged over 10 cardiac cycles for every F_C data point.

Two additional secondary endpoints were studied specifically during studies of ring stiffness (part of SA 1.B and SA 1.C). These were investigated due to their potential to uncover mechanisms underlying stiffness-related F_C dynamics. They were:

- *$F_{C,Ant}/F_{C,Post}$:* The ratio of mean anterior to mean posterior F_C, computed at each LVP_{max} level for each experiment.

- *$HWHM_{norm}$:* An expression of the proportion of the cardiac cycle during which each suture experienced load increase. This proportion was studied as the leading half-width at half-maximum (HWHM) force, normalized by cardiac cycle length, T:

$$HWHM_{norm} = \frac{t_2 - t_1}{T} \quad (3)$$

Here, t_2 is the instant of maximum force, and t_1 is the preceding instant of half-maximum force. This concept derives from full-width at half-maximum (FWHM), a well-established parameter for the description of peaks in waveforms that lack sharp edges.[131, 132] HWHM is a modified parameter that is used to describe of one side of an asymmetric peak.[133, 134] In this study, $HWHM_{norm}$ refers to the leading half of the suture force wave; it thus describes the suture force response to ventricular contraction, while neglecting any minute increases in F_C that may precede ventricular contraction. Larger $HWHM_{norm}$ values indicated that F_C takes a longer time to manifest.

The following figure graphically describes many of the above quantities.

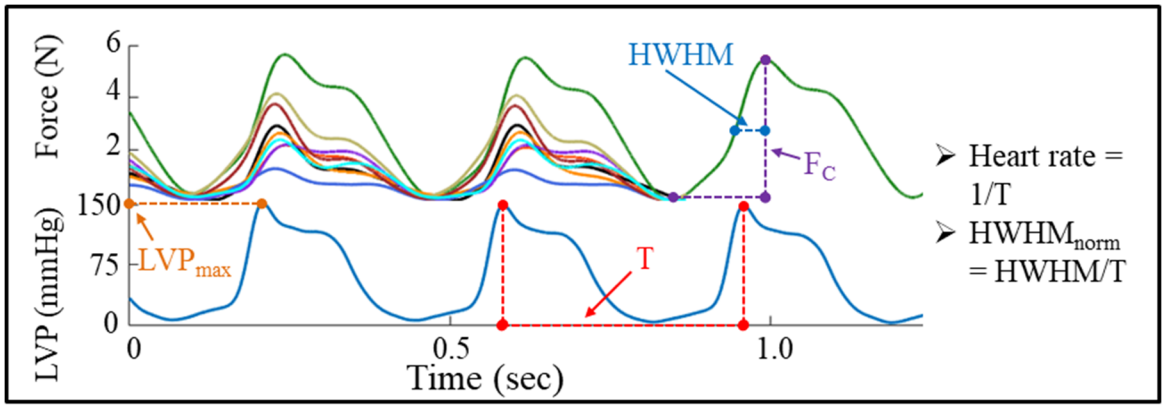

Figure 5-16 Graphical depiction of the experimental endpoints based on force and LVP recordings.

5.1.5.2 Suture Pullout Force Studies

The *suture pullout force (F_P)*, which can also be thought of as the suture holding strength of the tissue, was defined as the maximum recorded force. In the infrequent event that the testing arm reached maximum displacement before complete pullout occurred, the final (peak) load was used as F_P; this provided a conservative approximation of the true F_P.

To estimate suture dehiscence likelihood, a margin of safety, termed *residual strength (RS)*, was computed for each suture position as the difference between mean F_P and mean F_C at LVP_{max} = 150 mmHg. This elevated LVP_{max} was chosen as a worst-case scenario (highest F_C).

5.1.5.3 Collagen Quantification Studies

Mean pixel intensity (MPI) in each channel was quantified over the entire sample area via a custom MATLAB code. Before averaging across samples, each MPI was normalized by the mean MPI from that valve. That is, for the *normalized MPI (nMPI)* from valve *i*, position *j*:

$$nMPI_{i,j} = \frac{MPI_{i,j}}{MPI_{i,mean}} \tag{4}$$

5.1.6 Statistical Analysis

5.1.6.1 Analysis of Variance (ANOVA) Primer

The central statistical tool used in SA 1 for evaluating the multi-factorial dynamics of the observed suture forces and tissue properties was *Analysis of Variance (ANOVA)*. ANOVA is a form of hypothesis testing, with many similarities to the more well-known Student's t-test. However, whereas the t-test is only able to test differences between two groups, ANOVA has no such limit. A one-way ANOVA accounts for multiple *levels* of (i.e., categories within) a single factor. Multi-way ANOVA accounts for multiple levels of multiple factors, and may also test for significant interactions between factors. ANOVA determines the expected *contributions* to the observation due to each level of each factor.

For example, consider a two-way ANOVA model describing the sensitivity of F_C to LVP_{max} (from the three possible levels tested here) suture position (from the ten positions tested here). If two-factor interaction is included, this model would be written as:

$$F_{C,ijk} = \mu_0 + \alpha_i + \beta_j + (\alpha\beta)_{ij} + \varepsilon_{ijk} \quad (5)$$

$F_{C,ijk}$ refers to the k^{th} F_C observation having LVP_{max} level i and suture position j. $F_{C,ijk}$ is the sum of: μ_0, the grand mean F_C across all observations; α_i, the contribution to F_C due to LVP_{max} level i, β_j, the contribution due to suture position j; $(\alpha\beta)_{ij}$, the contribution due to interaction between LVP_{max} level i and suture position j; and ε_{ijk}, the residual error in the observation.

The assessment of significance of each factor (as a whole) is made according to that factor's F-value (a ratio of the variance between groups to the variance within groups) and accompanying p-value. Pairwise comparisons between any two levels of a single factor can also be made. However, this leads to the *multiple-comparison problem:* the larger the number of pairwise comparisons, the greater the risk of erroneous findings. A range of post-hoc corrections are commonly used to effectively compensate for this risk. It is also critical to note that ANOVA requires certain assumptions about the data to be met. These include normality of the model's residuals, independence of observations, and homogeneity of variances among groups. For further information on ANOVA and related topics, the interested reader is referred to *Statistics for Bioengineering Sciences*.[135]

5.1.6.2 Analyses Used

All statistical analyses were performed using MATLAB and/or Minitab (Minitab Inc., State College, PA). For hypothesis tests between two groups, Student's t-test was used. However, as noted above, the central statistical tool was the one-way or multi-way ANOVA. F_C, $HWHM_{norm}$, F_P, RS, and nMPI were each treated as the dependent variable in various ANOVA models. Independent variables in these models included combinations of LVP_{max}, ring type, ring size, and suture position or suture region, as appropriate for the specific questions of interest. For multi-way ANOVAs, each model was run first without interaction terms to assess main effects, then with all possible two-factor interactions. Tukey's Honestly Significant Difference post-hoc correction was used in all cases to test for pairwise differences. Each ANOVA model is detailed in Table 5-1.

Table 5-1 ANOVA models used in SA 1.

Sub-aim	Model	Dependent Variables	Independent Variables
	1	F_C	LVP_{max}, suture position
	2	F_C	LVP_{max}, suture region*
	3	F_P	suture position
SA 1.A	**4**	nMPI (collagen), nMPI (non-specific fibers)	suture position
	5	F_C	LVP_{max}, ring type, ring-annulus size, suture position
	6	F_C	LVP_{max}, ring type, ring-annulus size, suture region*
	7	F_C	LVP_{max}, suture position, ring stiffness
	8	F_C	LVP_{max}, suture region*, ring stiffness
	9	$F_{C,Ant}/F_{C,Post}$	LVP_{max}, ring stiffness
SA 1.B	**10**	$HWHM_{norm}$	LVP_{max}, suture region, ring stiffness

*sutures grouped into regions as anterior (including left trigone, 11 o'clock, 1 o'clock, and right trigone) or posterior (including 3-9 o'clock).

Additionally, in order to test the causal relationship between collagen content and suture dehiscence likelihood, RS and nMPI were correlated. To facilitate this correlation, 12 o'clock and 6 o'clock RS were estimated by averaging their two closest positions (11 and 1 o'clock or 5 and 7 o'clock, respectively).

5.2 Specific Aim 2 Methods

5.2.1 *Establishment of Target Dimensions for Devices and Heart Selection Criteria*

Two key measurements of the mitral annulus were used as heart selection criteria throughout SA 2, for mock TMV plug dimensions, and for REFT dimensions: inter-trigonal distance and total perimeter. These parameters were chosen for three primary reasons. First, each is an established descriptor of the mitral annulus for TMVR sizing.[136, 137] Second, inter-trigonal distance is also the standard annular dimension used for annuloplasty ring selection (and is therefore most relevant to SA 1).[69, 138] Third, it was essential to control for perimeter in these studies, as they aimed to investigate phenomena occurring *at the perimeter* (i.e. paravalvular leak and radial force).

To establish the specific inter-trigonal distances and perimeters of interest, a preliminary assessment of the available hearts was performed. The assessment determined (a) the range of sizes commonly available from the slaughterhouse, and (b) the correlation between annular perimeter and inter-trigonal distance. Mitral annuli from 10 hearts were sized in terms of their perimeter (measured by photogrammetry using a ruler and MATLAB) and inter-trigonal distance (measured with an annuloplasty sizing tool from Edwards LifeSciences).

A strong linear relationship was found (perimeter = 3.866*(inter-trigonal distance) – 7.548; $R^2 = 0.863$). Using this relationship, it was determined that selected hearts would have mitral annuli with inter-trigonal distance of 30 mm, and perimeter as close as possible to 108.4 mm.

Accordingly, mock TMV plugs and REFTs were designed for true-sized and oversized geometries as given in Table 5-2. Another key aspect of these devices was the cross-sectional shape of their annulus-contacting regions. For circular devices this was trivial. For D-shaped devices this shape was based on published images of the Tiara TMV (Neovasc, Richmond, Canada; as shown in Figure 5-17). Its inter-commissural (IC) to septal-lateral (SL) diameter ratio was 1.30. Based on the best available images for Tendyne (Abbott Laboratories, Chicago, IL) another D-shaped TMV, its IC to SL diameter ratio is similar.

Table 5-2 Dimensions for annulus-contacting regions of mock TMV plugs and REFTs.

Device-Annulus Sizing	Profile Perimeter	Associated Inter-trigonal Distance	Circular profile diameter	D-shaped profile diameter	
				SL	IC
+0	108.4	30	34.5	28.8	37.5
+2	116.2	32	37.0	30.8	40.2
+4	123.9	34	39.4	32.9	42.9
+6	131.6	36	41.9	34.9	45.5

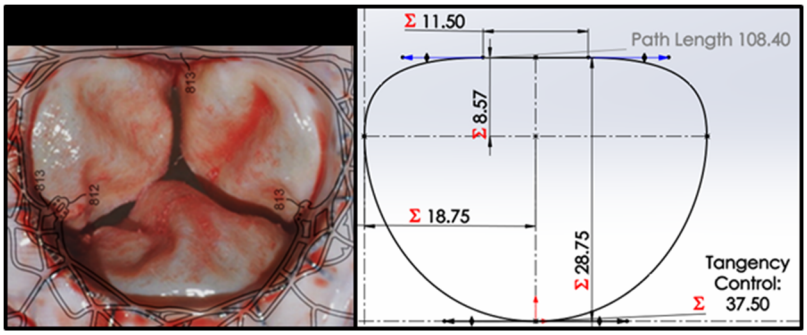

Figure 5-17 D-shaped profile design. Left: overlaid published images of the Tiara stent design[139] and a manufactured Tiara valve.[140] Right: Spline fit to Tiara profile.

5.2.2 Mock TMV Plugs: Design and Fabrication (SA 2.A)

5.2.2.1 Mock TMV Plug Design

Mock TMV plugs were designed for use in PVL studies. These devices featured three key components, shown in Figure 5-17 and further explained below.

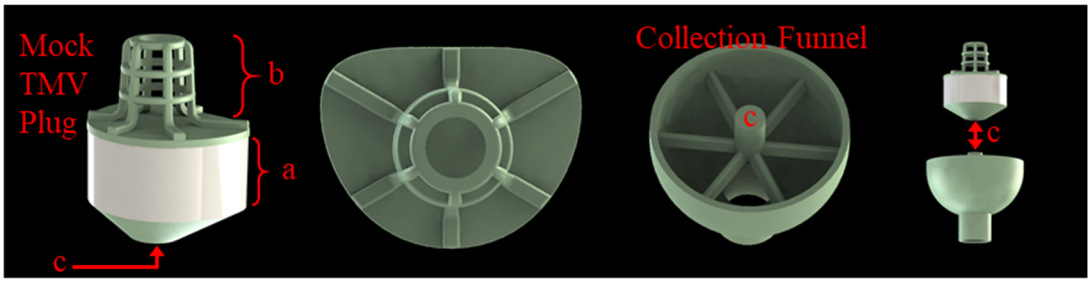

Figure 5-18 CAD renderings of mock TMV plug (side and top views) and collection funnel used for handling plug and directing leakage flow toward a spill plate. a) Annulus-contacting region (with polyester fabric skirt, height 20 mm). b) Ventricular cage (height 23 mm, minimum OD 15 mm). c) Screw connection (threading not shown).

Annulus-contacting region. This was a straight, circular or D-shaped section, 20 mm in height. This height was selected for two reasons. First, 20 mm would slightly exceed the range of annular saddle heights (14-18 mm) anticipated based on prior experience with the same supply of hearts, allowing the device to contact the entirety of the annulus. Second, this height approximately matches that of some existing TMVR stent designs (e.g., 19 mm in a device originally reported by Young et al[141]). This region was wrapped with a polyester fabric designed for cardiovascular devices.

Collection funnel. This additional tool was 3D printed, acetone vapor-polished, and threaded through the same techniques as the plugs themselves. It was designed to quickly screw into any given plug, and to serve two functions. First, it enabled easy handling of the plugs during deployment. Second, it captured the bulk of spray resulting from leakage flow, neatly routing it toward a spill tray.

Ventricular cage. This region featured a wide-cell mesh that served to transiently prop the native leaflets open (rendering their seal incompetent) during device deployment. Its dimensions were empirically derived and held constant across all plug designs. As illustrated in Figure 5-19, this feature was necessary because the hearts used in this study were healthy, and the mitral leaflets, when closed, exhibited redundant coaptation length. In the absence of this cage, the leaflets extended far enough across the plug to maintain a seal. In this event, no PVL would occur because the annulus was not exposed to fluid at all. The cage held the leaflets open without pressing on the left ventricular wall.

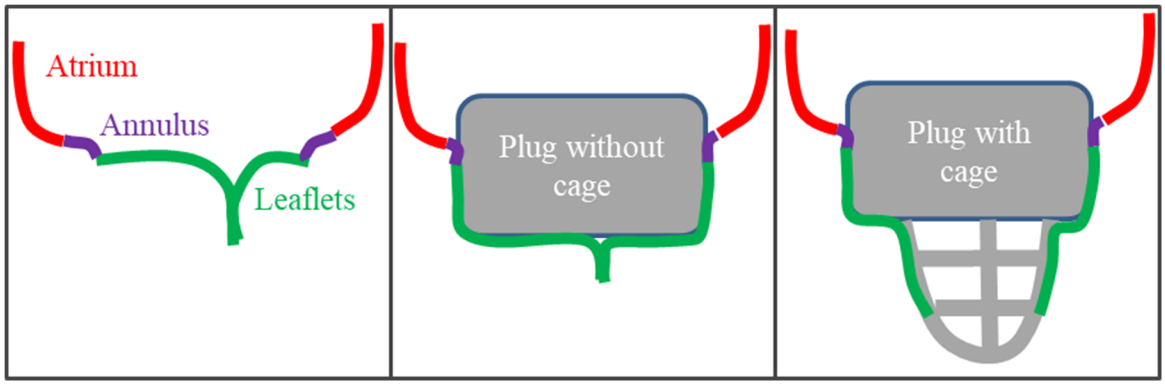

Figure 5-19 Rationale for the ventricular cage feature in the mock TMV plugs. Cage transiently rendered the mitral leaflets incompetent, enabling fluid to reach the annulus-contacting region and thus enabling PVL quantification.

5.2.2.2 Mock TMV Plug Fabrication

After 3D printing and acetone vapor-polishing the plug, it was wrapped with laser-cut polyester fabric. The fabric was adhered using a thin layer of RTV silicone.

5.2.3 Steady Back-Pressure Test System: Transducer Calibration

5.2.3.1 Pressure Transducer Calibration

The pressure transducer output a voltage in response to an applied pressure. It was calibrated by applying at least six known pressures ranging from -40 to 220 mmHg using a Delta-Cal^{TM} pressure transducer simulator/tester (650-950, Utah Medical) and recording the voltage response. This relationship was highly linear, with R^2>0.99 in all instances.

5.2.3.2 Flow Transducer Calibration

The flow probes output a voltage in response to an applied flow rate. They were calibrated by applying at least six known flow rates ranging from 2 to 200 ml/sec using a hydrostatic pressure head and recording the mean voltage response during this period. This relationship was highly linear, with $R^2 > 0.99$ in all instances.

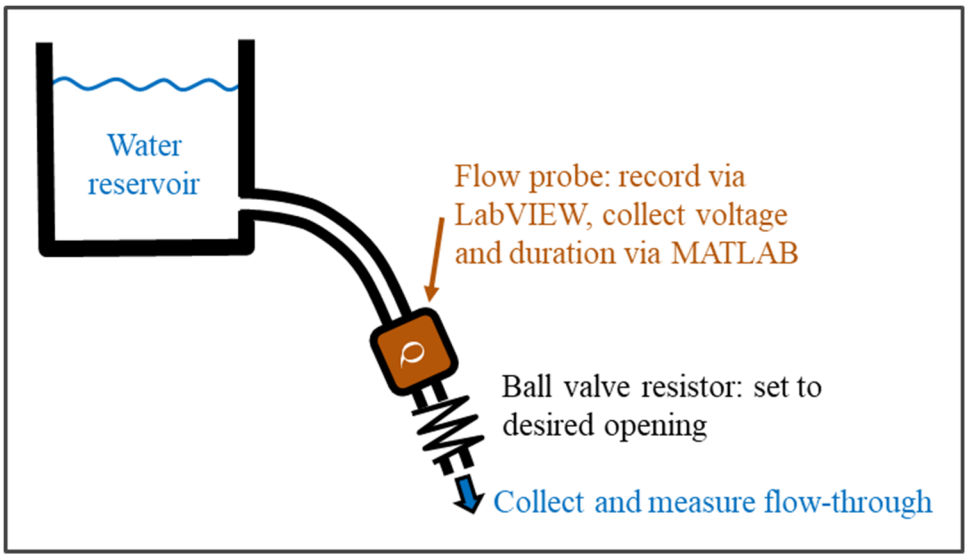

Figure 5-20 Setup for flow probe calibration across a range of flow-rates. Known flow-rate was derived from measured flow-through volume and measured flow interval. Flow interval and transducer output voltage were both determined via MATLAB.

5.2.4 Radial Expansion Force Transducers: Design, Fabrication, and Characterization (SA 2.B)

Note, a review of basic strain gage principles is presented in Section 5.1.1.1.

5.2.4.1 Radial Expansion Force Transducer Design

In this work, a dedicated force transducer was designed, manufactured, and instrumented with strain gages. As in the case of SA 1's Suture Force Transducers, strains in this system were not, themselves, of interest. Instead, the system was calibrated such that forces of interest could be measured, as described below.

The fundamental concept of the REFT was for a set of four arms, housed within a central hub, to be placed within the mitral annulus of an explanted porcine heart, then driven radially outward by a central piston. The radially inward, resistive force imparted to the arms by the tissue could be detected using strain gages installed on each arm. Arms were located at 12, 3, 6, and 9 o'clock (with 12 o'clock representing the mid-anterior annulus). By averaging of the signals at 12 and 6 o'clock or 3 and 9 o'clock, forces along the septal-lateral (SL) or inter-commissural (IC) axes were obtained. Arms would extend along a pre-determined path, tracing out either a circular or a D-shaped profile of the same dimensions studied in SA 2.A's PVL experiments. The C-REFT and D-REFT designs were nearly identical, differing only as needed to generate the target profiles. The components of the assembly were as follows. Note, REFT performance is discussed in Section 7.2.2.1.

Arms. Each arm was composed of an annulus-contacting pad and a straight shaft (Figure 5-21). The pad's height was 20 mm, matching the height of the annulus-contacting region in the mock TMV plugs used for PVL studies. The pad occupied 23.7 mm of annular perimeter. Thus, total contact area of each pad was 474 mm^2. The shaft had a step region. This allowed application of strain gages, wiring, and coatings, without increasing the

shaft's maximum height. This made it possible to pass the instrumented arms through the hub during initial assembly. The shaft's piston-contacting face had a pitch matching that of the corresponding face on the piston.

Each arm used four strain gages, two each on top and bottom, with each pair aligned orthogonally and wired in a full-bridge configuration (type III, as described in National Instruments white paper 3642; http://www.ni.com/white-paper/3642/en/#toc3). This configuration improved strain sensitivity, eliminated temperature sensitivity, and eliminated any response due to bending (thus isolating compression/extension).

While all four arms were identical for the C-REFT, the asymmetry in the D-REFT profile led it to possess four unique arms. Also, because the 23.7 mm pad perimeter was held constant across all arms, the 3 and 9 o'clock arm shafts of the D-REFT were each rotated 13° posteriorly from the IC axis. The 13° rotation implied a 2.6% differential between measured forces at 3 or 9 o'clock and their components in the IC direction. This is an acknowledged design limitation, which is considered negligible in light of (a) the small magnitude of the differential, and (b) the likely similar resistive force facing the chosen arm design and a theoretical, alternate design in which the 3 and 9 o'clock arms were aligned on the true IC axis.

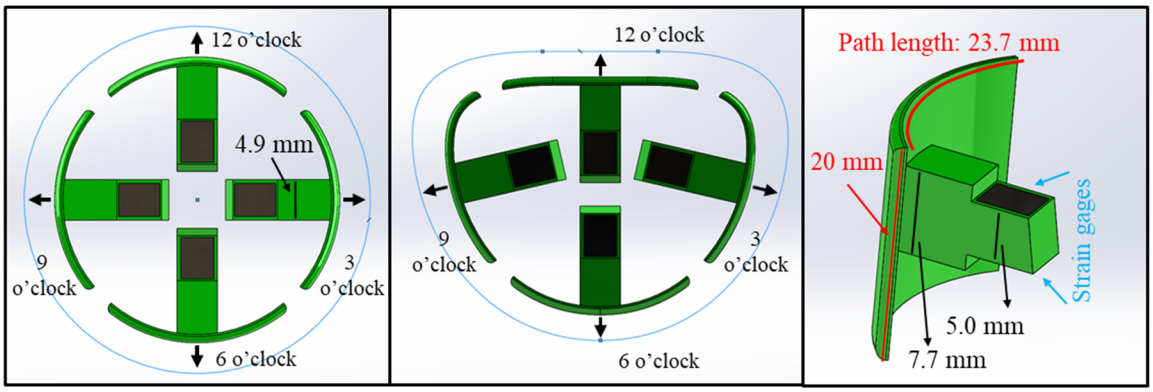

Figure 5-21 From left to right: C-REFT arms, D-REFT arms, and one C-REFT arm from side view. Blue contours depict target profiles for +6 size; arms sat along this profile after piston was fully depressed. Arms were positioned at 12, 3, 6, and 9 o'clock.

Piston. The piston was comprised of a steel rod and a plastic wedge, which were permanently bonded together at a precise position to enable the desired annular oversizing levels. The user operated the REFT by depressing the piston toward the LV apex, which drove the wedge between the arms and slid them radially outward into the MV annulus. Four pinholes were cut in the rod. A pin could be passed through the cap and any hole in the rod to lock the REFT to the +0, +2, +4, or +6 configuration. The wedge's total height was 25.9 mm (C-REFT) or 22.4 mm (D-REFT). The spacing between pinholes was 7.0 (C-REFT) or 5.8 mm (D-REFT).

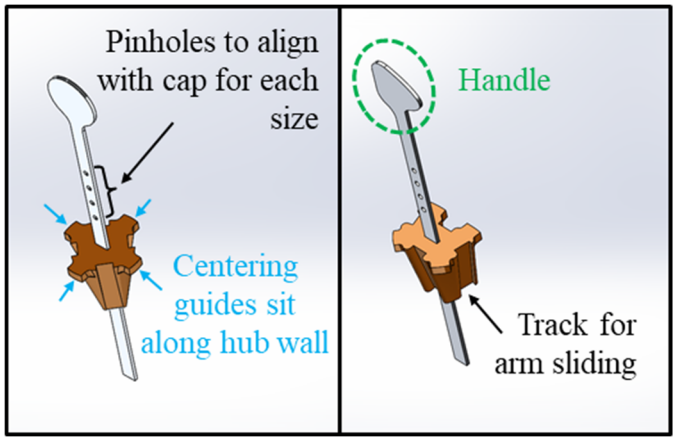

Figure 5-22 From left to right: C-REFT piston and D-REFT piston. The wedge (orange) was permanently bonded to the rod.

Hub (with screw extender).

The REFT hub's key features were holes for each arm to slide through, a cavity that housed and stabilized the piston, and seats for the cap. Additionally, an aluminum screw extender was permanently bonded to the hub. As further explained in 5.2.5.2, the screw and tapered region of the hub were passed through the MV annulus, and the base plate was screwed onto the extender until flush with the LV's cut surface. Further, the hub possessed tabs for mounting to the calibration apparatus.

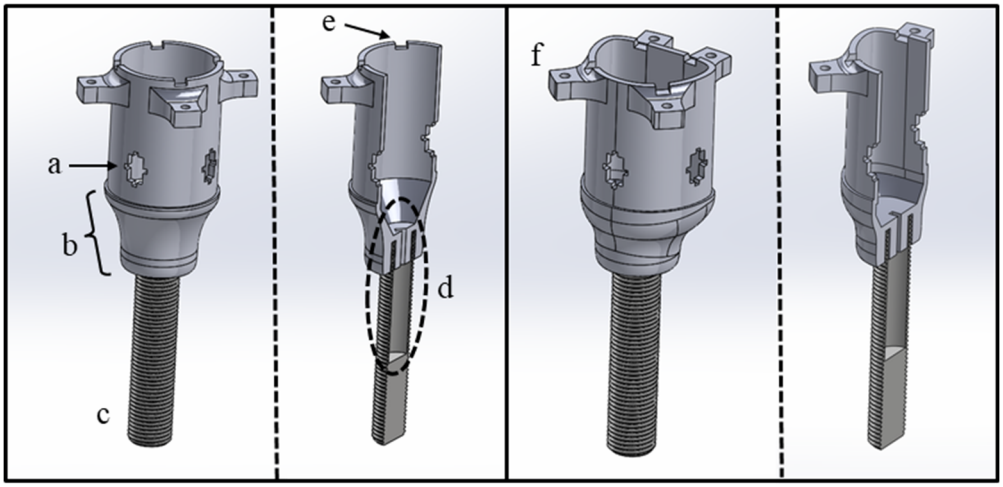

Figure 5-23 From left to right: Full and section views of C-REFT hub, and full and section views of D-REFT hub. a) arm holes, b) taper to ease passage through MV and into LV, c) permanently bonded ½"-20 screw extender to secure REFT to base plate at optimal height for each heart, d) open channel for piston rod, with narrow entry to obstruct piston wedge from over-depression, e) seats for cap, f) mounting tabs for calibration apparatus.

Cap. The cap's function was to both stabilize the piston and provide a way to set the piston (and, in turn, the arms) to target positions. The piston was free to glide up or down through the cap, and a pin could be passed through the cap and any desired hole in the piston rod to establish +0, +2, +4, or +6 sizing. The cap was not permanently fixed to the hub, so that the piston could be removed and lubricant re-applied between uses. Strain gage wiring easily passed out of the hub between the spokes of the cap.

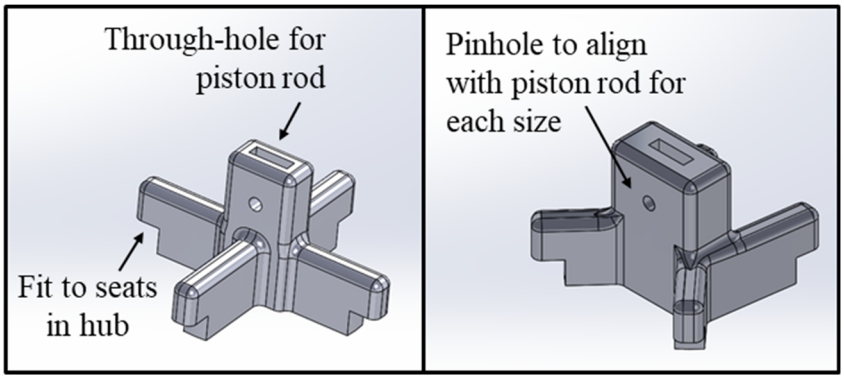

Figure 5-24 From left to right: C-REFT cap and D-REFT cap. The cap was pressed firmly onto the hub during use, held securely within seats in the hub. The piston could glide freely through the cap.

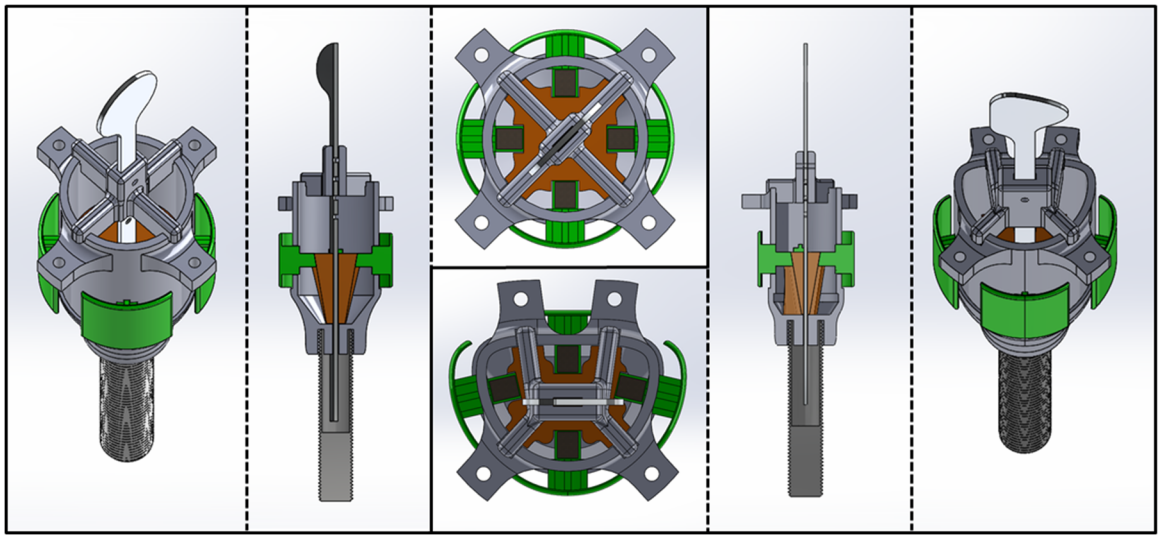

Figure 5-25 Full and section views of the fully-assembled C-REFT (left) and D-REFT (right) designs.

5.2.4.2 Radial Expansion Force Transducer Fabrication

To assemble the REFT, the 1/2”-20 threaded aluminum rod was first prepared by drilling a 1.5” hole with a W bit on a lathe and cutting the total length to 2.5.” The open end was bonded to the groove in the underside of the hub, using Loctite 4014 adhesive. Next, the piston rod was cut from the steel sheet using a water jet; lines were lightly etched to demarcate where the wedge would sit. *Before bonding the wedge to the rod, the cap was passed onto the rod from the bottom, past the bonding site for the wedge*. The wedge was carefully bonded into place using Loctite 4014 adhesive. Next, the strain gages were installed, using the protocol that follows.

Steps 1-4: Strain gage preparation; spring element surface preparation; strain gage alignment; strain gage adhesion. These steps were identical to Steps 1-4 for Suture Force Transducer fabrication; see Section 5.1.1.3. After completing Steps 1-4 for the upper gages, Steps 1-4 were repeated for the lower gages. For correct strain measurement, it was critical that the solder terminals faced opposite directions for the top and bottom gages (this ensured that gages directly on top of one another had the parallel pattern alignment).

Step 5: Strain gage wiring. Each solder terminal was tinned, by first depositing a tiny drop of flux to the terminal, then depositing a round spot of solder. Next, a 4’ length of three-stranded 336-FTE wire was slightly unwound and a miniscule length of outer Teflon coating was burned away to expose the metallic interior. Wires were bonded to each terminal, using the pattern indicated by National Instruments for use with the strain sensing tool within LabVIEW (for Type III Full-Bridge configuration). *The wires were oriented*

backwards overtop of the gage; this allowed more of the wire to be trapped under the protective coating, and relieved strain on the solder terminals when passing the instrumented arm through the hub.

Step 6: Application of strain gage dual protectant. Using a thin piece of steel wire as an applicator, a small amount of Loctite 3321 UV-curable adhesive was deposited atop one edge of the gage and immediately cured using a UV light wand. Care was taken to ensure the adhesive did not extend beyond the edges of the surface on which the gage was attached. More adhesive was applied and cured in additional small increments, until the gage and wire terminals were well-coated. This coating provided both mechanical and moisture protection. After completing Steps 5-6 for the upper gages, Steps 5-6 were repeated for the lower gages.

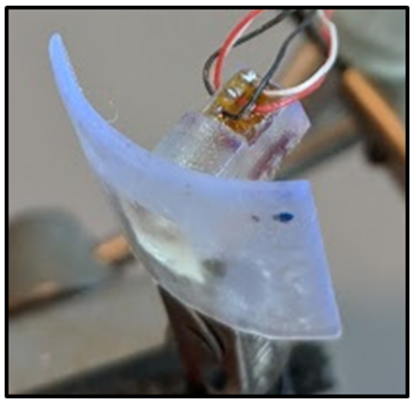

Figure 5-26 Post-Step 6. Clear UV-curable adhesive was carefully applied to encapsulate each gage and wire terminal.

Step 7: Final treatments for wiring. Next, each arm was guided carefully into the hub and wires were externalized through its top. Each arm's wires were carefully adhered to the wall of the hub using UV-curable adhesive. The 12 and 3 o'clock wires and the 6 and 9 o'clock wires were each bundled within heat-shrink tubing. Their twelve wires were drawn through lengths of tubing, by transiently tying them with thin suture to a 0.5 mm diameter braided metal wire, and carefully guiding the wire through the tubing.

Next, the free ends of the wires were burned to expose ~2-3 mm of their metallic cores, and each wire was soldered into a pin or sleeve (corresponding to the gender of the plug to which it would ultimately be mated). Groups of pins or sleeves were inserted into their respective housings.

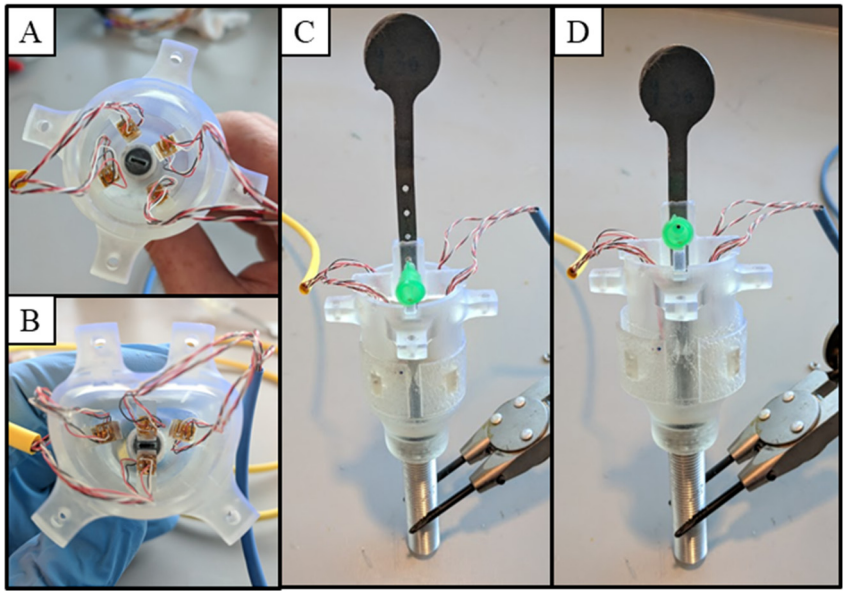

Figure 5-27 (A-B) Completed C-REFT and D-REFT, with cap and piston removed, and arms fully retracted, for clarity. (C-D) Completed C-REFT with cap and piston inserted, at +0 and +6 positions.

5.2.4.3 Radial Expansion Force Transducer Calibration

To enable the measurement of TMV radial expansion forces within the MV annulus, the electrical outputs of the strain gages adhered to the REFT arms were calibrated within a well-defined calibration apparatus (Figure 4-12). The REFT was first loaded into the calibration apparatus using four #3-48 screws passed through the hub's dedicated mounting tabs and through the calibration apparatus. The assembly was submerged in a water tank heated to 37 ± 2 °C. The REFT piston was depressed to move the arms to the +6 position (helping the arms to engage the screw-piston-spring-pusher assembly shown in Figure 4-13). With the LabVIEW program running, each screw was tightened one full rotation past the point at which a strain response was first detected. This ensured each arm was fully engaged with its pusher. All strain signals were zeroed.

Calibration was then performed as follows. Both arms along a given axis were calibrated simultaneously by alternately applying force on each arm. For example, when calibrating the 12 and 6 o'clock arms, the 12 o'clock screw was turned 360°, then the 6 o'clock screw was turned 360°, then 12 o'clock, etc., until reaching 14 full turns (7 per screw). Each turn applied 4.44 N along the axis, thus, peak loading was 62.16 N (this loading range was determined based on preliminary testing). This process was repeated four times per axis, alternating which screw was turned first. The voltage vs. force curve was computed; R^2 was between 0.976-0.999 in all instances.

Note, transducers were calibrated before and after use, to account for any changes in their sensitivity that may have occurred during use. During data analysis, force values were generated according to the *averaged* calibration factors from before and after use.

5.2.5 Sample and Test System Preparation

5.2.5.1 Paravalvular Leakage Studies

Pre-selected hearts (with inter-trigonal distance 30 mm and perimeter approximately 108.4 mm) were prepared as follows.

Step 1: Remove unwanted structures. The pre-selected heart was trimmed to remove any pericardium, and any large vessels other than the aorta. The aorta was transected proximal to the brachiocephalic artery. Both atria were removed, taking care to leave a consistent length of tissue (~1-1.5 cm) superior to the mitral annulus.

Step 2: Transect coronary circulation. Heart handling at the slaughterhouse and during experimental prep exposed many small coronary vessels which could leak significantly when the left ventricle and aorta were pressurized. To resolve this, the left and right main coronaries were carefully exposed close to the coronary ostia, and sealed with umbilical clamps.

Step 3: Attach flow loop fittings. First, the apical port was connected by cutting a hole in the apex, passing the inner component through, and screwing on the outer component until tight (see Figure 4-10). Next, a barbed 0.75" ID connector tube was placed inside the aorta and secured with two cable ties. This tube was modified with a luer port on its side for pressure transducer attachment.

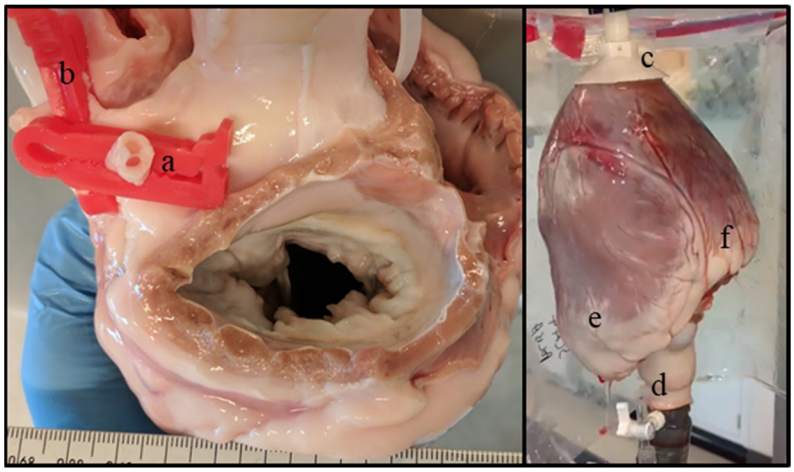

Figure 5-28 From left to right: post-Step 2, post-Step 3. a) clamped left main; b) clamped right main; c) installed apical port; d) aorta with installed connector; e) right ventricle; f) left ventricle.

The flow loop was then prepared as shown in Figure 5-29. R1 and R2 in this diagram were ball valves, whose degree of opening modulated LVP. The entire setup was arranged overtop a spill tray with drainage line. The apical port was gripped by a clamp approximately 24" above the tray, such that the heart was hanging by its apex in an *inverted* orientation. Note, with the ventricle pressurized and the atrial face of the mitral valve exposed to atmosphere, LVP and trans-mitral pressure gradient (ΔP) were equivalent quantities.

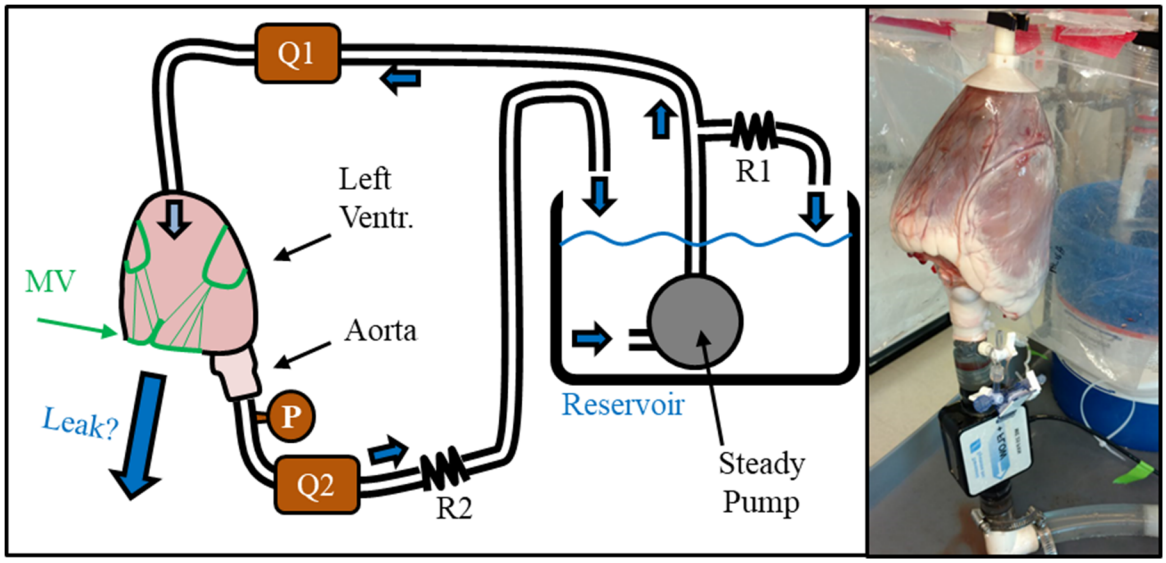

Figure 5-29 Schematic and photograph of steady back-pressure test system used for PVL studies. R1, R2: adjustable resistors; P: pressure transducer; Q1, Q2: flow transducers. Leakage flowrate was computed as the difference, Q1 – Q2.

5.2.5.2 Radial Expansion Force Studies

Pre-selected hearts (with inter-trigonal distance 30 mm and perimeter approximately 108.4 mm) were prepared as follows.

Step 1: Remove unwanted structures. The pre-selected heart was trimmed to remove any pericardium, and any large vessels other than the aorta. The aorta was transected proximal to the brachiocephalic artery. Both atria were removed, taking care to leave a consistent length of tissue (~2.5 cm) superior to the mitral annulus.

Step 2: Transect ventricle(s). A planar cut was made through the left ventricle (typically some amount of right ventricle was also cut). The cut was *inferior* to the papillary muscles to avoid disrupting any mechanical interaction between annulus and papillary muscles via the leaflets and chordae tendineae. It was also critical that the cut plane was parallel to the annulus mid-plane.

Figure 5-30 Left ventricle transected after Step 2.

Step 3: Implant and secure REFT. The heart was pre-assigned to receive either the C-REFT or D-REFT. The REFT was implanted by passing the screw through the MV and out the left ventricle opening. The acrylic base plate was screwed onto the hub and tightened until the LV was supported at optimal REFT positioning. Optimal REFT positioning was defined as having the mid-plane of the arms coincident with that of the annulus, and with the 12 o'clock arm centered between the left and right trigones. The base plate was then placed onto its stand.

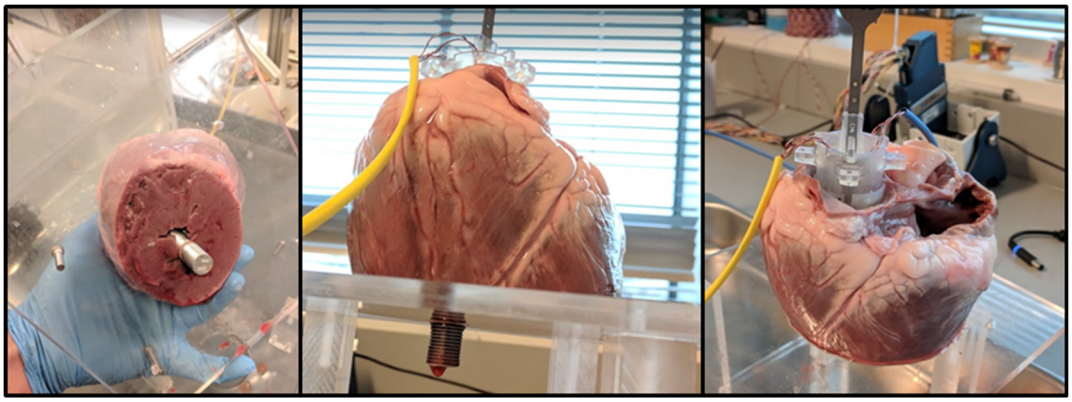

Figure 5-31 Various views post-Step 3. The REFT has been positioned within the heart and then screwed onto the base plate. The base plate has been placed onto its stand.

Step 4: Submerge in water bath and pressurize aorta. The heart was submerged in a water bath maintained at 37 ± 2 °C. A barbed 0.75" ID connector tube was placed inside the aorta and secured with two cable ties. This tube was modified with a luer port on its side for pressure transducer attachment. A steady flow loop, used to establish 120 mmHg aortic pressure, was prepared as shown in Figure 5-32. R1 and R2 in this diagram were ball valves, whose degree of opening modulated aortic pressure. The entire setup was arranged overtop a spill tray with drainage line.

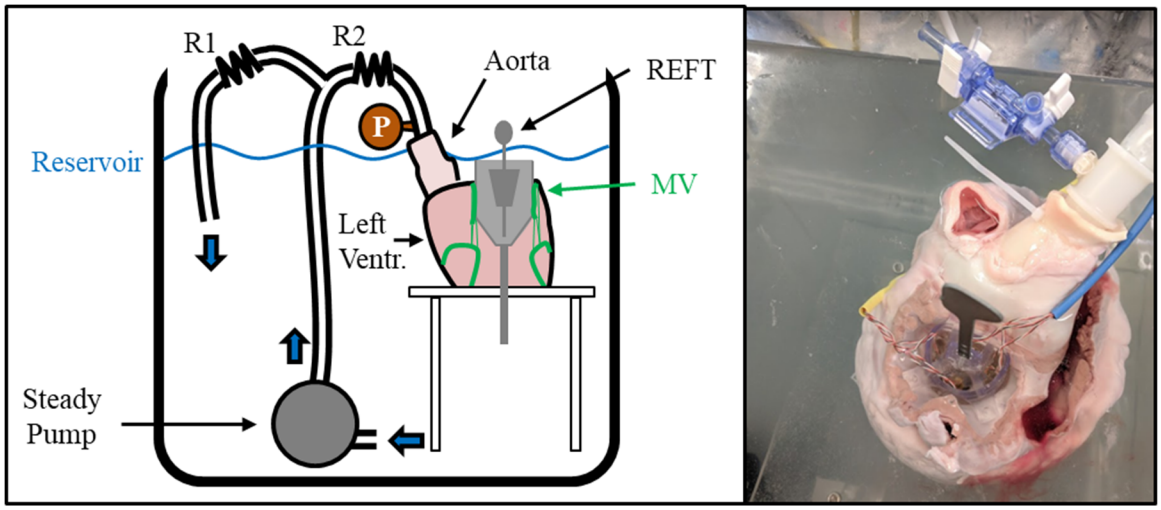

Figure 5-32 Schematic and photograph of full REFT setup. R1, R2: adjustable resistors; P: pressure transducer. Resistors were tuned to establish 120 mmHg aortic pressure.

5.2.6 Experimental Protocols

5.2.6.1 Paravalvular Leakage Studies (SA 2.A)

The reservoir was filled with water heated to 37 ± 2 °C. The pump was turned on and held to a constant power (70% variac power throughout all experiments), which generated approximately 130 ml/sec output. Air bubbles were purged from the tubing, as they would otherwise interfere with flow transducer readings. The vertical offset distance between the pressure transducer and the MV mid-plane was measured; the associated hydrostatic pressure was computed. Within the LabVIEW program, this pressure was input as a correction offset, such that the pressure signal would then reflect the true ΔP driving leakage flow through the annulus. The annular saddle height at ΔP = 120 mmHg was measured.

A repeatable approach for device placement/positioning was used, with a single operator performing every deployment. With the operator holding the collection funnel, the mock TMV plug was oriented such that the skirt's seam aligned with the mid-point of the anterior annulus (12 o'clock). It was guided past the mitral orifice and into the LV, until the mid-planes of the annulus and of the device's skirt were coincident. Coincidence was defined according to the 20 mm skirt height and the pre-measured annular saddle height. For example, for a 16 mm saddle, 2 mm of the skirt would extend below the annulus' most basal points (i.e. 12 and 6 o'clock). Finally, the device was gently rocked about its 12 o'clock to 6 o'clock axis until the maximum possible ΔP was achieved.

PVL data collection was comprised of multiple "acquisitions." One acquisition entailed deploying a single device with R1 completely closed (i.e., with LVP between 85-95 mmHg), then toggling R1 and R2 to systematically attain five *approximate* ΔP targets: 60 mmHg, 90 mmHg, 120 mmHg, 150 mmHg, and max LVP, i.e. the LVP produced by completely closing R1 and R2 (typically 160-200 mmHg). These targets were chosen based on ISO guideline 5840-3, which considers ΔP levels of 60, 120, 150, and 180 as the peak pressure differentials across a closed mitral valve corresponding to hypotensive, normotensive, mild hypertensive, or severe hypertensive states, respectively.[112] These targets were intentionally only approximate, both to facilitate more rapid data collection, and to provide more robust input data to the General Linear Model used to analyze the system (see section 5.2.8). Each target LVP was held steady (i.e., the resistors were left untouched) for 8 seconds. To provide robustness against potential variation in deployment positioning, three acquisitions were collected for each of the eight mock TMV plugs. The

sequence of acquisitions was in order of increasing size, alternating circular (C) and D-shaped (D) devices of each size according to a snaking pattern as shown below:

Table 5-3 The sequence in which each of the 24 PVL data acquisitions was performed in each experiment. Each acquisition was performed with one device, having a given size and shape (e.g. D+0, etc). One acquisition consisted of five data points at target LVPs.

Acquisition	**1**	**2**	**3**	**4**	**5**	**6**	**…**	**19**	**20**	**21**	**22**	**23**	**24**
Size	**+0**	**+0**	**+0**	**+0**	**+0**	**+0**	…	**+6**	**+6**	**+6**	**+6**	**+6**	**+6**
Shape (odd expts)	D	C	C	D	D	C	…	D	C	C	D	D	C
Shape (even expts)	C	D	D	C	C	D	…	C	D	D	C	C	D

Throughout the experiment, three key actions were performed at regular intervals. These were (a) hydration of the epicardial surface via a water spray bottle, (b) re-filling of the reservoir with water at 37 ± 2 °C, and (c) "baseline" recordings covering 5 or more LVPs ranging from 50-210 mmHg with no plug in place (so that baseline leakage through tubing and/or ports could later be offset from the PVL data, as detailed in Section 5.2.7.1).

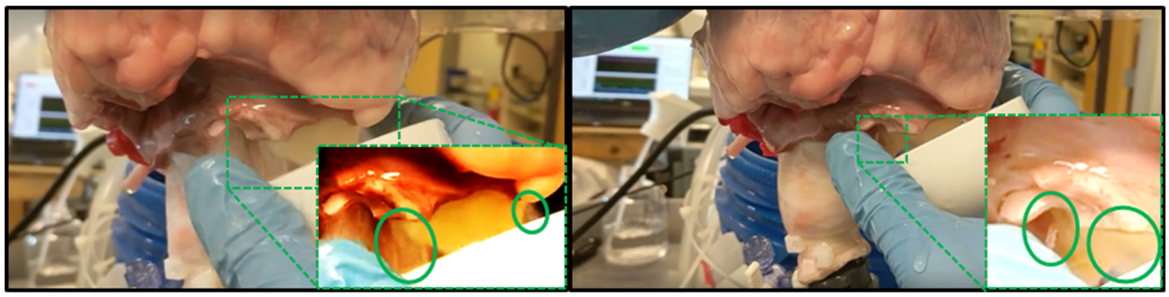

Figure 5-33 Representative images of paravalvular leakage experiment. Inset images are zoomed in on mock TMV plug extending out from the MV annulus. Left inset image is enhanced to improve visibility of leakage flow. Two time points are also shown to ease the reader's recognition of leakage flow (green circles).

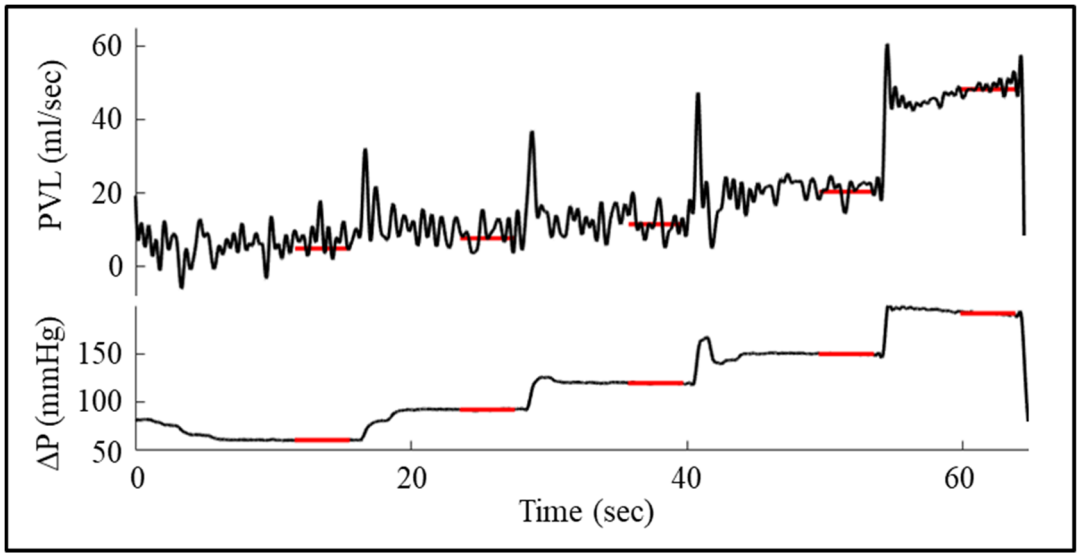

Figure 5-34 Representative data from a single acquisition, which demonstrates the PVL experimental protocol. With the mock TMV plug in place, five ΔP levels were established and held as PVL rate was measured. Red lines: average ΔP and PVL values over a four-second interval.

5.2.6.2 Radial Expansion Force Studies (SA 2.B)

Throughout the experiment, the water tank was maintained at 37 ± 2 °C. The pump was maintained at a constant power (50-60% variac power); the ball valves were adjusted as needed to establish 120 mmHg aortic pressure. 120 mmHg was chosen to replicate the aortic pressure during peak systole.

Each acquisition began with the pin in place at the +0 size and proceeded as follows. After a five second recording, the pin was removed and the piston depressed to establish either the +2, +4, or +6 size. The pin was inserted and held in place for five seconds. The pin was removed and the piston drawn back to re-establish the +0 size. The pin was inserted and held in place for five seconds. 24 acquisitions were collected per heart: eight with

expansion to +2, followed by eight with expansion to +4, followed by eight with expansion to +6.

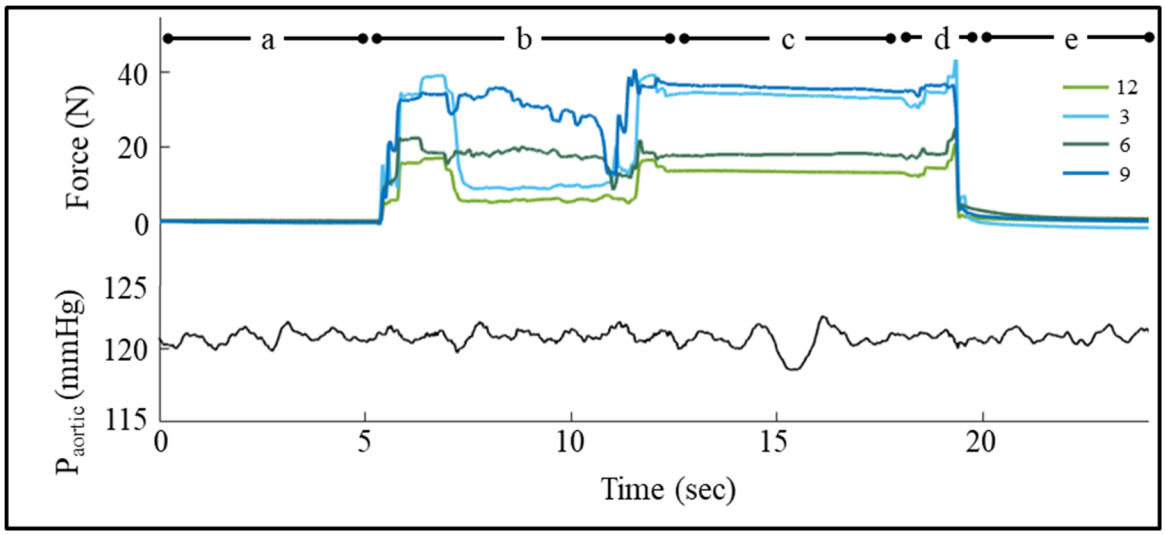

Figure 5-35 Representative data depicting the REFT experimental protocol. (a) Force signals are zeroed with REFT at +0 size, (b) piston is depressed until the pin can be inserted to lock the REFT to the desired expanded size, (c) expanded size is maintained for five seconds, (d) +0 size is re-established, (e) +0 size is maintained for five seconds.

After completing all REFT experiments, one additional porcine heart was subjected to micro-computed tomography imaging to generate a clear depiction of the anatomical features that may underlie the observed force dynamics. The heart had its atria removed, and a ring of 20 small sand markers glued to the annular hinge line to delineate it clearly post segmentation. These markers and their usage have been described by Pierce et al.[142] Imaging used a Siemens Inveon scanner and Inveon Acquisition Workplace software (Siemens Medical Solutions USA, Inc., Malvern, PA), with settings optimized for soft tissue visualization (80 kV, 500 mA, 550 ms integration time). Volumes were composed

of 43.29 μm isotropic voxels. Following data acquisition, images were analyzed using Inveon Research Workplace.

5.2.7 Data Processing and Experimental Endpoints

5.2.7.1 Paravalvular Leakage Studies (SA 2.A)

Recorded data were processed offline using custom MATLAB scripts. The primary endpoints were the *trans-mitral pressure gradients (ΔP)* established by adjusting the resistors, and their corresponding *paravalvular leakage rates (PVL).* Five (ΔP, PVL) data points were obtained from each acquisition. Each value was computed by averaging 4 seconds of data.

PVL values were then corrected for any incidental leakage through the apical, aortic, or other connections. This correction made use of the aforementioned baseline recordings that did not use a TMV plug. The series of (ΔP, PVL) points from each baseline recording were computed, and used to define an *incidental leakage curve* across the full ΔP range. This curve was computed using the Piecewise Cubic Hermite Interpolating Polynomial (PCHIP) method. The PCHIP is a "shape-preserving" form of the more common cubic spline fit. Unlike splines, PCHIPs enforce monotonicity of each piece. As a result, the curve has no overshoots beyond the range of the data points,[143] and is thus a more conservative model of incidental leakage. Based on the average of the incidental leakage curves before and after each mock TMV plug acquisition, an incidental leakage

rate at the instant of each (ΔP, PVL) data point was estimated, and subtracted from the PVL value.

Further, it is important to note that the flow probes used here each possessed an absolute accuracy of 4% (per manufacturer specifications). PVL was calculated from the difference between *two* flow probe measurements, thus, the theoretical worst case PVL uncertainty was 8% of the pump output (i.e., approximately 10 ml). Owing to this error, PVL values were occasionally near zero or slightly negative after incidental leakage correction. To correct for this, in any experiments for which the minimum PVL recording was below 1 ml/sec, *all* PVL samples from that experiment were offset uniformly, such that the minimum PVL recording became 1 ml/sec.

One of the statistical models used to assess differences in sealing among device shapes and sizes did so in a pressure-normalized sense (see Section 5.2.8.2). To achieve this, each PVL observation, PVL_i was first converted to a unitless quantity, referred to as normalized PVL, or $PVL_{norm,i}$:

$$PVL_{norm,i} = \frac{\left(\frac{PVL}{(\Delta P)^2}\right)_i}{\left(\frac{PVL}{(\Delta P)^2}\right)_{mean}} - 1 \quad (6)$$

PVL_{norm} was a key secondary endpoint, which quantified the percent change in pressure-normalized leakage of each observation, *relative to the average value across all observations*. Results were reflective of the overall sealing performance of each device. For example, if PVL_{norm} for a given device type were 0.1, this would signify 10% more normalized leakage *across all pressures* using this device, as compared to the average

device. The use of $(\Delta P)^2$, rather than ΔP itself, was based on the empirically observed quadratic relationship between PVL and ΔP (described in detail in Section 7.2.1.2). PVL_{norm} enabled comparisons between each device *as a whole*, rather than specific to a given pressure level.

Additional secondary endpoints included:

- *Inter-trigonal distance:* Measured using an annuloplasty ring sizer set (Edwards LifeSciences), before and after all PVL measurements.

- *Annular 2-D perimeter and area:* Measured by photogrammetry, before and after all PVL measurements (Figure 5-36).

- *SL diameter and IC diameter:* Measured by photogrammetry, before and after all PVL measurements. Measurements were made per current recommendations for TMVR.[144, 145] A line was first drawn between the trigones. A perpendicular line bisecting the inter-trigonal line defined the SL diameter. Another line, perpendicular to the SL diameter and passing through the annulus centroid (i.e., the SL midpoint), defined the IC diameter (Figure 5-36).

- *Annulus saddle height:* Measured directly with a ruler, after mounting the heart and pressurizing to $\Delta P = 120$ mmHg.

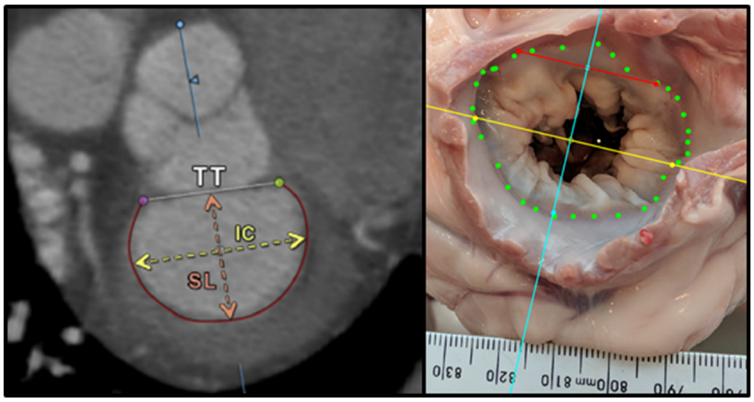

Figure 5-36 Left: Recommended approach for mitral annular sizing for TMVR (modified from Naoum et al[145]). Right: Representative MV used for PVL or REFT studies, after measuring relevant dimensions.

5.2.7.2 Radial Expansion Force Studies (SA 2.B)

Throughout all acquisitions, aortic pressure was maintained at 120 mmHg. Any acquisitions in which aortic pressure unintentionally deviated by more than 10 mmHg were noted during data processing and discarded. Recorded data were processed offline using custom MATLAB scripts.

The primary endpoints were the *septal-lateral and inter-commissural forces (F_{SL} and F_{IC})* during each acquisition. F_{SL} was obtained by averaging the force signals at 12 and 6 o'clock; F_{IC} was obtained by averaging the force signals at 3 and 9 o'clock. Secondary endpoints included *inter-trigonal distance, annular 2-D perimeter and area, SL diameter and IC diameter*, each measured as described for SA 2.A (Section 5.2.7.1).

5.2.8 Statistical Analysis

5.2.8.1 Further Comments on ANOVA and the General Linear Model (GLM)

The fundamental concepts of ANOVA are described in Section 5.1.6.1, as an introduction to its extensive usage for SA 1. Two additional introductory comments are pertinent to the analyses used in SA 2.

First, it is important to note that ANOVA is only one instance of a broader statistical modeling format known as the *General Linear Model (GLM)*. In ANOVA, the independent variables must be categorical. In contrast, the well-known counterpart to ANOVA, multiple linear regression, requires that independent variables are continuous. GLM allows for either categorical or continuous independent variables. GLM requires the same assumptions to be met as does ANOVA, but additionally, it assumes that the dependent variable is *linearly* related to each continuous independent variable. For further information on GLM, the interested reader is referred to *Regression, ANOVA, and the General Linear Model: A Statistics Primer*.[146]

Second, for both GLM and ANOVA, it is noted that in instances where model residuals are not normally distributed, and/or the relationships between dependent and continuous independent variables are non-linear, data transformations (such as log or square root of the dependent variable) are a common solution.[147]

5.2.8.2 Analyses Used

All statistical analyses were performed using MATLAB and/or Minitab (Minitab Inc., State College, PA). To understand the correlation between ΔP and PVL, linear and quadratic regressions were each performed. For hypothesis tests between two groups, Student's t-test was used. The central statistical tool was the GLM, one instance of which was multi-way ANOVA. PVL_{norm}, sqrt(PVL), PVL, F_{SL}, F_{IC}, and sqrt(F_{IC}/F_{SL}) were each treated as the dependent variable in various GLM or ANOVA models. Independent variables in these models included TMV shape, TMV size, and (for PVL studies) ΔP. Each model was run first without interaction terms to assess main effects, then with all possible two-factor interactions. For ANOVA, Tukey's Honestly Significant Difference post-hoc correction was used to test for pairwise differences. Each model is detailed in Table 5-4. Further explanation of each model follows.

Table 5-4 GLMs used in SA 2.

Sub-aim	Model	Dependent Variables	Independent Variables
	1	PVL_{norm}	TMV shape, TMV size
	2	sqrt(PVL)	TMV shape, TMV size, ΔP*
SA 2.A	**3****	PVL	TMV shape, TMV size
SA 2.B	**4**	F_{SL}, F_{IC}, sqrt(F_{IC}/F_{SL})	TMV shape, TMV size

*continuous variable; **only included samples having ΔP between 110-130 mmHg.

To investigate differences in PVL dynamics between device types in SA 2.A, three complementary statistical methods were used:

- GLM 1: compared across all pressures simultaneously, by converting leakage to a *pressure-normalized* term, PVL_{norm}. PVL_{norm} is defined in Section 5.2.7.1; it

reflected the proportion change in pressure-normalized leakage of any given observation relative to the average observation. For example, if PVL_{norm} for a given device type were 0.1, this would signify 10% more leakage using this device than the average device, *across all pressures*. This approach had the advantage of encapsulating data from all pressures simultaneously, but the disadvantage is that its units are relative.

- GLM 2: accounted for ΔP as a continuous, independent variable, enabling generation of a 95% confidence interval for each device type at any ΔP. This approach had two advantages. First, it offered easy comparison among devices at any exact pressure level of interest (these were 60, 90, 120, 150, and 180 mmHg, per ISO guideline 5840-3[112]). Second it offered increased sensitivity relative to ANOVA, which would require binning of observations into pressure categories. However, its disadvantage was that the GLM assumes a linear relationship between the continuous independent and dependent variables. Due to the empirically observed quadratic relationship between PVL and ΔP (see Section 7.2.1.2), this assumption was satisfied by using the *square root of PVL* as the dependent variable. Thus, this model's units, although absolute, may be less familiar for most readers.
- GLM 3: compared within a narrow pressure range of interest by wholly neglecting the influence of pressure within that range. Due to the relevance of 120 mmHg as both the approximate mean ΔP in these experiments, and as the peak ΔP under normal physiologic conditions, GLM 3 included samples obtained in the 120 ± 10 mmHg range. This approach had the advantage that it avoided the need to transform

PVL to sqrt(PVL), and thus its output was expressed in real-world units (ml/sec). Its disadvantage was reduced sensitivity relative to GLM 2.

As a final note, GLM 4 from SA 2.B used sqrt(F_{IC}/F_{SL}) instead of F_{IC}/F_{SL}; this was necessary to satisfy the assumption of normally distributed residuals.

CHAPTER 6. RESULTS AND DISCUSSION – SPECIFIC AIM 1

6.1 Introduction to Specific Aim 1 Results and Discussion

For the reader's convenience, the experimental schematic for Specific Aim 1 is reproduced here, followed by an experimental matrix:

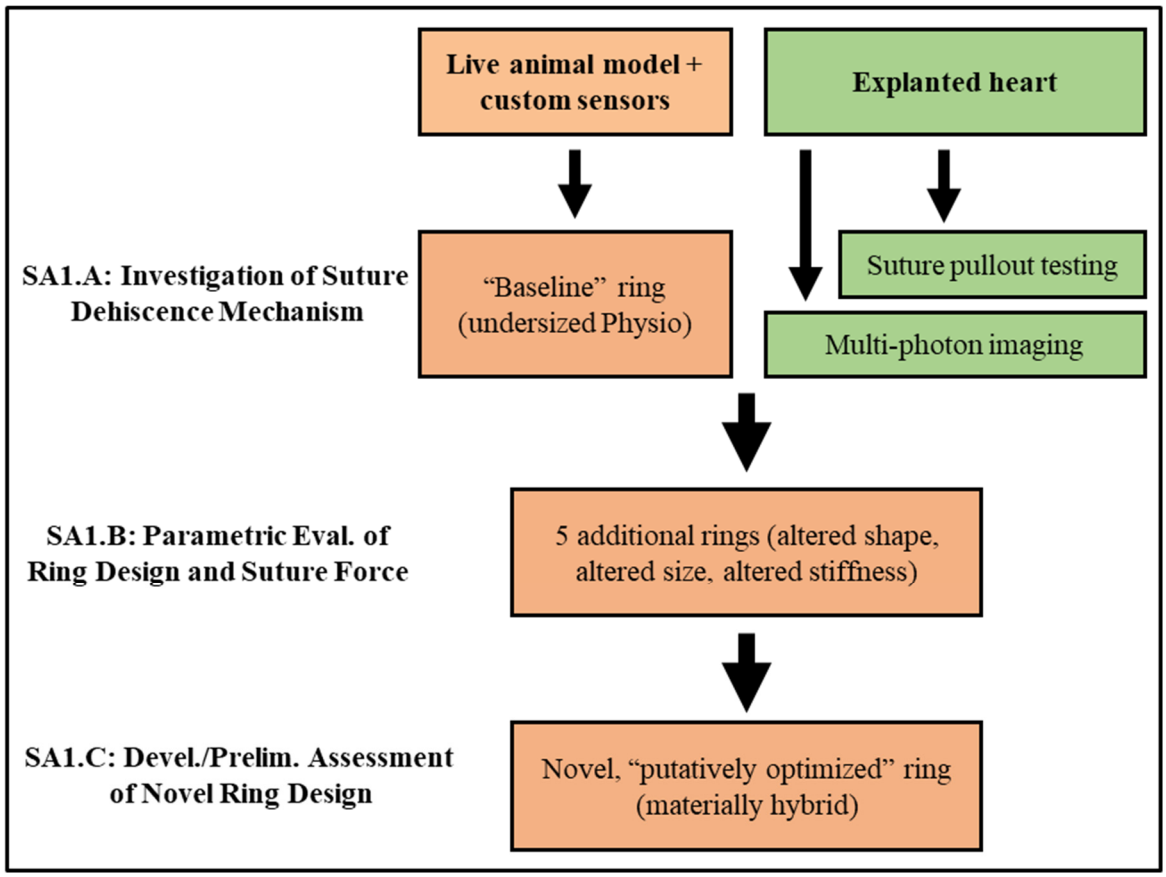

Figure 6-1 Schematic of Specific Aim 1 Experiments (duplicated from CHAPTER 3).

Table 6-1 Experimental matrix for SA 1.

	Test	Expts	Suture positions	LVPs	Data points
SA 1.A	*in vivo*, ovine, w/ undersized Physio	5	10	3	**150**
	ex vivo, ovine, suture pullouts	12	10	N/A	**120**
	in vitro, ovine, multi-photon imaging	5	4	N/A	**20**
SA 1.B	*in vivo*, ovine, w/ true-sized Physio	5	10	3	**150**
	in vivo, ovine, w/ undersized Profile 3D	6	10	3	**180**
	in vivo, ovine, w/ true-sized Profile 3D	7	10	3	**210**
	in vivo, ovine, w/ undersized rigid prototype	6	10	3	**180**
	in vivo, ovine, w/ undersized flexible prototype	5	10	3	**150**
SA 1.C	*in vivo*, ovine, w/ undersized hybrid prototype	3	10	3	**90**

The experimental designs for Specific Aims 1.B and 1.C were finalized according to the insights gained in the sub-aims preceding them. Therefore, in this chapter, brief comments are provided following the results of SA 1.A and SA 1.B (Sections 6.2.1.4 and 6.2.2.4), in advance of a full discussion of the entire Aim (Section 6.3).

Note, many of the graphs that follow provide results in terms of both (a) mean ± standard deviation (SD), represented with bars, and (b) mean ± 95% confidence interval (CI) *following ANOVA with Tukey's post-hoc corrections*, represented with dots. Text values are provided as mean ± SD. Also, orange or purple background in the following graphs denotes the anterior or posterior region of the annulus, respectively. For the reader's convenience, Table 5-1, which summarized all ANOVA models used in SA 1, is reproduced here as Table 6-2.

Table 6-2 ANOVA models used in SA 1 (duplicated from CHAPTER 5).

Sub-aim	Model	Dependent Variables	Independent Variables
SA 1.A	1	F_C	LVP_{max}, suture position
	2	F_C	LVP_{max}, suture region*
	3	F_P	suture position
	4	nMPI (collagen), nMPI (non-specific fibers)	suture position
SA 1.B	5	F_C	LVP_{max}, ring type, ring-annulus size, suture position
	6	F_C	LVP_{max}, ring type, ring-annulus size, suture region*
	7	F_C	LVP_{max}, suture position, ring stiffness
	8	F_C	LVP_{max}, suture region*, ring stiffness
	9	$F_{C,Ant}/F_{C,Post}$	LVP_{max}, ring stiffness
	10	$HWHM_{norm}$	LVP_{max}, suture region, ring stiffness

*sutures grouped into regions as anterior (including left trigone, 11 o'clock, 1 o'clock, and right trigone) or posterior (including 3-9 o'clock).

6.2 Specific Aim 1 Results

6.2.1 Specific Aim 1.A: Investigation of the Basic Mechanism of Suture Dehiscence

A description of the sample populations used in SA 1.A is presented in Table 6-3. The F- and p-values from all ANOVA models used in SA 1.A are presented in Table 6-4.

Table 6-3 Data set summary for Specific Aim 1.A.

***In vivo* - cyclic forces**	**Sample size**	5
	Positions tested	10
	Animal Weight (kg)	58.2 ± 12.4
	Annulus size	30 ± 0
	Ring size	26
	HR at LVP_{max} = 100 mmHg (bpm)	111 ± 14
	HR at LVP_{max} = 125 mmHg (bpm)	122 ± 13
	HR at LVP_{max} = 150 mmHg (bpm)	134 ± 15
***Ex vivo* - pullout forces**	**Sample size**	12
	Positions tested	10
	Successful pullouts	112/120
***In vitro* - microstructural analysis**	**Sample size**	5
	Positions tested	4

Table 6-4 Results of all ANOVA models used in SA 1.A, before post-hoc analysis. ANOVA models are fully described in Table 6-2.

		Factor	**F**	**p**
Model 1 (F_C)	**Main effects**	LVP_{max}	2.44	0.091
		Suture position	8.81	<0.001
	Interactions	LVP_{max}:Suture position	0.04	>0.999
Model 2 (F_C)	**Main effects**	LVP_{max}	1.91	0.1515
		Suture region	23.93	<0.001
	Interactions	LVP_{max}:Suture region	0.05	0.956
Model 3 (F_P)	**Main effect**	Suture position	3.98	<0.001
Model 4 (nMPI for collagen)	**Main effects**	Suture position	7.86	0.002
Model 4 (nMPI for non-specific fibers)	**Main effects**	Suture position	0.35	0.791

6.2.1.1 Cyclic Suture Force (In Vivo) Studies

Instrumented Physio rings were successfully implanted in five healthy ovine subjects. In every case, the mitral annulus was size 30, and a size 26 ring was used. Cyclic contractile force (F_C) was measured successfully at three target LVP_{max} levels as described in Section 5.1.4.1. Under anesthesia, the Doppler-derived mean transmitral pressure gradient increased by 1.8 ± 2.1 mmHg after ring implantation (measured at resting heart rate and normotensive conditions, immediately before and after cardiopulmonary bypass). Representative suture force and LVP tracings are presented below.

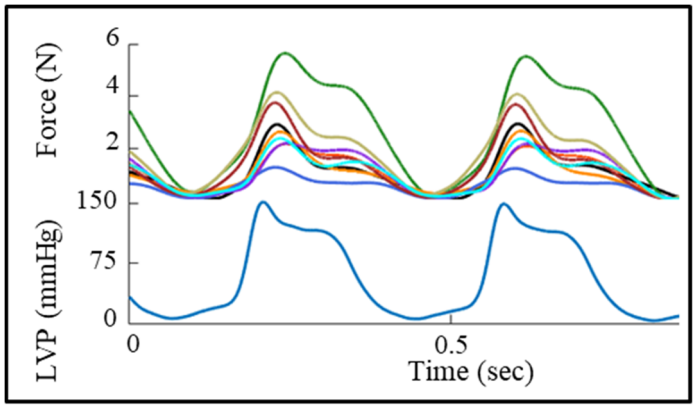

Figure 6-2 Representative, coupled tracings of annuloplasty suture forces and left ventricular pressure (LVP). Each force tracing corresponds to a single annuloplasty suture. Note, baseline pre-tension (i.e. the minimum absolute force in each tracing) has been zeroed to highlight the amplitude differences among the ten sutures.

In Figure 6-2, the rise and fall in suture force throughout the cardiac cycle was closely coupled to LVP. Ventricular contraction and relaxation were clearly associated with sharp rises and falls in suture forces, with forces peaking near mid-systole. These observations were consistent across all experiments.

The influences of LVP and suture position on F_C were quantified through ANOVA model 1, and that of suture region was quantified through ANOVA model 2. The results of these models are presented in Figure 6-3 through Figure 6-7, and described in the text following Figure 6-7.

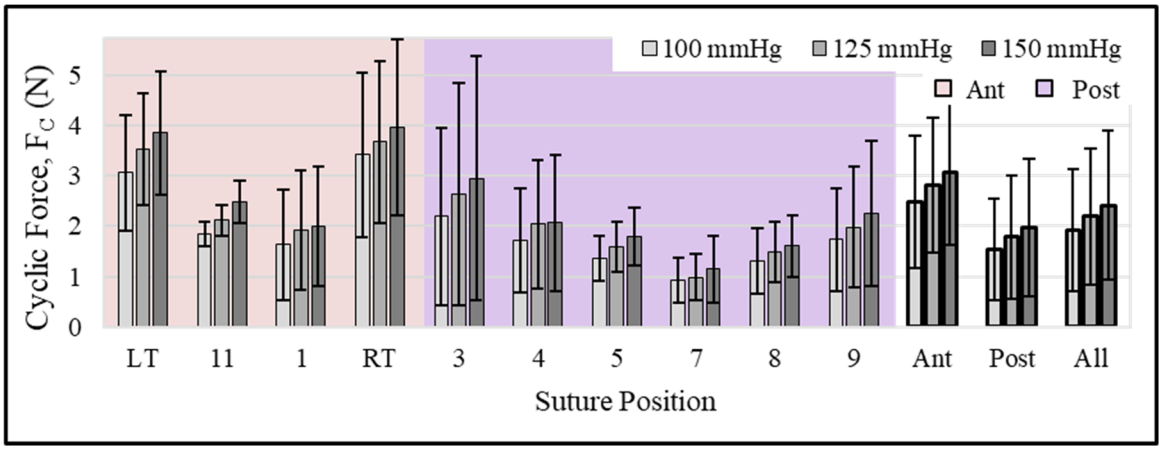

Figure 6-3 F_C results from undersized Physio rings, in terms of mean ± standard deviation (SD) for each suture position at each LVP_{max}. Although trends are apparent, statistical significance of these trends cannot be assessed until after ANOVAs 1 and 2 (see Figure 6-4 through Figure 6-6).

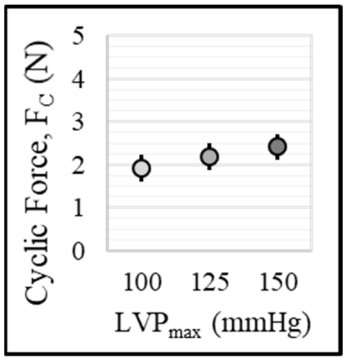

Figure 6-4 F_C results from undersized Physio rings, in terms of mean ± 95% confidence interval (CI) for each LVP_{max} (after ANOVA 1). Pairs whose 95% CIs do not overlap differ significantly ($p<0.05$). The trend of LVP_{max} versus F_C was positive but insignificant.

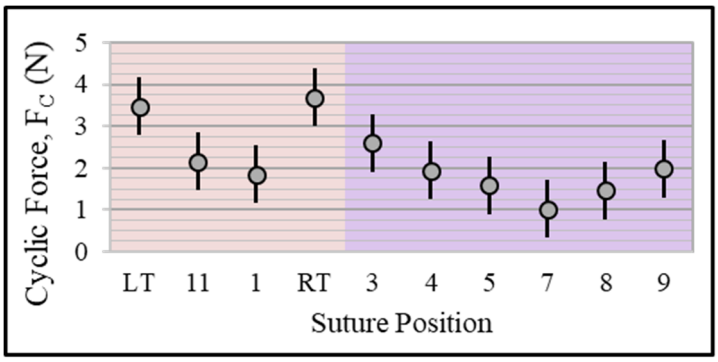

Figure 6-5 F_C results from undersized Physio rings, in terms of mean ± 95% CI for each suture position (after ANOVA 1). Pairs whose 95% CIs do not overlap differ significantly ($p<0.05$). F_C was significantly greater at either trigone than at numerous other positions.

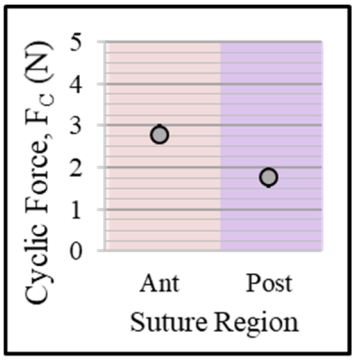

Figure 6-6 F_C results from undersized Physio rings, in terms of mean ± 95% CI for either suture region (after ANOVA 2). F_C was significantly greater for anterior sutures.

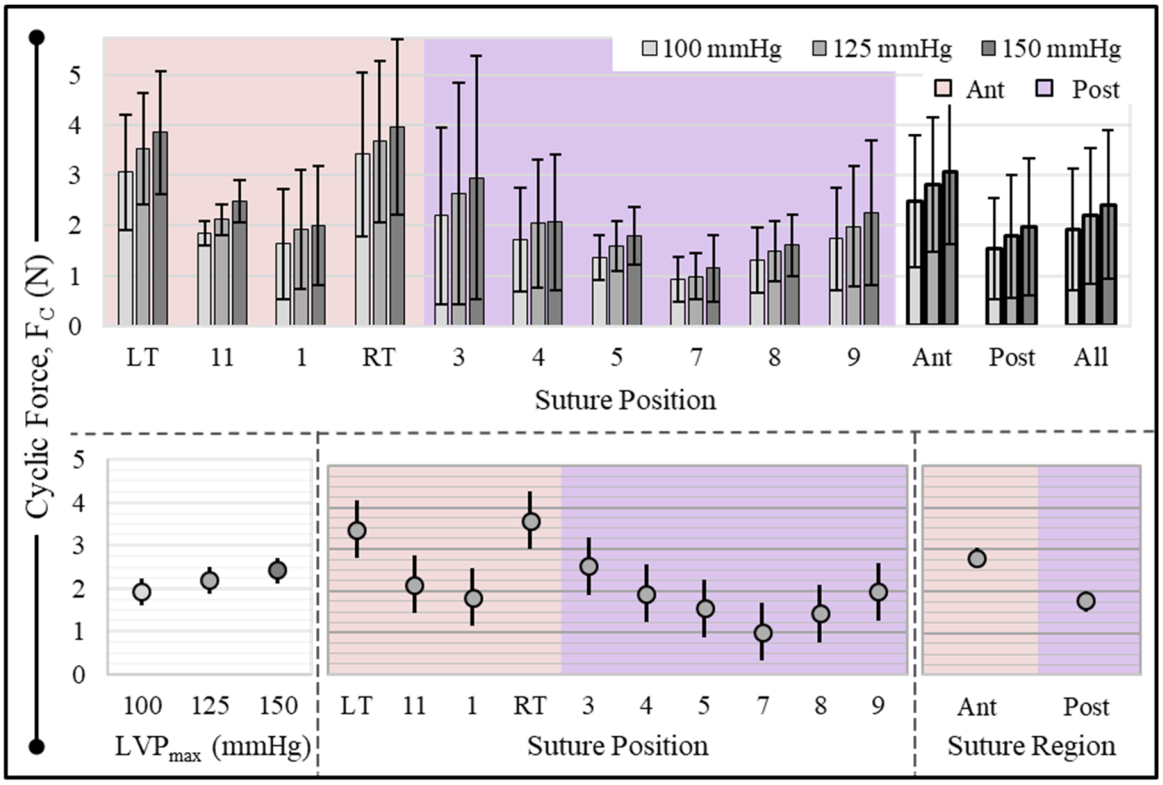

Figure 6-7 F_C results from undersized Physio rings, duplicated from Figure 6-3 through Figure 6-6. Top: mean ± SD for each suture position at each LVP_{max}. Bottom: mean ± 95% CI for each LVP_{max} and suture position (after ANOVA 1), or suture region (after ANOVA 2). Within each plot, pairs whose 95% CIs do not overlap differ significantly ($p<0.05$).

The mean F_C across all sutures was 2.2 ± 1.4 N. Among all 50 sutures, the absolute minimum and maximum F_C were at 100 mmHg/4 o'clock and 150 mmHg/3 o'clock (0.2 and 7.3 N, respectively). Averaged over all five subjects, the minimum and maximum F_C were at 7 o'clock and RT (respectively, and in order of increasing LVP: 0.9 ± 0.4, 1.0 ± 0.5, 1.1 ± 0.7 N, and 3.4 ± 1.6, 3.7 ± 1.6, 4.0 ± 1.8 N).

Based on Figure 6-7, it is apparent that F_C exhibited a positive, but statistically insignificant, trend versus LVP_{max}. Specifically, each successive 25 mmHg increase in

LVP_{max} caused a change in F_C of 14 ± 16% (p=0.091). A series of significant differences between pairs of positions were also observed. Nearly all such differences in F_C were between either LT or RT and a posterior position. When pooling F_C by region, it was shown that anterior F_C exceeded posterior F_C by 1.0 N (mean ± SD: 2.8 ± 1.4 vs. 1.8 ± 1.2 N, p<0.001 by ANOVA model 2).

6.2.1.2 Suture Pullout Force and Residual Strength Studies

The influence of suture position or suture region on F_P was quantified through ANOVA model 3 or two-sample t-test, respectively. Results are presented in Figure 6-8 through Figure 6-11, and described in the text following Figure 6-11.

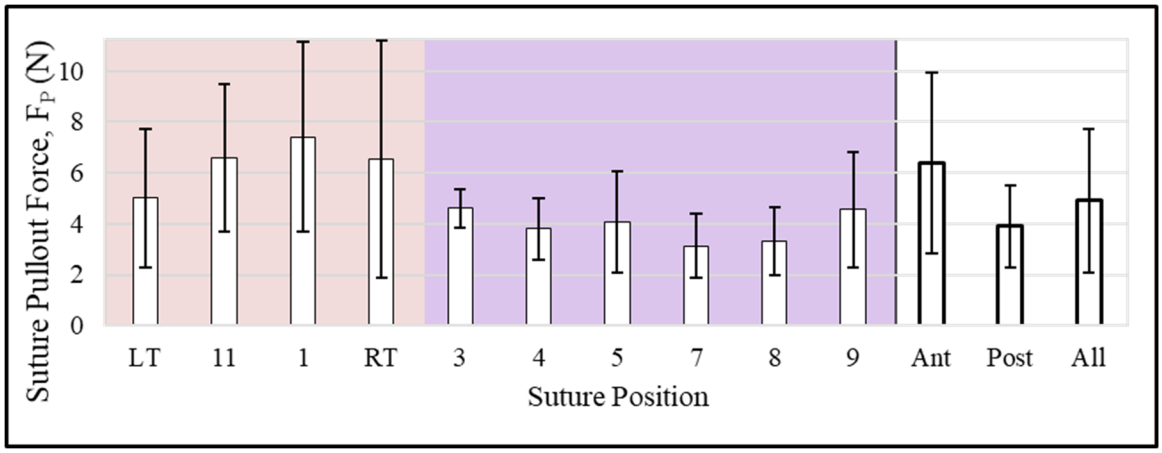

Figure 6-8 F_P results in terms of mean ± SD for each suture position. Although trends are apparent, statistical significance of these trends cannot be assessed until after ANOVA 3 and regional t-test (see Figure 6-9 and Figure 6-10).

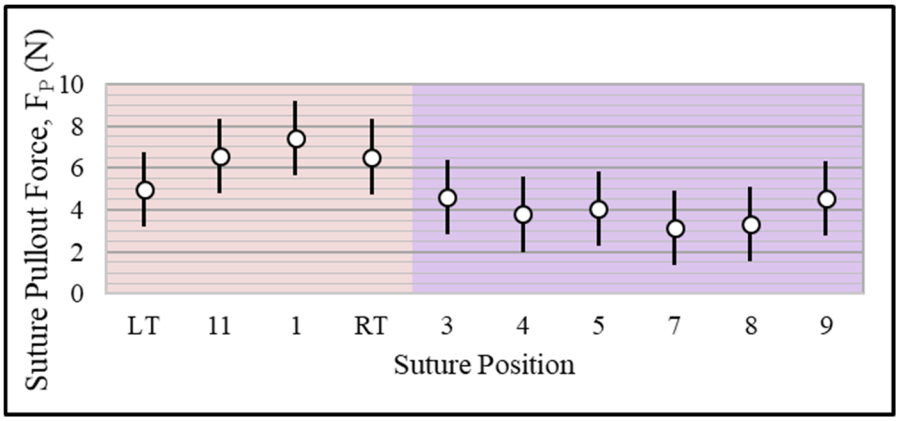

Figure 6-9 F_P results, in terms of mean ± 95% CI for each suture position (after ANOVA 3). Pairs whose 95% CIs do not overlap differ significantly ($p<0.05$). F_P was significantly greater at each of various anterior positions than at each of numerous posterior positions.

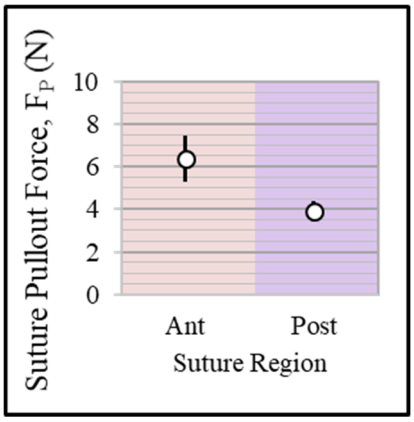

Figure 6-10 F_P results, in terms of mean ± 95% CI for either suture region. F_P was significantly greater for anterior sutures.

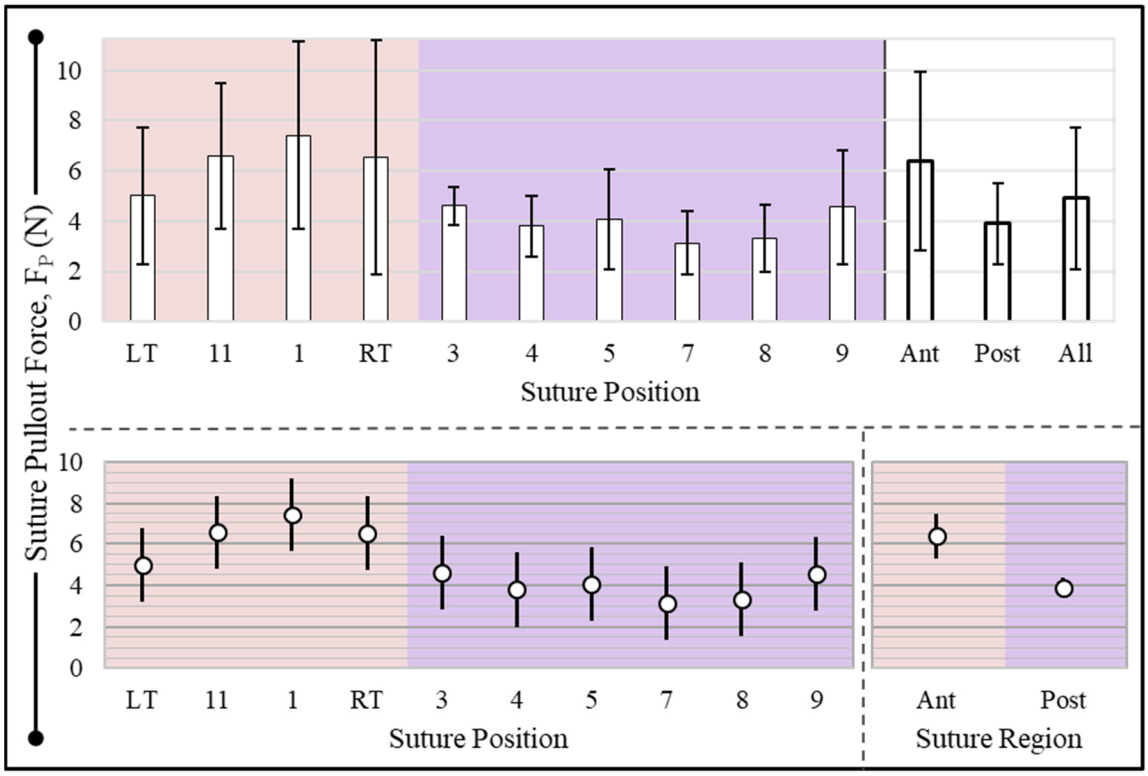

Figure 6-11 F_P results, duplicated from Figure 6-8 through Figure 6-10. Top: mean ± SD for each suture position. Bottom: mean ± 95% CI for each suture position (ANOVA 3), or suture region (t-test). Within each plot, pairs whose 95% CIs do not overlap differ significantly ($p<0.05$).

The suture successfully pulled from the annulus in 93.3% of trials (Table 6-3). Each of the eight unsuccessful trials was due to the testing system's arm reaching its displacement limit before pullout occurred; also, each trial was along the Ant aspect. The global mean ± SD for F_P was 4.9 ± 2.8 N. Among all 120 sutures, the absolute minimum and maximum F_P were 1.3 and 17.6 N (8 o'clock and RT, respectively). Among all 10 positions, the weakest and strongest positions were, respectively, 7 o'clock (3.1 ± 1.3 N) and 1 o'clock (7.4 ± 3.7 N).

The variation of F_P by position was qualitatively observed to correlate with that of F_C. However, whereas the two largest F_C magnitudes were located at either trigone, the two largest F_P magnitudes were between the trigones (with RT and LT the third- and fourth-strongest locations). ANOVA revealed a series of differences between F_P pairs. All significant differences were between 11 o'clock, 1 o'clock or RT and a posterior position. Pooled by region, anterior F_P exceeded posterior F_P by 2.5 N (6.4 ± 3.6 vs. 3.9 ± 1.6 N, $p < 0.001$).

Residual Strength (RS) at each suture position is given in Figure 6-12. Mean RS was 2.5 N; minimum and maximum RS were 1.1 and 5.4 N (LT and 1 o'clock, respectively). Despite the low LT value, the anterior annulus still exhibited greater mean RS than the posterior 1.4 N (3.3 ± 1.8 vs. 1.9 ± 0.3 N, $p=0.104$). The lack of significance of this finding is likely attributable to the fact that RS was computed from *mean* F_C and *mean* F_P at each position, leading to small sample sizes (four anterior and six posterior positions). Grouped differently, anterior sutures placed *between* the trigones (i.e. at 11 and 1 o'clock) exhibited mean RS of 4.8 ± 0.9 N, versus 1.9 ± 0.5 N everywhere else ($p<0.001$).

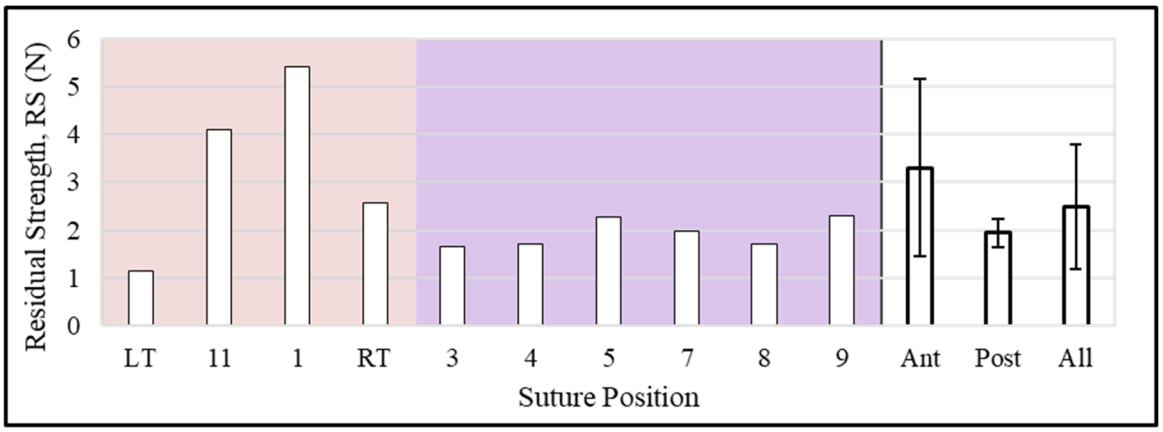

Figure 6-12 Residual Strength (RS) at each position using undersized Physio rings. RS is defined for a given ring type as the difference between that position's mean F_P and its mean F_C at LVP = 150 mmHg.

6.2.1.3 Collagen Quantification Studies

Annulus tissue microstructure was clearly visible by autofluorescence, without histologic staining. A sharply delineated collagenous band was typically located toward the endocardial surface. The thickness and density of this band varied among samples (Figure 6-13).

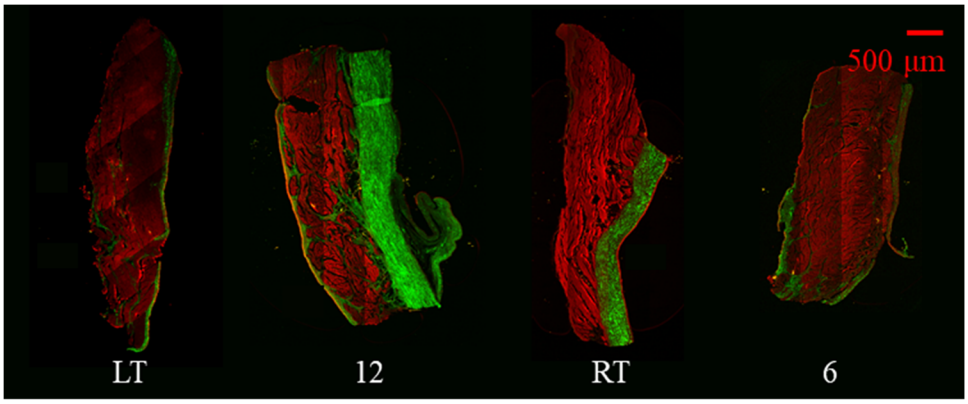

Figure 6-13 Representative sections of each annulus position at sites of suture passage, under two-photon excitation fluoroscopic imaging. In each case, the endocardial surface is along the right edge, with the annular hinge point at bottom right. Green: collagen; red: non-specific fibers.

As shown in Figure 6-14, collagen nMPI ranged from 1.69 ± 0.37 (12 o'clock) to 0.69 ± 0.23 (LT). The 12 o'clock position exhibited 92-145% greater collagen density than each other position (12 o'clock vs. each other position, $p<0.05$ following ANOVA model 4). In contrast, non-specific fiber nMPI showed far less variation, ranging from 0.87 ± 0.25 (LT) to 1.10 ± 0.62 (12 o'clock). No pairwise differences in non-specific fiber density existed among positions (ANOVA model 4). This supports the specificity of the collagen detection method and findings.

Collagen density correlated modestly to F_P ($R^2 = 0.501$, $p = 0.293$), and strongly to RS ($R^2 = 0.94$, $p = 0.033$; Figure 6-15). Note, suture forces were not measured at 12 and 6 o'clock. Therefore, RS at 12 or 6 o'clock were estimated by averaging 11 and 1 o'clock or 5 and 7 o'clock, respectively.

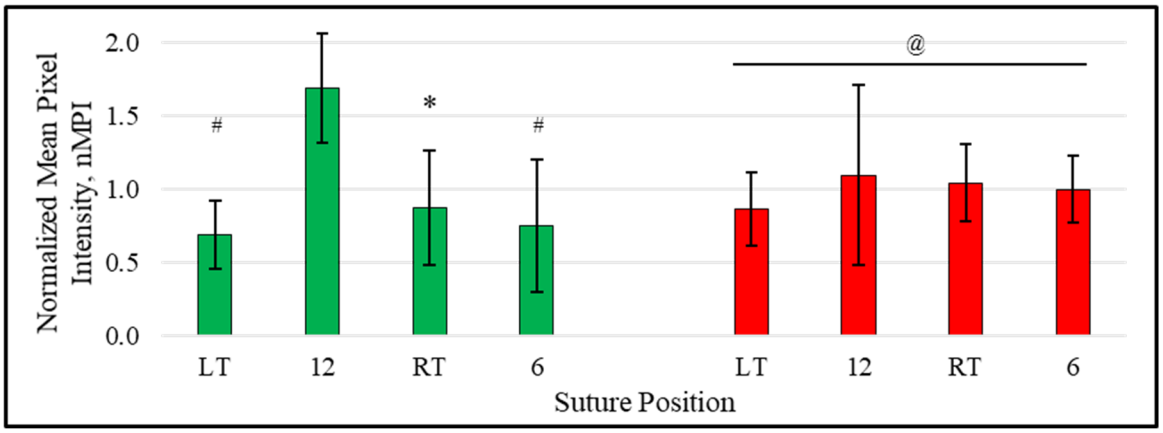

Figure 6-14 Mean ± SD of nMPI for both collagen (green) and non-specific fibers (red). *p<0.05 vs. 12 o'clock; #p<0.005 vs. 12 o'clock; @p>0.05 for all pairs (95% CIs not shown). All statistics after ANOVA 4.

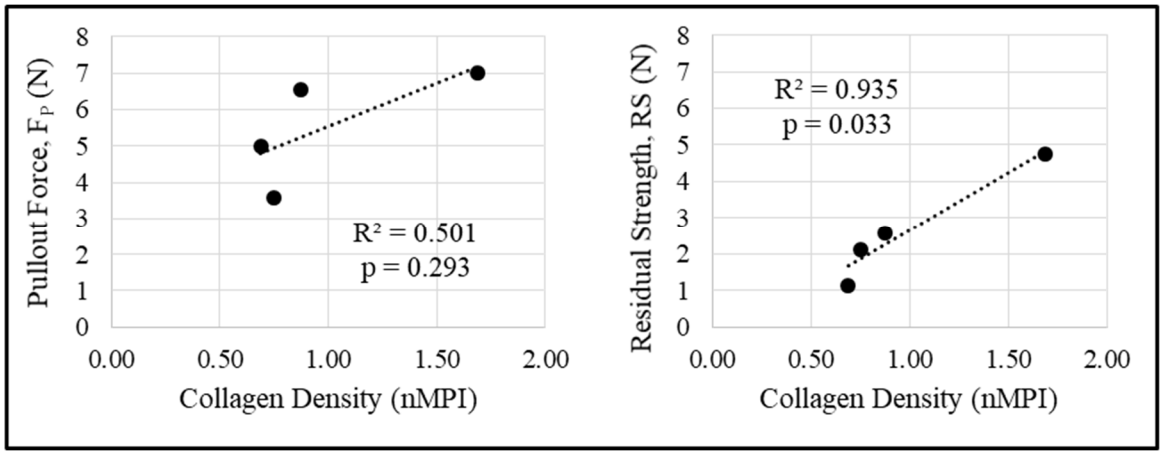

Figure 6-15 Collagen density at a given suture position, indicated by nMPI, correlated to either pullout force or residual strength at that position.

6.2.1.4 Comment

Later in this chapter, SA 1.A is discussed fully. However, before SA 1.B results are presented, it is critical to highlight the key findings from SA 1.A, insofar as they guide SA

1.B's experimental goals. It was found that, although F_C was lower on the posterior annulus than the anterior, F_P followed the same trend, by an even greater margin. As a net effect, RS was lower on the posterior annulus. From a biomechanical standpoint this implies a greater likelihood of suture dehiscence in this region, which is supported by the clinical predominance of posterior annular dehiscence.[7, 89, 91-99] **SA 1.A's findings therefore motivate a goal of identifying annuloplasty ring design parameters that systematically reduce F_C in the weaker posterior annulus.**

6.2.2 Specific Aim 1.B: Parametric Evaluation of Ring Design and Suture Forces

6.2.2.1 Investigation of Ring Size and Shape

A description of the sample populations used in SA 1.B's investigations of ring size and shape (not including the undersized Physio samples already described) is presented in Table 6-5. Instrumented Physio and Profile 3D rings were successfully implanted in 18 healthy ovine subjects, in addition to the 5 subjects receiving undersized Physio rings detailed in SA 1.A. Among all cases, mitral annulus sizes ranged between 26-32, and rings of size 26-30 were used (either true-sized to the annulus, or undersized by two sizes). Across all undersized or true-sized annuloplasty cases, the post-procedural increase in transmitral pressure gradient was 1.9 ± 1.6 mmHg for undersized rings or 0.9 ± 0.4 mmHg for true-sized rings (measured at resting heart rate and normotensive conditions, immediately before and after cardiopulmonary bypass). The F- and p-values from all ANOVA models used to analyze these rings are presented in Table 6-6.

Table 6-5 Data set summary for SA 1.B investigation of ring size and shape.

	T-Ph	U-3D	T-3D
Sample size	5	6	7
Animal weight (kg)	58.2 ± 10.6	57.0 ± 5.8	57.4 ± 6.8
Annulus size	28.8 ± 2.3	30.0 ± 0.0	27.7 ± 1.8
Ring size	28.8 ± 2.3	26.0 ± 0.0	27.7 ± 1.8
HR at LVP_{max} = 100mmHg (bpm)	106.0 ± 25.1	126.5 ± 24.6	136.0 ± 26.8
HR at LVP_{max} = 125mmHg (bpm)	117.0 ± 25.0	130.2 ± 25.8	148.1 ± 23.4
HR at LVP_{max} = 150mmHg (bpm)	126.2 ± 25.5	137.8 ± 33.2	159.3 ± 22.3

Table 6-6 Results of all ANOVA models used in SA 1.B investigations of ring size and shape, before post-hoc analysis. ANOVA models are fully described in Table 6-2.

		Factor	F	p
Model 5 (F_C)	**Main effects**	LVP_{max}	16.87	<0.001
		Ring type	1.12	0.29
		Ring-annulus sizing	11.56	0.001
		Suture position	14.74	<0.001
	Interactions	LVP_{max}:Ring type	0.05	0.95
		LVP_{max}:Ring-annulus sizing	0.03	0.968
		LVP_{max}:Suture position	0.27	0.999
		Ring type:Ring-annulus sizing	4.05	0.045
		Ring type:Suture position	6.59	<0.001
		Ring-annulus sizing:Suture position	2.16	0.023
Model 6 (F_C)	**Main effects**	LVP_{max}	15.15	<0.001
		Ring type	0.93	0.334
		Ring-annulus sizing	10.66	0.001
		Suture region	42.72	<0.001
	Interactions	LVP_{max}:Ring type	0.04	0.959
		LVP_{max}:Ring-annulus sizing	0.03	0.972
		LVP_{max}:Suture region	1.3	0.273
		Ring type:Ring-annulus sizing	3.41	0.065
		Ring type:Suture region	0.12	0.731
		Ring-annulus sizing:Suture region	8.28	0.004

The mean ± SD values for F_C across these 23 animals (5 from SA1 and 18 additional here) are presented below, grouped two ways. First, Figure 6-16 reports F_C for each cohort individually (i.e. undersized Physio, U-Ph, true-sized Physio, T-Ph, undersized Profile 3D, U-3D, and true-sized Profile 3D, T-3D). Next, Figure 6-17 reports the data parametrically (i.e. all Physio, all Profile 3D, all undersized, and all true-sized). In these and in all following figures reporting mean ± SD throughout the remainder of this chapter, only data from the *intermediate* LVP_{max} (i.e. 125 mmHg) is shown. Every trend visible in these graphs is consistent across each LVP_{max} level (with a shift down or up at 100 or 150 mmHg). This trend is then quantified via the ANOVA plots.

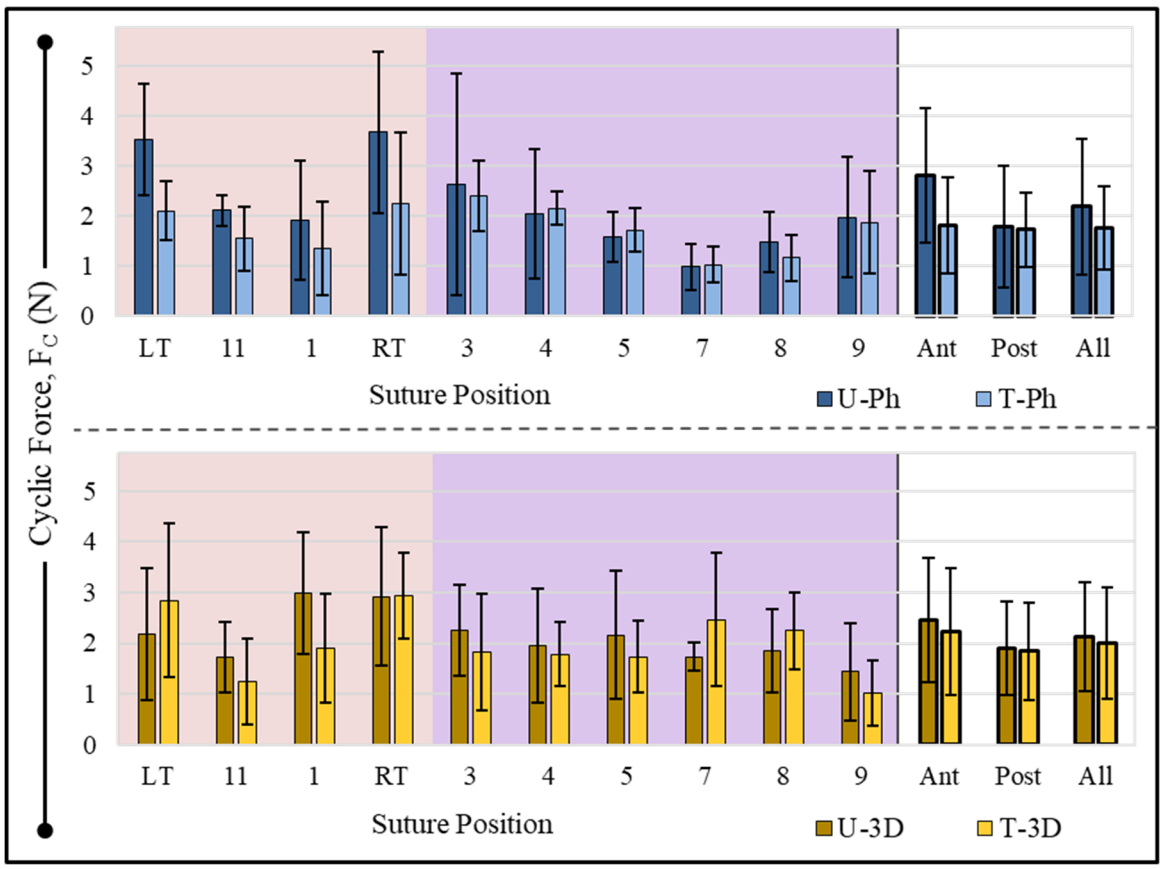

Figure 6-16 F_C results from undersized (U) or true-sized (T) Physio (Ph) or Profile 3D (3D) rings. Mean ± SD values are given at LVP_{max} = 125 mmHg. Although trends are apparent, statistical significance of these trends cannot be assessed until after ANOVAs 5 and 6 (see Figure 6-18 and Figure 6-19).

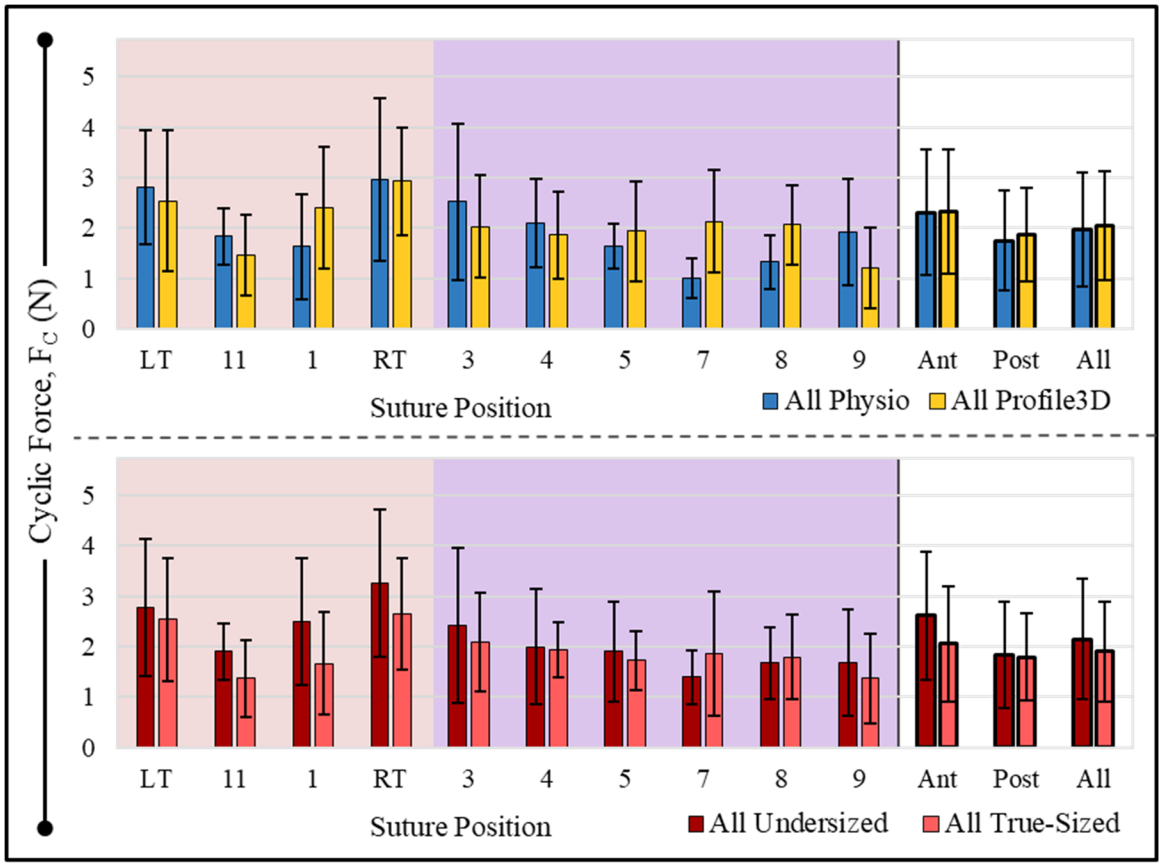

Figure 6-17 F_C results from all Physio or Profile 3D rings, across sizes (top), and all undersized or true-sized rings, across types (bottom). Mean ± SD values are given at LVP_{max} = 125 mmHg. Although trends are apparent, statistical significance of these trends cannot be assessed until after ANOVAs 5 and 6 (see Figure 6-18 and Figure 6-19).

From Figure 6-16, true-sizing reduced F_C, both for Physio and Profile 3D. In every ring type, the trigones exhibited the greatest or near-greatest F_C. From Figure 6-17, it can be further noted that, although F_C values for Physio and Profile 3D differ to varying degrees at each suture position, they agree closely both in the anterior and posterior regions. Lastly, it is noted that in Figure 6-17 that true-sizing reduced F_C at 8/10 positions, including by 0.5-0.8 N between 11 o'clock and RT, but by no more than 0.3 N elsewhere.

The influences of ring type (Physio vs. Profile 3D) and ring size (undersized vs. true-sized to the annulus) were quantified through ANOVA model 5. This model also accounted for LVP and suture position, which were found in SA 1.A to impact or potentially impact F_C. ANOVA model 6 replicated model 5, but grouped sutures as anterior or posterior.

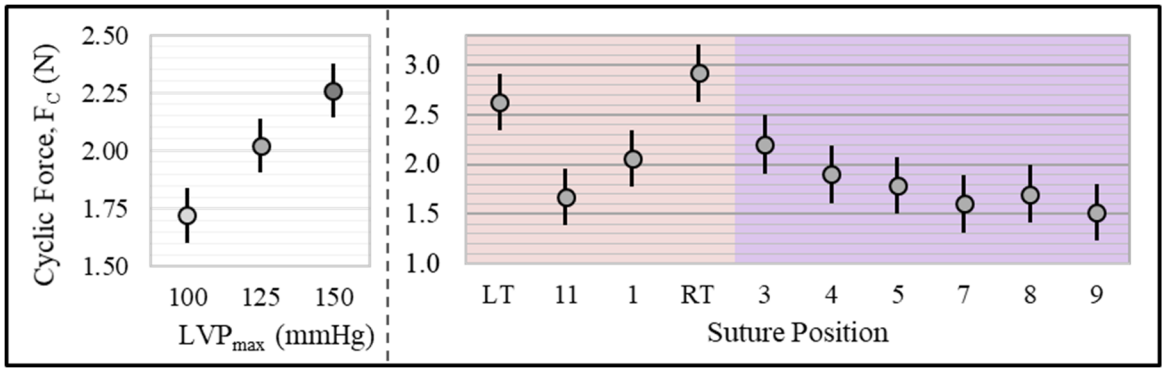

Figure 6-18 Mean ± 95% CI for each LVP_{max} or suture position (after ANOVA 5). Within each plot, pairs whose 95% CIs do not overlap differ significantly ($p<0.05$). Increasing LVP_{max} significantly increased F_C. F_C was significantly greater at either trigone than at numerous other positions.

Among all 23 animals, LVP_{max} showed similar trends to those seen in the five undersized Physio cases investigated in isolation in SA 1.A (Figure 6-7). That is, each 25 mmHg increase in LVP_{max} led to a 0.2-0.3 N increase in F_C. However, whereas this trend was not significant with N=5 subjects, in this larger cohort, each LVP_{max} level was significantly different from each other level ($p<0.05$). After accounting for all possible two-factor interactions, it was noted that LVP_{max} did not significantly interact with any other factor, revealing that elevated LVP_{max} affected F_C uniformly across ring type, ring size, or suture position. Suture position findings in ANOVA model 5 were very similar to those of

model 1 (Figure 6-7): nearly all pairwise significant differences were between either LT or RT and a posterior position. Further key results from ANOVA model 5 are shown in Figure 6-19 A-C. Further key results from ANOVA model 6 are shown in Figure 6-19 D.

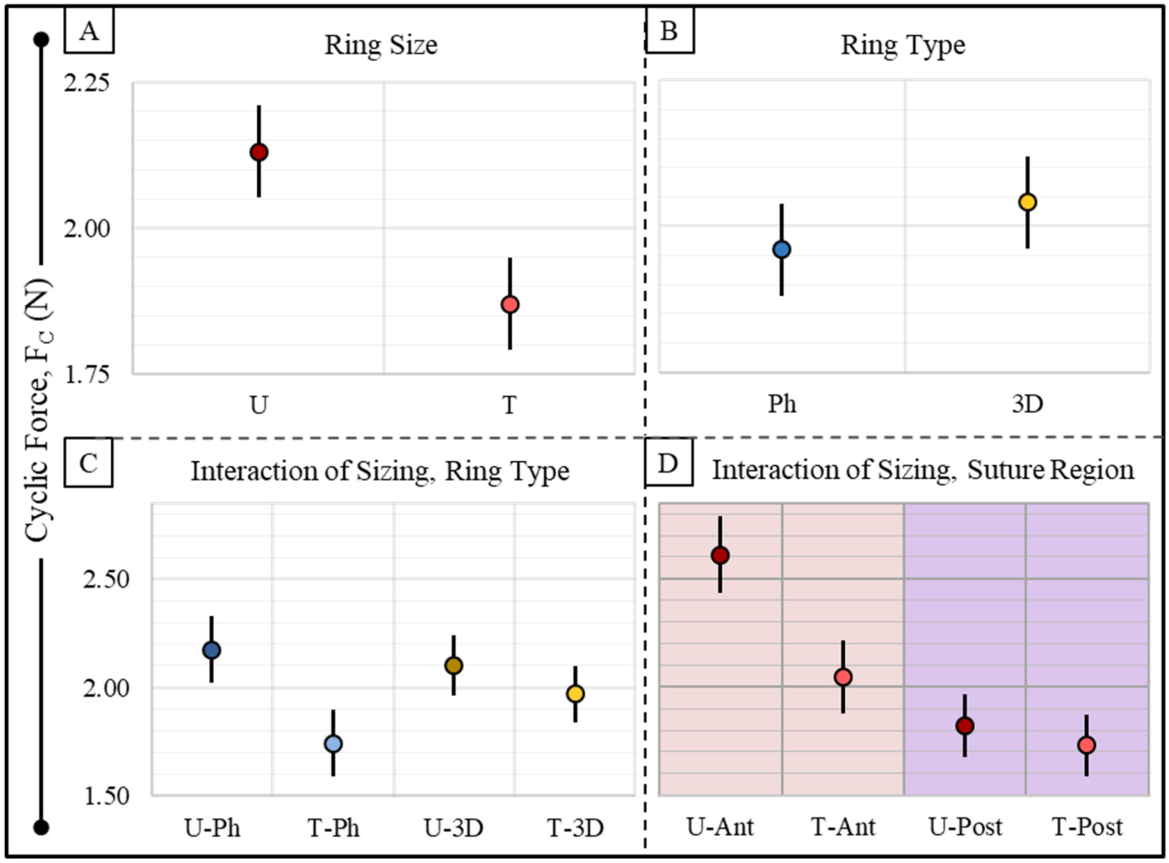

Figure 6-19 Mean ± 95% CI for each (A) ring size, (B) ring type, (C) ring type of a given size, or (D) suture region within a given ring size. (A-C) after ANOVA 5, (D) after ANOVA 6. Within each plot, pairs whose 95% CIs do not overlap differ significantly ($p<0.05$). U, undersized; T, true-sized; Ph, Physio; 3D, Profile 3D; Ant, Anterior; Post, Posterior.

True-sizing reduced F_C by a statistically significant margin (undersized vs. true-sized: 2.1 ± 1.2 vs 1.9 ± 1.0 N, $p<0.001$; Figure 6-19 A). In contrast, ring type did not significantly affect mean F_C (Physio vs. Profile 3D: 2.0 ± 1.2 vs. 2.0 ± 1.1 N, $p=0.290$;

Figure 6-19 B). Ring sizing and ring type interacted: whereas, with Physio rings, true sizing conferred significant F_C reduction (undersized Physio vs. true-size Physio: 2.2 ± 1.4 vs. 1.7 ± 0.9 N, $p<0.001$), undersized and true-sized Profile 3D rings did not differ significantly in F_C (2.1 ± 1.1 vs. 2.0 ± 1.1 N, $p=0.545$; Figure 6-19 C). Significant interactions also existed between suture position and either ring type or ring-annulus sizing. However, these data are more clearly understood after grouping sutures by region.

Thus, ANOVA model 6 replicated model 5, but grouped sutures as anterior or posterior. Comparable to the results of SA 1.A, anterior sutures endured greater F_C than posterior (2.3 ± 1.3 vs. 1.8 ± 1.0 N, $p<0.001$). No significant interaction was observed between suture region and ring type ($p=0.731$). Interaction between suture region and ring-annulus sizing was more complex (Figure 6-19 D). Anterior F_C exceeded posterior, across sizes (undersized anterior vs. undersized posterior: 2.6 ± 1.3 vs. 1.8 ± 1.1 N, $p<0.001$; true-sized anterior vs. true-sized posterior: 2.1 ± 1.2 vs. 1.7 ± 0.9 N, $p=0.031$). Importantly, the aforementioned capacity for true-sizing to relieve F_C was driven exclusively by differences along the anterior annulus (undersized anterior vs true-sized anterior, $p<0.001$; undersized posterior vs true-sized posterior, $p=0.812$).

Lastly, it was noted that when undersizing, use of the Profile 3D led to more uniform F_C across positions. Pooled standard deviation was significantly higher for the undersized Physio than the undersized Profile 3D (0.9 vs. 0.5 N, $p=0.036$, Levene's test). No such differences were observed when true-sizing.

6.2.2.2 Development of Fully-Rigid and Fully-Flexible Ring Prototypes

Next, the effect of ring stiffness was investigated, using the semi-rigid Physio ring and fully-rigid and fully-flexible ring prototypes designed to match the Physio geometry. Visual comparison shows that the Physio geometry was reproduced successfully (see Figure 4-3). Among multiple copies a given ring, stiffness exhibited coefficient of variation (standard deviation/mean) of approximately 20%. Force-deflection curves for each ring type were linear (Figure 6-20). Stiffnesses for the rigid, semi-rigid, and flexible designs were 10.12, 0.67, and 0.05 N/mm (all based on size 26 ring). That is, the rigid and flexible Physio prototypes were over one order of magnitude more or less stiff, respectively, than the semi-rigid (commercial) ring.

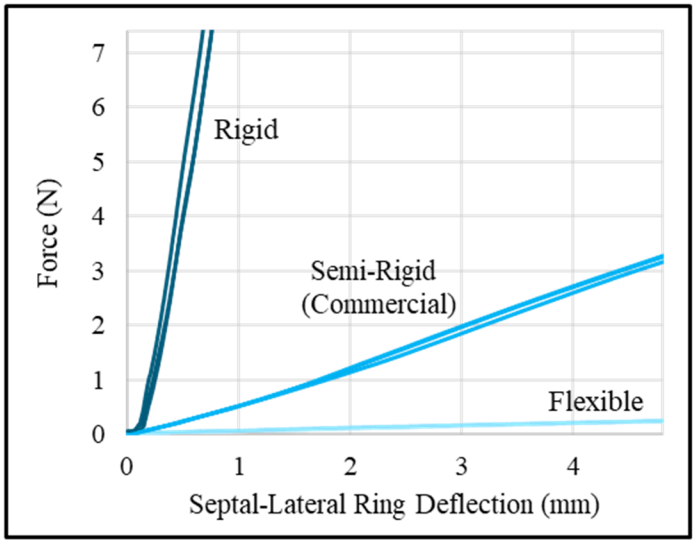

Figure 6-20 Force-deflection data for each ring stiffness, under uniaxial compressive testing (three trials apiece).

6.2.2.3 Investigation of Ring Stiffness

A description of the sample populations used in SA 1.B's investigations of ring stiffness (not including the undersized Physio samples already described) is presented in Table 6-7. Instrumented fully-rigid and fully-flexible prototype rings were successfully implanted in 11 healthy ovine subjects, in addition to the 5 subjects receiving undersized Physio rings detailed in SA 1.A. Among all cases, mitral annulus sizes ranged between 30-34, and rings of size 26-30 were used (*each undersized by two sizes* relative to the annulus). The F- and p-values from all ANOVA models used to analyze these rings is presented in Table 6-8.

Table 6-7 Data set summary for SA 1.B investigation of ring stiffness.

	Fully-Rigid	**Fully-Flexible**
Sample size	6	5
Animal weight (kg)	54.0 ± 6.0	63.6 ± 9.5
Annulus size	32.4 ± 0.9	32.4 ± 1.7
Ring size	28.4 ± 0.9	28.4 ± 1.7
HR at LVP_{max} = 100mmHg (bpm)	118.5 ± 38.8	115.0 ± 22.6
HR at LVP_{max} = 125mmHg (bpm)	119.2 ± 34.8	115.8 ± 26.3
HR at LVP_{max} = 150mmHg (bpm)	120.2 ± 31.9	123.8 ± 30.2

Table 6-8 Results of all ANOVA models used in SA 1.B investigations of ring stiffness, before post-hoc analysis. ANOVA models are fully described in Table 6-2.

		Factor	F	p
Model 7 (F_C)	**Main effects**	LVP_{max}	9.23	<0.001
		Suture position	12.18	<0.001
		Ring stiffness	12.69	<0.001
	Interactions	LVP_{max}:Suture position	0.09	>0.999
		LVP_{max}:Ring stiffness	0.24	0.917
		Suture position:Ring stiffness	3.32	<0.001
Model 8 (F_C)	**Main effects**	LVP_{max}	8.56	<0.001
		Suture region	60.95	<0.001
		Ring stiffness	11.29	<0.001
	Interactions	LVP_{max}:Suture region	0.3	0.74
		LVP_{max}:Ring stiffness	0.21	0.933
		Suture region:Ring stiffness	8.6	<0.001
Model 9 ($F_{C,Ant}/F_{C,Post}$)	**Main effects**	LVP_{max}	0.04	0.9583
		Ring stiffness	10.66	<0.001
	Interactions	LVP_{max}:Ring stiffness	0.06	0.993
Model 10 ($HWHM_{norm}$)	**Main effects**	LVP_{max}	1.93	0.146
		Suture region	9.87	0.002
		Ring stiffness	6.37	0.002
	Interactions	LVP_{max}:Suture region	0.05	0.955
		LVP_{max}:Ring stiffness	0.21	0.933
		Suture region:Ring stiffness	5.1	0.007

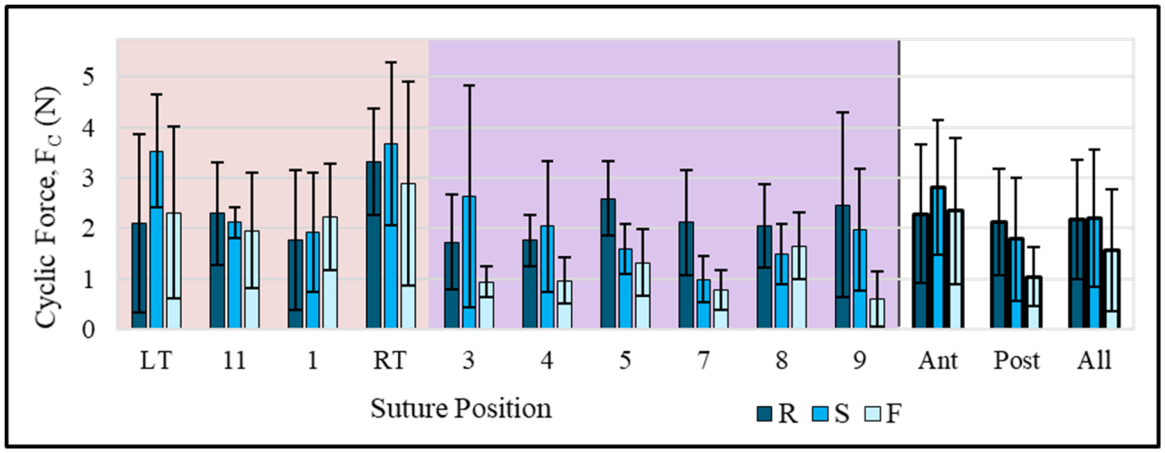

Figure 6-21 F_C results from undersized rings in the Physio geometry, across three stiffnesses. Mean ± SD values are given at LVP_{max} = 125 mmHg. R, rigid; S, semi-rigid (commercial); F, flexible. Although trends are apparent, statistical significance of these trends cannot be assessed until after ANOVAs 7 and 8 (see Figure 6-22 through Figure 6-27).

The mean ± SD values for F_C across these 16 animals are presented in Figure 6-21, grouped by ring stiffness. It can be observed that for each ring type, F_C was greatest at RT, and overall higher along anterior sutures than posterior sutures. Comparing among ring types, it is also notable that the rigid and semi-rigid rings experienced the highest F_C at 5/10 and 4/10 positions, respectively. Flexible rings experienced the lowest F_C at 7/10 positions, including 5/6 posterior positions.

The influence of ring stiffness was quantified through ANOVA model 7. This model also accounted for LVP and suture position. ANOVA model 8 replicated model 7, but grouped sutures as anterior or posterior.

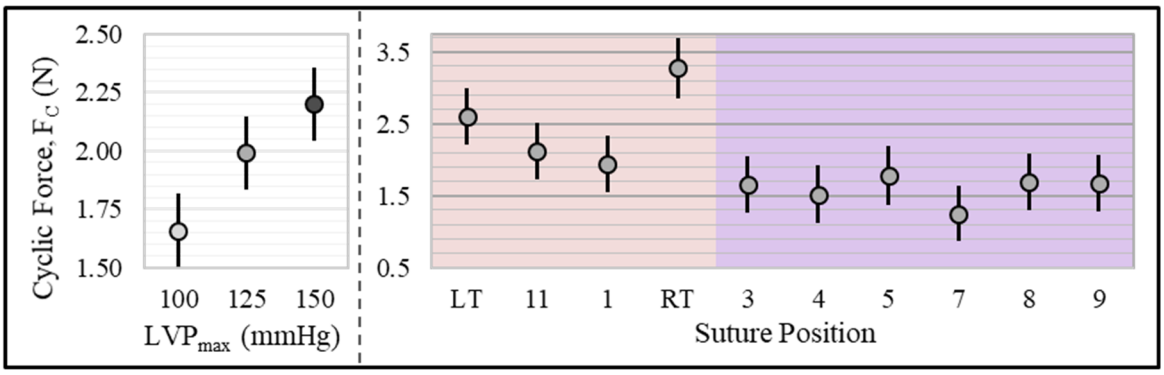

Figure 6-22 F_C results, in terms of mean ± 95% CI for each LVP_{max} or suture position (after ANOVA 7). Within each plot, pairs whose 95% CIs do not overlap differ significantly ($p<0.05$).

In this 16 animal cohort, LVP_{max} showed similar trends to those seen in Figure 6-7 and Figure 6-18. That is, each 25 mmHg increase in LVP_{max} led to a 0.2-0.3 N increase in F_C. In this cohort, F_C at the lowest LVP_{max} (100 mmHg) was significantly reduced versus each higher level, but 125 vs. 150 mmHg did not achieve significance ($p=0.233$). Consistent with earlier cohorts, it was noted after accounting for two-factor interactions that LVP_{max} did not significantly interact with any other factor. Suture position findings in ANOVA model 7 were very similar to those of model 1 (Figure 6-7) and model 5 (Figure 6-18): nearly all pairwise significant differences were between either LT or RT and a posterior position. However, here, RT was also significantly different from 11 and 1 o'clock. Further key results from ANOVA model 7 are shown in Figure 6-23, Figure 6-26, and Figure 6-27 A and D. Further key results from ANOVA model 8 are shown in Figure 6-24, Figure 6-25, and Figure 6-27 B-C.

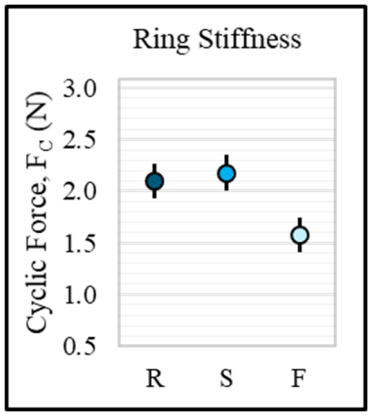

Figure 6-23 F_C results, in terms of mean ± 95% CI for each ring stiffness, after ANOVA 7. R, rigid; S, semi-rigid; F, flexible. Pairs whose 95% CIs do not overlap differ significantly ($p<0.05$). F_C was significantly reduced using flexible rings.

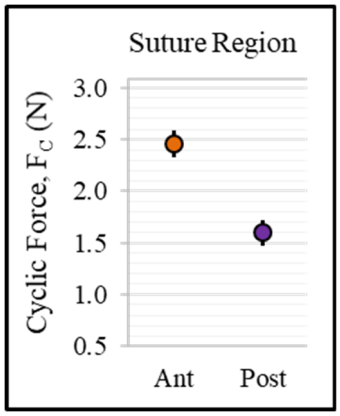

Figure 6-24 F_C results, in terms of mean ± 95% CI for either suture region, after ANOVA 8. Pairs whose 95% CIs do not overlap differ significantly ($p<0.05$). F_C was significantly reduced on posterior sutures.

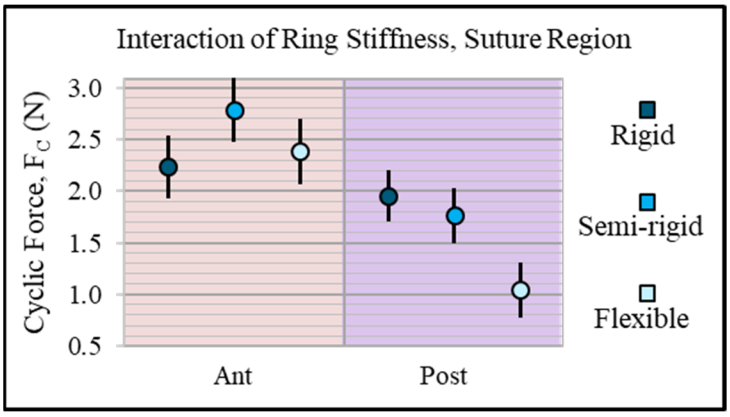

Figure 6-25 F_C results, in terms of mean ± 95% CI for each ring stiffness/suture region combination, after ANOVA 8. Pairs whose 95% CIs do not overlap differ significantly ($p<0.05$). The reduction in F_C using flexible rings was specifically on posterior sutures.

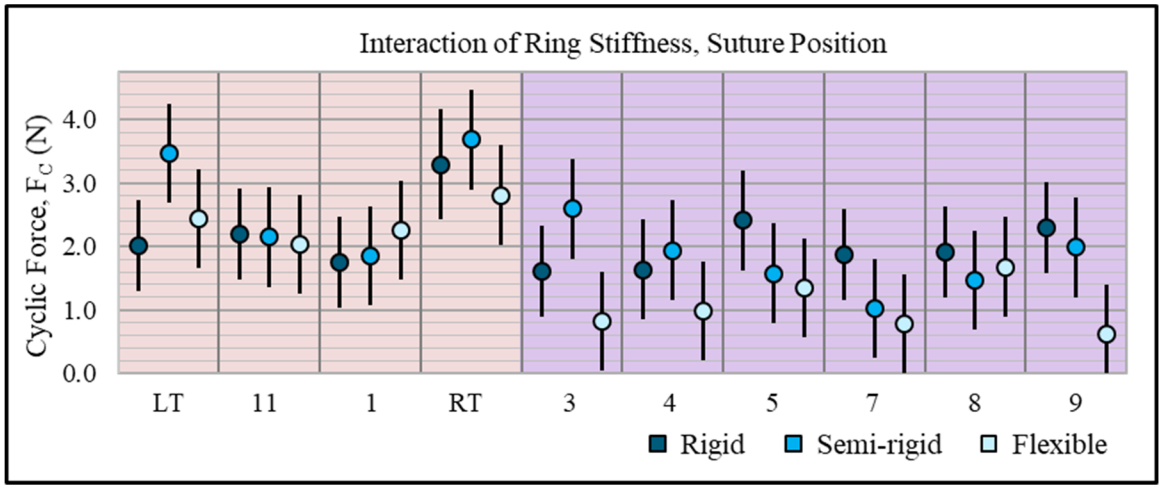

Figure 6-26 F_C results, in terms of mean ± 95% CI for each ring stiffness/suture region combination, after ANOVA 7. Pairs whose 95% CIs do not overlap differ significantly ($p<0.05$). The reduction in F_C using flexible rings occurred at most suture positions, but was only statistically significant at 3 and 9 o'clock.

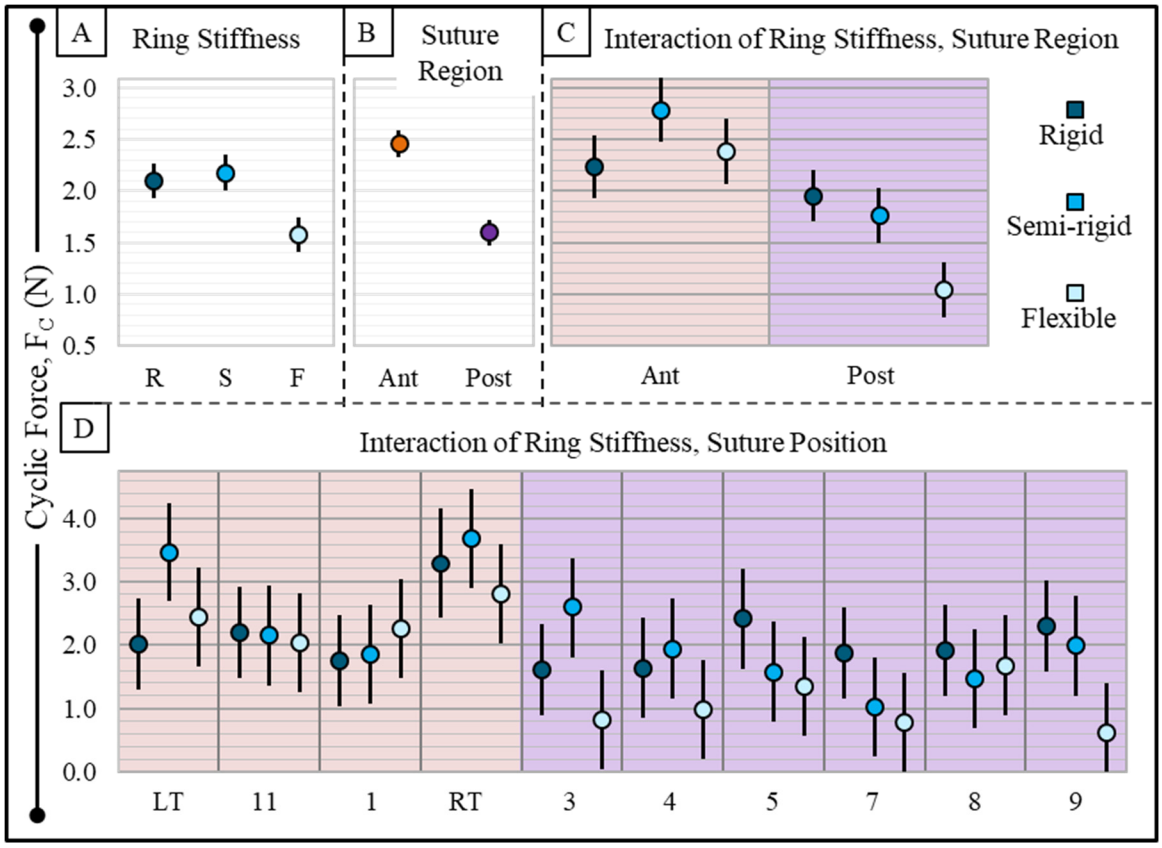

Figure 6-27 Mean ± 95% CI for each (A) ring stiffness, (B) suture region, (C) suture region within a given ring stiffness, or (D) suture position within a given ring stiffness, duplicated from Figure 6-23 through Figure 6-26. (A, D) after ANOVA 7; (B-C) after ANOVA 8. Within each plot, pairs whose 95% CIs do not overlap differ significantly ($p<0.05$). R, rigid; S, semi-rigid (commercial); F, flexible; Ant, Anterior; Post, Posterior.

Relative to both semi-rigid and rigid rings, use of a flexible ring reduced mean F_C by over 0.5 N ($p<0.001$; Figure 6-27 A). As previously seen with earlier cohorts (especially when undersizing), F_C was significantly reduced along the posterior annulus (in this cohort by 0.9 N: anterior vs. posterior, 2.5 ± 1.4 vs. 1.6 ± 1.0 N, $p<0.001$; Figure 6-27 B). The magnitude of this reduction depended on the selected ring's stiffness. That is, posterior F_C was less than anterior F_C by 0.2, 1.0, and 1.3 N on average for rigid, semi-rigid, and flexible

rings, respectively. Suture region and ring stiffness interacted significantly (Figure 6-27 C): whereas increasing flexibility was not found to affect anterior F_C, it did reduce posterior F_C (rigid, semi-rigid, and flexible: 2.0 ± 1.0, 1.8 ± 1.2, 1.0 ± 0.6 N, respectively; $p<0.001$). Ring stiffness also significantly influenced forces on individual sutures (Figure 6-27 D). Of note, flexible rings experienced a statistically significant reduction in F_C only at the two positions immediately posterior of the trigones, i.e. at 3 o'clock ($p=0.004$ vs. semi-rigid) and 9 o'clock ($p=0.005$ vs. rigid).

It was qualitatively observed that increasing ring flexibility affected the *ratio* of anterior F_C to posterior F_C. To quantify this observation, ANOVA model 9 investigated the ratio $F_{C,\,Ant}/F_{C,\,Post}$ as a function of ring stiffness and LVP_{max}. Figure 6-28 demonstrates that this ratio scaled positively with increasing ring flexibility (rigid: (1.08 ± 0.46):1, semi-rigid: (1.67 ± 0.66):1, flexible: (2.33 ± 1.18):1; $p<0.001$).

It was hypothesized that the reduced posterior F_C using flexible rings may relate to differences in the *duration* of suture loading in response to ventricular contraction. To test this hypothesis, ANOVA model 10 investigated $HWHM_{norm}$ as a function of ring stiffness, suture region, and LVP_{max}. Figure 6-29 demonstrates that for anterior sutures, $HWHM_{norm}$ did not show sensitivity to ring stiffness. However, for posterior sutures, $HWHM_{norm}$ was significantly larger when a flexible ring was used (rigid: 0.08 ± 0.04, semi-rigid: 0.08 ± 0.02, flexible: 0.13 ± 0.11; $p<0.001$ for flexible vs. rigid or semi-rigid).

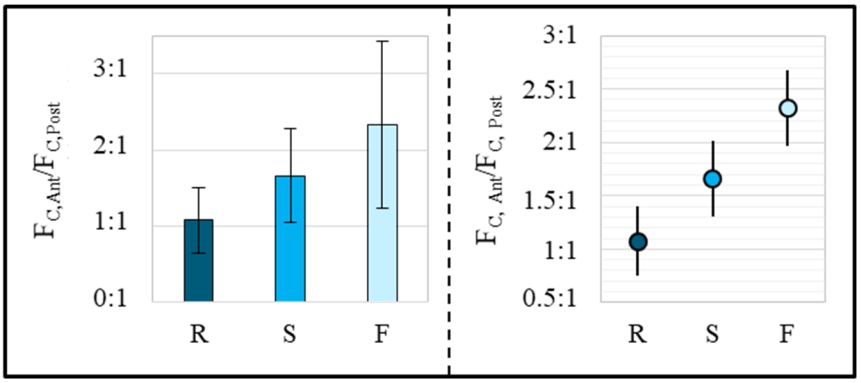

Figure 6-28 Ratio of anterior F_C to posterior F_C for each ring stiffness, averaged across suture positions and LVP_{max} levels. Left: mean ± SD. Right: mean ± 95% CI (after ANOVA 9). Pairs whose 95% CIs do not overlap differ significantly ($p<0.05$). R, rigid; S, semi-rigid (commercial); F, flexible.

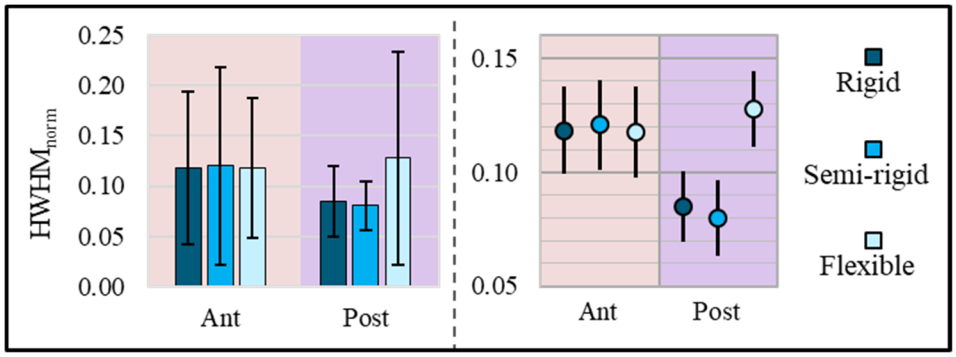

Figure 6-29 Normalized half-width at half-maximum ($HWHM_{norm}$) for each suture region within a given ring stiffness. Larger $HWHM_{norm}$ indicates a longer proportion of the cardiac cycle during which suture loading occurred. Left: mean ± SD. Right: mean ± 95% CI (after ANOVA 10). Pairs whose 95% CIs do not overlap differ significantly ($p<0.05$).

Finally, the Residual Strength (RS) values for each ring stiffness were calculated. The resulting RS heat maps, shown below, are illustrative of the relative suture dehiscence risk for each ring.

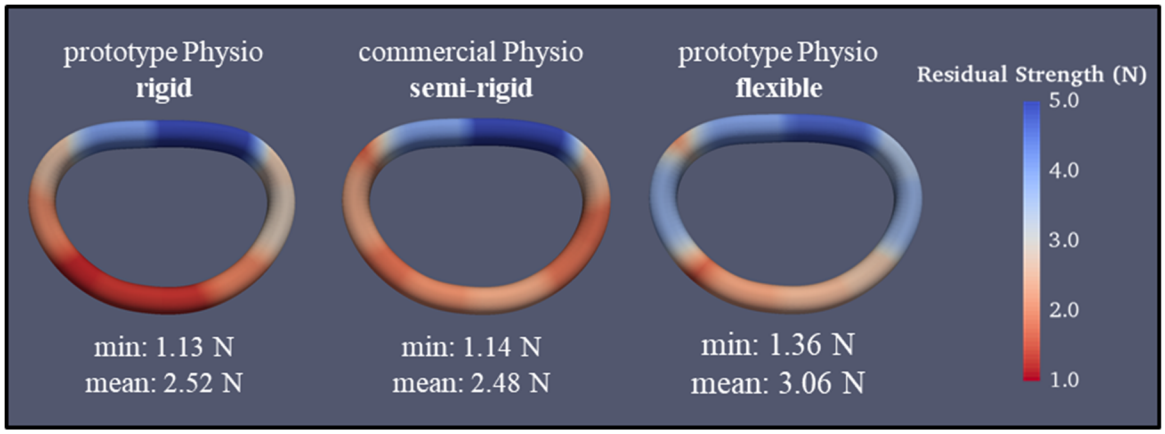

Figure 6-30 Residual Strength around the annular circumference, following use of each undersized ring in the Physio geometry (lower Residual Strength implies greater suture dehiscence likelihood).

6.2.2.4 Comment

Later in this chapter, SA 1.B is discussed fully. However, before SA 1.C results are presented, it is critical to highlight the key findings from SA 1.B, insofar as they guide SA 1.C's experimental goals. It was shown that use of true-sized rings does indeed reduce F_C as compared to undersized rings, but only on the anterior annulus. Use of larger rings (i.e. true-sized to the annulus) can therefore be rejected as a solution to the challenge of reducing dehiscence likelihood in the posterior annulus. Ring shape was not fully explored; a comparison of the flat Physio vs. saddle-shaped Profile 3D was confounded by the differing stiffness between the two rings. Nevertheless, no significant differences in posterior F_C was observed between these rings. Meanwhile, use of more flexible rings reduced F_C specifically on the posterior annulus, as desired. Given the known benefits in terms of resulting valve geometry and MR volume reduction of (a) undersized rings, (b) saddle-shaped rings, and (c) semi-rigid or rigid rings, **SA 1.B's findings motivate materially**

hybrid rings as one potential solution for reducing the likelihood of posterior annuloplasty ring suture dehiscence.

6.2.3 Specific Aim 1.C: Development and Preliminary Assessment of a Novel Ring Design

The successful manufacturing and implementation of the hybrid rings, with their rigid anterior and posterior segments and flexible commissural segments, is shown in Figure 6-31. In these images, strings tied at 10 and 4 o'clock, and pulled radially outward, induced fully flexible ring prototypes to deform along their entire circumference. In contrast, the hybrid rings only deformed in their commissural segments. These rings were instrumented and successfully implanted in three ovine subjects. A description of SA 1.C's hybrid ring sample population is presented in Table 6-9.

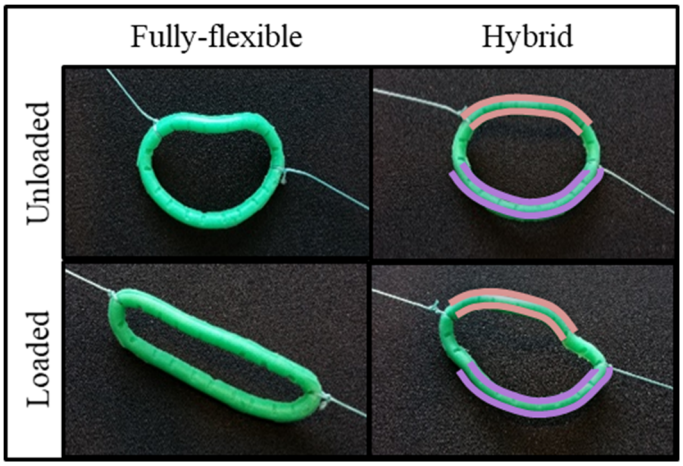

Figure 6-31 Comparison of the hybrid ring (left) versus a fully flexible prototype in the same geometry (right). On left, rigid inserts along anterior (orange) and posterior (purple) are highlighted to reveal that they retain their shape under mechanical loading.

Table 6-9 Data set summary for SA 1.C preliminary hybrid ring investigation.

	Hybrid
Sample size	3
Animal weight (kg)	69.0 ± 8.5
Annulus size	34.0 ± 0
Ring size	30
HR at LVP_{max} = 100mmHg (bpm)	111.1 ± 2.8
HR at LVP_{max} = 125mmHg (bpm)	116.4 ± 9.3
HR at LVP_{max} = 150mmHg (bpm)	125.1 ± 22.5

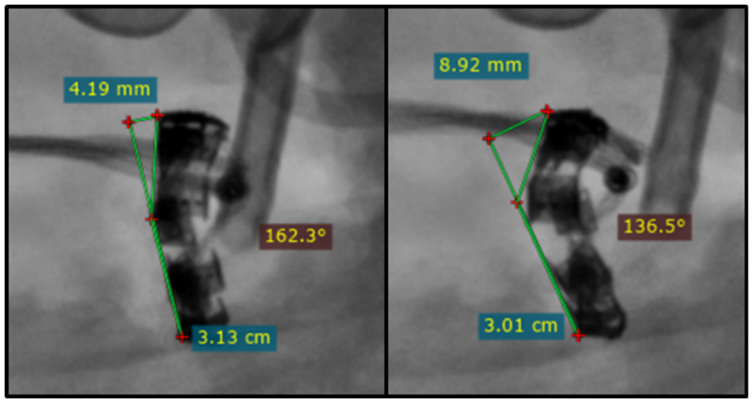

Figure 6-32 Fluoroscopic images of an implanted hybrid ring during diastole (left) and systole (right) of a single cardiac cycle. Cyclic changes in saddle height and angle are annotated.

During *in vivo* use of all instrumented rings, the force transducer spring elements were easily visualized under fluoroscopic imaging. For the hybrid rings, this approach enabled tracking the spring element positions to reveal the extent of cyclic flexure. In the representative case shown in Figure 6-32, the ring's saddle height and angle changed from 4.19 mm and 162.3° during diastole to 8.92 mm and 136.5° during systole.

Mean ± SD F_C values are presented below for preliminary investigations using the hybrid rings.

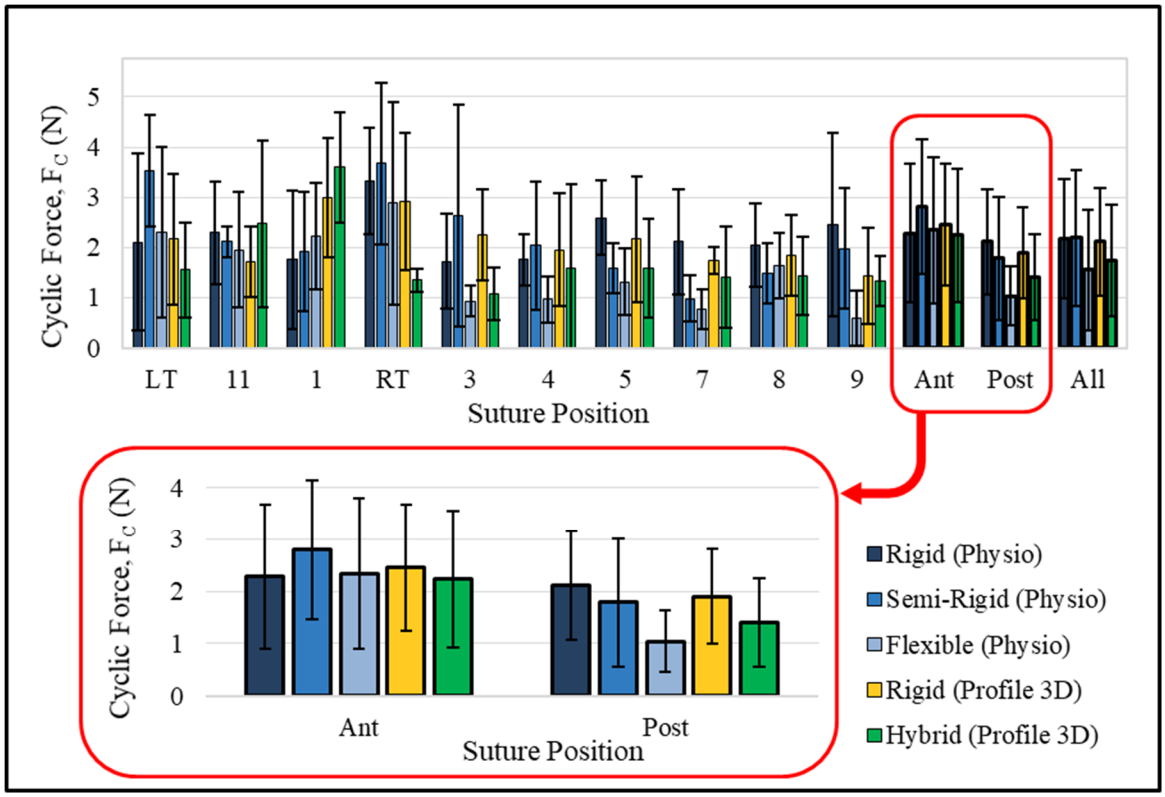

Figure 6-33 Preliminary F_C results from undersized hybrid rings, shown alongside all prior undersized ring cohorts. Mean ± SD values are given at LVP_{max} = 125 mmHg. Red box: regional F_C values enlarged for ease of viewing.

Small sample size prohibited statistical analyses. However, a few observations from Figure 6-33 were noteworthy. First, across all sutures, F_C using the hybrid ring (1.7 ± 1.1 N) was most similar to the fully flexible ring. Second, although anterior F_C using the hybrid ring (2.2 ± 1.3 N) was similar to that of each other ring type, posterior F_C (1.4 ± 0.8 N) was most similar to the semi-rigid or flexible rings. Finally, using the hybrid ring, the concentration of F_C at the *intra-trigonal* positions (i.e. 11 and 1 o'clock) is noted. The ratio of intra-trigonal to trigonal F_C using the hybrid ring was 2.09:1; for each other ring type this quantity fell between 0.56:1 and 0.93:1.

In SA 1.B, it was demonstrated for rings in the Physio geometry that increasing flexibility increased the ratio of anterior to posterior F_C. Figure 6-34 suggests a similar phenomenon with the hybrid ring. Its $F_{C,\,Ant}/F_{C,\,Post}$ ratio ((1.65 ± 0.36):1) was greater than that of the fully-rigid Profile 3D ring ((1.65 ± 0.36):1 vs. (1.47 ± 0.61):1, respectively), and most similar to the semi-rigid Physio ring ((1.67 ± 0.61):1). Finally, in Figure 6-35, the RS heat maps generated in Figure 6-30 were extended to include the commercial Profile 3D and the hybrid rings. Hybrid rings showed the highest *minimum* RS at any one position of all tested rings. Its *mean* RS across all positions was higher than all but the fully-flexible ring.

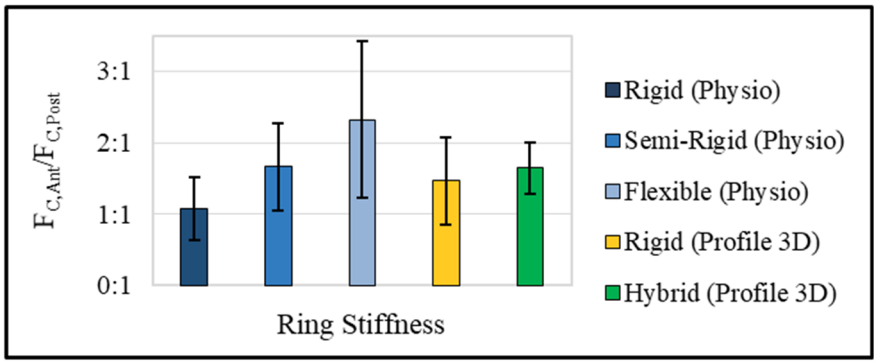

Figure 6-34 Ratio of anterior F_C to posterior F_C, averaged across suture positions and LVP_{max} levels. Preliminary hybrid ring data is shown along with all prior undersized cohorts.

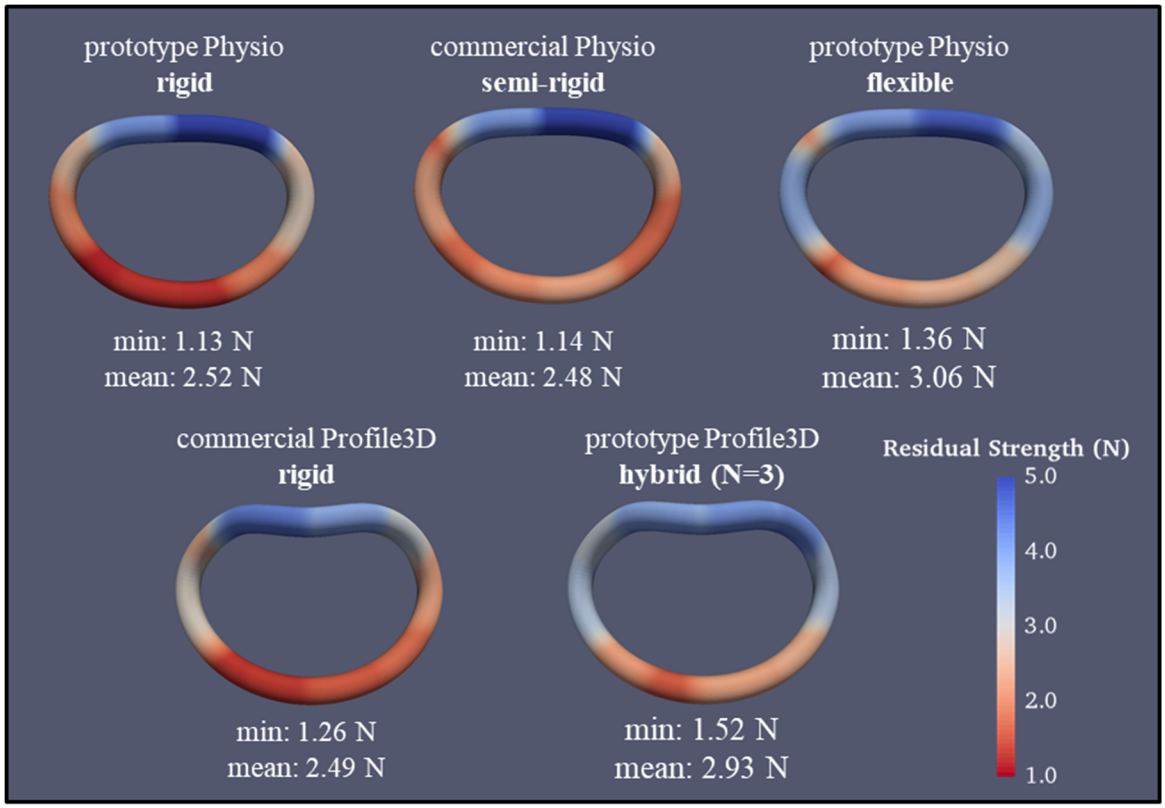

Figure 6-35 Residual Strength around the annular circumference, following use of each tested undersized ring design (lower Residual Strength implies greater suture dehiscence likelihood).

6.3 Specific Aim 1 Discussion

6.3.1 Specific Aim 1.A: Investigation of the Basic Mechanism of Suture Dehiscence

Specific Aim 1.A utilized large animal and *ex vivo* models to explore the *in vivo* cyclic suture forces, *in vitro* suture pullout forces, and regional variation in microstructure within the mitral annulus. These studies successfully demonstrated how regional variations in collagen content impact the likelihood of suture dehiscence, seemingly through a combined

effect on *in vivo* suture forces in the beating heart and the forces necessary to tear sutures from the annular tissue.

Extending from an earlier pilot experiment,[24] this work has provided measurements of cyclic suture forces (F_C) for a common ring used for restrictive annuloplasty. At all suture positions, F_C rose in systole, and fell in diastole (Figure 6-2). Three primary aspects of cardiac contraction likely contribute to this phenomenon. First, the native shape of the annulus is constrained to that of the flat, undersized ring. During systole, aortic root filling causes the central anterior annulus to rise, while ventricular contraction pulls the trigones apically. This accentuation of the annulus' out-of-plane saddle shape is opposed by the annuloplasty ring, with the sutures absorbing the resulting tension. Second, when contracting myocardial fibers shorten along their length during systole, they also expand radially. This thickening will further tense the loops of suture, which are already tied taut around the fibers. Finally, systolic pressure on the leaflets has been shown to pull the annulus radially inward;[148] this tension, which is greatest on the anterior aspect, likely propagates through the tissue to the sutures. As a net effect, F_C was observed to trend positively with LVP_{max}, but to vary significantly with suture position.

The observation of greater anterior F_C, when considered in isolation, appears to contradict the clinical predominance of annuloplasty suture dehiscence from the posterior annulus.[7, 89, 91-99] Yet, *ex vivo* suture pullout force (F_P) also varied by position, with significantly higher anterior suture F_P. Taken together, the F_C and F_P data provided a margin of safety at each suture position, whose results *supported* clinical experience. This data is best represented by trigonal sutures exhibiting a RS approximately 2.5 fold higher than all other positions (Figure 6-12).

Anchor detachment is a recognized mode of failure in ISO 5840-3 and FDA guidance for heart valve replacements and annuloplasty rings.[112, 114, 149] This mode of failure, investigated in the present work for suture, recognizably extends to other anchor types (e.g. hooks, pledgets, or coils) that are common design features of minimally invasive or percutaneous MV repair devices. When such detachment potential is identified, pullout testing is recommended to determine the strength of annular anchoring. As current devices and anchoring methods vary widely,[150] the justification of *in vitro* test methods and reference values becomes critical for anchor design validation and risk assessment.

Descriptions of such *in vitro* test methods and reference values for annular anchor pullout testing are limited in literature. Notably, in one study evaluating the safety of valvular prostheses for magnetic resonance imaging, annular suture pullouts were conducted.[151] Among patients with varying valvular disease, single sutures were shown to tear from the annular tissue at 4.9 ± 3.6 N. These forces agree with the present F_P values (4.9 ± 2.8 N).

The non-uniformity in RS in this investigation is most likely explained by the non-uniformity in collagen around the annulus. Two-photon excitation autofluorescence revealed significantly denser collagen between the trigones (12 o'clock) than at the LT, RT, or 6 o'clock. This was tightly correlated to RS (R^2 = 0.947); a 50% reduction in collagen from the 12 o'clock position to elsewhere was associated with a 3 N drop in RS. (Figure 6-15).

Unexpectedly, nMPI correlated more weakly to F_P (R^2 = 0.501) than to RS. This suggests that mitral annular sutures more effectively engaged collagen fibers during cardiac

contraction (F_C) than during *in vitro* suture pullout (F_P). One plausible explanation for this is that at higher stress states (i.e., during pullout), collagen fibers rotate and/or become more uniformly aligned,[152] making their alignment of greater consequence to F_P than their density. In porcine mitral annuli, Gunning et al recently showed that unloaded collagen fibers are predominantly (though not completely) aligned in the circumferential direction.[43] This is parallel to the annuloplasty suture path; if these fibers become more uniformly aligned at high loads, this would inhibit the suture's ability to engage their load-bearing capacity, potentially weakening the correlation between nMPI and F_P. The relationship between annular collagen and F_P is explored further in supplemental studies using ovine tricuspid valves and a small cohort of human mitral and tricuspid valves in APPENDIX C and APPENDIX D.

Gunning et al further showed that annular collagen is the principal driver of porcine annular mechanical strength under circumferential stretch.[43] Further, higher collagen content was observed on the anterior quadrant of the annulus. However, this colorimetric analysis used an atrial view of the entire quadrant, at relatively low spatial resolution. Thus, the critical zone of transition from high to low collagen density remained to be defined. Our data complement this work, suggesting the average location of this transition zone must be interior from either trigone. These findings provide motivation to consider annular heterogeneity in the development of catheter-based devices that do not use discrete anchors, as well. Transcatheter mitral valve replacements (TMVRs), for example, anchor and seal in part through radial expansion against the annulus. Specific Aim 2 investigates TMVR sealing mechanics as a function of device conformity to the annulus.

The heightened F_C at the trigones may be explained on a biomechanical basis. Both collagen and myocardium are viscoelastic;[153, 154] under contractile loading, suture tension would induce these materials to strain in a time-dependent fashion, counteracting additional gains in tension. In contrast, the trigones do not possess such compliance. Sutures placed directly atop the trigones may therefore be expected to reach greater tensions more quickly, as systolic contraction tends to pull them radially inward and apically. Yet, the lower collagen density atop the trigones also adversely affects that region's F_P. In this way, the trigonal combination of high rigidity/moderate failure strength presents similar risk to the posterior aspect's low rigidity/low failure strength. In contrast, the high-collagen inter-trigonal region (exclusive of the trigones themselves) features high failure strength and only moderate rigidity. It is thus uniquely established as an optimal suture anchoring zone, as evidenced by its superior margin of safety. These findings may explain the more common clinical observation of posterior device dehiscence.

These findings provide a first step in informing novel device design as well as improved surgical decision-making and technique, toward the ultimate reduction in the incidence of suture dehiscence. In a recent editorial titled "A Chain is Only As Strong as Its Weakest Link," Dr. Patrick McCarthy emphasized that a network of annuloplasty sutures is only as strong as its *weakest* suture.[155] In light of this concept, **SA 1.A's findings motivate a goal of identifying annuloplasty ring design parameters that systematically reduce F_C in the weaker posterior annulus.** Sections 6.2.2 and 6.2.3 describe findings from SA 1.B and 1.C, in pursuit of this goal.

6.3.2 Specific Aim 1.B: Parametric Evaluation of Ring Design and Suture Forces

Clinical reports of suture dehiscence following mitral annuloplasty may be easy to dismiss as a result of mere surgical error. However, SA 1.A demonstrated that suture forces that may lead to dehiscence are influenced by annular position and left heart function. SA 1.B recapitulates this finding, and further establishes that suture forces further vary according to the properties of the selected ring (i.e. its size relative to the annulus, its shape, and its stiffness).

In the comparison among true-sized and undersized Physio and Profile 3D rings, use of a true-sized ring reduced F_C. However, it was effective only by way of reducing *anterior* forces. As shown in Figure 6-11, mitral annular suture holding strength is greater on the anterior aspect, creating a higher likelihood of dehiscence from the posterior. Thus, although true-sizing certainly appears beneficial for anchoring stability as a whole, it does not directly affect the most pertinent anchoring region. **Use of larger rings (i.e. true-sized to the annulus) can therefore be rejected as a solution to the challenge of reducing dehiscence likelihood in the posterior annulus.**

Saddle-shaped annuloplasty rings have quantitatively demonstrated benefits over flat rings, including increased leaflet coaptation and curvature,[122-125] reduced annular forces,[128] and likely reduced leaflet and chordal stresses.[45, 126, 127] A similar benefit to F_C was hypothesized. Contrary to expectations, use of the saddle-shaped Profile 3D did not significantly relieve F_C, as compared to the flatter Physio ring. Although the exact mechanical basis for this observation cannot be confirmed from this study, it is likely that the Profile 3D's increased rigidity as compared to the "semi-rigid" Physio plays an

important role. A stiffer ring could increase F_C overall by complying less with cyclic annular motion. Yet, it might also reduce variability between positions by more thoroughly transmitting force around its circumference. Based on this cohort, we speculate that when undersizing, the impact of the Profile 3D's rigid, saddle-shaped design manifested as forces that are overall slightly reduced but significantly more balanced. However, the benefits of true-sizing were meaningfully diminished when using Profile3D, as the effects of its rigidity dominated. While these results provide a direct comparison between two prominent commercially-available rings, they do not decouple the distinct influences of ring shape and stiffness on cyclic suture force.

These findings were not sufficient to conclusively reject ring shape as an effector of F_C on posterior annular sutures. However, they did implicate ring stiffness as a critical, and as-yet-unexplored, design parameter. This motivated the quantification of the isolated effects of ring material properties, presented in Section 6.2.2.3. F_C dynamics were compared among the semi-rigid Physio ring and rigid and flexible ring prototypes of the same geometry. As demonstrated in earlier cohorts, anterior sutures endured greater F_C than did posterior sutures. Importantly, whereas the earlier tests of ring design parameters that may relieve posterior suture forces were negative for ring size and inconclusive for ring shape, **this study revealed for the first time that ring stiffness can preferentially affect suture forces in the posterior annulus.** On the anterior side, no pairwise differences were detected. Figure 6-30 illustrates RS for the presently studied rings, based on F_P data from SA 1.A. It is evident that increasing ring flexibility elevates the annulus' Residual Strength both in the mean (across locations) and at its minimum (at any single location).

Expressing the ring stiffness data differently, the anterior/posterior F_C ratio became greater with increasing flexibility, with the mean ratio rising from 1.08:1 to 1.67:1 to 2.33:1 ($p<0.001$ for rigid vs. flexible, but $p>0.05$ for semi-rigid vs. either other stiffness). These findings suggest a potential biomechanical mechanism whereby anatomic and physiologic factors local to the annulus initially apply greater force to anterior sutures than to posterior sutures. Specifically, systolic expansion of the aortic root (which sits adjacent to the anterior annulus), cyclic changes in the anterior saddle geometry,[46] and the stiffer/more collagenous anterior annular tissue (as demonstrated by Gunning et al[43] and in Figure 6-14) each likely contribute. Subsequently, when multiple annular sutures are connected via an annuloplasty ring or valve replacement, the device serves as a conduit that transfers forces around the suture network (i.e. higher anterior suture forces transfer to posterior sutures). Our data demonstrates that the efficiency of transfer depends on the device's flexibility. Rigid annuloplasty rings appear to enable near-total equilibration of anterior and posterior F_C. Increasing flexibility apparently serves to inhibit such equilibration. For posterior sutures specifically, $HWHM_{norm}$ was 54% greater using flexible rings than either other ring. The observation that posterior sutures take longer to achieve their peak load when a flexible ring is used suggests that one mechanism by which flexible rings maintain lower posterior F_C is by slowing down force transfer around the ring.

Independent of ring sizing or saddle shape, annuloplasty ring flexibility seems to offer a unique capacity to reduce forces on the annular region most clinically susceptible to dehiscence. However, these findings should not be taken to indicate that flexible rings are the superior option in all MR repairs. Notably, specifically in those cases in which a flexible ring is appropriate, the use of a running suture (rather than a series of interrupted

sutures as studied here) has been shown to offer further benefit to anchoring strength.[23, 156] However, for regurgitant valves exhibiting annular distortion (especially those with ischemic MR and/or annular dilation), semi-rigid and rigid rings remain important remodeling tools.[63, 72]_ENREF_23 Some degree of rigidity is also necessary for the ring to re-establish the anterior saddle. A design that retains critical features of both rigid and flexible annuloplasty rings could provide desirable performance from both a safety (suture retention) and efficacy (functional outcomes) standpoint.

Based on the collective findings of SA 1.A and 1.B, **we propose materially hybrid rings as one potential solution for reducing the likelihood of posterior annuloplasty ring suture dehiscence.** Such a design may feature rigid anterior and posterior regions, separated by short flexible segments near the commissures (approximately 3 and 9 o'clock). This may disrupt F_C transfer from anterior to posterior, while still allowing for well-defined anterior saddle curvature and posterior annular restriction. Incidentally, these are the exact two positions for which the flexible ring offered significant F_C relief (Figure 6-27), which may further support such a hybrid configuration. SA 1.C consists of the development and preliminary testing of one such hybrid ring design (ring design shown in Figure 4-4).

6.3.3 Specific Aim 1.C: Development and Preliminary Assessment of a Novel Ring Design

Findings from SA 1.B showed that rigid rings, although known to offer the greatest benefit for annular remodeling and MR volume reduction, exhibited the highest posterior F_C and

accordingly the highest suture dehiscence likelihood. Flexible rings, though lacking the material strength to effectively remodel the mitral annulus, exhibited significant F_C reduction, and associated reduction in suture dehiscence likelihood. Thus, fully-rigid and fully-flexible rings within this study can be considered extreme ends of both the repair efficacy spectrum and the suture dehiscence likelihood spectrum. When assessing novel ring designs in terms of repair efficacy and suture retention, the ideal ring will possess the remodeling capacity of a rigid (and saddle-shaped) ring, and the low dehiscence likelihood of a flexible ring.

One such novel design was developed and preliminarily tested in SA 1.C. Note, its repair efficacy has not been investigated at this time; follow-up studies using an ovine model of ischemic mitral regurgitation are planned. However, F_C dynamics were assessed in three cases using the healthy ovine model, with promising results. Anterior suture F_C using the hybrid ring was similar to that of each other ring type. However, posterior F_C using the hybrid ring was most similar to the flexible and semi-rigid rings (Physio geometry); the hybrid ring's posterior F_C was reduced by 24% relative to the rigid Profile 3D, and by 27% relative to the rigid prototype in the Physio geometry. The anterior/posterior F_C ratio using the hybrid rings was increased relative to either rigid ring, and was most similar to the semi-rigid Physio.

Two major implications appear likely based on the present hybrid ring data. First, they provide strong support for the *force transmission hypothesis* developed based on the first ring stiffness investigations. We proposed that anterior sutures are subjected to greater *initial* loading during cardiac contraction, and these forces are transmitted around the ring to less secure posterior sutures, with the completeness of this transmission scaling with the

ring's rigidity. The hybrid rings, by offering 24% relief of posterior F_C versus fully-rigid Profile 3D rings of matching geometry, validate the proposed mechanism of posterior F_C elevation via anterior-to-posterior force transmission through a rigid ring conduit.

Further, the favorable F_C dynamics establish early practical promise for the hybrid ring concept. The hybrid iteration tested here exhibited an excellent RS distribution, with the highest *minimum* RS at any one position of all tested rings. Its *mean* RS across all positions was higher than all but the fully-flexible ring. An unanticipated benefit using the hybrid rings was the concentration of F_C at 11 and 1 o'clock, i.e. in the intra-trigonal region. Whereas all previously tested rings showed greater force at the trigones than between them (with $F_{C,\text{Intra-trigonal}} - F_{C,\text{Trigonal}}$ differential ranging from -0.1 to -1.6 N), the opposite was true for the hybrid rings (+1.6 N). This differential aligns much more closely with the differential in F_P (+1.2 N), and leads to a more uniform RS distribution in the anterior annulus (Figure 6-35). One likely mechanism leading to this observation is that the saddle shape's benefit to F_C becomes more pronounced when the saddle region is free to rotate about the flexible commissural "joints" (as shown by fluoroscopy in Figure 6-32). However, it may also be an artifact of small sample size.

Additional testing will be necessary to assess the implications of this design, as further discussed in CHAPTER 8 (Conclusions and Future Work). It should also be noted that a different specific configuration of rigid and flexible segments may ultimately prove superior to the configuration tested here. Although posterior F_C using hybrid rings (1.4 ± 0.8 N) was reduced versus the rigid rings (rigid/Physio, 2.1 ± 1.1 N; rigid/Profile 3D, 1.9 ± 0.9 N), it was still not as low as in the fully-flexible/Physio case (1.0 ± 0.6 N). It is possible that larger flexible segments could further reduce posterior F_C; the extent to which

any of these iterations would compromise repair efficacy remains unknown. The early success of the hybrid ring manufacturing techniques employed here establishes a viable approach for preparing any such future iteration.

6.3.4 Integrated Specific Aim 1 Discussion

With more than 20 mitral annuloplasty ring product lines commercially available in the United States, surgeons performing mitral annuloplasty must select from a range of ring sizes, shapes, and stiffnesses for a given patient lesion and etiology. The findings of SA 1 demonstrate that these attributes systematically affect cyclic suture forces in the beating heart (F_C), and suggest that suture dehiscence is not merely a consequence of technical error during ring implantation. An engineered approach to reduce suture dehiscence likelihood via improved device designs and usage strategies is a promising pursuit.

Important mechanistic insights surrounding annuloplasty suture retention dynamics have been uncovered through this work. The clinical predominance of suture dehiscence from the posterior mitral annulus is a likely consequence of both (a) the lesser suture holding strength along the posterior annulus relative to the anterior, and (b) the relative F_C balance between the anterior and posterior annulus. Although F_C was distributed asymmetrically toward anterior sutures in all tested ring types, the *extent* of this asymmetry was inadequate to compensate for the weaker posterior tissue. These dynamics were shown to likely derive, at least in part, from underlying annular collagen content, which was two-fold higher at the mid-anterior annulus versus the mid-posterior or either trigone. In the assessment of ring flexibility as a potential means to reduce F_C relative to anterior,

important suture force dynamics were uncovered. Greater initial loads on anterior sutures (likely arising from its material properties, aortic root expansion, and out-of-plane motion) are transmitted around the annuloplasty ring toward posterior sutures, tending to equilibrate anterior F_C and posterior F_C. The completeness of this equilibration scales with ring rigidity. The early experience with materially hybrid rings, in which short flexible commissural segments in an otherwise rigid ring led to reduced posterior F_C, appears to validate this mechanism.

In the pursuit of better ring design and usage strategies, it was shown that use of true-sized rings does indeed reduce F_C as compared to undersized rings, but only on the anterior annulus. Use of flat versus saddle-shaped rings was not fully explored; a comparison of the flat Physio vs. saddle-shaped Profile 3D was confounded by the differing stiffness between the two rings. Nevertheless, no significant differences in posterior F_C was observed between them. Use of more flexible rings reduced F_C specifically on the posterior annulus, as desired. Given the known benefits in terms of resulting valve geometry and MR volume reduction of (a) undersized rings, (b) saddle-shaped rings, and (c) semi-rigid or rigid rings, we propose that an "optimized" ring from a repair efficacy and suture retention standpoint would be undersized and saddle-shaped, and would possess both the repair benefits of rigidity and the retention benefits of a flexible ring. The materially hybrid ring concept developed and preliminarily tested here shows strong potential to achieve this goal. Further testing is necessary, as further discussed in CHAPTER 8 (Conclusions and Future Work).

6.3.5 *Clinical and Engineering Implications*

Suture dehiscence is an increasingly reported, often catastrophic form of mechanical failure after ring annuloplasty, yet little engineering work has ever explored a basis for its occurrence. By demonstrating that both annular tissue properties and fundamental device design parameters systematically impact annuloplasty ring suture force dynamics, this study successfully established promising new inroads toward reducing the occurrence of dehiscence. This work showed that ring flexibility specifically reduced forces in the weaker posterior annulus, and further suggested that ring shape and size changes did *not* do so. An anterior-posterior suture force transfer mechanism was uncovered. This mechanism pointed toward the development of a novel, materially hybrid ring design, as a means to exploit the demonstrated benefits of ring flexibility for suture forces, without compromising the known benefits of ring rigidity for valve repair effectiveness. The eventual success of this design, or of any other related designs that derive from this work, may directly benefit patient outcomes.

In parallel to the work included in this Specific Aim, a series of supplemental studies were also completed. These studies offered preliminary insights into the implications of suture tie-down force, suture placement error, and variation in suture pullout force between species (ovine vs. human) or valves (mitral vs. tricuspid); they are reported in APPENDIX A through APPENDIX D. Collectively, the studies included in SA 1 and these supplemental studies have elicited six unique editorial responses to date from leading surgeons in the field.[155, 157-161] The consensus opinions from these commentaries are that (a) the work has moved our field closer toward the identification of optimal ring designs and implantation techniques, (b) much additional work remains to be done toward

this end, and (c) the tools and techniques developed throughout these studies hold significant potential for such follow-up pursuits.

Beyond guiding the development of new concepts in ring design and/or surgical practice, the data reported in these studies will provide a baseline for interpreting the impact of MV disease phenotypes on annuloplasty sutures. These data may be further applied as reference values for novel device comparison. Currently, annuloplasty rings may cleared for use in the U.S. market via the FDA's 510[k] pathway. Among annuloplasty ring 510[k] submissions to date, suture pullout testing has been nearly ubiquitous. In effect, these comparisons aim to establish that the likelihood of dehiscence is substantially equivalent to existing devices. However, this work demonstrates that dehiscence likelihood for a given device may not be solely determined by pullout performance. The spatial distribution of suture forces generated during cardiac contraction varied significantly among the tested rings. Quantification of *in vivo* loading may prove an important criterion for device performance assessment; to that end, the present data may function as references for devices implanted using annular sutures. *In vivo* loading may also be important to assess in next-generation percutaneous devices, many of which utilize novel anchor types and placement patterns.

It bears mentioning that anchor dehiscence is not solely a problem for suture-based device implantation. The significant variability in suture force dynamics observed in this work, coupled with the clinical experience with suture dehiscence, together serve as a cautionary tale for the next-generation of hopeful transcatheter mitral valve repair devices. Many of these devices rely on novel anchor types, such as hooks, pledgets, or coils. One such example is Cardioband (Edwards Lifesciences), a catheter-based annuloplasty band

that anchors to the annulus with a series of screw components, and which has CE Mark approval for commercial use in Europe. Notably, Cardioband underwent a recall in February 2018 due to "implant dehiscence" (https://www.tctmd.com/news/edwards-voluntarily-recalls-cardioband-anchors-used-mitral-and-tricuspid-repair). Understanding of the loads that novel anchor types can withstand and/or can be expected to encounter during use may prove critical to their clinical success.

An additional, direct application of the present data may be as an input to computational modeling for device design. Computational research is increasingly utilized in the medical device industry; recent reports by the FDA have embraced its importance in the design process.[162, 163] Modeling of 'virtual patients' serves to enable simulation of complex *in vivo* dynamics, at times offering value to preclinical testing unmatched by in vitro, cadaver, or animal studies. Ground-truth data describing pullout forces and/or contractile loading of annular sutures may constitute critical boundary conditions and/or reference points to validate model performance. F_P values, which exist independent of ring type, are likely applicable to a range of mitral implants. F_C data should be applied to computational simulations more conservatively, on a device-specific and sizing-specific basis.

6.3.6 Limitations

Several limitations of the present experimental materials and methods are noteworthy. First, although various data suggest overall comparable annular mechanics between sheep and humans,[107] some differences are likely. One key difference which may favor higher F_C

in humans is degree of systolic annular motion; systolic annular area reduction has been shown to be 10% in sheep, versus 26% in humans.[37, 46] Also, although suture tie-down force (i.e. pre-tension) is not expected to impact F_C, it may be an important component of total suture force, and may vary according to surgeon, patient anatomy, or other factors. Each of these aspects has been preliminarily investigated in studies supplemental to this work; these are reported in APPENDIX A through APPENDIX D.

Three caveats must be acknowledged regarding comparisons among rings of different stiffnesses. First, the true Physio ring, although semi-rigid, is not materially homogeneous. Its greater anterior rigidity may be one reason the rigid and semi-rigid ring F_C data agreed more closely than did the semi-rigid and flexible. Next, sensors were fixed to the prototype rings via a slightly different method than that for the true Physio, as shown in Section 5.1.1.4. However, the sensor's range of motion relative to the ring was negligible in every case. Finally, the rigid transducers likely had some consistent stiffening effect on all rings. Manual manipulation of the instrumented rings suggested that this effect was minor. Nevertheless, this may have subtly dampened the effect size across stiffnesses, suggesting the reported differences are conservative.

During *in vitro* studies, use of previously frozen, post-rigor mortis hearts are expected not to have affected collagen *content*, but may have slightly compromised collagen *strength*. Fresh and/or living tissue is expected to be slightly more durable with respect to suture pullout.

In terms of statistical analysis, we note that, ANOVA testing among individual positions was less sensitive than other tests, due to limited sample size. It is possible that some true pairwise differences between suture positions went undetected.

CHAPTER 7. RESULTS AND DISCUSSION – SPECIFIC AIM 2

7.1 Introduction to Specific Aim 2 Results and Discussion

For the reader's convenience, the experimental schematic for Specific Aim 2 is reproduced here, followed by an experimental matrix:

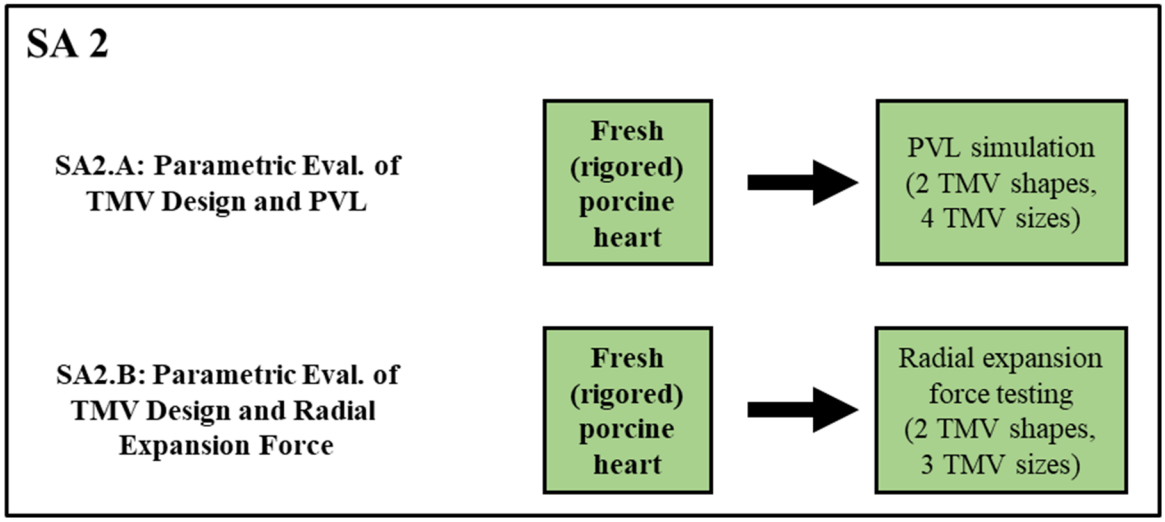

Figure 7-1 Schematic of Specific Aim 2 Experiments (duplicated from CHAPTER 3).

Table 7-1 Experimental matrix for SA 2.

	Test	Expts	Shapes	Sizes	Acquisitions per shape-size combo	Data points per acquisition	Data points
SA 2.A	*ex vivo,* porcine, PVL	7	2	4	3	5	**840**
SA 2.B	*ex vivo*, porcine, C-REFT	6	1	3	8	1	**144**
	ex vivo, porcine, D-REFT	6	1	3	8	1	**144**

Note, many of the graphs that follow provide results in terms of both (a) mean ± standard deviation (SD), represented with bars, and (b) mean ± 95% confidence interval (CI), represented with dots. Text values are provided as mean ± SD. For the reader's convenience, Table 5-4, which summarized all general linear models (GLMs) used in SA 2, is reproduced here as Table 7-2.

Table 7-2 GLMs used in SA 2 (duplicated from CHAPTER 5).

Sub-aim	Model	Dependent Variables	Independent Variables
	1	PVL_{norm}	TMV shape, TMV size
	2	sqrt(PVL)	TMV shape, TMV size, ΔP*
SA 2.A	**3****	PVL	TMV shape, TMV size
SA 2.B	**4**	F_{SL}, F_{IC}, sqrt(F_{IC}/F_{SL})	TMV shape, TMV size

*continuous variable; **only included samples having ΔP between 110-130 mmHg.

7.2 Specific Aim 2 Results

7.2.1 Specific Aim 2.A: Parametric Evaluation of TMV Design and PVL

7.2.1.1 Steady Back-Pressure System Performance

The steady back-pressure system designed for use in SA 2.A was constructed successfully. Upon the installation of a fresh porcine heart having a competent MV, trans-mitral ΔP could be easily manipulated according to the fluid mechanics analog of Ohm's Law. Under

these steady flow conditions, this equation states that LVP (equivalent to ΔP, because the MV's atrial face was exposed to ambient air pressure) can be adjusted by changing either the flowrate through the LV and/or the resistance to said flow. As such, to increase ΔP required either (a) increasing the pump speed and/or closing the bypass valve (each of which increased rate of LV inflow through the apex) or (b) closing the downstream valve (which increased resistance to LV outflow through the aorta).

Under nominal conditions (no mock TMV plug), ΔP was easily adjusted to between 40-215 mmHg, and held steady within 1-2 mmHg. When a TMV plug was deployed, the resulting leakage gaps reduced the total resistance to LV outflow and reduced the maximum achievable ΔP. Nevertheless, even in the presence of mitral regurgitation exceeding 70 ml/sec, ΔP values above 160 mmHg were attained. Across all experiments, the system sealed effectively: incidental leak through apical, aortic, or other connections was 3.3 ± 3.0 ml/sec (this was quantified and detrended from PVL data, as described in Section 5.2.7.1).

7.2.1.2 PVL Results

Testing of each porcine heart for SA 2.A's investigation of TMV design and PVL dynamics commenced 7-11 hours post-mortem. The saddle height, which was measured in each heart to guide mock TMV plug positioning as discussed in METHODS XXXX, had mean ± SD 15.4 ± 1.6 mm. Additional key geometric descriptors of the hearts used are presented in Table 7-3. Metrics before and after PVL testing are included. As detailed in Section 5.2.1,

the selection criteria for these hearts included inter-trigonal distance of 30 mm and annular perimeter of approximately 108.4 mm.

Table 7-3 Geometric descriptors for the hearts used in SA 2.A investigation of TMV design and PVL.

	Pre-procedure	**Post-procedure**
Inter-trigonal distance (mm)	30.0 ± 0	31.3 ± 1.6
Perimeter (mm)	105.9 ± 10.5	128.1 ± 7.8
Area (cm^2)	7.5 ± 1.6	11.9 ± 1.9
D_{SL} (mm)	23.5 ± 4.4	31.2 ± 4.8
D_{IC} (mm)	35.0 ± 5.9	41.3 ± 3.4
D_{IC}/D_{SL}	1.54 ± 0.44	1.46 ± 0.34

The PVL experimental protocol caused plastic deformation of the MV annulus. On average, the PVL protocol caused 20.9% increase in valve perimeter, 58.6% increase in valve area, 32.7% increase in D_{SL}, and 18.0% increase in D_{IC}. The implications of this stretch are discussed in Section 7.3.5.

In total, 840 total leakage observations were collected (from 168 acquisitions). These were comprised of 3 acquisitions (5 pressure levels each), using each of 8 plugs, in each of 7 hearts. Across all samples, ΔP ranged from 52-209 mmHg and PVL ranged from 1-88 ml/sec. The F- and p-values from all GLMs used in SA 2.A are presented in Table 7-4. Representative ΔP and PVL data are presented in Figure 7-2.

Table 7-4 Results of all GLMs used in SA 2.A, before post-hoc analysis. GLMs are fully described in Table 7-2.

		Factor	F	p
Model 1 (PVL_{norm})	**Main effects**	Shape	47.75	<0.001
		Size	7.70	<0.001
	Interactions	Shape:Size	1.39	0.245
Model 2 (sqrt(PVL))	**Main effects**	Shape	56.44	<0.001
		Size	7.18	<0.001
		ΔP	1822.21	<0.001
	Interactions	Shape:Size	2.16	0.091
		Shape:ΔP	9.83	0.002
		Size:ΔP	0.55	0.645
Model 3 (PVL, for samples with ΔP between 110-130 mmHg)	**Main effects**	Shape	22.21	<0.001
		Size	3.75	0.012
	Interactions	Shape:Size	0.05	0.984

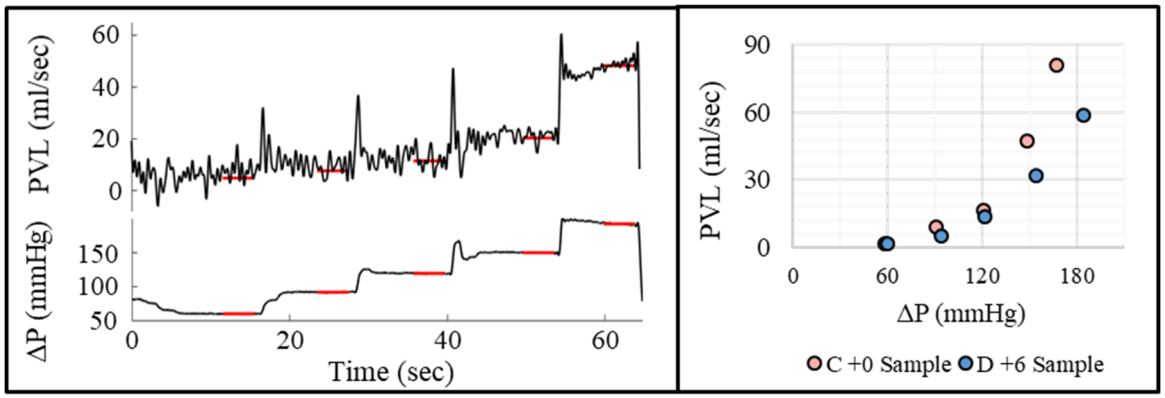

Figure 7-2 Left: Representative plots of ΔP and PVL versus time from a single acquisition. The system was tuned to establish and hold each ΔP level, such that ΔP and PVL could be averaged over a 4 second interval (red lines). Right: Scatterplots of ΔP vs. PVL relationship from two acquisitions, using either the smallest circular device (C+0) or the largest D-shaped (D+6) device.

Two important observations can be made from Figure 7-2. As shown in the left panel, it was found that leakage rates as a whole exhibited oscillations with frequency of

approximately 1-2 Hz, and with amplitude of approximately 5-10 ml/sec. Nevertheless, leakage rates were stable in the mean, indicating that ΔP and PVL endpoints could be appropriately obtained from a 4 second window average.

As shown in the right panel of Figure 7-2, changes to PVL in response to changes in ΔP were non-linear. This was qualitatively observed in real-time throughout all experiments, and was subsequently quantified across all acquisitions. Two sets of correlation coefficients were produced from each of the 168 acquisitions, using either linear or quadratic fits. For quadratic fits, a slope of 0 was enforced at $\Delta P = 0$ (on the conservative assumption that leakage rates would not decrease as pressure increased). Mean ± standard deviation R^2 values for linear and quadratic fits were, respectively, 0.826 ± 0.111 and 0.905 ± 0.082 ($p<0.001$ by paired Student's t-test). Thus, a quadratic relationship between ΔP and PVL was concluded.

Subsequent analyses were conducted accordingly. To visualize the ΔP vs. PVL relationship for each device, quadratic curves were fit to the data from each device in two ways. First, curves were fit to data collected with each device from *each heart separately*. These curves (56 total) are presented in Figure 7-3. Next, curves were fit to data collected with each device *across all hearts* (8 total). These curves, together with their 95% confidence intervals, are presented in Figure 7-4.

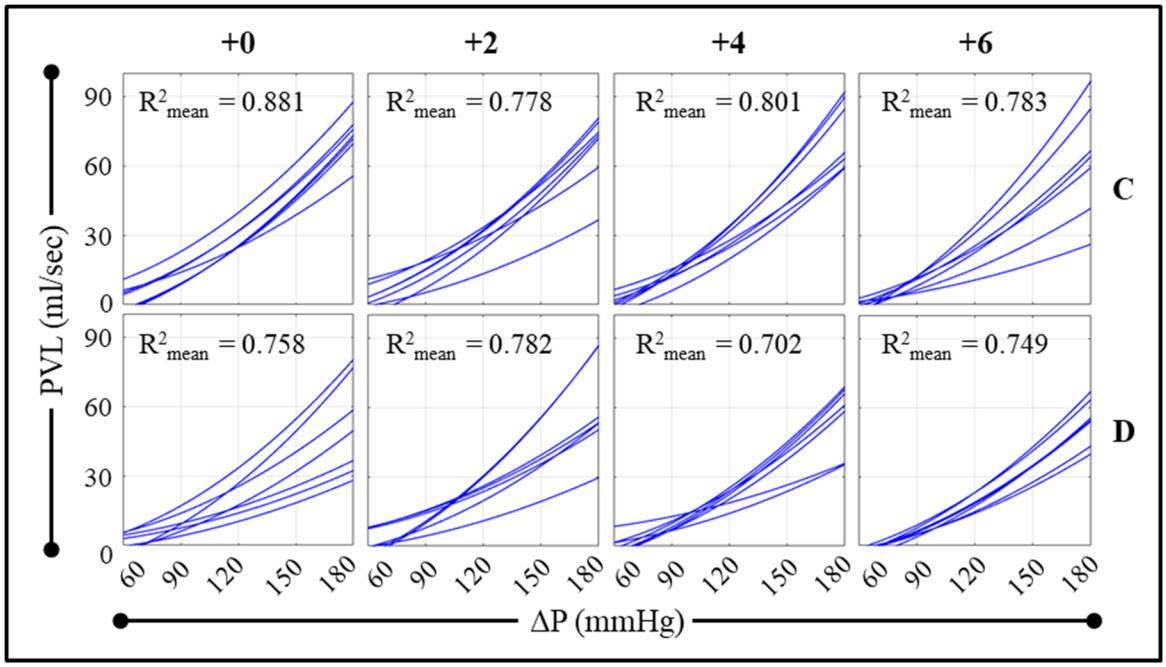

Figure 7-3 ΔP vs. PVL curve fits. Each subplot includes seven curves from a single mock TMV plug. Each curve is fit to all data points collected from a single heart with a single device.

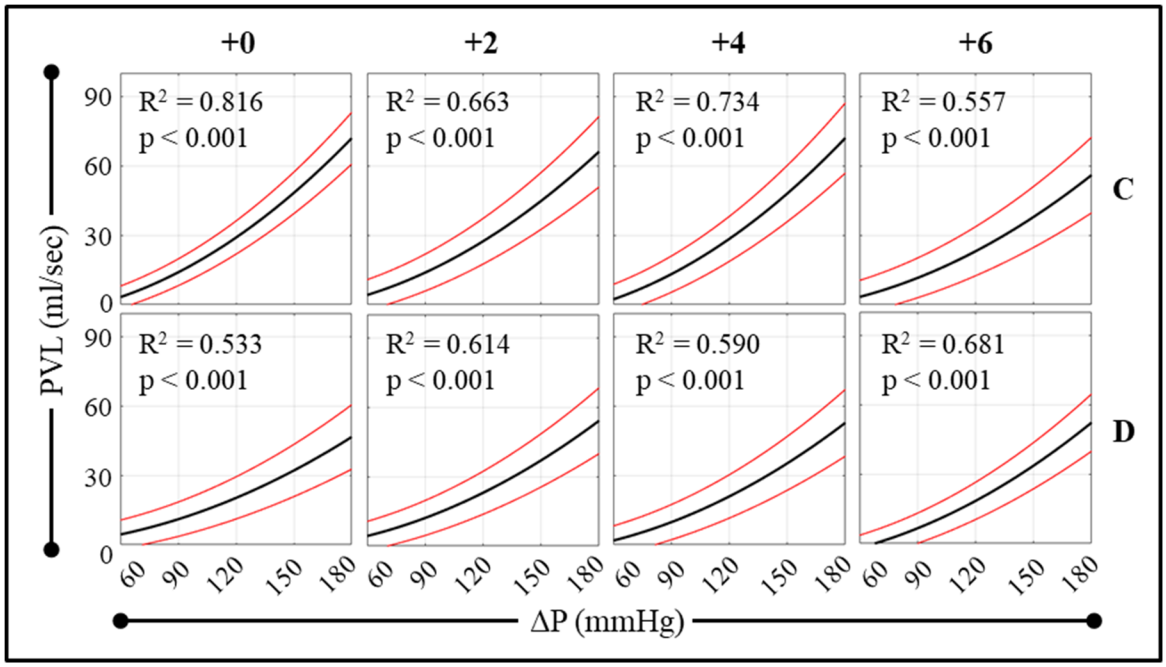

Figure 7-4 ΔP vs. PVL curve fits. Each subplot includes an overall curve fit (black) with 95% confidence interval (red), from a single mock TMV plug. Each curve is derived from testing in *all* seven hearts.

Key observations from Figure 7-3 were as follows. First, for every device, mean R^2 across every heart was 0.702 or better, indicating a clear and consistent relationship between pressure and leakage. The diversity in the curves within each subplot indicates a variability in leakage dynamics among the seven hearts for every device. This variability was greater for some devices than others (e.g., the seven curves exhibit greater spread for the D+0 device than the D+6 device). Across all devices, PVL rates ranged from near 0 ml/sec at ΔP = 60 mmHg (hypotension), to 30-90 ml/sec at ΔP = 180 mmHg (severe hypertension).

From Figure 7-4, it is notable that each curve in Figure 7-4 was highly significant ($p<0.001$). This indicates that for each tested mock TMV plug, a real relationship existed

between pressure and leakage across hearts, even in spite of the variability between hearts. Across all devices, mean PVL rates ranged from near 0 ml/sec at ΔP = 60 mmHg (hypotension), to 45-75 ml/sec at ΔP = 180 mmHg (severe hypertension).

In both Figure 7-3 and Figure 7-4, it appears that PVL rates were, in most instances, reduced for D-shaped devices and/or larger devices. However, *significance of differences in leakage dynamics among the eight mock TMV plug designs cannot be assessed from these representations*. To that end, three complementary statistical methods were employed. Each is detailed in full in Section 5.2.8.2. In brief, they were:

- GLM 1: compared performances of each device *as a whole*, by converting leakage to the pressure-normalized term, PVL_{norm}. PVL_{norm} is defined in Section 5.2.7.1; it reflected the proportion change in leakage of any given observation relative to the average observation. For example, if PVL_{norm} for a given device type were 0.1, this would signify 10% more normalized leakage using this device than the average device, *across all pressures*. Results are presented in Figure 7-5 through Figure 7-9 (and described in the text following Figure 7-9).
- GLM 2: compared device performance in terms of sqrt(PVL) at each of 5 key pressure levels, by accounting for ΔP as a continuous independent variable. Results are presented in Figure 7-10.
- GLM 3: compared device performance in terms of PVL, for all observations having normotensive ΔP (i.e., 110-130 mmHg). Results are presented in Figure 7-11 through Figure 7-15 (and described in the text following Figure 7-15).

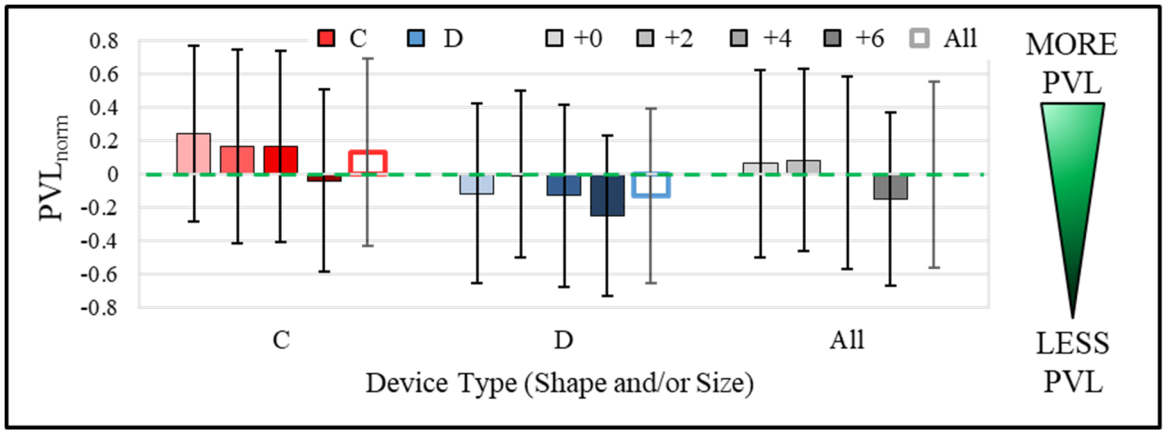

Figure 7-5 PVL_{norm} results, in terms of mean ± standard deviation (SD) for each mock TMV plug type (included: individual devices, binned by shape, binned by size, and all shapes/sizes). Although trends are apparent, statistical significance of these trends cannot be assessed until after GLM 1 (see Figure 7-6 through Figure 7-8). Green line: mean leakage across all samples.

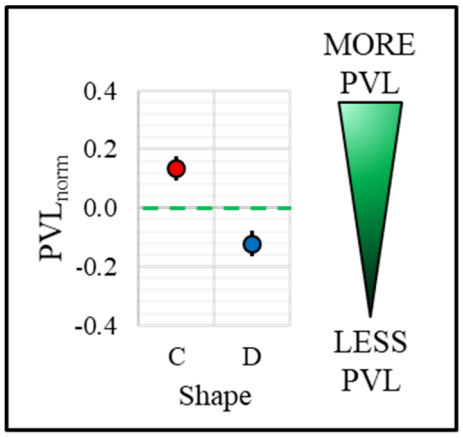

Figure 7-6 PVL_{norm} results in terms of mean ± 95% confidence interval (CI) using either device shape (after GLM 1). Pairs whose 95% CIs do not overlap differ significantly ($p<0.05$). Green line: mean leakage across all samples. The D-shape significantly reduced PVL_{norm}.

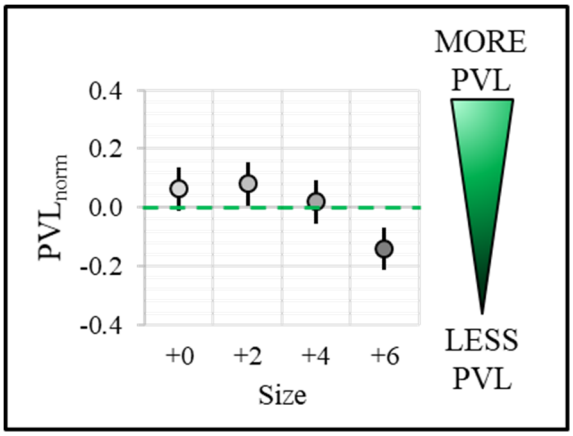

Figure 7-7 PVL_{norm} results in terms of mean ± 95% CI using each device size (after GLM 1). Pairs whose 95% CIs do not overlap differ significantly ($p<0.05$). Green line: mean leakage across all samples. The +6 devices significantly reduced PVL_{norm} versus each other device size.

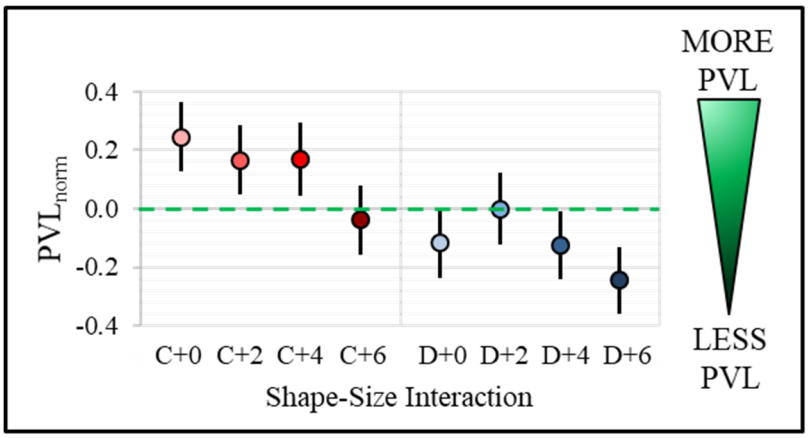

Figure 7-8 PVL_{norm} results in terms of mean ± 95% CI using each device shape-size combination (after GLM 1). Pairs whose 95% CIs do not overlap differ significantly ($p<0.05$). Green line: mean leakage across all samples. The only circular device that did not exhibit significantly greater PVL_{norm} than at least one of the D-shaped devices was C+6.

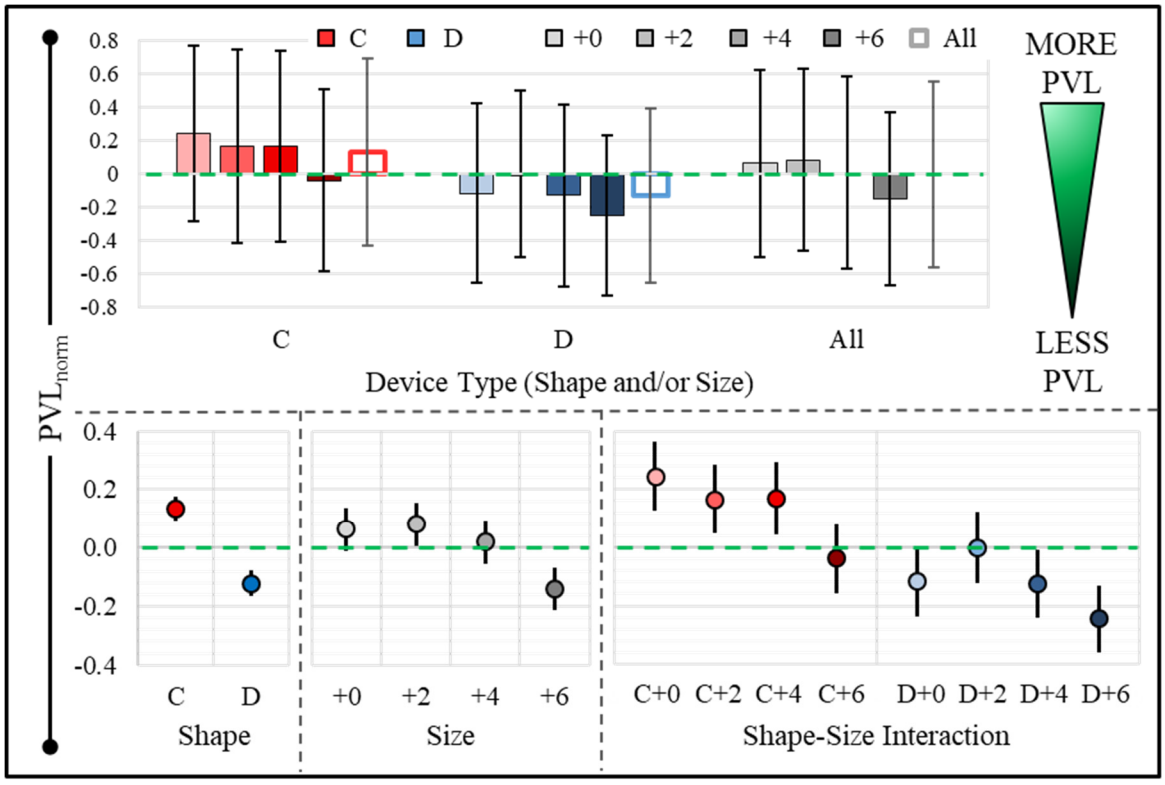

Figure 7-9 PVL_{norm} results, duplicated from Figure 7-5 through Figure 7-8. Top: mean ± SD for each mock TMV plug type (included: individual devices, binned by shape, binned by size, and all shapes/sizes). Bottom: mean ± 95% CI for each mock TMV plug shape, size, or shape-size combination (after GLM 1). Within each plot, pairs whose 95% CIs do not overlap differ significantly ($p<0.05$). Green line: mean leakage across all samples. Overall, shape was an equal or greater effector of PVL_{norm} than size.

The global mean ± SD for PVL_{norm} was 0 ± 0.558. The best-sealing device was D+6 (-0.246 ± 0.481) and the worst-sealing device was C+0 (0.244 ± 0.529). These devices also exhibited the single best-sealing (-0.958) and worst-sealing (2.299) observations, respectively. PVL_{norm} differed substantially among device types. Across all device sizes, use of the D-shape offered significant reduction in PVL_{norm} versus the circular shape (-0.127 ± 0.523 vs. 0.133 ± 0.564, $p<0.001$). Across all shapes, increasing size also

significantly reduced PVL_{norm}, but only when comparing the +6 size (-0.147 ± 0.521) to any smaller size (+0: 0.064 ± 0.563, p<0.001 vs. +6; +2: 0.084 ± 0.547, p<0.001 vs. +6; +4: 0.008 ± 0.576, p=0.012 vs. +6). Shape and size were found not to interact significantly as a whole (p=0.245, Table 7-4). Yet, it is notable that the D-shape outperformed the circular shape at all sizes; this was significant for each size except +2 (p=0.345). Further, it is notable that oversizing offered a significant advantage only when comparing +6 to +0 (for circular shape; p=0.003) or +6 to +2 (for D-shape; p=0.019).

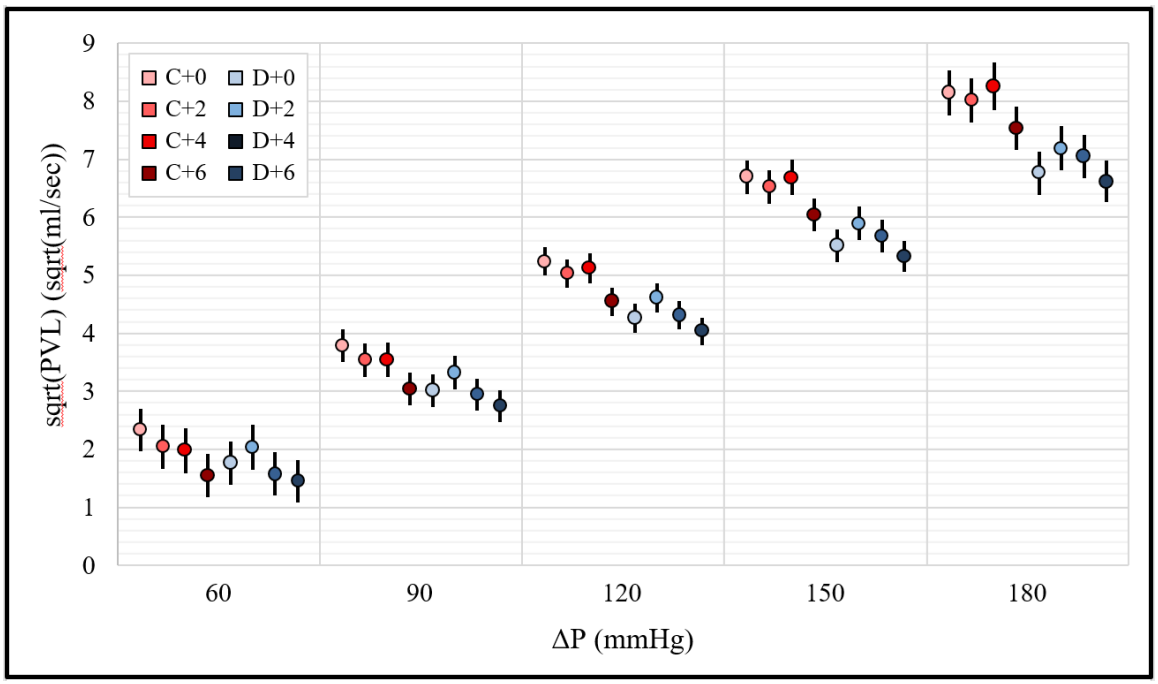

Figure 7-10 sqrt(PVL) results after modeling ΔP as a continuous variable. Mean ± 95% CI for each mock TMV plug at each of five key ΔP levels (after GLM 2). Pairs whose 95% CIs do not overlap differ significantly (p<0.05).

It is evident from Figure 7-10 that, based on GLM 2, each 30 mmHg increase in ΔP significantly increased leakage. For any given device, no two 95% CIs from different ΔP

levels overlapped. When comparing leakage among devices, most trends found using PVL_{norm} (Figure 7-9) were mirrored at each single ΔP level. For example, the D-shape offered significant reduction in leakage versus the circular shape (for at least one pair of devices) at every pressure. The C+6 device exhibited significantly less leakage versus C+0 at most pressures, as did the D+6 versus D+2.

However, some important findings varied based on ΔP. For example, at 60 mmHg, no significant differences in leakage were detected between circular and D-shaped devices at matching sizes. But as ΔP increased, the annular sealing benefits of the D-shape became more pronounced. At 180 mmHg, D-shaped devices exhibited significantly less leakage than circular devices when holding size constant, at *every* size. While the effects of shape were most pronounced at 180 mmHg, the effects of size *within* each shape were least pronounced. Within all circular or all D-shaped devices, no significant differences were detected among sizes at 180 mmHg.

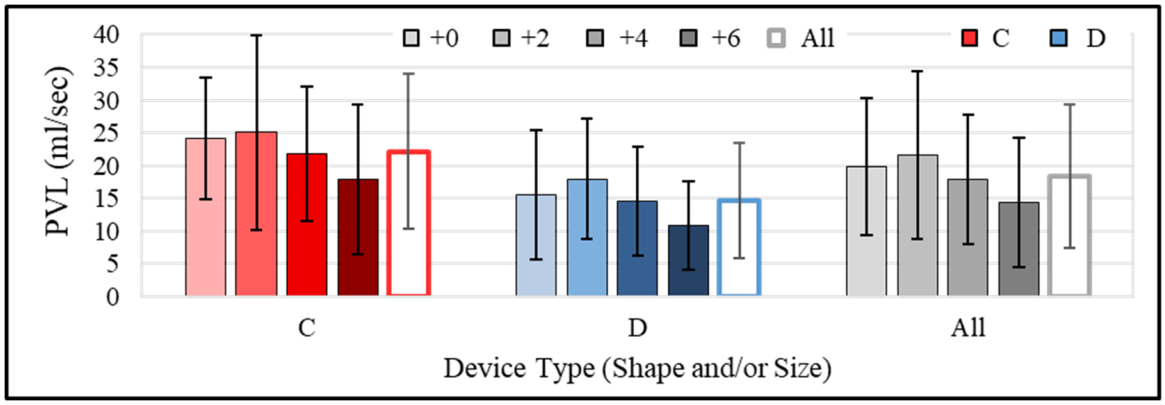

Figure 7-11 PVL results for the normotensive state (i.e., ΔP between 110-130 mmHg), in terms of mean ± SD for each mock TMV plug type (included: individual devices, binned by shape, binned by size, and all shapes/sizes). Although trends are

apparent, statistical significance of these trends cannot be assessed until after GLM 3 (see Figure 7-12 through Figure 7-14).

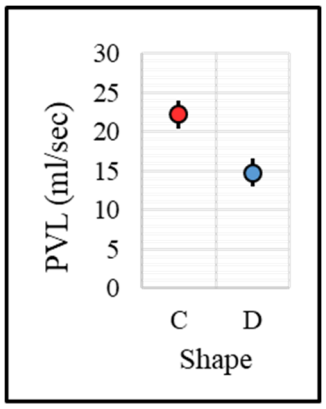

Figure 7-12 PVL results for the normotensive state (i.e., ΔP between 110-130 mmHg), in terms of mean ± 95% CI using either device shape (after GLM 3). Pairs whose 95% CIs do not overlap differ significantly ($p<0.05$). The D-shape significantly reduced PVL.

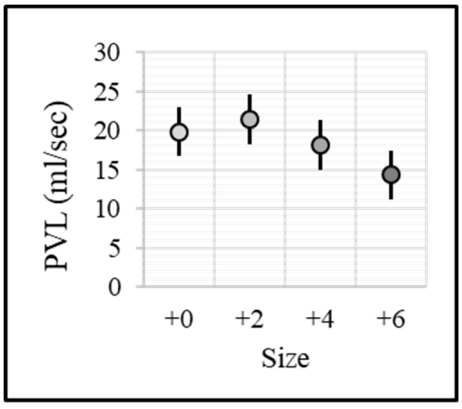

Figure 7-13 PVL results for the normotensive state (i.e., ΔP between 110-130 mmHg), in terms of mean ± 95% CI using each device size (after GLM 3). Pairs whose 95% CIs do not overlap differ significantly ($p<0.05$). The +6 size significantly reduced PVL as compared to +2, and nearly versus +0.

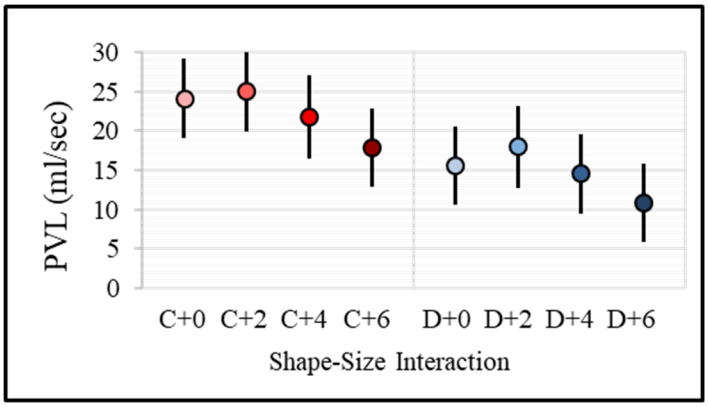

Figure 7-14 PVL results for the normotensive state (i.e., ΔP between 110-130 mmHg), in terms of mean ± 95% CI using each shape-size combination (after GLM 3). Pairs whose 95% CIs do not overlap differ significantly ($p<0.05$). Within either shape, no significant differences in PVL were detected due to size. The only circular device that did not exhibit significantly greater PVL than at least one of the D-shaped devices was C+6.

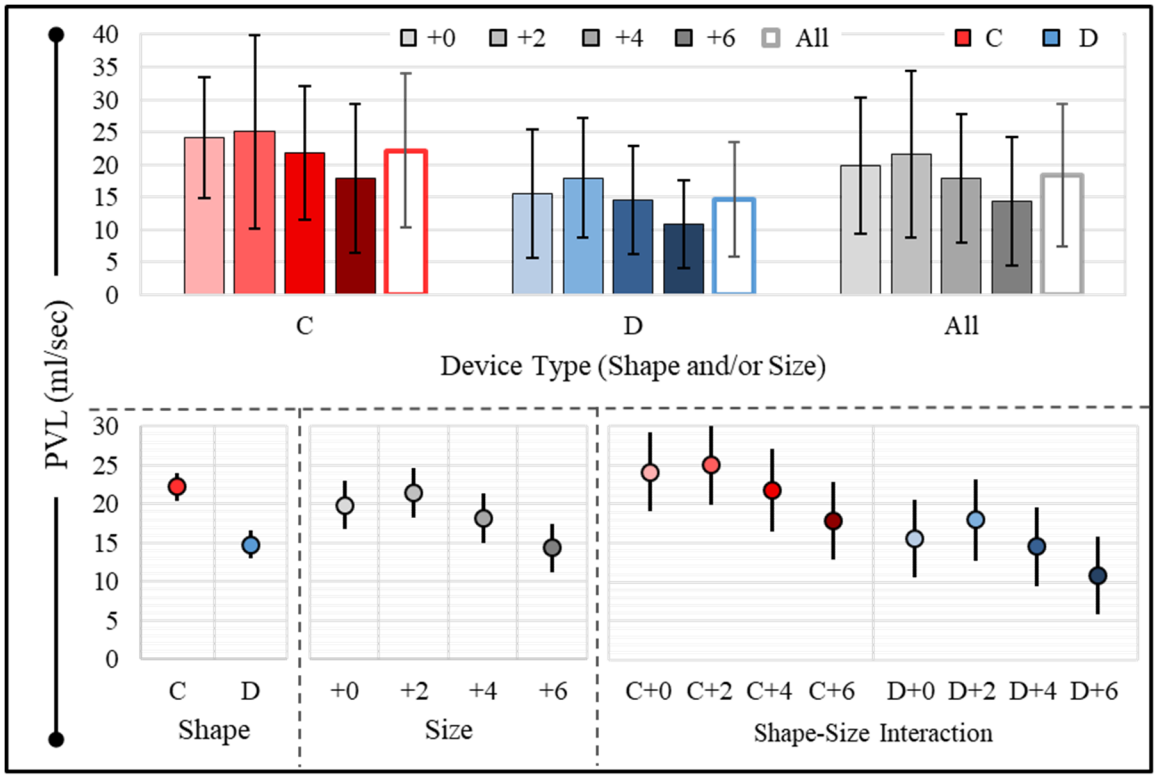

Figure 7-15 PVL results, duplicated from Figure 7-11 through Figure 7-14. Top: mean ± SD for each mock TMV plug type (included: individual devices, binned by shape, binned by size, and all shapes/sizes). Bottom: mean ± 95% CI for each mock TMV plug shape, size, or shape-size combination (after GLM 3). Within each plot, pairs whose 95% CIs do not overlap differ significantly ($p<0.05$). Overall, shape was an equal or greater effector of PVL than size.

Averaged across all observations having ΔP between 110-130 mmHg, PVL was 18.4 ± 11.0 ml/sec. Circular plugs leaked 51.2% more than D-shaped plugs (22.2 ± 11.8 vs. 14.7 ± 8.8 ml/sec, $p<0.001$). Across shapes, again oversizing led to significant benefit, but only when comparing the +6 size (14.3 ± 9.9 ml/sec) to +2 (21.6 ± 12.8 ml/sec, $p=0.008$), or nearly when comparing to +0 (19.9 ±10.4, $p=0.061$). Within circular or within D-shaped devices, no significant differences were detected among sizes. Likewise, within each size, no significant differences were detected between shapes. The trends in these

comparisons mirror those in Figure 7-9 and Figure 7-10; the lack of significance likely reflects the reduced sensitivity of this approach.

7.2.2 Specific Aim 2.B: Parametric Evaluation of TMV Design and Radial Expansion Force

7.2.2.1 Qualification of REFT Performance

The REFT design was completely novel. It was constructed from multiple high-precision, rapid prototyped components, with electronic sensors installed by hand. Its performance was systematically qualified according to the following criteria.

Dimensional verification. The dimensions of the arms were measured in triplicate along its two major axes, at each of 4 sizes. Mean absolute error across all devices/sizes was 142 μm. This was within the expected total error due to the 25 μm resolution of multiple printed parts, the water jet cutting process, and the steel piston rod's thickness tolerance (127 μm).

Linearity of voltage response. In each of the 8 REFT arms, the voltage response to applied force was linear throughout the full force range applied during calibration (R^2: 0.976-0.999). Further detail is provided in Section 5.2.4.3.

Validation of REFT force measurements. Once calibration values were obtained, 16 forces from across the calibration range were re-applied to the four REFT arms. The mean relative error between true and measured forces was 4.3%.

Sensitivity. In general, a force transducer's sensitivity is the smallest force magnitude that can be reliably resolved from any underlying noise in the system. For the REFT, it was observed that increments as small as 0.1 N could be easily detected.

Drift. Each data acquisition was performed over approximately 30 seconds. Drift in the REFT signals over this time interval was approximately 0.05-0.1 N. To remove the influence of drift, the baseline force signal was taken as the average signal before and after REFT expansion (as descried in Section 5.2.6.2).

Cross-talk between measurement arms. The design of the REFT featured orthogonal or near-orthogonal arm orientations, and also featured a central hub that dampened force transmission between arms. Both of these attributes were intended to minimize "cross-talk" between septal-lateral (SL) and inter-commissural (IC) force measurements. Nevertheless, it was observed that peak loading (62.1 N) along one measurement axis slightly influenced force detection on the perpendicular axis. Mean relative error between the true force applied on one axis and the force measured on the perpendicular axis was 1.1%.

Uncertainty estimation. The above noted 4.3% and 1.1% mean relative errors between true and measured forces propagate to a theoretical worst-case uncertainty of 5.4%.

7.2.2.2 Radial Expansion Force Results

Testing of each porcine heart for SA 2.B's investigation of TMV design and radial expansion forces commenced 5-11 hours post-mortem. Key geometric descriptors of the hearts used are presented in Table 7-5. Metrics before and after REFT testing are included. As detailed in Section 5.2.1, the selection criteria for these hearts included inter-trigonal distance of 30 mm and perimeter of approximately 108.4 mm.

Table 7-5 Geometric descriptors for the hearts used in SA 2.B investigation of TMV design and radial expansion force. Each heart was assigned to receive either the C-REFT or D-REFT; differences between sample populations were assessed by Student's t-test.

Pre-procedure			
	C-REFT	**D-REFT**	**p (C vs. D)**
Inter-trigonal distance (mm)	30.0 ± 0	30.0 ± 0	-
Perimeter (mm)	109.1 ± 4.0	108.7 ± 5.4	0.879
Area (cm^2)	8.5 ± 0.5	8.2 ± 0.9	0.513
D_{SL} (mm)	26.2 ± 2.4	25.1 ± 3.1	0.507
D_{IC} (mm)	35.1 ± 4.1	34.4 ± 4.3	0.784
D_{IC}/D_{SL}	1.35 ± 0.24	1.40 ± 0.30	0.783
Post-procedure			
	C-REFT	**D-REFT**	**p (C vs. D)**
Inter-trigonal distance (mm)	30.0 ± 0	30.0 ± 0	-
Perimeter (mm)	121.8 ± 4.2	124.1 ± 9.0	0.575
Area (cm^2)	10.6 ± 0.8	10.9 ± 1.7	0.647
D_{SL} (mm)	29.2 ± 1.8	30.0 ± 4.4	0.693
D_{IC} (mm)	38.9 ± 3.7	40.3 ± 3.6	0.538
D_{IC}/D_{SL}	1.34 ± 0.14	1.37 ± 0.25	0.800

Importantly, no differences were detected between the shapes of the MV annuli assigned to the C-REFT and D-REFT groups. The REFT experimental protocol caused plastic deformation of the MV annulus, although to a lesser degree than did the PVL protocol (Table 7-3). On average, the REFT protocol caused 12.9% increase in valve perimeter, 28.7% increase in valve area, 15.9% increase in D_{SL}, and 14.0% increase in D_{IC}. The implications of this stretch are discussed in Section 7.3.5.

In total, after discarding samples with aortic pressure below 110 or above 130 mmHg, 262 acquisitions (48.9% using C-REFT) were collected from 12 hearts (50% using C-REFT). Aortic pressure across all acquisitions was 119.6 ± 3.1 mmHg. The F- and p-

values from all ANOVA models used in SA 2.B are presented in Table 7-6. Representative data from one acquisition is presented in Figure 7-16.

Table 7-6 Results of all ANOVA models used in SA 2.B, before post-hoc analysis. ANOVA models are fully described in Table 7-2.

		Factor	F	p
Model 4 (F_{SL})	**Main effects**	Shape	9.55	0.002
		Size	39.75	<0.001
	Interactions	Shape:Size	5.45	0.0048
Model 4 (F_{IC})	**Main effects**	Shape	9.72	0.002
		Size	95.67	<0.001
	Interactions	Shape:Size	21.95	<0.001
Model 4 (sqrt(F_{IC}/F_{SL}))	**Main effects**	Shape	46.55	<0.001
		Size	1.09	0.338
	Interactions	Shape:Size	5.99	0.003

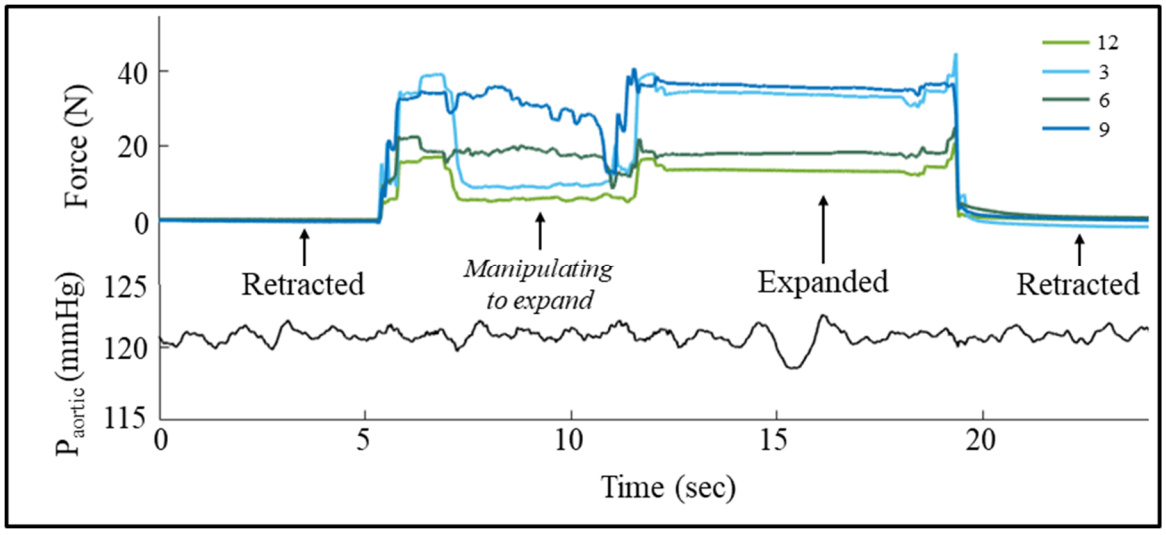

Figure 7-16 Representative plots of force measured on each REFT arm from a single acquisition. With aortic pressure at approximately 120 mmHg, the arms were deployed to an expanded state, held, and retracted, such that force and pressure could be averaged over a 1.5 second interval.

It is apparent from Figure 7-16 that the aortic pressurization system was effective in maintaining within 1-2 mmHg of the 120 mmHg target. Forces were stable over time, with minimal drift during either the retracted (true-sized to the annulus) or expanded (over-sized) state. Accordingly, deriving ΔP and PVL endpoints from a 1.5 second window average was appropriate. Note, these data reflect the forces preliminarily measured on *each* arm. All force data is reported hereafter as septal-lateral force (F_{SL}, from an average of the measurements at 12 and 6 o'clock) and inter-commissural force (F_{IC}, from an average of the measurements at 3 and 9'oclock).

GLM 4 accounted for the effects of TMV shape and TMV size on each of three dependent variables. F_{SL} findings are presented in Figure 7-17 through Figure 7-21 and described in the text following Figure 7-21. F_{IC} findings are presented in Figure 7-22 through Figure 7-26 and described in the text following Figure 7-26. Sqrt(F_{IC}/F_{SL}) findings are presented in Figure 7-27 through Figure 7-31 and described in the text following Figure 7-31. Note, Figure 7-27 provides F_{IC}/F_{SL} data *before* square root transformation, because this figure presents mean ± SD only, prior to the statistical model, and thus the transformation was unnecessary at that point.

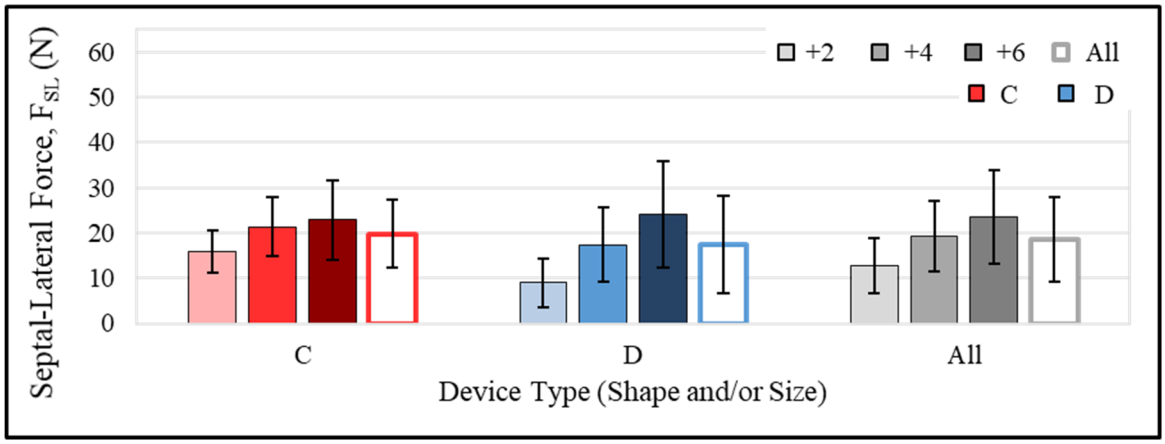

Figure 7-17 F_{SL} results in terms of mean ± SD for each expansion geometry (included: individual geometries, binned by shape, binned by size, and all shapes/sizes). Although trends are apparent, statistical significance of these trends cannot be assessed until after GLM 4 (see Figure 7-18 through Figure 7-20).

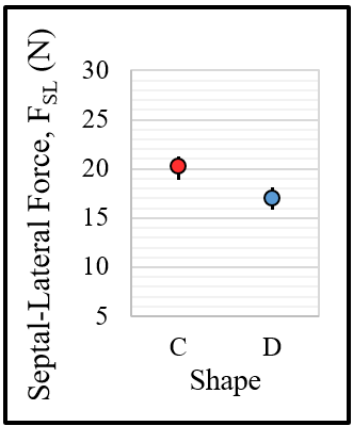

Figure 7-18 F_{SL} results in terms of mean ± 95% CI using either shape (after GLM 4). Within each plot, pairs whose 95% CIs do not overlap differ significantly ($p<0.05$). The D-shape led to a significant reduction in F_{SL}.

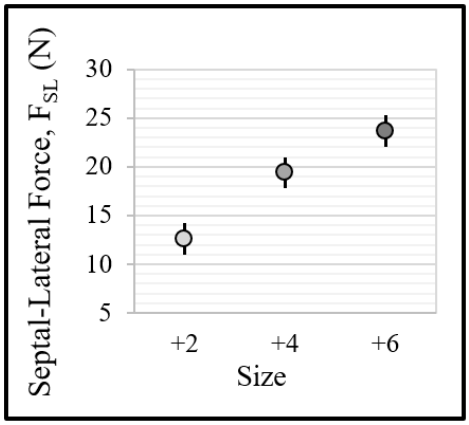

Figure 7-19 F_{SL} results in terms of mean ± 95% CI for each level of annular oversizing (after GLM 4). Within each plot, pairs whose 95% CIs do not overlap differ significantly ($p<0.05$). Each increase in oversizing significantly increased F_{SL}.

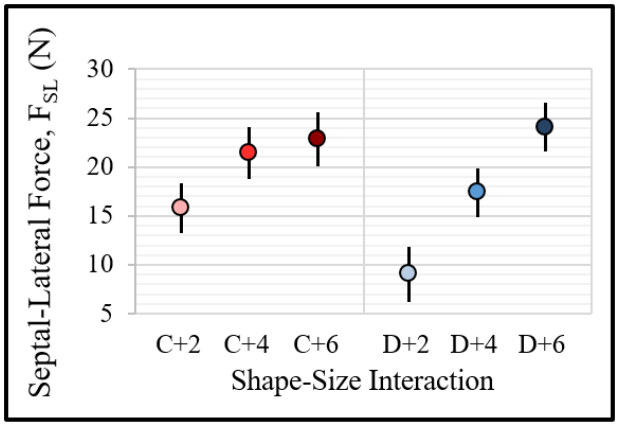

Figure 7-20 F_{SL} results in terms of mean ± 95% CI for each shape-size combination (after GLM 4). Within each plot, pairs whose 95% CIs do not overlap differ significantly ($p<0.05$). The D-shape was more sensitive to degree of oversizing than was the circular shape.

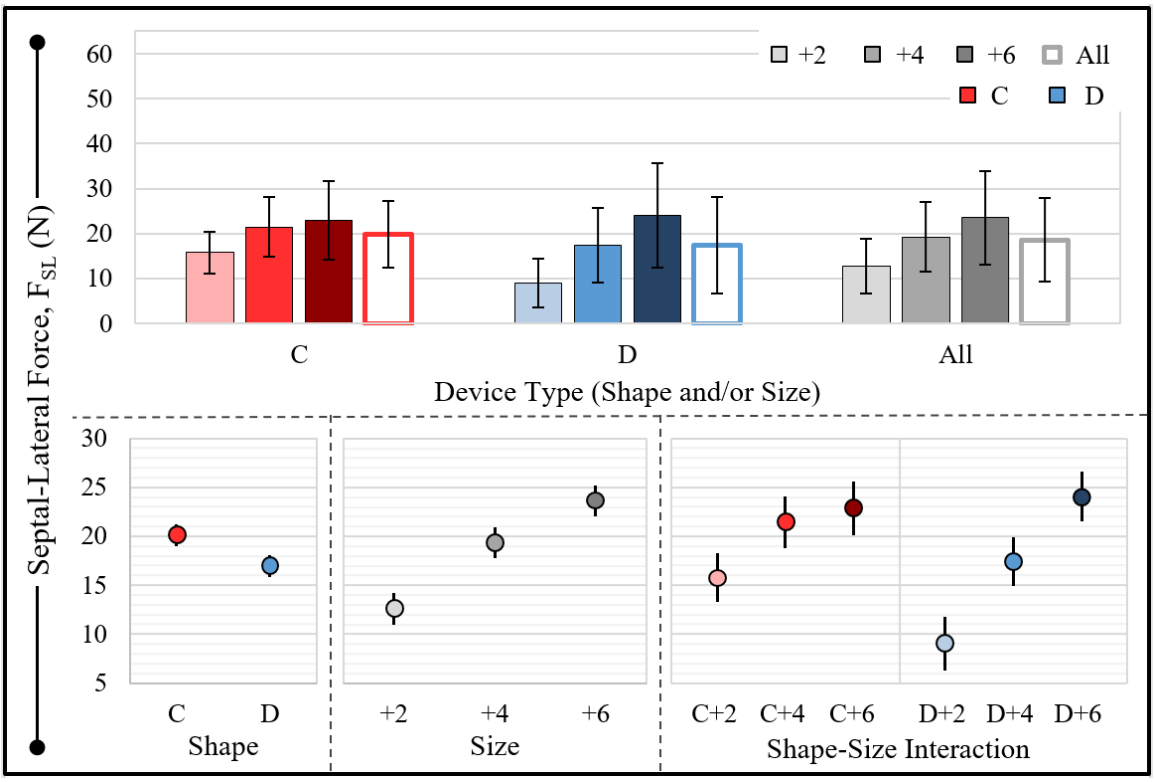

Figure 7-21 F_{SL} results, duplicated from Figure 7-17 through Figure 7-20. Top: mean ± SD for each expansion geometry (included: individual geometries, binned by shape, binned by size, and all shapes/sizes). Bottom: mean ± 95% CI for each shape, size, or shape-size combination (after GLM 4). Within each plot, pairs whose 95% CIs do not overlap differ significantly ($p<0.05$). Size was a stronger effector of F_{SL} than shape.

The global mean ± SD for F_{SL} was 18.6 ± 9.4 N. Averaged across all sizes, 13.9% more F_{SL} was required using the C-REFT versus the D-REFT (19.8 ± 7.4 vs. 17.4 ± 10.8 N, respectively; $p=0.002$). Averaged across shapes, increase in oversizing from +2 to +4, or from +4 to +6, required a 51.3% or 22.1% increase in F_{SL}, respectively (+2 vs. +4 vs. +6: 12.7 ± 6.0 vs. 19.3 ± 7.8 vs. 23.5 ± 10.4 N, respectively; each pair $p\leq0.001$).

The effects of sizing on F_{SL} were driven mostly by the D-REFT: whereas the C-REFT required 44.7% more F_{SL} to expand to +6 versus +2, the D-REFT required 166.6%

more F_{SL} to do the same. Whereas every pair of sizes within the D-REFT differed significantly in required F_{SL} (each $p<0.001$), no significant difference was detected between C+4 and C+6 (21.4 ± 6.6 vs. 22.8 ± 8.7 N, respectively; $p=0.964$). Also of note, significantly more F_{SL} was required to establish the C+2 geometry than D+2 (15.8 ± 4.7 vs. 9.0 ± 5.4 N, $p=0.002$).

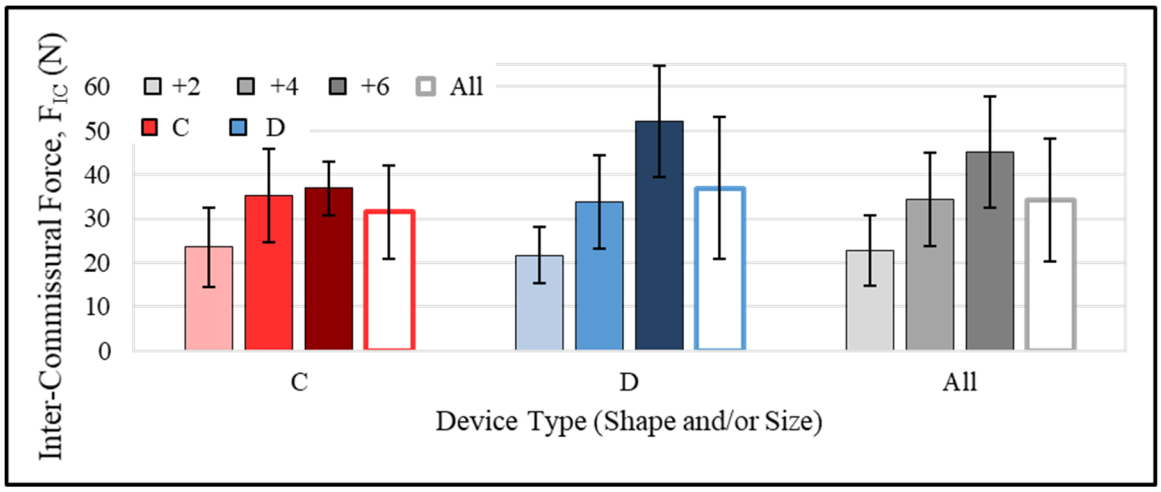

Figure 7-22 F_{IC} results in terms of mean ± SD for each expansion geometry (included: individual geometries, binned by shape, binned by size, and all shapes/sizes). Although trends are apparent, statistical significance of these trends cannot be assessed until after GLM 4 (see Figure 7-23 through Figure 7-25).

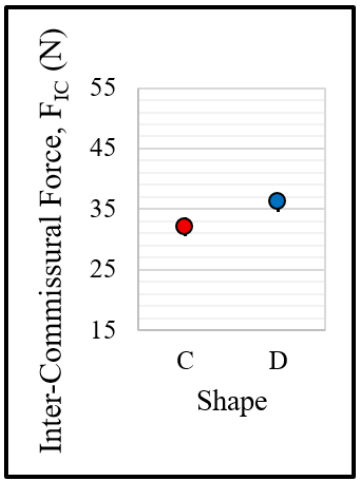

Figure 7-23 F_{IC} results in terms of mean ± 95% CI using either shape (after GLM 4). Within each plot, pairs whose 95% CIs do not overlap differ significantly ($p<0.05$). The D-shape led to a significant increase in F_{IC}.

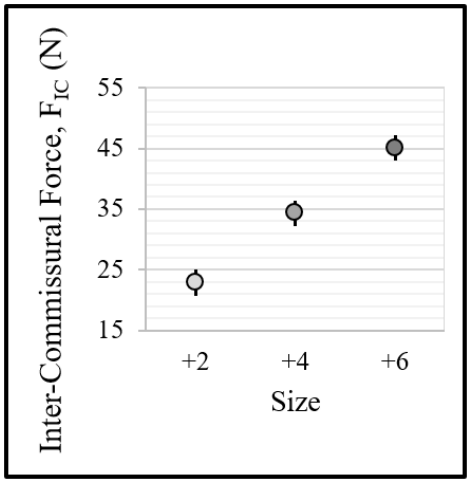

Figure 7-24 F_{IC} results in terms of mean ± 95% CI for each level of annular oversizing (after GLM 4). Within each plot, pairs whose 95% CIs do not overlap differ significantly ($p<0.05$). Each increase in oversizing significantly increased F_{IC}.

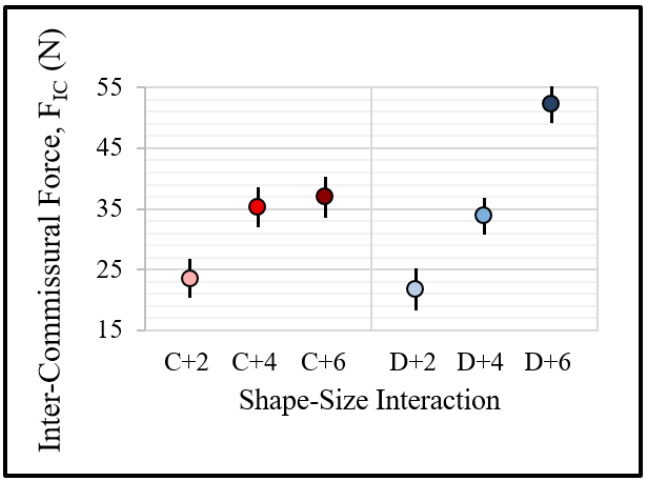

Figure 7-25 F_{IC} results in terms of mean ± 95% CI for each shape-size combination (after GLM 4). Within each plot, pairs whose 95% CIs do not overlap differ significantly ($p<0.05$). The D-shape was more sensitive to degree of oversizing than was the circular shape.

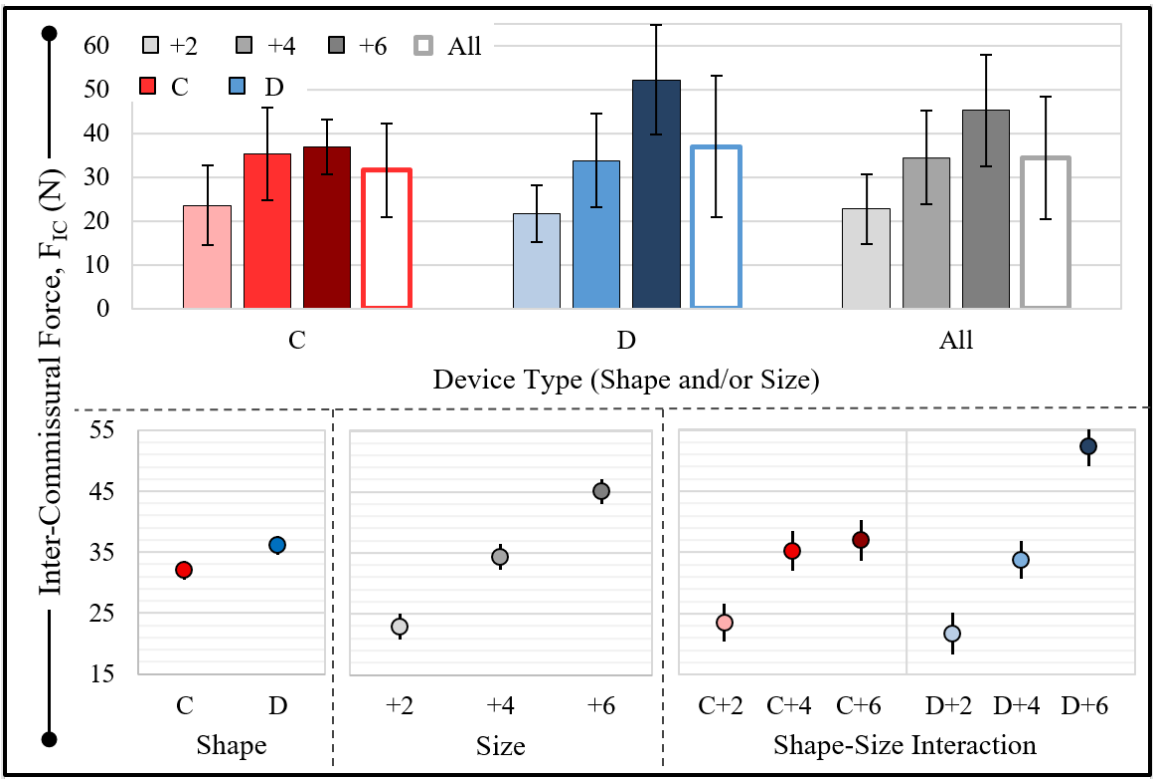

Figure 7-26 F_{IC} results, duplicated from Figure 7-22 through Figure 7-25. Top: mean ± SD for each expansion geometry (included: individual geometries, binned by shape, binned by size, and all shapes/sizes). Bottom: mean ± 95% CI for each shape, size, or shape-size combination (after GLM 4). Within each plot, pairs whose 95% CIs do not overlap differ significantly ($p<0.05$). Size was a stronger effector of F_{IC} than shape.

The global mean ± SD for F_{IC} was 34.3 ± 14.0 N. Averaged across all sizes, 14.6% less F_{IC} was required using the C-REFT versus the D-REFT (31.5 ± 14.0 vs. 36.9 ± 16.2 N, respectively; $p=0.002$). Averaged across shapes, increase in oversizing from +2 to +4, or from +4 to +6, required a 51.8% or 31.3% increase in F_{IC}, respectively (+2 vs. +4 vs. +6: 22.7 ± 8.0 vs. 34.5 ± 10.6 vs. 45.2 ± 12.7 N, respectively; each pair $p\leq0.001$).

Similarly to F_{SL}, the effects of sizing on F_{IC} were driven mostly by the D-REFT: whereas the C-REFT required 56.8% more F_{IC} to expand to +6 versus +2, the D-REFT

required 140.6% more F_{IC} to do the same. Whereas every pair of sizes within the D-REFT differed significantly in required F_{IC} (each $p<0.001$), no significant difference was detected between C+4 and C+6 (35.2 ± 10.5 vs. 36.9 ± 6.2 N, respectively; $p=0.969$). Also of note, significantly less F_{IC} was required to establish the C+6 geometry than D+6 (36.9 ± 6.2 vs. 52.2 ± 12.6 N, $p<0.001$).

Although the F_{IC} trends closely mirrored those of F_{SL}, it was noted that F_{IC} was consistently and substantially larger than F_{SL}. Indeed, the ratio of the mean F_{IC} to the mean F_{SL} for each tested heart ranged from 0.94-3.26, and exceeded 1.00 for 11 of 12 hearts. To quantify force eccentricity, the ratio F_{IC}/F_{SL} was investigated. For the purposes of GLM 4, the square root of this ratio was used to satisfy the GLM assumption of normally distributed residuals.

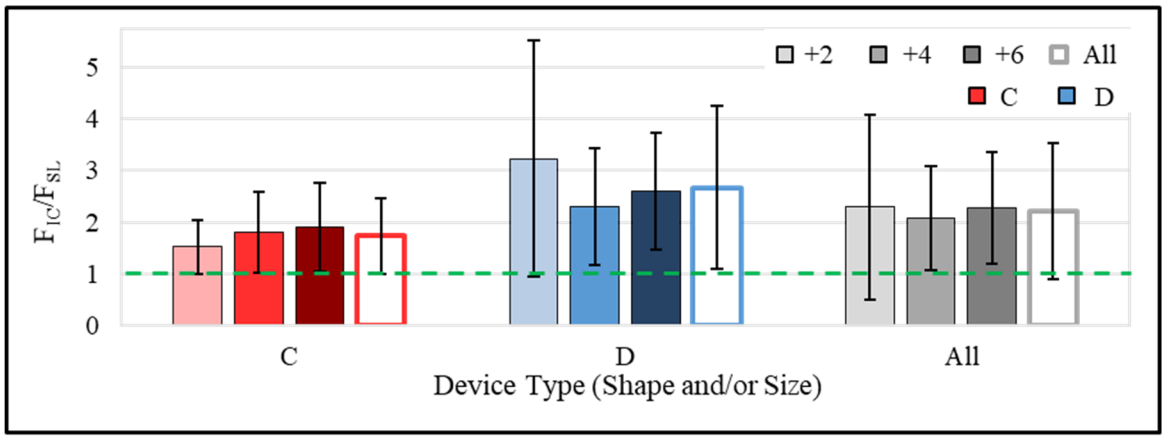

Figure 7-27 Force eccentricity for each expansion geometry, expressed as mean ± SD for F_{IC}/F_{SL} (included: individual geometries, binned by shape, binned by size, and all shapes/sizes). Green line: $F_{SL}=F_{IC}$. Although trends are apparent, statistical significance of these trends cannot be assessed until after GLM 4 (see Figure 7-28 through Figure 7-30).

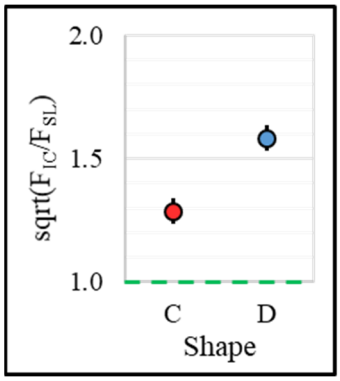

Figure 7-28 Force eccentricity for each shape, expressed as mean ± 95% CI for sqrt(F_{IC}/F_{SL}) (after GLM 4). Within each plot, pairs whose 95% CIs do not overlap differ significantly ($p<0.05$). Green line: $F_{SL}=F_{IC}$. Forces were eccentric for each shape (i.e., the 95% Cis did not intersect 1.0); eccentricity was significantly greater using the D-shaped profile.

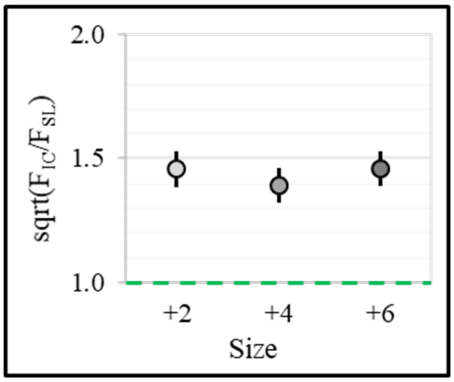

Figure 7-29 Force eccentricity for each size, expressed as mean ± 95% CI for sqrt(F_{IC}/F_{SL}) (after GLM 4). Within each plot, pairs whose 95% CIs do not overlap differ significantly ($p<0.05$). Green line: $F_{SL}=F_{IC}$. Size was not found to have any effect on force eccentricity.

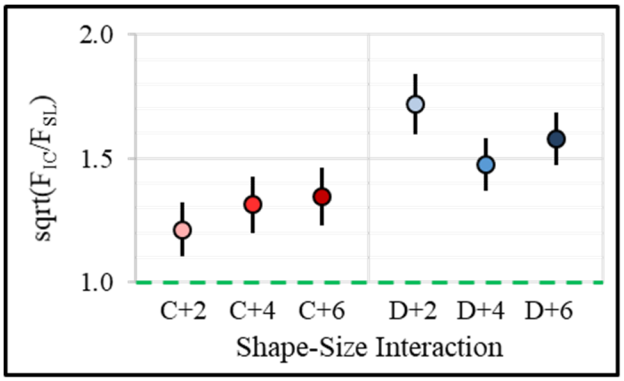

Figure 7-30 Force eccentricity for each shape-size combination, expressed as mean ± 95% CI for sqrt(F_{IC}/F_{SL}) (after GLM 4). Within each plot, pairs whose 95% CIs do not overlap differ significantly ($p<0.05$). Green line: $F_{SL}=F_{IC}$. All shape-size combinations had 95% CI not intersecting 1.0; D+2 was significantly greater than D+4.

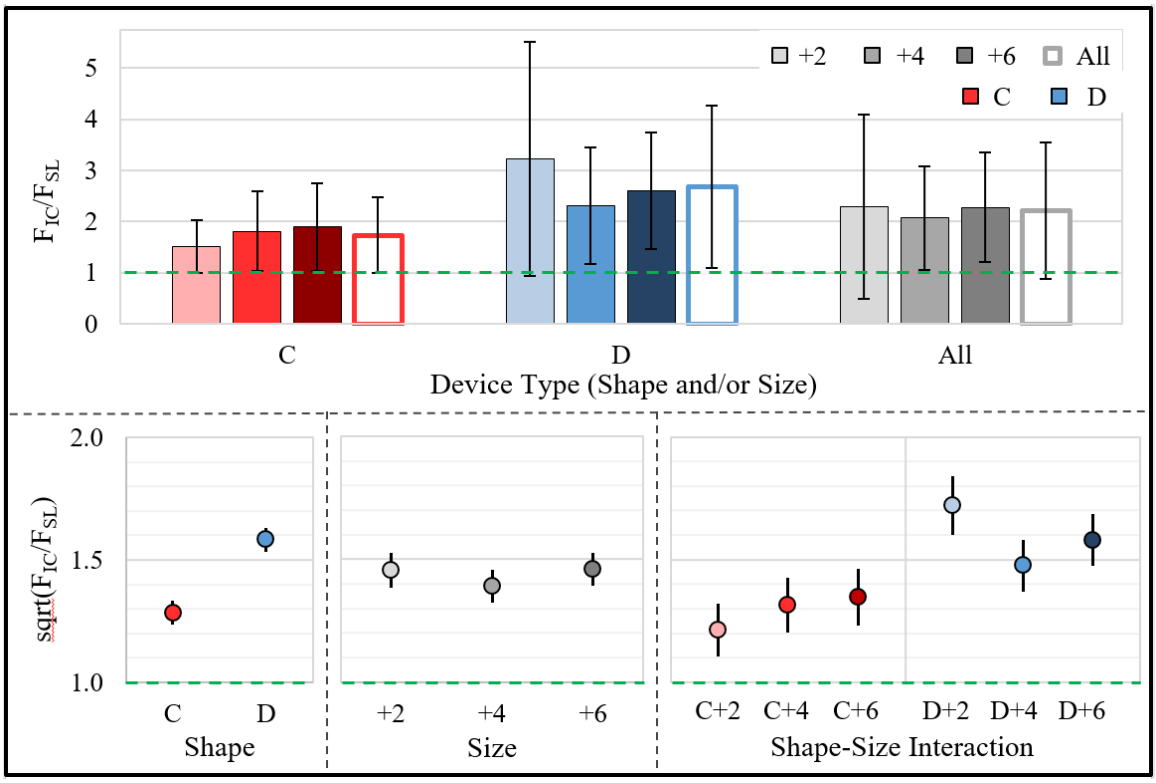

Figure 7-31 Graphs duplicated from Figure 7-27 through Figure 7-30. Top: force eccentricity results for each expansion geometry, expressed as mean ± SD for

F_{IC}/F_{SL} (included: individual geometries, binned by shape, binned by size, and all shapes/sizes). Bottom: force eccentricity results for each shape, size, or shape-size combination, expressed as mean ± 95% CI for sqrt(F_{IC}/F_{SL}) (after GLM 4). Within each plot, pairs whose 95% CIs do not overlap differ significantly ($p<0.05$). Green line: $F_{SL}=F_{IC}$.

The global mean ± SD for F_{IC}/F_{SL} was 2.21 ± 1.33. Averaged across all sizes, F_{IC}/F_{SL} was 35.3% lower using the C-REFT versus the D-REFT (1.73 ± 0.74 vs. 2.67 ± 1.59, respectively; $p<0.001$ based on sqrt(F_{IC}/F_{SL})). Averaged across shapes, no significant differences were detected based on the degree of oversizing.

When investigating shape-size interaction, two findings were notable. First, each geometry exhibited a 95% CI entirely above 1, implying the observed force eccentricity was significant for each. Second, the D+2 geometry was notable, in that it had the greatest force eccentricity (3.23 ± 2.29), which significantly exceeded that of D+4 (2.30 ± 1.14; $p=0.014$ based on sqrt(F_{IC}/F_{SL})). However, D+2 also exhibited greater than double the standard deviation in F_{IC}/F_{SL} versus every other geometry, suggesting some risk of a false positive in this comparison.

7.2.2.3 Micro-Computed Tomography of Left Ventricle

Following the observation that mean F_{IC} exceeded mean F_{SL} for both device shapes, for all device sizes, and in 11 of 12 hearts, a subsequent analysis of the porcine heart anatomy was conducted. The investigation sought to assess the approximate amount of tissue being displaced by a radially expanding TMV. A micro-computed tomography scan was

performed, using a lightly pressurized balloon to hold the aorta open and the anterior leaflet away from the ventricular septum. A series of high-contrast markers were applied to the mitral annulus to guide image processing.

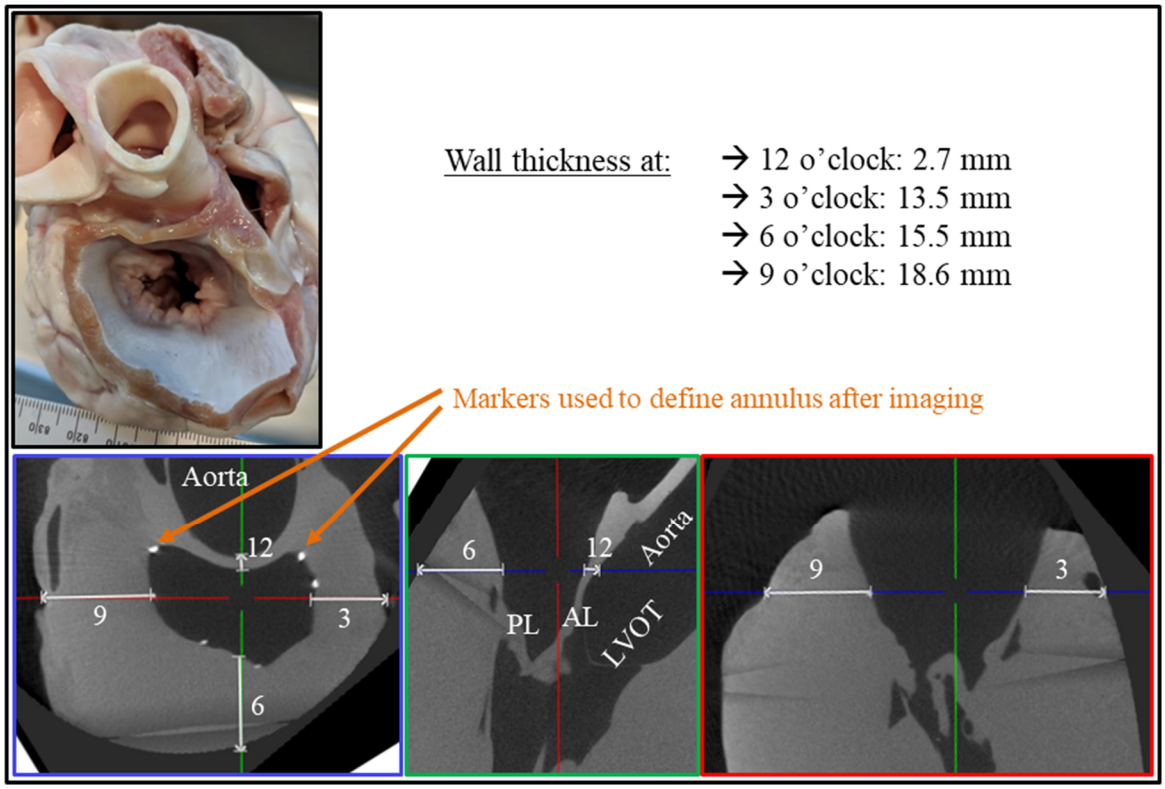

Figure 7-32 Investigation of tissue thickness in the vicinity of the mitral annulus of a porcine heart. Top: photograph of heart. Bottom: multi-planar reconstruction of heart, obtained by micro-computed tomography. Blue border: annulus mid-plane. Green border: septal-lateral mid-plane. Red border: inter-commissural mid-plane. LVOT: left ventricular outflow tract.

It is evident from Figure 7-32 that the amount of tissue opposing a radially expanding TMVR varies circumferentially. Along the annulus mid-plane, the wall thicknesses at 3, 6, or 9 o'clock (13.5 mm or more) were each at least five-fold greater than was the wall thickness at 12 o'clock (2.7 mm). Further, it appeared that the basal ventricular

myocardium (i.e., the tissue immediately inferior to the annulus mid-plane) was thicker still than that of the annular mid-plane, for all positions except 12 o'clock. At 12 o'clock, there is no myocardium inferior to the annulus mid-plane, but rather, the left ventricular outflow tract.

7.3 Specific Aim 2 Discussion

7.3.1 Specific Aim 2.A: Parametric Evaluation of TMV Design and PVL

Although the potential for PVL post-TMVR has been demonstrated through early clinical experience,[26-30] its eventual incidence upon wider use of TMVR remains to be determined. However, it is clear that PVL is (a) lethal in the TAVR setting, even when mild,[31] (b) deadlier at the mitral than at the aortic position,[32] (c) likely far more challenging to prevent in the TMVR setting than the TAVR setting, due to numerous biomechanical disadvantages,[12-14] (d) difficult to diagnose, especially when mild or moderate,[33] and (e) especially difficult to treat in surgically inoperable patients.[34, 35] In light of the wide diversity of TMV designs currently under development, and the paucity of existing engineering data in this scenario, SA 2.A sought to develop and employ a test system to evaluate PVL rates as a function of simple parametric TMV models.

The *ex vivo* test system, which utilized fresh, whole porcine hearts, was developed and implemented successfully. Trans-mitral pressure gradients as high as 215 mmHg could be easily established in the absence of mitral leak. As more PVL was introduced, the maximum possible gradient dropped, yet even in the presence of PVL over 70 ml/sec, ΔP

values above 160 mmHg were attained. **Thus, it was routinely feasible to measure PVL at or near the five targeted trans-mitral ΔP values: 60, 90, 120, 150, and 180 mmHg.** Based on ISO guideline 5840-3 for the testing of transcatheter heart valves,[112] 60, 120, 150, and 180 mmHg represented peak ΔP for hypotensive, normotensive, or mildly/moderately hypertensive, and severely hypertensive patients, respectively.

For all 8 mock TMV plugs, the relationship between ΔP and PVL was empirically determined to obey an approximately quadratic relationship (Figure 7-2, Figure 7-3, Figure 7-4). This relationship can be understood from a physical standpoint by considering the leakage flowrate, Q, as the product of velocity, v, and cross-sectional area, A, then considering the relationships between ΔP and either v or A. The Bernoulli equation states that, within the assumptions of laminar and inviscid flow along a streamline, v is proportional to sqrt(ΔP). Meanwhile, it can be expected that any increase in ΔP (which was achieved by increasing LVP) would increase the force being applied normal to the wall(s) of the leakage gap(s). This force would likely push the soft tissue outward, thereby increasing A.

Thus, increasing ΔP should induce *both* an increase in v and an increase in A. To understand whether these effects are indeed sufficient to generate a quadratic relationship between ΔP and Q, it is helpful to investigate the amount by which the gap dimensions would need to change to cause what was observed experimentally. This question depends on the specific gap shape(s), which is unknown, but a conservative range can be bounded as follows. Consider the following Scenario 1, in which all leakage emanates from a single circular orifice at an arbitrary position along the annular circumference. On the other

extreme, consider Scenario 2, in which leakage emanates uniformly from around the entire annular circumference:

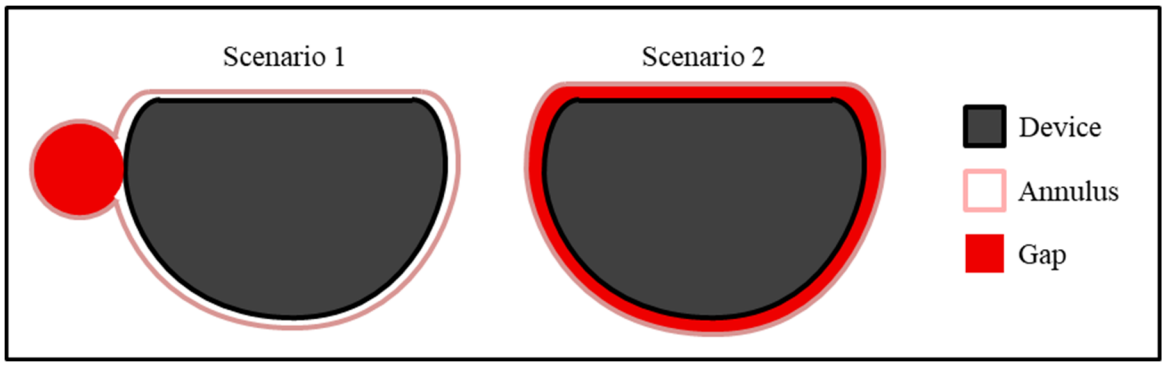

Figure 7-33 Schematic depiction of two bounding scenarios describing the theoretical location/form of PVL gaps. In Scenario 1, all leakage emanates from a single circular orifice at an arbitrary position along the annular circumference. In Scenario 2, leakage emanates uniformly from around the entire annular circumference.

In Scenario 1, leakage flow may be approximated by Poiseuille's Law for flow through a circular pipe:

$$r = \left(\frac{8\mu LQ}{\pi(\Delta P)}\right)^{\frac{1}{4}} \tag{7}$$

Here, we assume dynamic viscosity (of water at 37 °C), μ, is 0.0007 Pa*s, and leakage gap length, L, is 0.01 m.

The radius, r, can then be calculated based on (ΔP, Q) pairs obtained from empirical data. Based on Figure 7-4, we utilize the representative values of (60 mmHg, 15 ml/sec), (120 mmHg, 45 ml/sec), and (180 mmHg, 90 ml/sec). Respectively, these correspond to

radii of 6.7, 7.4, and 8.0 mm. In Scenario 2, we can approximate the gap width by assuming an equivalent total leakage gap area to that in Scenario 1, and dividing the area by the device perimeter. The gap width would be smallest in the case of a +6 device, having perimeter 131.6 mm. For the same three (ΔP, Q) pairs analyzed in Scenario 1, Scenario 2 would have gap widths of 1.1, 1.3, and 1.5 mm. So, when ΔP increased from 60 to 180 mmHg, the gap's diameter (Scenario 1) or thickness (Scenario 2) would have needed to increase by approximately 0.4-2.6 mm, depending on gap shape. The findings of SA 2.B shed further light on the *likelihood* that a 120 mmHg pressure increase would cause such expansion of the annulus. This is discussed further in Section 7.3.3. Provided that this tissue response is indeed plausible, this analysis demonstrates that the observed quadratic relationship between ΔP and PVL very likely derived from the combined effects of increasing velocity (per the Bernoulli equation) and increasing gap area.

As evident from Figure 7-3, even when holding device shape and size constant, the pressure-leakage curves varied substantially among hearts. Some portion of this variability can be attributed to procedure, as the TMV plug was positioned manually. This was partially compensated for through the use of a strict positioning protocol and repeated acquisitions within each heart. The remaining variability could be attributed to variation between hearts. Despite the careful heart selection process according key annular dimensions, some variability in these dimensions, and in other metrics such as ventricular mass, leaflet size, and tissue properties, was inevitable.

The range of measured leakage rates is noteworthy. Figure 7-3 reveals that even in the worst-sealing instances, leakage at 60, 90 120, 150, or 180 mmHg were approximately 15, 25, 45, 60, or 90 ml/sec, respectively. Given a normal systolic period of approximately

0.3 sec, all of these instances would likely translate to mild MR (per the American Heart Association's threshold for moderate MR of 30 ml/beat[164]). Under different circumstances, an upward shift in all PVL rates might be expected. Device positioning included a final step of carefully angulating it to maximize the initial ΔP (see Section 5.2.6.1). Further, the healthy porcine hearts possessed thick myocardium, which likely offered greater radial resistive force than would exist in frail/diseased hearts. These procedural and anatomic factors likely enhanced sealing.

The specific TMV parameters modeled in this work were stent shape (circular versus D-shaped) and size (+0, +2, +4, and +6 mm oversizing, relative to the native annulus' inter-trigonal distance). Significant differences in leakage were detected among mock TMV plug shapes and sizes. **Irrespective of pressure level, or of specific statistical method used, D-shaped plugs exhibited significantly reduced leakage** (for example, at 120 mmHg, circular plugs leaked 51.2% more than D-shaped plugs)**.** The superiority of the D-shaped devices was expected, as they more closely conformed to the shape of the native annulus. However, based on the data from SA 2.A alone, it remains unclear which of two potential mechanisms actually explain this phenomenon. It is plausible that this greater congruence equates to more uniform radial force when expanding a D-shaped device, rather than a circular device, into the annulus. Alternatively, it may be the case that a large proportion of TMV sealing fundamentally derives from stent-*leaflet* contact. The exception to this scenario would be near the commissures, where little-to-no leaflet tissue exists, and sealing must derive from stent-*annulus* contact. In this scenario, it would be plausible that the D-shape's advantage derives merely from greater radial force near the commissures. SA 2.B offered further insights to this question, as discussed in the next sections.

Oversizing effects were also largely consistent across analysis methods. **Oversizing led to no significant benefit until reaching +6 mm in inter-trigonal distance (23.2 mm in perimeter)**. For example, at 120 mmHg, the worst sealing oversizing level (+2) leaked 50.5% more than the +6 level. This may reflect the degree of oversizing necessary for the stents to adequately contact the commissural annular tissue. Alternatively, it may be a consequence of plastic stretch occurring within the myocardium during the experiment. Potential for tissue fatigue is a noted limitation of *ex vivo* whole heart testing, and is discussed further in Section 7.3.5.

TMV designers must make decisions about both outer profile shape and intended approach for annular oversizing. A circular TMV is likely the simplest to develop, and is the most robust with regards to rotational orientation during implantation. Yet, circular designs may be expected to encounter greater PVL, as observed in the present study. Therefore, one relevant question is whether the potential trade-offs of a circular shape in terms of PVL can be compensated for through greater oversizing. In the present work, D-shaped devices reduced mean normalized leakage by 12.7% versus average. C+0, C+2, and C+4 each *increased* mean normalized leakage by at least 8.7% versus average. C+6 reduced normalized leakage by 2.0% versus average. Thus, within the limitations of the test system used here, even though the D-shaped plugs offered uniformly better sealing, the discrepancy was reduced by approximately half when C+6 was used. It is likely that +0 through +4 circular devices were ineffective in establishing effective contact with the commissural regions of the annulus. This is depicted schematically in Figure 7-34.

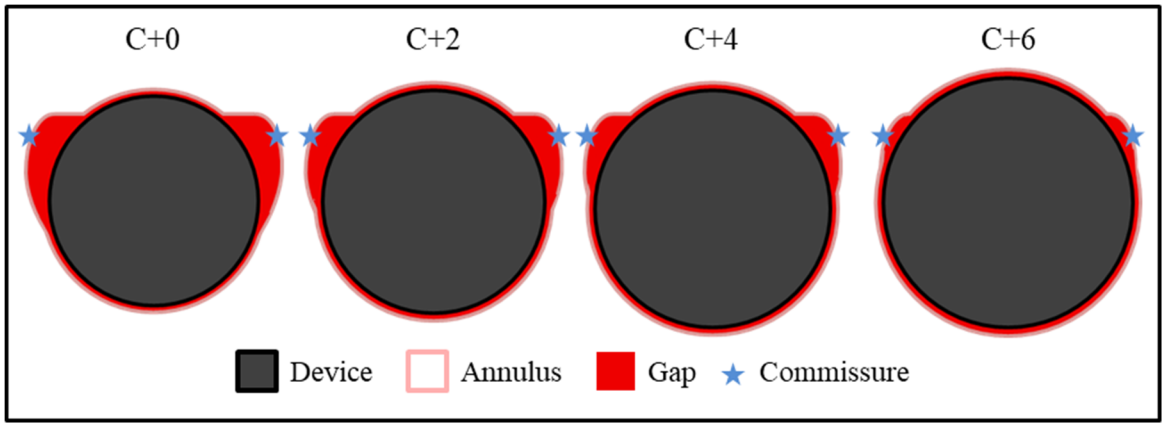

Figure 7-34 Illustration of a potential explanation for the finding that, although circular devices leaked more than D-shaped devices, the discrepancy was meaningfully reduced with use of C+6. At C+0 through C+4, the circular profile may fail to engage the commissural annulus, where the leaflets offer little contribution to sealing. The D-shaped profile more easily reaches the commissural annulus, at every size.

7.3.2 Specific Aim 2.B: Parametric Evaluation of TMV Design and Radial Expansion Force

For any given TMV design, there exists some range of operating conditions that favor optimal performance. Two such conditions are its final shape and degree of oversizing (relative to the native annulus). Thus, the TMV stent's fundamental design can be meaningfully informed by an understanding of the annular resistive forces it must overcome to achieve a target shape/size post-deployment. The Circular and D-shaped Radial Expansion Force Transducers (C-REFT and D-REFT) were developed for this purpose, with the goal to quantification of the resistive forces imparted by the porcine mitral annulus as the REFT arms extended radially along defined paths. Forces were quantified simultaneously along the septal-lateral and inter-commissural axes (F_{SL} and

F_{IC}), for either circular or D-shaped TMV profiles, each over a range of oversizing levels. Each device was designed, manufactured, calibrated, and implemented successfully.

REFT performance fell within an acceptable range: signal drift was minimal, sensitivity was 0.1 N (0.38% of the mean recorded force), and theoretical worst-case uncertainty of 5.4%. REFTs were tested in rigored hearts, to mimic the geometry and material properties of the systolic, contracted state,[120, 121] and thus to model the *peak* annular forces the TMV will encounter in the beating heart in a simple, inexpensive manner.

Previous studies have reported select forces associated with novel TMV stent designs. For example, in Young et al's report on a 19 mm tall "winged" stent design, a computational simulation found that 36.0 N radial force was required to fully expand a $1/12^{th}$ segment of the stent from its crimped state.[141] More recently, Loger et al measured the force required to embolize stents of various designs after their fixation in the porcine annulus (finding an average of 23.4 N for D-shaped varieties or 27.7 N for oval varieties).[165] However, to our knowledge, this is the first study to measure the radial forces necessary to deploy an oversized TMV or TMV-like device in the mitral annulus. The closest parallel comes from Siefert et al,[107] who investigated *in vivo* the septal-lateral and inter-commissural forces associated with cardiac contraction. A rigid, D-shaped transducer was surgically affixed to the mitral annulus, in normal ovine subjects (implanted in the flaccid, cardioplegic heart). For the sake of comparison, it may be roughly considered to have oversized the systolic annulus to diastolic dimensions. Siefert et al reported a *peak* cyclic contractile force of 9.2 N (septal-lateral). Using the REFTs, the mean recorded

expansion force across all samples was 24.4 N, and the highest mean within any one configuration was 52.2 N ($F_{IC,}$ using D+6).

Three main factors likely contributed to the present study's higher forces. First, the *in vivo* transducer's pads were under 3 mm in height, versus a REFT arm pad height of 20 mm. Second, the porcine left ventricle is substantially greater in mass and wall thickness than the ovine left ventricle. Third, the normal ovine mitral annulus has been reported to contract approximately 12% by area throughout the cardiac cycle;[46] the +6 profile tested here was 47% larger by area than the +0 profile. Thus, **the relatively high force observed here likely derived from displacing a taller section of annular tissue, having greater wall thickness, by a greater distance, as compared to the prior work from Siefert et al**.[107]

Two other notable findings using the REFTs agreed with expectations. Fundamental mechanics suggests that greater radial expansion could only be achieved via greater applied radial force. Thus, the finding that both F_{SL} and F_{IC} scaled positively with degree of oversizing was expected. Similarly, the finding that the C-REFT required greater mean F_{SL} and less F_{IC} than the D-REFT, was expected. This is because, whereas with each oversizing step the circular profile expanded 2.46 mm along either axis, the D-shaped profile expanded 2.05 mm in the septal-lateral direction and 2.68 mm in the inter-commissural direction (Table 5-2).

Other findings were not expected. **Across all shapes and sizes, the force eccentricity, F_{IC}/F_{SL}, was 2.21 ± 1.33. This represents a deviation from other aspects of annular mechanics.** For example, Siefert et al's *in vivo* transducer found lower

contractile forces on IC axis than the SL axis.[107] Gunning et al reported the anterior quadrant of the annulus (which sits along the SL axis) to possess the greatest circumferential stiffness.[43] SA 1 of this thesis found the anterior annulus to possess the greatest suture holding strength. The fact that SA 2.B observed greater force was needed to expand along the IC axis likely owes to the unique geometry under investigation in this scenario. Each of the aforementioned studies investigated phenomena within a few millimeters in height and/or depth of the leaflet hinge line. The REFT, meanwhile, applied force against a 20 mm tall ring of tissue, centered along the leaflet hinge line. Further, it functioned by radially displacing the entire thickness of the tissue emanating outward from its contact surface.

In the annular plane of a representative porcine heart, the tissue's radial thickness was at least five-fold greater at 3, 6, and 9 o'clock than at 12 o'clock (Figure 7-32). Sub-annularly, the basal ventricular myocardium at 3-9 o'clock thickened even further, while at 12 o'clock only the anterior leaflet was present. On the contrary, expansion of the REFT's 12 o'clock arm was further resisted by 120 mmHg aortic pressure. Yet, given the pad's total contact area of 474 mm^2, this pressure would impart a theoretical maximum of 7.6 N resistive force (whereas even at +2 oversizing, mean F_{IC} was 22.7 N). Altogether, this analysis reveals that **the septal-lateral arms encountered far less resistance to expansion than did the inter-commissural arms, due to fundamental anatomic differences in the tissue region *surrounding* the region traditionally referred to as the "annulus," namely the basal myocardium.** Any TMV stent having a significant sub-annular portion may encounter similar dynamics. This includes many of the leading TMVs currently in clinical trials, such as Intrepid (Medtronic, Dublin, Ireland), Tendyne (Abbott

Laboratories, Chicago, IL) and Tiara (Neovasc, Richmond, Canada), as well as earlier stage stent concepts reported in literature, such as those from Young et al[141], Meredith et al,[166] or Loger et al.[165] Effective stent design to achieve targeted levels of "annular" oversizing likely must account for the observed dynamics of this broader tissue region.

Also unexpectedly, significantly greater eccentricity was observed between F_{SL} and F_{IC} with use of the D-REFT. The opposite was anticipated, on account of the D-shape conforming more closely to the native annular profile. This finding results from two of the aforementioned phenomena. As expected, the D-shape elevated F_{IC} and reduced F_{SL} relative to the circular shape. However, whereas this was expected to bring these orthogonal forces in closer proximity to one another, because the F_{IC} unexpectedly exceeded F_{SL} even with the circular shape, it instead drove them further apart.

A final noteworthy finding was the D-REFT's heightened sensitivity to sizing. The C-REFT required 45% greater F_{SL} and 57% greater F_{IC} to achieve +6 oversizing than +2; the D-REFT required 167% greater F_{SL} and 140% greater F_{IC} to do the same. As the two devices expanded in a perimeter-matched fashion, the D-shape required significantly less F_{SL} to oversize to +2, but required significantly more F_{IC} to oversize to +6. We hypothesize that, for +2 oversizing, the D-REFT required less force simply because it did less to distort the annulus from its nominal geometry. But, at progressively larger perimeters, the D-shape also expanded more quickly in the IC direction than did the circular shape. This effect apparently predominated at +6, where the D_{IC} was 3.64 mm greater in the D-shaped profile than the circular profile (Table 5-2).

7.3.3 Integrated Specific Aim 2 Discussion

SA 2 was successful in developing two *ex vivo* test systems (a steady back-pressure system for PVL quantification, and a radial expansion force transducer) to describe pre-clinically and clinically relevant aspects of TMV-annulus interaction. First, complex dynamics were revealed in terms of the distinct influence of TMV shape, TMV size, and trans-mitral ΔP on PVL rates. Circular devices exhibited significantly greater leakage than D-shaped devices. Oversizing reduced leakage, as expected, but the effect was not significant until the final size level (+6 mm in inter-trigonal distance, or 23.2 mm in perimeter) was reached. For every device type, PVL exhibited a strong, quadratic relationship to ΔP.

Subsequently, further dynamics were revealed in terms of the influence of TMV shape and size on the force necessary to expand radially against the annulus. As expected, expanding the D-shaped profile required more force along the inter-commissural annulus, but less on the septal-lateral axis, versus the circular profile. Interestingly, over 2 times more force was necessary to expand along the inter-commissural axis versus the septal-lateral axis, across all observations.

After analyzing the PVL findings, two key questions remained, which were further informed by the radial expansion force data. The first question regarded whether increasing trans-mitral ΔP from 60 to 180 mmHg (an increase of 120 mmHg) could press the soft tissue boundary of the leakage gap radially outward by a sufficient amount to explain the quadratic relationship that was observed between ΔP and PVL. Analysis of the relevant physics suggested that the tissue would need to displace radially by between 0.4-2.6 mm

(depending on the precise gap shape, which remains unknown). The REFT sheds light on this question. It was found that, for the D-REFT to expand by 2.0 mm along the SL axis, 9.0 N force was required on average. For the C-REFT to expand by 2.5 mm along the IC axis, 23.5 N force was required on average. Given the area of two annular contacting pads was 948 mm^2, these values equate to required *pressure* of 71.2-185.9 mmHg. It is therefore plausible that a 120 mmHg increase in ΔP could enlarge the gap area by 0.4-2.6 mm. In conclusion, the notion that the quadratic relationship between ΔP and PVL derives from a combination of increasing fluid velocity and increasing gap area is well-supported.

The second remaining question after the PVL study regarded the underlying reason why the D-shape offered such a sizable sealing advantage. Was this because the D-shaped device applied force more uniformly along the annular circumference? Or, is it possible that TMV sealing derives largely from stent contact with the native *leaflets*, and thus at the commissures, where little-to-no leaflet tissue exists, the D-shape gains advantage by establishing greater contact with the annulus? Viewing the findings from both sub-aims simultaneously, an answer becomes apparent. It is notable that the forces were significantly *less* uniform for the D-REFT than the C-REFT. It is also notable that, whereas radial forces were much more greatly influenced by size than shape, PVL depended slightly more on shape.

For devices such as the mock TMV plugs tested here, whose sealing is generated purely by contact between the tissue and a straight tubular section, these facts suggest that radial force is *not* the primary determinant of sealing. In turn, they imply that the D-shape's benefit for PVL indeed derives from the ability to better reach the commissural regions of the annulus, where leaflet tissue is scarce. The notion that leaflet tissue plays a central role

in TMV sealing supports the notion of fabric covering the TMV stent through the entire region of potential leaflet contact. Such is the case in most reported TMV designs,[15] but *not* in Edwards Lifesciences' Sapien, whose off-label use at the mitral position is of growing interest.[84] The notion that expanding with more uniform force against the annulus is less effective way to improve sealing than merely expanding in the optimal position is profound and potentially impactful. This may indicate stent flexibility as a critical, as-yet-unexplored variable to optimize sealing performance. Although specific stiffness data for leading TMV stent designs is not publicly available, some designs, such as Medtronic's Intrepid, emphasize optimized stiffness to improve anchoring and sealing.[27]

7.3.4 Clinical and Engineering Implications

Among the wide range of TMVR systems currently in development, none has yet achieved regulatory approval for market use. Two critical challenges in the advancement of these systems are the lack of available mechanical data describing relationships between TMV design parameters and performance, and the lack of consensus on best practices for TMV testing. By developing and employing novel benchtop systems for the assessment of PVL rates and radial expansion forces as functions of TMV stent shape and size, the present study has attempted to address both of these challenges.

Some TMVR systems have recently reported initial promise.[167] For example, Tendyne reported positive outcomes in a 30 patient cohort, with only one patient exhibiting significant PVL.[168] Clinical trials for Intrepid and Tiara are also currently recruiting, with estimated enrollment of 115 and 1380 patients, respectively (www.clinicaltrials.gov).

These mark meaningful milestones toward the goal of bringing TMVR to market. However, it is important to note the carefully selected patients in these trials. Muller et al emphasize that the 30 patients receiving Tendyne "were selected to maximize the likelihood of procedural success."[168] The Intrepid and Tiara trials include "anatomic contraindications" and "unsuitable cardiac structures," respectively, as patient exclusion criteria. Thus, despite positive early clinical data, it remains uncertain at present what aspects of TMV design will prove effective amidst the anatomic variability of the larger MR population. In the present work, using an *ex vivo* system featuring porcine hearts whose annular dimensions were carefully selected, SA 2.A found substantial sealing variability *within* each mock TMV plug design (Figure 7-3), owing largely to anatomic factors. This finding clearly emphasizes that the conclusions drawn from such early, limited patient populations should remain conservative. TMVR performance is likely to vary widely upon broader clinical use.

Despite the variability encountered in PVL rates between hearts, a decisive advantage in annular sealing was found using a rigid D-shaped design versus a rigid circular design. It was further shown that the performance discrepancy between shapes could be reduced by approximately half, by oversizing the circular stent to +6 mm in inter-trigonal distance (23.2 mm in perimeter). Designers of new TMV devices, who may face choices between D-shaped and circular stent designs, should ultimately reconcile these data with other relevant criteria. These include, but are not limited to, ease of production and implantation, risk of inducing LVOT obstruction or coronary vessel compression, anchor retention, and robustness against misplacement (e.g., D-shaped devices must anchor in the

correct rotational orientation). These topics were not investigated in the present work; they remain poorly understood in the public domain.

Beyond merely *determining* the target degree of annular oversizing and post-implantation shape and for a given TMV device, designers must ensure an ability to *achieve* these targets. This can derive from an understanding of the native tissue properties of the TMV landing zone, namely the annulus' radial resistive force, which the expanding device must overcome. The present work revealed that these properties, in normal porcine hearts, are non-trivial. 1.7 fold greater radial force was required to expand along the inter-commissural axis versus the septal-lateral axis, when enforcing a circular profile (for the D-shaped profile, this reached 2.2 fold). This radial expansion force data, much like the suture force data collected throughout SA 1, may also offer significant value to computational modeling (as discussed in Section 6.3.5).

The present investigations also serve as a testimonial on the suitability of whole porcine hearts as an *ex vivo* model for benchtop TMV performance assessment. ISO guideline 5840-3, which concerns the testing of transcatheter heart valve replacements, provides key test conditions that should be met, but does not specify the operational environments to achieve these conditions.[112] Potential environments include rigid models (e.g, acrylic), flexible synthetic models (e.g., silicone), organic models (e.g., ovine, porcine, or human tissue), or combinations thereof. Using the present porcine model, challenges included the limited heart supply and tissue fatigue (as described in Table 7-3 and Table 7-5). Synthetic models derived from imaging data could resolve each of these challenges, while also offering diseased and/or human anatomies. Yet, they would likely fall short in areas where the porcine heart excelled. Tissue material properties were

represented in terms of both bulk mechanics and surface-fluid interaction. Critically, geometrically and materially complex surrounding structures (e.g., the chordae tendineae, ventricular septum, and aorta), which may be difficult to fabricate, were intact. The porcine hearts proved effective, enabling the identification of clear differences in leakage and radial expansion forces according to device type. Ultimately, silicone and organic models will likely serve complementary roles in industry. A tester such as the REFT could prove an effective tool for silicone model validation, by establishing comparable radial expansion force behavior between the model and hearts of interest (e.g., cadaver).

The successes of the present work, outlined above, represent important first steps toward improved understanding of TMV design-performance relationships, and toward best practices for device assessment. Numerous important future directions exist on both fronts. These are discussed in Section 8.2.2.

7.3.5 Limitations

All experiments in Specific Aim 2 were conducted using healthy porcine hearts. The healthy porcine model is an established and appropriate tool for both benchtop *ex vivo* and preclinical *in vivo* testing of heart valve devices.[165, 169, 170] While the observed *relative* trends are likely widely applicable across species including humans, absolute values for PVL and radial expansion forces may best represent what could be expected during *preclinical* TMV evaluation in porcine subjects. The thick, strong porcine myocardium may enhance annular sealing, and elevate radial expansion forces, relative to aged, human

hearts. These quantities are likely further influenced by disease morphologies, especially in the case of secondary mitral regurgitation results from annular remodeling.

It must also be acknowledged that the PVL and REFT experimental procedures resulted in plastic stretch in the annulus (Table 7-3, Table 7-5). This is an inevitable consequence of mechanically loading explanted tissue. Due to the scarce supply of hearts with desired dimensions, each heart was tested across every oversizing level, in order of increasing size. This potentially exacerbated PVL and reduced radial forces at larger sizes. However, it likely influenced results across shapes, and across test methods, uniformly. Further testing using the methods employed in SA 2, but with only one oversizing level per heart, would offer additional insights.

It is noteworthy that all testing was conducted with hearts in a rigored, contracted state, and that the basis for cardiac contraction, whether during rigor mortis or systole, is actin-myosin fiber interaction. The likely mode of plastic stretch in these experiments is that enforcing oversized and/or incongruous geometries disrupted actin-myosin bonds, which were then unable to generate tension. At this time, it is unclear the extent to which this phenomenon represents what should be expected *in vivo*. *In vivo*, stretch in a sarcomere (i.e., a functional actin-myosin unit) has been shown to affect the tension it generates during contraction according to sliding filament theory;[171] in over-stretched sarcomeres, the myosin heads may fail to contact the actin fibers altogether.[172]

PVL studies in SA 2.A used water as the working medium, rather than a fluid such as water-glycerine, which can be matched to the viscosity of blood (i.e., 1.8 times higher than water). This was necessary due to the high volume of fluid needed for each

experiment. Greater viscosity would be expected to uniformly reduce leakage flow rates, but would have no impact on relative differences between devices.

One additional limitation specific to SA 2.B is noteworthy. The REFT's four annulus-contacting pads were shaped to match the +0 profile, with 3.4 mm gaps between pads. Inevitably, when oversizing, these gaps grew larger, and the path described by the contact pads deviated from a true circle or a true D-shape at larger sizes. This deviation was considered negligible in terms of its impact on radial expansion force.

CHAPTER 8. CONCLUSIONS AND FUTURE WORK

8.1 Specific Aim 1

8.1.1 Conclusions

- Suture Force Transducers were successful in detecting forces acting on individual annuloplasty sutures in the normal, beating ovine heart, using a range of annuloplasty ring designs.
- Across all tested rings, cyclic contractile forces on annular sutures trended positively with peak LVP, and were greater on sutures in the anterior annulus than those in the posterior annulus.
- Suture pullout force was also greater for sutures in the anterior annulus than those in the posterior annulus. This differential was larger for suture pullout force than for cyclic contractile force, indicating a lower margin of safety for suture dehiscence in the posterior annulus.
- Annular collagen density was greater at the suture position corresponding to the mid-anterior annulus than at the suture position corresponding to either trigone or at the mid-posterior annulus.
- As compared to undersized ring annuloplasty, true-sized ring annuloplasty conferred a cyclic contractile force reduction for anterior annulus sutures, only.
- As compared to the semi-rigid/flat Physio ring, the rigid/saddle-shaped Profile 3D ring showed no effect on suture forces in the anterior region as a whole or on the

posterior region as a whole. When undersizing, Profile 3D did confer a reduction in force variability among individual positions.

- Increasing ring flexibility conferred a cyclic force reduction to posterior annulus forces.
- A novel hybrid ring design possessing rigid anterior and posterior segments interposed with small, flexible commissural segments appeared to yield the same effects on anterior-posterior balance of cyclic contractile forces as did the fully-flexible design. Additional sample size is required.
- The ring prototyping, force measurement, and force analysis techniques developed in this work, in combination with established echocardiography-based analysis of mitral valve function, comprise the means to further explore novel annuloplasty ring designs for the optimization of suture retention and repair effectiveness.

8.1.2 Future Work

SA 1 provided important research in pursuit of advanced strategies for the reduction in annuloplasty suture dehiscence rates. The most direct application of this research will be toward the subsequent development of improved ring designs. These designs may include the hybrid concept tested preliminarily in SA 1.C. Next steps in this development process should include:

- *Further testing of the current hybrid ring concept*. Additional data points in normal ovine subjects would enable statistical testing. Studies in an ischemic MR model would clarify this design's capacity to restore effective valve function.

- *Development and testing of other hybrid design iterations*. These may include altered positioning of flexible segments and/or varied material properties within the segments.

Beyond ring design, other related questions regarding annular suture dehiscence remain. In parallel to the work included in SA 1, a series of additional studies have already been conducted, which highlight specific questions that demand further attention. These include:

- *Impact of suture tie-down force.* From a large group of the animal studies conducted in SA 1, suture tie-down forces were also quantified. Significant differences were found in the force used between implanting surgeons, suggesting these practices may meaningfully impact dehiscence likelihood. These data are presented in APPENDIX A. Additional research is needed to assess the degree to which tie-down force evolves post-operatively (on account of tissue viscoelasticity, weaning from cardiopulmonary bypass, and longer-term myocardial remodeling), and to work toward an eventual consensus on *optimal* suture tying techniques.
- *Robustness against suture mal-positioning*. In one failed *in vivo* experiment investigating annuloplasty suture forces, a likely suture misplacement (too high above the annular hinge line) culminated in extreme force magnitudes on one suture, which ultimately dehisced at high LVP. This experience is described in APPENDIX B. Increased understanding of the implications of suture bite width,

depth, and location for suture dehiscence likelihood would significantly benefit the surgical training process.[173]

- *Tricuspid valve annular suture force dynamics*. No longer the "forgotten valve," the tricuspid valve is now the focus of steadily expanding device design efforts. Annuloplasty suture dehiscence is a noted problem for the tricuspid valve, as well.[174, 175] We have measured suture holding strength and collagen content in ovine tricuspid annuli. The findings, presented in APPENDIX C, reveal a complex structure in need of further study. *In vivo* suture force measurements in the tricuspid annulus, akin to those performed in SA 1, would provide crucial information.
- *Discrepancies between normal ovine and diseased human annular mechanics*. All experiments within SA 1 used normal ovine hearts. Although sheep are widely accepted as a model for human cardiac physiology, some differences between ovine and human mitral/myocardial mechanics are known.[37, 46, 107] To begin to address this discrepancy, we have measured suture holding strength and collagen content in a cohort of six human mitral annuli (from donors aged 60-79, with no history of heart disease). This work is presented in APPENDIX D. Additional samples across a broader age range, and including valve disease, would be of value.

Although SA 1 limited its investigations to surgical annuloplasty rings, related questions involving transcatheter technologies also deserve further attention. These include:

- *Mechanics of novel anchor types used with transcatheter repair devices*. One such example is Cardioband (Edwards Lifesciences), a catheter-based annuloplasty band

that anchors to the annulus with a series of screw components, and which has CE Mark approval for commercial use in Europe. Notably, Cardioband underwent a recall in February 2018 due to "implant dehiscence" (https://www.tctmd.com/news/edwards-voluntarily-recalls-cardioband-anchors-used-mitral-and-tricuspid-repair).

- *Valve-in-ring procedures using the hybrid ring concept*. Off-label placement of a TAVR device within a mitral annuloplasty ring to correct recurrent MR is a growing research area. However, rigid and/or semi-rigid D-shaped rings may cause problematic distortion of the circular TAVR stent. If the hybrid ring developed in SA 1.C proves non-inferior to existing rigid or semi-rigid rings in terms of repair effectiveness, its utility for valve-in-ring procedures will warrant further investigation. It is likely that its three-dimensional shape and flexible commissural segments may enable it to "unfold" to better accommodate a circular stent.

8.2 Specific Aim 2

8.2.1 *Conclusions*

- A steady back-pressure test system was successfully developed to investigate paravalvular leakage dynamics in fresh, rigored, normal porcine hearts, as a function of the shape and size of mock transcatheter mitral valve plugs.
- Additionally, circular and D-shaped Radial Expansion Force Transducers were successfully developed to quantify the forces necessary to expand the rigored, normal porcine mitral annulus to shapes and sizes matching the plugs.

- PVL rates were proportional to the square of the trans-mitral pressure gradient.
- D-shaped plugs offered significantly improved sealing against PVL compared to circular plugs. The performance discrepancy was reduced by approximately half when the circular plug was oversized to the annulus by +6 mm (inter-trigonal distance).
- Unlike PVL dynamics, radial expansion force dynamics were much more sensitive to device sizing than to device shape.
- Approximately two-fold more radial force was necessary to expand the annulus along the inter-commissural axis than the septal-lateral axis.
- The forces necessary to oversize the annulus were less sensitive to the *amount* of oversizing when the shape of the device was circular rather than D-shaped.
- For biomechanics research pertinent to TMVR development, the rigored, normal porcine heart is a relevant and convenient model for the anatomies and tissue properties encountered both in preclinical device testing and, to a lesser degree, in the clinic. An important limitation, however, is the capacity for plastic tissue deformation under sustained loads.

8.2.2 Future Work

SA2 developed two new test systems to investigate TMVR performance mechanics, and employed these systems to study clinically and industrially relevant implications of TMV shape and size. This represents one of the only studies to date to parametrically assess

relationships between TMV design and performance. Numerous additional future studies should follow to enhance, further, and/or complement the present work. These include:

- *Investigation of PVL and/or radial expansion force according to TMV stiffness.* The circular and D-shaped devices used here represented final (post-implantation) TMV shapes. Notably, all stents possess some degree of flexibility, such that even a circular device may take on an oval, D-shaped, or other conformation post-implantation. Two potential future ways to investigate this phenomenon are to vary stiffness of the mock TMV plug, or vary the geometries of the mock TMV plug (and/or REFT) to mimic alternative post-implant geometries of interest.
- *Further data acquisitions in additional hearts.* Though cumbersome, additional tests using one size level per heart would largely address the noted limitation of plastic fatigue within the tissue. Also, testing in cadaver hearts would more closely represent the patient anatomies and tissue properties that a TMV would encounter.
- *Other steady back-pressure system and REFT system modifications.* Specific to the steady back-pressure test system, modifications to accommodate pulsatile pressure waveforms (physiologic or pathophysiologic) would enable numerous other investigations of TMV performance dynamics. Specific to the REFT, it is noteworthy that, while all data in SA 2.B was collected with aortic pressure fixed to 120 mmHg, preliminary investigations suggest that radial expansion forces may vary with aortic pressure (data not shown). Further study could quantify this relationship across a wider range to represent hypotensive and hypertensive geometries.

- *Parametric investigation of left ventricular outflow tract obstruction (LVOTO) dynamics.* Likely important parameters include, but are not limited to, TMV shape, TMV size, and the anatomy of the ventricular septum and anterior leaflet, and aorto-mitral angle. Integration of LVOTO and PVL data may inform best practices for device size and shape.

CHAPTER 9. FUNDING AND OTHER SUPPORT

This work was primarily supported by grants from the National Heart, Lung, and Blood Institute of the National Institutes of Health (R01HL113216 and R01HL119297) and by a Graduate Research Fellowship award from the National Science Foundation (DGE-1148903). Additional consumables and materials were purchased through the support of grants from the National Heart, Lung, and Blood Institute (R01-HL092926) and the Food and Drug Administration (FDA-SOL-1119844). A grant from the National Center for Advancing Translational Sciences of the National Institutes of Health (UL1TR000454) further provided biostatistics consultation services with Dr. Branislav Vidakovic.

Special thanks is given to Holifield Farms, who graciously donated fresh porcine hearts for use in Specific Aim 2. Special thanks is also given to Josh Stover and Jason Daenzer of 3D Printing Tech (Atlanta, GA), for their tireless troubleshooting support and generosity during the design and fabrication of the Radial Expansion Force Transducer used in Specific Aim 2.B.

APPENDIX A. SUPPLEMENTAL STUDIES: ANNULOPLASTY SUTURE TIE-DOWN FORCES

A.1 Introduction

The *in vivo* studies conducted in Specific Aim 1 assessed the cyclic forces sutures experience in the beating heart (F_C). In one subset of these studies, the force initially applied during implantation of each suture (i.e. tie-down force, F_{TD}) was also recorded and analyzed, as described herein.

A.2 Materials and Methods

This study utilized the suture force transducers and normal ovine model described in Sections 4.1 and 5.1. Physio and Profile 3D rings were used. The experimental protocol was as described in Section 5.1.4.2. For each suture, F_{TD} was computed as the difference in force immediately before and after its tie-down. Statistical analysis was as described in Section 5.1.6, using the specific ANOVA models listed below.

Table A-1 ANOVA models used in this appendix.

Model	Dependent Variable	Independent Variables
1	F_{TD}	Ring type, ring-annulus sizing, suture position
2	F_{TD}*	Surgeon, suture position

*this model examined a subset of 11 Profile 3D cases, performed by either of two surgeons (no other surgeon performed >2 cases for which F_{TD} was collected)

A.3 Results

A description of the sample populations used in this supplemental study is presented in Table A-2 (note, each subject was also used in Specific Aim 1). In total, this cohort included 4 of 10 Physio cases and 13 of 13 Profile 3D cases (forces were not recorded during suture tie-down in the early cases using the Physio ring). Among all cases, mitral annulus sizes ranged between 26-32, and rings of size 26-30 were used (either true-sized to the annulus, or undersized by two sizes). Note, this sizing refers to the label size of the ring and its corresponding sizer, and is approximately equivalent to the inter-trigonal distance (in mm).

Figure A-1 provides representative force data on each of ten sutures, covering a six-minute period spanning from before the first suture tie-down to after the final suture tie-down. The F- and p-values from all ANOVA models used to analyze these ring implantations is presented in Table A-3.

Table A-2 Data set summary for this appendix. U: undersized; T: true-sized; Ph: Physio ring; 3D: Profile 3D ring

	U-Ph	T-Ph	U-3D	T-3D
Sample size	3	1	6	7
Surgeon 1 Frequency	0	0	1	5
Surgeon 2 Frequency	0	0	3	2
All Other Surgeons' Combined Frequency	3	1	2	0
Animal weight (kg)	49.7 ± 5.9	62	57.0 ± 5.8	57.4 ± 6.8
Annulus size	30.0 ± 0.0	32	30.0 ± 0.0	27.7 ± 1.8
Ring size	30.0 ± 0.0	32	26.0 ± 0.0	27.7 ± 1.8

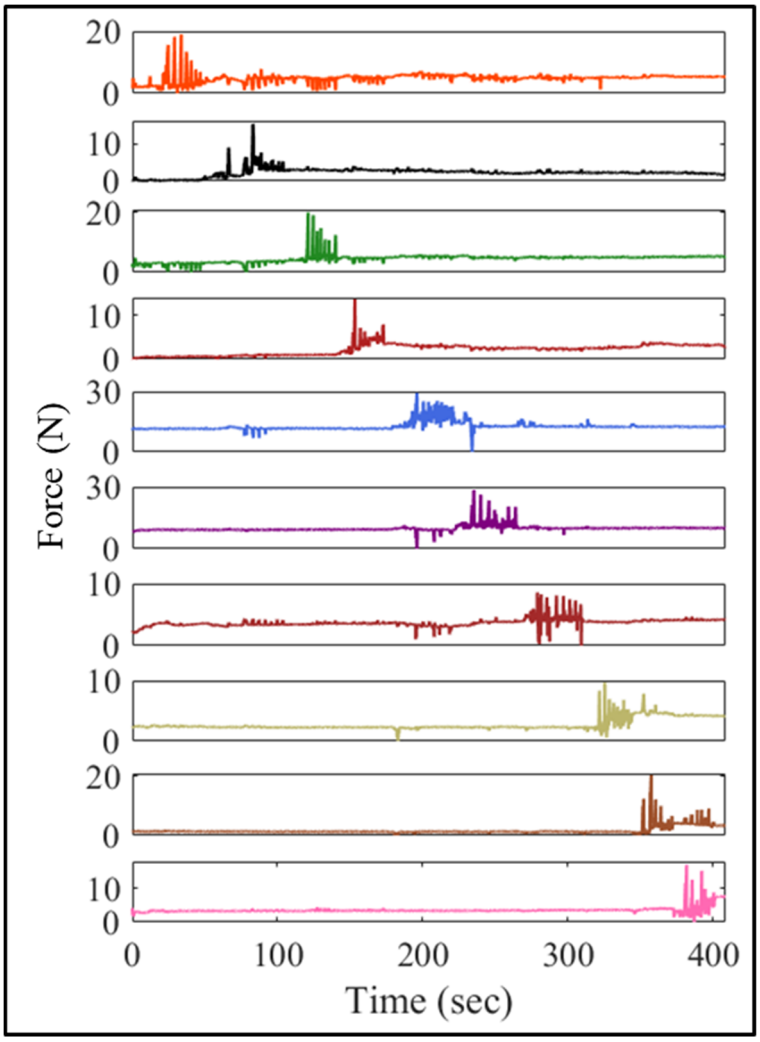

Figure A-1 Representative data used for F_{TD} measurement. Sutures were tied first to the left trigone (LT), then the right trigone (RT), then clockwise from 11 o'clock. F_{TD} was computed as the force differential immediately before/after tie-down (tie-down visible here as a series of quick spikes).

Table A-3 Results of ANOVA models used in this appendix, before post-hoc analysis.

		Factor	F	p
Model 1	Main effects	Ring type	0.76	0.385
		Ring-annulus sizing	2.08	0.152
		Suture position	1.93	0.051
	Interactions	Ring type:Ring-annulus sizing	0.03	0.855
		Ring type:Suture position	1.67	0.101
		Ring-annulus sizing:Suture position	0.8	0.621
Model 2	Main effects	Surgeon	7.8	0.006
		Suture position	1.8	0.078
	Interactions	Surgeon:Suture position	2.77	0.007

Across all sutures, mean ± standard deviation F_{TD} was 2.7 ± 1.4 N (range: 0.0-8.0 N). On the basis of ANOVA model 1, it was found that ring type, ring-annulus sizing, and suture position did not significantly affect F_{TD}. Furthermore, no significant pairwise interactions were found.

Next, noting that no significant differences due to ring type or ring-annulus sizing were found, and desiring to examine the impact of surgeon on F_{TD}, ANOVA model 2 was applied to a subset of 11 Profile 3D cases. These were performed by either of two surgeons (5 or 6 each), whereas no other surgeon performed more than two cases for which F_{TD} was collected. As shown in Figure A-2, independent of position, surgeon 2 applied 29% more F_{TD} than surgeon 1 (2.9 ± 1.2 N vs. 2.2 ±1.4 N, p=0.006). Independent of surgeon, only one pairwise significant difference was found among positions: sutures at 1 o'clock endured greater F_{TD} than those at 5 o'clock (3.6 ± 0.8 N vs. 1.9 ± 0.9 N, p=0.048). In addition, 1 o'clock sutures nearly achieved significance versus multiple other positions.

Interaction between surgeon and position was observed; notably, the final 9 o'clock suture was subjected to greater F_{TD} when implanted by surgeon 2 (3.9 ± 1.2 N vs. 1.3 ± 0.6 N, p=0.035).

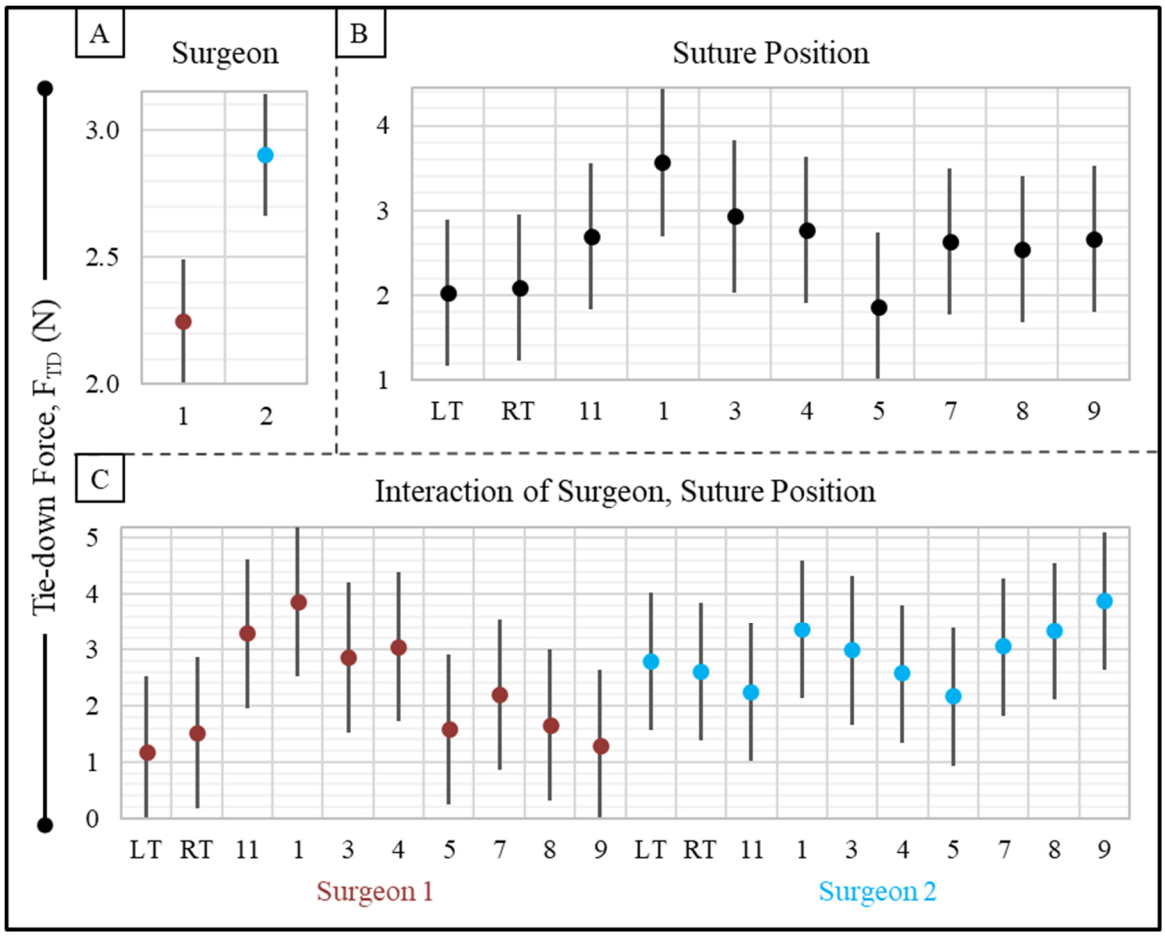

Figure A-2 Mean ± 95% CIs for each (A) surgeon, (B) suture position, or (C) suture position specific to the implanting surgeon. Model included a cohort of 11 Profile 3D cases split 5:6 among two surgeons. Within each plot, pairs whose 95% CIs do not overlap differ significantly (p<0.05). (B-C) Shown in order of suture implantation.

To understand the extent to which force used to tie down a suture dictates the eventual cyclic force on that suture during cardiac contraction (F_C), correlation between

F_{TD} and F_C was assessed. Among all 170 sutures for which F_{TD} was recorded, linear regression was conducted between F_{TD} and the corresponding F_C at LVP_{max} = 125 mmHg, revealing $R^2 = 0.003$ (p=0.467).

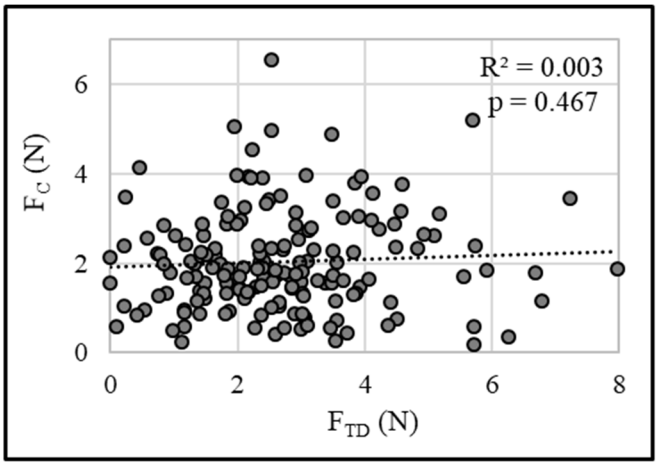

Figure A-3 Correlation between F_{TD} and F_C.

A.4 Discussion

Whereas clinical reports of suture dehiscence may be easily dismissed as a result of mere surgical error, Specific Aim 1 demonstrated that the force acting on annuloplasty sutures in the beating heart vary significantly as a function of the selected ring's properties. The results of this appendix complement this finding by further demonstrating the significant variability in suture tie-down force among surgeons.

Specific Aim 1 pursued strategies to reduce annuloplasty suture forces in the beating heart (F_C). The non-significance of the correlation between F_{TD} and F_C (Figure A-3) suggests that a more loosely tied knot is unlikely to relieve eventual F_C. However, the

unexpectedly high F_{TD} magnitudes, as compared with F_C, suggest knot-tying force may meaningfully affect dehiscence likelihood. Across the 170 sutures in this cohort, mean F_{TD} was 2.7 N, compared with 2.0 N F_C (averaged across all three LVP_{max} levels). Still, the summed quantity, $F_{TD} + F_C$, *cannot* be assumed to represent the total suture force in the beating heart. We speculate that that F_{TD}, measured immediately after suture tie-down, evolves postoperatively. Soft tissue viscoelasticity[153] is known to facilitate stress relaxation and creep; its impact in this context remains unknown. Baseline myocardial tone also may change after weaning from cardiopulmonary bypass and recovery from anesthesia.[176] Longer term, soft tissue is also capable of active remodeling in response to changes in homeostatic mechanical stresses. Such phenomena warrant further investigation.

With respect to suture anchoring, three main variables can be influenced by the surgeon. Among these, neither suture selection not suture placement (bite width, bite depth, or height above the leaflet hinge line) was explored in the present study, although we have observed dehiscence to occur after likely suture misplacement (see APPENDIX B). The third variable, knot tying force (F_{TD}), notably did not vary according to ring selection. However, it was shown to vary according to circumferential suture position. When exploring Profile 3D rings only, F_{TD} at 1 o'clock was highest (36% above mean F_{TD}), where it significantly exceeded that of 5 o'clock and nearly achieved significance versus multiple other positions. This may be explained by a combination of suture tie-down order (LT, then RT, then clockwise from 11 o'clock) and ring shape. The 1 o'clock and 9 o'clock sutures were unique in that they were each implanted after both of their respective adjacent sutures. At 1 o'clock, the higher annular collagen content (as reported in SA 1.A and by Gunning et al[43]) also might pose more resistance to suture knotting.

Further, significant discrepancies in F_{TD} were observed between the two primary implanting surgeons in these studies. Averaged across 6 or 5 procedures, respectively, surgeon 2 applied 29% more F_{TD} overall, and 201% more F_{TD} at 9 o'clock, than surgeon 1. Currently, it remains unclear what suture tie-down strategy, if any, is optimal for anchoring durability. If subsequent investigations are able to identify such an optimum, standardizing to that strategy across surgeons could create substantial value within the scope of the applicable procedures. Recent commentary has highlighted the vital role of surgical training for accurate and precise suture placement as a means to minimize the likelihood of dehiscence.[155] Surgical training may ultimately play a similar role in the context of knot-tying.

A.5 Conclusion

In this cohort of 17 annuloplasty ring implantations, suture tie-down force did not vary based on ring type or size, but varied significantly according to the suture position and/or the implanting surgeon. Tie-down force on a given suture exhibited no correlation to that suture's eventual cyclic force in the beating heart. Although it remains unknown to what extent the force used during suture tie-down persists postoperatively, tie-down force may play a determining role in suture dehiscence likelihood.

APPENDIX B. SUPPLEMENTAL STUDIES: A LIVE-RECORDED CASE OF ANNULOPLASTY SUTURE DEHISCENCE

B.1 Introduction and Background

The *in vivo* experiments conducted in Specific Aim 1 sought to understand suture dehiscence mechanics by quantifying the forces acting on mitral annuloplasty sutures during cardiac contraction. These studies did not attempt to actually induce suture dehiscence. However, in the course of completing these experiments, one unexpected incident of suture dehiscence occurred; this is described herein.

B.2 Materials and Methods

This study utilized the suture force transducers and normal ovine model, and surgical procedures described in Sections 4.1 and 5.1. An instrumented Profile 3D ring (final size 26 after accounting for transducers) was implanted in a size 30 annulus (subject weight, 45 kg). The experimental protocol was as described in Section 5.1.4.2. However, in addition to the neosynephrine and dobutamine used to elevate left ventricular pressure (LVP), a 0.2 μg intravenous bolus of epinephrine was also administered. Note, the forces reported in this appendix are absolute or peak forces, as indicated (i.e., not cyclic forces, F_C, which were the primary measured quantity in SA1 and other supplemental studies).

B.3 Results

It was noted that one suture, located at 11 o'clock, experienced peak force two-fold higher than any other suture, at all peak LVPs. The epinephrine bolus induced a rise in LVP to 195 mmHg over 30 to 40 seconds. At an LVP of 188 mmHg, a dramatic decrease in force was observed at 11 o'clock, from 16.7 to 0.6 N. Simultaneously, peak forces increased at the two adjacent sutures, one by 3.1 N and the other by 2.6 N. Two other sutures experienced small increases (1.3 N and 0.3 N), but force decreased at all other sutures. After the animal was euthanized, visual examination revealed that the suture in question had torn through the annulus tissue, likely owing to technical misplacement above the annular hinge. The suture itself remained intact. The ruptured tissue was not examined histologically.

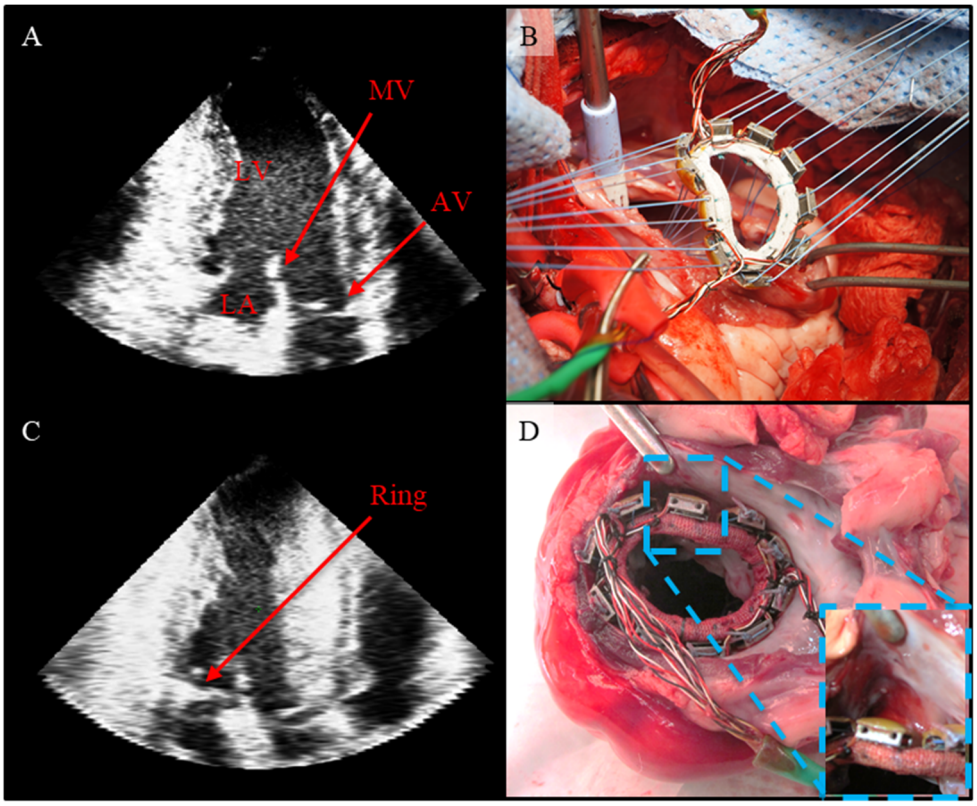

Figure B-1 (A-B) An annuloplasty ring, instrumented to record tensile forces on individual sutures, was implanted in the mitral valve of a healthy ovine subject using standard technique. (C) Implantation was unremarkable. (D) Following LVP elevation above 188 mmHg, one suture dehisced.

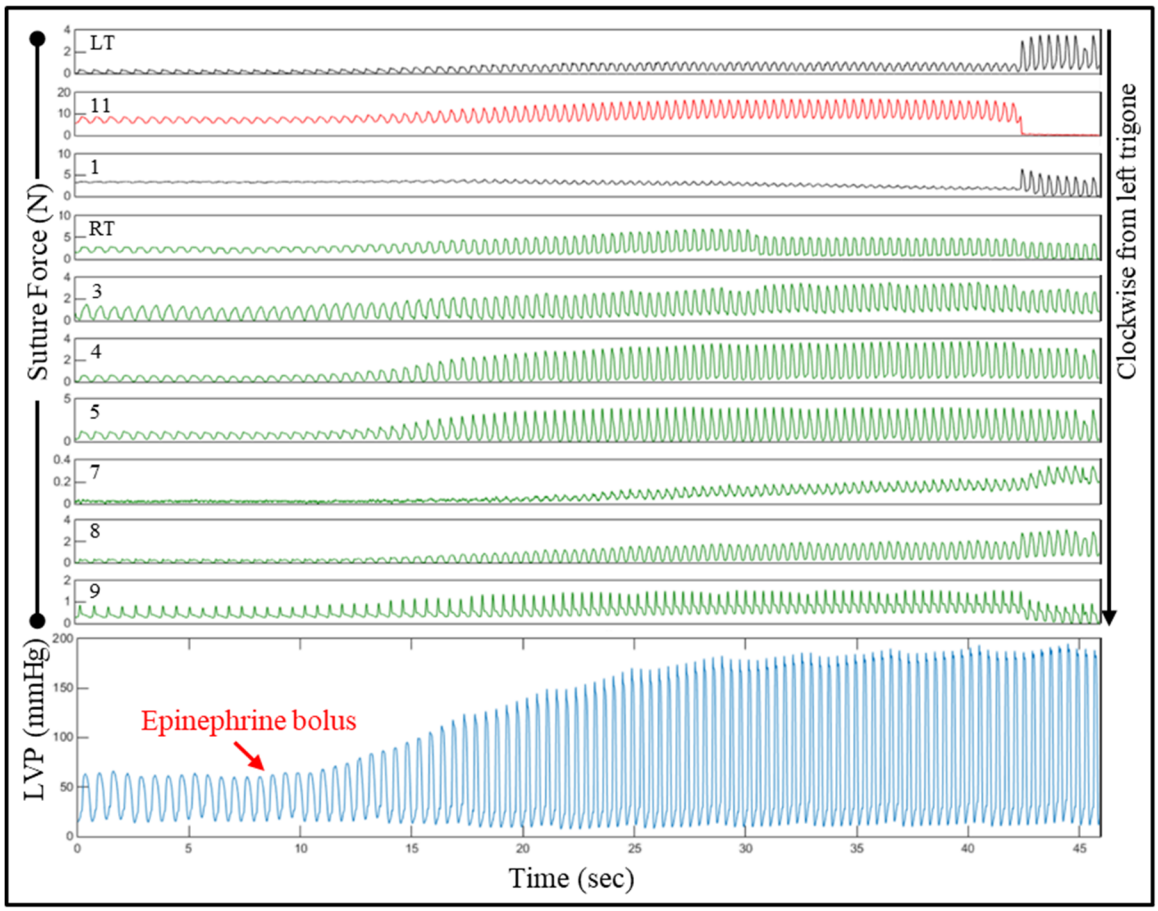

Figure B-2 The failed suture dehisced following a peak force of 16.7 N (red); 5.7 N of this force shifted to the two adjacent sutures (black). Loading on all other sutures (green) either increased slightly (i.e. < 1.3 N) or decreased.

B.4 Discussion

This case provides the first quantification of a tensile force responsible for annuloplasty ring suture dehiscence in the beating heart. After a 16.7 N load induced dehiscence, a combined 5.7 N shifted to the two adjacent sutures. This observation provides a likely mechanism whereby a single problematic suture could induce a cascade of dehiscence at

multiple anchor points, as observed clinically.[99] A less eccentric redistribution of force across the remaining sutures may be preferable.

Greater suture loads may be expected along the anterior annulus in general, due to systolic expansion of the aortic root (which sits adjacent to the anterior annulus), cyclic changes in the anterior saddle geometry,[46] and the stiffer/more collagenous anterior annular tissue (as demonstrated by Gunning et al[43] and in SA 1.A). Nonetheless, it is noteworthy that the observed force distribution was so highly concentrated on the single failed suture, even at lower LVPs. This case was likely a consequence of misplacement of the suture in question; we believe that placement too high above the annular hinge heightened suture tension by adding an out-of-plane force component at that position. Ultimately, any steps during device selection, suture placement, and suture tie-down that minimize sharp force concentrations on single sutures will likely help to ensure prosthesis security. This case particularly highlights the importance of accurate suture positioning to that end; a more rigorous quantification of these effects is the subject of ongoing work.

APPENDIX C. SUPPLEMENTAL STUDIES: OVINE TRICUSPID ANNULAR MECHANICS

C.1 Introduction and Background

Functional tricuspid regurgitation (FTR) is the most common disease of the tricuspid valve (TV).[177] In the past, FTR has often been ignored, and it continues to be undertreated.[178, 179] Patients are rarely referred for isolated tricuspid surgical repairs or replacements.[178, 179] Previous studies have asserted that FTR associated with left-heart conditions should be left to resolve itself after left-heart repair.[180] However, more recent studies show that FTR does not, in fact, resolve itself after mitral-valve surgery,[178, 181] and given that reoperation is risky and rarely performed,[178, 182] it is important to address tricuspid regurgitation (TR) at the time of left-heart surgery.[181, 183] Recent published opinions favor a more aggressive approach to correcting FTR,[178, 181, 184, 185], and increased attention is now being given to the tricuspid disease, both in terms of volume of surgical treatments.[183, 185] and breadth of corrective devices.[182, 184, 186] Whenever possible, TV repair (largely centering around ring annuloplasty) is preferred over replacement [185].

TV repair is often triggered by an annulus diameter of greater than 40 mm, and an approach to sizing these cases may be to undersize by *at least* two ring sizes. However, the "normal" size of the tricuspid annulus is very close to 28 mm in all patients, suggesting that undersizing by two ring sizes may not be sufficient. Huffman examined patients who underwent mitral valve repair with an undersized, rigid, complete annuloplasty ring, and who concomitantly underwent TV repair using the same size TV annuloplasty ring.[187]

Findings suggest that the same ring size can be used for TR as was used for MR, without development of significant tricuspid stenosis or negative effects on right heart function. These findings were confirmed by three large clinical trials by Desai (USA), Mukherjee (USA), and Bertrand (Europe), which showed that the RV improves when functional TR is repaired.[188, 189] Furthermore, this "normalize size" approach seems to prevent the recurrence of significant TR. Ghoreishi has shown that the application of a normal size tricuspid ring (28 mm) results in very little recurrent regurgitation and no stenosis.[190]

With respect to ring stiffness, there is currently little direct comparative evidence to discern between rigid and flexible options. However, similarly to functional MR, rigid rings are commonly considered more effective to treat FTR. In recent analyses of the existing literature, Rogers concluded the superiority of rigid or semi-rigid rings,[185] owing to multiple clinical series.[191-193] Zhu, meanwhile, noted that while flexible and rigid rings perform comparably in the short-term, rigid rings exhibit potential advantage in terms of sustaining postoperative TR grade.[185, 194]

Yet, as has been demonstrated in Specific Aim 1 of this thesis for the mitral valve, suture dehiscence is a potential drawback to rigid rings at the tricuspid position.[194] Tricuspid annuloplasty ring dehiscence data is currently limited, and its exact incidence varies from series to series. However, one revealing report comes from Pfannmuller, who reported a 4.8% dehiscence rate among 820 tricuspid annuloplasties performed for moderate-to-severe, non-organic TR.[195] Within this cohort, flat rigid rings (Carpentier-Edwards Classic, Edwards Lifesciences LLC, Irvine, CA) and flexible bands (Cosgrove-Edwards, Edwards Lifesciences LLC) dehisced in 8.7% and 0.9% of cases, respectively. Dehiscence risk may become even more significant with the next generation of

transcatheter tricuspid repair devices, many of which anchor using unprecedented techniques.[184]

Specific Aim 1 showed significant variation in mitral annular collagen density, and an associated variation in suture holding strength. This suggested that shifting the distribution of annuloplasty suture forces more towards the anterior mitral annulus (i.e. towards the septum) could decrease the incidence of dehiscence. An analogous characterization of the tricuspid annulus could similarly inform anchor design in current and next-generation tricuspid devices. This study aimed to quantify the tricuspid annulus' suture holding strength and its correlation to underlying collagen structure.

C.2 Materials and Methods

All testing was performed using fresh, never-frozen ovine hearts (Superior Farms, Dixon, CA). Suture pullout testing (N=15 hearts) was performed using the materials and methods described in Sections 4.1.4, 5.1.3.1, and 5.1.4.2. All sutures were placed by a single operator (note, this was a different operator than in SA 1.A suture pullout tests). Twelve sutures were tested per sample, at the positions shown in Figure C-1. Annular microstructure (i.e. collagen and non-specific fiber density) was quantified in a separate cohort of hearts (N=7) using the materials and methods described in Sections 4.1.5, 5.1.3.2, and 5.1.4.3. However, rather than excise small cubes of tissue prior to paraffinization, the entire tricuspid annulus was paraffinized. Sectioning and imaging were performed on larger regions of tissue, as shown in Figure C-2 below. Pixel intensities were then

quantified over a 2 x 3 mm region of interest extending superiorly and into the tissue, respectively, from the leaflet hinge.

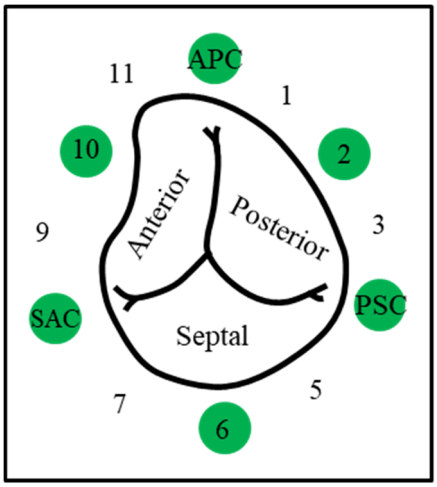

Figure C-1 Positions included in data collection. Suture pullout testing included all twelve positions. Fluoroscopic imaging included those positions with green circles. SAC, septal-anterior commissure; APC, anterior-posterior commissure; PSC, posterior-septal commissure.

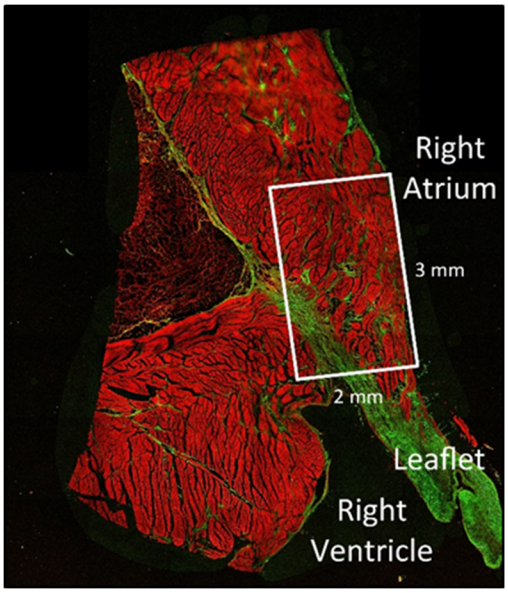

Figure C-2 Representative image collected by two-photon autofluorescence, demonstrating the region of interest for colorimetric quantification (white box). Green, collagen fibers; red, non-specific fibers.

Statistical analysis was performed using Minitab (Minitab, Inc., State College, PA) and MATLAB (MathWorks, Natick, MA). For suture pullout forces, a nested ANOVA model was used, with suture positions nested within regions (regions were defined as anterior leaflet, posterior leaflet, septal leaflet, and commissural). For normalized mean pixel intensity (nMPI), one-way ANOVA models accounting for each position were used.

C.3 Results

All 180 suture pullout attempts were successful. Across all suture positions, mean ± standard deviation F_P was 6.5 ± 2.2 N. The absolute minimum F_P was 1.9 N (SAC), and the absolute maximum value was 17.0 N (6 o'clock).

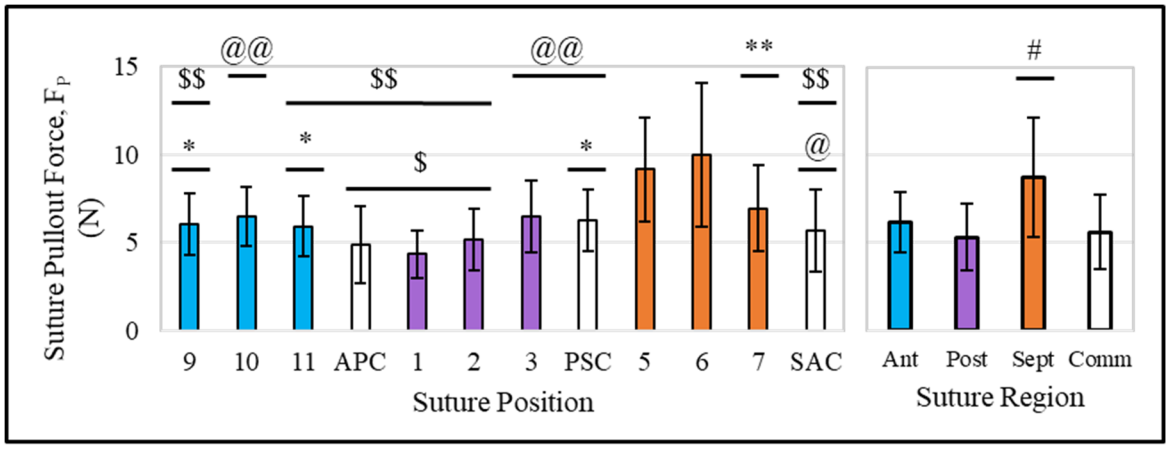

Figure C-3 Mean ± SD F_P results, with ANOVA results depicted by symbol notation. *p<0.05 vs. 5 o'clock; **p<0.05 vs. 6 o'clock; @p<0.005 vs. 5 o'clock; @@p<0.005 vs. 6 o'clock; $p<0.001 vs. 5 o'clock; $$p<0.001 vs. 6 o'clock; #p<0.001 vs. all other regions.

The lowest average pullout force was 4.3 ± 1.3 N at the posterior aspect near the anterior-posterior commissure (1 o'clock), and the highest was 10.0 ± 4.1 N at the mid-septal annulus (6 o'clock). Two positions in the septal annulus (5 and 6 o'clock) had significantly higher F_P than nearly every other position. By region, the septal annulus (8.7 ± 3.4 N) exhibited higher F_P than each other region.

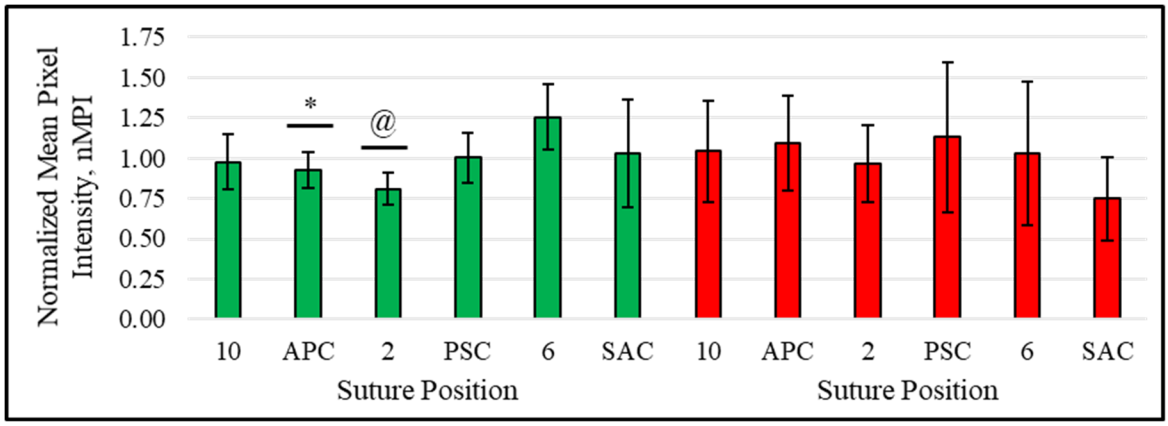

Figure C-4 Mean ± SD nMPI results, with ANOVA results depicted by symbol notation. *p<0.005 vs. 6 o'clock; @p<0.005 vs. 6 o'clock.

Collagen nMPI peaked at 6 o'clock (1.26 ± 0.08) and decreased with progressive distance from the septum. ANOVA showed significant differences in nMPI between the 6 o'clock and either 2 o'clock or APC. Non-specific myocardial fibers were also imaged; no significant variation in this signal was observed.

As shown below, a strong linear correlation was found between collagen density and suture holding strength ($R^2 = 0.82$, $p = 0.013$). No such correlation was found between non-specific fibers and suture holding strength ($R^2 = 0.02$, $p = 0.806$), demonstrating the specificity of the relationship between holding strength and collagen density.

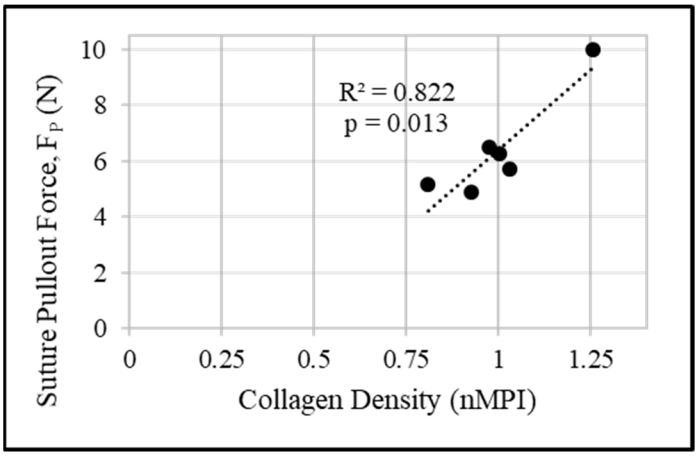

Figure C-5 Linear regression of each position's mean suture pullout force versus normalized mean pixel intensity (nMPI). Only positions subjected to both measurements were included (i.e. each commissural and mid-leaflet position).

C.4 Discussion

The present study characterized the local suture holding strength around the annulus and the annular collagen density that may underlie it. It was observed that suture holding strength and collagen density were highest in the septal annulus. Each was also higher at positions above leaflet midpoints compared to commissures. Consistent with findings from SA1 at the mitral position, collagen density was found to be a strong predictor of tricuspid annular suture holding strength. It can be observed in Figure C-5 that an approximate 1/3 decrease in TV annular collagen content equated to a 5 N decrease in holding strength. One implication of this finding is that, in forms of organic valvular regurgitation hallmarked by adverse collagen remodeling,[53, 196] alternative suturing techniques may be preferable. In all disease states, care should also be taken to protect against dehiscence when tying the stitches in the least robust areas, and to avoid tying when there is over-distraction from

retraction. Reinforcing pledgetted sutures can also be used in areas of perceived or known weakness.

The increased suture holding strength in the septal annulus initially appears to contradict the clinical tendency toward suture dehiscence at the septal annulus.[195] However, we note four possible explanations for this discrepancy. First, the report of predominantly septal dehiscence was following use of Carpentier-Edwards rings. Given the out-of-plane annular motion near the trigone,[197] these planar rings may eccentrically load sutures along the septal annulus. Second, this report followed ring implantation in the beating heart; beating heart annuloplasty has shown a trend toward heightened dehiscence rates.[198] The septal aspect of the ring is typically the last to be secured to the beating heart, which could predispose sutures in this region to misplacement and/or higher tie-down forces. Third, efforts taken to avoid damaging the atrioventricular node during tricuspid annuloplasty may result in too few sutures and/or too shallow bites being used along the septal aspect, causing diminished anchoring strength there. Finally, it is possible that higher contractile forces experienced along the septal annulus *in vivo*, independent of ring type and implantation method, may be sufficient to overcome its greater holding strength.

The notion that contractile forces at the tricuspid septum outweigh its superior tissue strength would represent a striking difference from the mitral valve, where the septal annulus is a superior anchor site.[199] Yet it is plausible on the basis of the TV annulus' dynamic motion. Even when dilated, the tricuspid annulus experiences a greater systolic reduction in circumference than the mitral annulus,[197, 200] potentially elevating TV cyclic suture tension. Most FTR annular dilation occurs along the septal-lateral axis; rigid ring

annuloplasty most severely restricts motion along this axis,[201, 202] suggesting that *in vivo* suture forces may be greatest near the septum or lateral wall. Further, the septal aspect, owing to the trigone and the heightened collagen content, is the TV annulus' least compliant region and may thus experience uniquely high suture tension.

In the pursuit of strategies to reduce dehiscence risk, this study highlights key differences between the MV and TV. A chain is only as strong as its weakest link[203] – that is to say, the most practical approach to minimizing dehiscence likelihood is to address the sutures with the lowest margin of safety between strength and loading. At the mitral position, SA1 showed that sutures placed in the septal annulus experience greater loading *in vivo* but also have the highest margin of safety. Thus, for the mitral valve, approaches that redistribute cyclic suture forces *towards* the septum are of interest to improve anchoring stability. On the other hand, at the tricuspid position, evidence suggests suture forces appear to be too high at the septal annulus, despite its superior strength. Thus, improved approaches for TV devices may involve a redistribution of cyclic suture forces *away* from the septum. For example, the use of nonplanar rings has been shown to be effective in treating tricuspid regurgitation without need for reoperation.[204] Animal studies are necessary to fully characterize the force distribution on tricuspid annuloplasty sutures.

Although technically, undersized ring annuloplasty for FTR is relatively straightforward, careful attention should be given to surrounding structures. Specifically, in functional TR repairs, numerous annular stitches, even to the point of overlapping, should be utilized, as the annulus is usually "under-developed" as compared to the mitral

annulus and the distracting force from the geometric distortion of the RV must be counteracted. The annuloplasty sutures should be taken parallel with and travel in the annulus. One common source of failure of tricuspid annuloplasty is the dehiscence of the ring from inadvertently applying the stitches to the atrial wall or in the leaflet tissue. One general approach for FTR has been to place stitches only from 10 o'clock to 6 o'clock, avoiding the AV node, the lower septal area and the triangle of Koch.

The present data, though most directly applicable to existing surgical TV repair or replacement devices, have further implications for transcatheter devices. The field of transcatheter TV repair is growing rapidly, with MitraClip (Abbott Laboratories, Minneapolis, MN) already being used to achieve a percutaneous edge-to-edge-type repair of the TV, and with several additional devices in preclinical or clinical trials.[184, 186] Many of these use novel mechanisms, such as corkscrews or foldable pledgets, to anchor to the annulus.[205] Although the present reported force values are not necessarily representative of the exact annular strength in the presence of alternate anchor types, analogous positional heterogeneity likely exists for these devices. Ultimately, these novel mechanisms place unprecedented mechanical demands on the annulus that must be objectively characterized. Percutaneous delivery in the absence of direct visual access and without arresting the heart will likely challenge the precision of anchor placement.[204] Anchor robustness in the presence of this variability is essential. The complexity of the TV annular tissue shown here, in combination with the increasing diversity in anchoring technology, creates a critical need for unified testing standards that ensure acceptable post-operative outcomes.

C.5 Conclusion

The septal region of the tricuspid annulus has an increased collagen density and increased suture holding strength. Both parameters were higher at positions above leaflet midpoints compared to commissures. For all positions tested, collagen density was a strong indicator of suture holding strength. The clinical tendency for dehiscence along the septal annulus[195] suggests that adverse suturing techniques in this region may be common, and/or that this region may experience higher cyclic forces *in vivo*. Further exploration of the factors influencing dehiscence risk and annular tissue failure are needed to improve device designs and implantation techniques.

APPENDIX D. SUPPLEMENTAL STUDIES: HUMAN MITRAL AND TRICUSPID ANNULAR MECHANICS

D.1 Introduction and Background

Investigations of suture pullout mechanics and collagen content were conducted in Specific Aim 1.A (for the mitral valve) and in APPENDIX C (for the tricuspid valve). As noted earlier, one limitation of these studies was the use of normal ovine tissue. This tissue's material properties and composition may differ from the human tissue in which sutures are anchored in the clinical setting due to species,[206] age,[206, 207] and pathology.[208]

A second limitation of these studies was that distinct cohorts of hearts were used for suture pullout testing and collagen quantification. Suture pullout testing, once complete, left the annular tissue disrupted to such an extent that accurate, *in situ*, quantitative imaging was not possible (*in situ* imaging is shown, for example, in Figure C-2). Although this *in situ* approach was cost-effective and provided spatial information about collagen concentrations within each section, it necessitated use of a separate cohort of hearts for collagen quantification. If the same samples were used for both tests, correlation of collagen content to suture pullout force (F_P) would have been possible on a point-by-point basis; instead, only mean values at each suture position could be correlated.

A third limitation was in the collagen quantification technique itself. The two-photon excitation fluoroscopy technique was effective to assess *relative* differences in collagen content among multiple positions of a given valve annulus (with units of *normalized* mean pixel intensity, nMPI). Its effectiveness derived from the use of constant

imaging settings for all positions *within each valve annulus*. Because nMPI from a given sample signified collagen density in that sample, *relative to the mean among all samples from that valve*, the ovine mitral and tricuspid nMPI data cannot be compared to one another. Relatedly, two different operators were used for MV suture placement and TV suture placement, making direct comparison of F_P values between the valves unreliable.

In an effort to address these limitations, an additional data series was collected. From a cohort of six human hearts age 60-79, *both* the MV and TV annuli were subjected to suture pullout testing (with all sutures placed by a single operator). Subsequently, the tissue from each tested suture position was subjected to a collagen quantification assay that used *digested* tissue. The tissue injury post-suture pullout that inhibited *in situ* annular imaging was of no concern for this digest-based assay.

D.2 Materials and Methods

D.2.1 *Donor Criteria, Sample Preparation, and Positions Tested*

Hearts from donors with no history of heart disease (N=6) were acquired from Science Care, Inc. (Phoenix, AZ). Immediately upon receipt, mitral and tricuspid annular tissue were excised as described in Section 5.1.3.1. Each specimen was cryopreserved using a 90% RPMI-1640 and 10% DMSO solution at -80 °C.[209, 210] Before testing, specimens were thawed through incremental dilution of DMSO with 0.9% saline solution over the course of 40 minutes.

From each valve, ten positions (for MV) or twelve positions (for TV) were tested. Every sample was subjected to *both* suture pullout and collagen testing. These are the same positions for which suture pullout was conducted in SA 1 and in APPENDIX C. However, regional grouping is different in the present cohort, in support of a unified design between the MV and TV data.

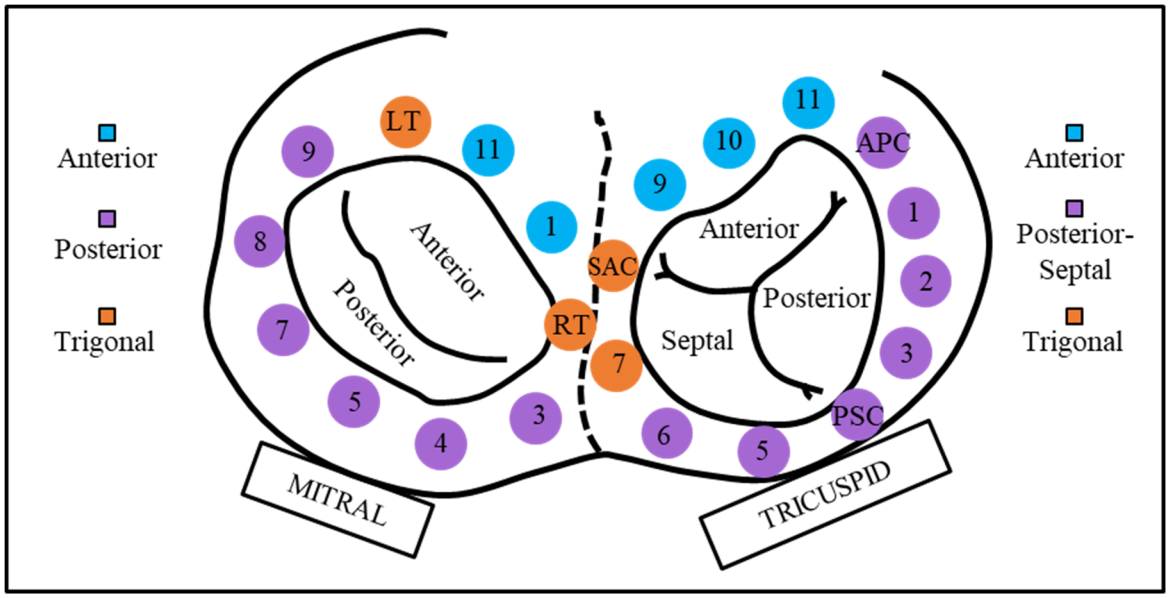

Figure D-1 Annular positions/regions tested. All positions were subjected to both suture pullout and collagen quantification testing. These are the same positions subjected to suture pullout testing in SA 1 and APPENDIX C. However, regional grouping is different in the present cohort, in support of a unified design between the MV and TV data. LT, left trigone; RT, right trigone; APC, anterior-posterior commissure; PSC, posterior-septal commissure; SAC, septal-anterior commissure.

D.2.2 *Suture Pullout Testing*

The valve annulus was mounted to the suture pullout test plate described in Section 4.1.4. Mounting and suture placement were performed as described in Section 5.1.3.1. All sutures were placed by a single operator. Mounted specimens were submerged in a 0.9% saline

solution at 37° C. Suture pullout was conducted with a TestResources 100Q Universal Testing Machine (Shakopee, MN). The axial force was measured using a 500 lbf load cell (TestResources SM-500-294) and recorded through a custom LabVIEW code. As in the earlier studies, the suture was tied to the upper arm and pulled at 1 mm/sec until it tore through the tissue. In terms of native MV or TV geometry, this pulling was approximately radially inward, i.e. the approximate direction of suture tension following undersized annuloplasty *in vivo*.

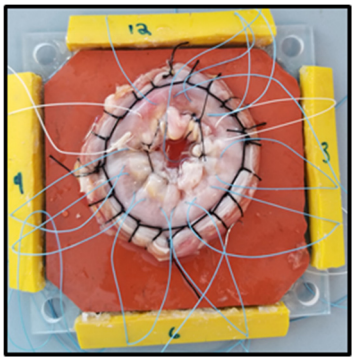

Figure D-2 Mitral annulus sample from a donor heart, after preparation for suture pullout testing.

D.2.3 Collagen Quantification Testing

After all sutures from a valve were pulled out, tissue samples from each suture position were carefully excised. The excised section was a rectangular prism with boundaries approximately 1 mm beyond the suture path in all directions. Each sample was homogenized by grinding with submersion in liquid nitrogen. Each sample was then hydrolyzed at 120 °C for 3 hours, using 200 µl 6 M HCl per 10 mg sample mass.

The hydrolysate was tested for mass of hydroxyproline per unit volume, via a commercial assay (MAK008, Sigma-Aldrich, St. Louis, MO). Hydroxyproline is a major component of collagen, where it serves to stabilize the helical structure. Because it is largely restricted to collagen, the measurement of hydroxyproline levels is a standard metric for collagen content. Using a series of 96-well plates, the assay was performed for each sample in duplicate, according to the supplier's protocol. Absorbance readings for each sample, in addition to three sets of hydroxyproline standards per plate, were obtained at 560 nm using a Synergy^{TM} H4 plate reader (BioTek, Winooski, VT).

D.2.4 Data Processing and Statistical Analysis

F_P values were the maximum recorded force during suture pullout testing. For collagen quantification testing, based on the absorbance readings from the hydroxyproline standards, a standard curve was computed for each plate (R^2>0.98 in all cases). This curve was used to compute mg hydroxyproline per well, and in turn mg hydroxyproline per mg tissue (i.e. hydroxyproline mass fraction, HYP).

Statistical analysis was performed using Minitab (Minitab, Inc., State College, PA) and MATLAB (MathWorks, Natick, MA). For both F_P and HYP, nested ANOVA models were used, with suture positions nested within regions as shown in Figure D-1. Tukey's Honestly Significant Difference post-hoc correction was used to test for pairwise differences. Separate ANOVA models were used for MV and TV data. Although these ANOVA models exhibited normally distributed residuals, the F_P or HYP results themselves were not normally distributed. Therefore, F_P or HYP results were compared

between valves via Mann-Whitney U-test. Additional comparisons between valves were made after excluding the TV trigonal region. This is of interest because the atrioventricular node sits very close to this region, and surgeons often avoid placing sutures in this region to minimize risk of introducing cardiac rhythm defects. Additionally, in order to test the causal relationship between collagen content and suture holding strength, HYP and F_P were correlated. Distinct correlations were assessed for each valve. Correlations were computed both on a point-by-point basis and on a positionally-averaged basis.

D.3 Results

Key donor descriptors are shown in Table D-1. 50% of donors were male.

Table D-1 Descriptors of donor hearts (N=6). Post-mortem interval is the total time between donor death and tissue cryopreservation.

	Min	Mean	Max
Age	60	71	79
Post-mortem interval (days)	3	5.7	8
Body mass index	16.7	22.5	28.6

D.3.1 Pullout Testing

Pullout was successful for 58/60 mitral and 71/72 tricuspid sutures (with three failures due to experimental error). Among all MV or all TV positions, mean ± standard deviation F_P was 7.8 ± 2.9 N or 8.2 ± 6.1 N, respectively. Median (inter-quartile range) F_P was 7.4 (6.0-9.1) N for MV or 6.6 (5.2-8.2) N for TV. These were not significantly different by Mann-

Whitney U-test (p=0.115). Excluding the trigonal region, TV F_P was 6.3 (4.6-7.6) N, which was significantly less than MV F_P (p<0.001). Positional and regional analyses are presented below.

Table D-2 ANOVA results for F_P, before post-hoc analysis.

	Factor	F	p
Mitral	Position (nested within region)	0.20	0.984
	Region	2.16	0.126
Tricuspid	Position (nested within region)	4.48	<0.001
	Region	46.83	<0.001

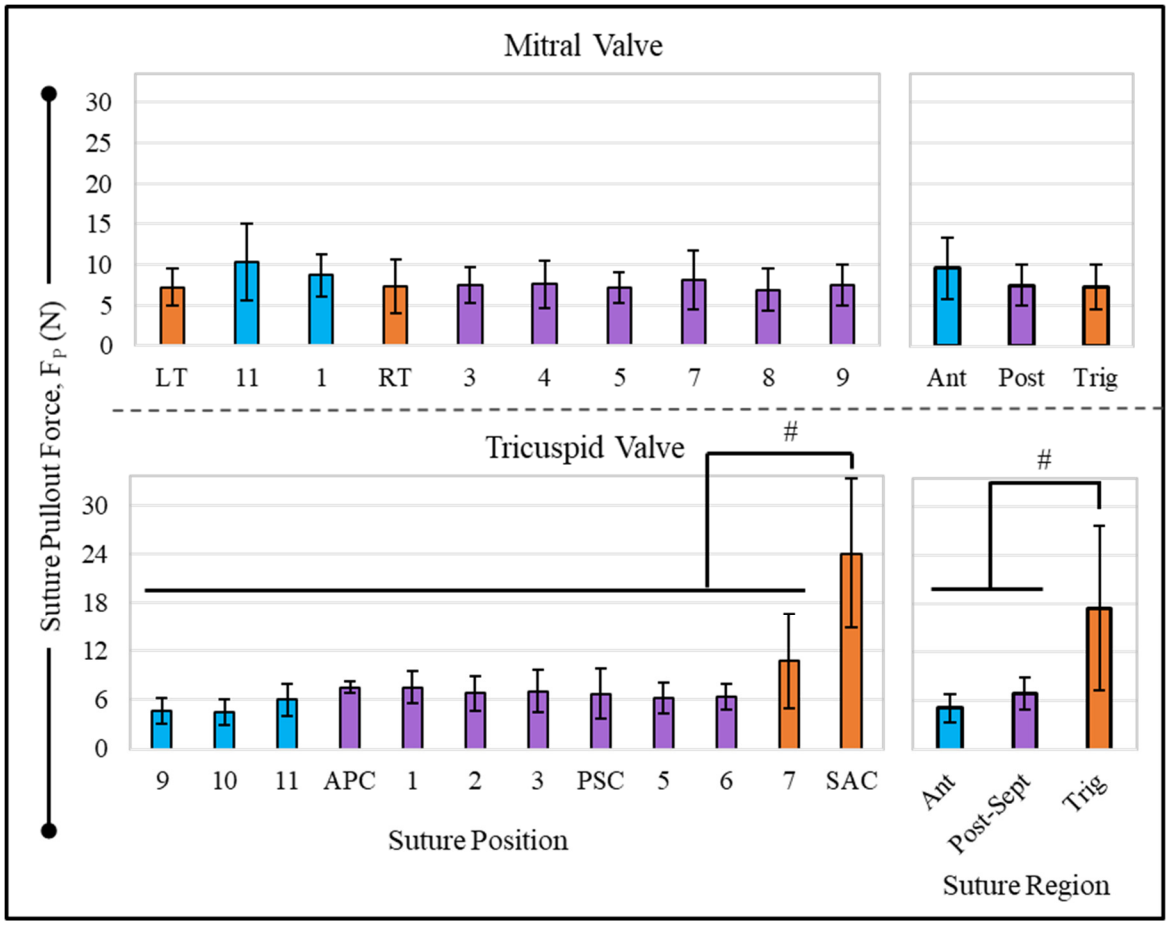

Figure D-3 Mean ± SD F_P results, with ANOVA results depicted by symbol notation. #p<0.001.

The weakest and strongest MV positions were 8 o'clock, in the posterior region, and 11 o'clock, in the anterior region (mean ± standard deviation, 6.9 ± 2.6 N and 10.3 ± 4.7 N, respectively). The ANOVA model for MV F_P did not detect significance in either position or region. Accordingly, no pairwise differences by position or region were found (although anterior sutures showed a trend toward higher F_P, with p=0.130 or 0.201 versus posterior or trigonal sutures).

Whereas mean F_P for every MV position fell within 3.3 N, pullout forces were more diverse for the TV. The weakest and strongest TV positions were 10 o'clock, in the anterior region, and SAC, in the trigonal region (mean ± standard deviation, 4.5 ± 1.6 N and 24.0 ± 9.3 N, respectively). 7 o'clock, also in the trigonal region, had F_P of 10.8 ± 5.8 N; no other position had mean F_P over 7.5 N. SAC was significantly stronger than every other position, and the trigonal region (F_P=17.4 ± 10.1 N), was significantly stronger than every other region (each $p<0.001$).

D.3.2 Hydroxyproline Fraction Testing

HYP was successfully measured in 57/60 mitral and 71/72 tricuspid sutures (with failures due to experimental error either during the preceding suture pullout test or during tissue excision). Among all MV or all TV positions, mean ± standard deviation HYP was 8.4 ± 4.1 mg/g or 5.0 ± 2.7 mg/g, respectively. Median (inter-quartile range) HYP was 6.8 (5.1-11.2) mg/g for MV or 4.4 (3.3-6.1) mg/g for TV. Excluding the trigonal region, TV HYP was 4.2 (3.1-5.5 N). With or without the TV trigonal region, TV HYP was significantly less than MV HYP ($p<0.001$). Positional and regional analyses are presented below.

Table D-3 ANOVA results for HYP, before post-hoc analysis.

	Factor	**F**	**p**
Mitral	Position (nested within region)	1.31	0.265
	Region	6.93	0.002
Tricuspid	Position (nested within region)	0.96	0.480
	Region	24.76	<0.001

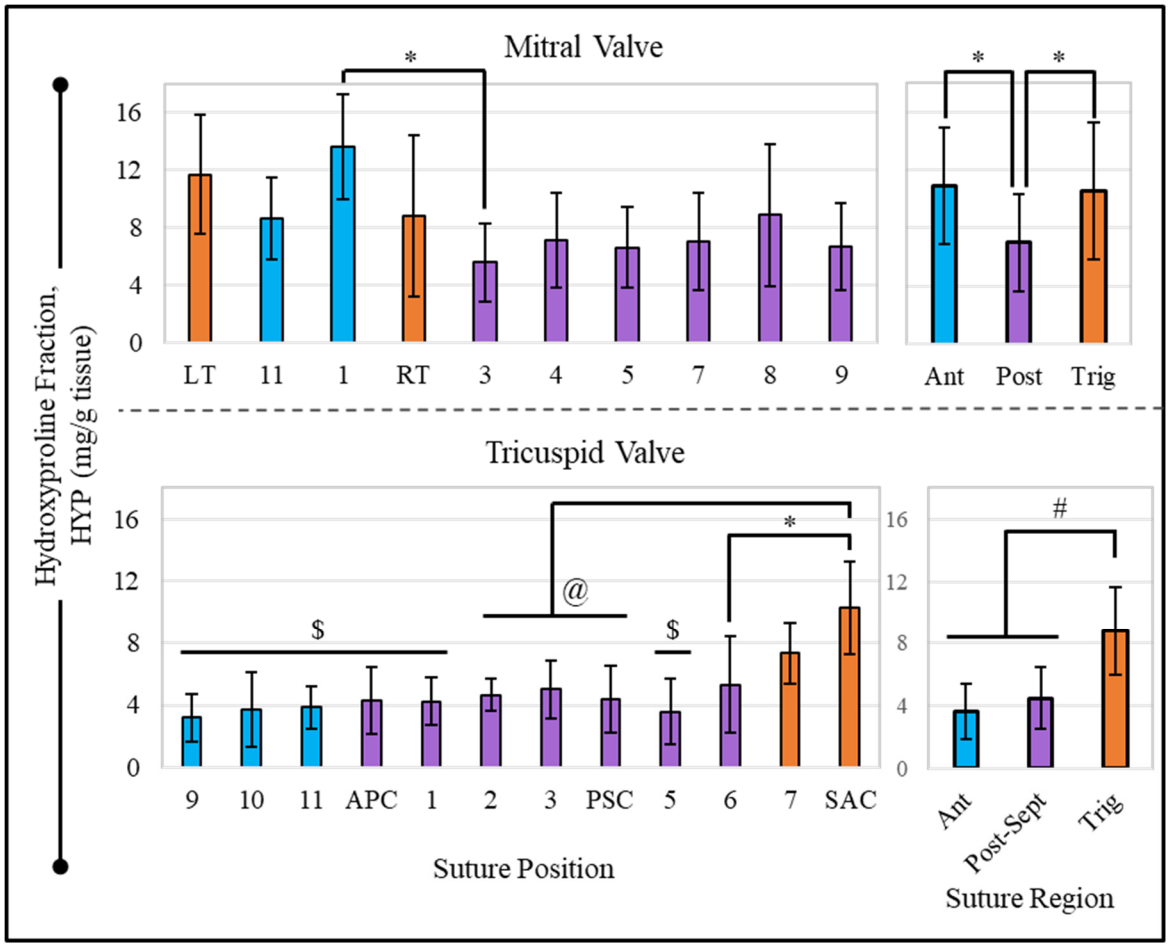

Figure D-4 Mean ± SD HYP results, with ANOVA results depicted by symbol notation. *p<0.05; @p<0.005; #p<0.001; $p<0.001 vs. SAC.

For the MV, the least and most dense HYP positions were 3 o'clock, in the posterior region, and 1 o'clock, in the anterior region (5.6 ± 2.7 mg/g and 13.6 ± 3.7 mg/g). 1 o'clock HYP was significantly greater than 3 o'clock (p=0.022); no significant differences were detected among suture positions, the posterior region (HYP=7.0 ± 3.3 mg/g) was less dense than each other region (p=0.006 vs. anterior, p=0.047 vs. trigonal).

For the TV, the least and most dense HYP positions were 9 o'clock, in the posterior region, and SAC, in the trigonal region (3.2 ± 1.5 mg/g and 10.3 ± 3.0 mg/g). Similarly to

F_P results, 7 o'clock exhibited the second-highest HYP (7.3 ± 2.0 mg/g); no other position had mean HYP over 5.3 mg/g. SAC had significantly greater HYP than all other positions except for 7 o'clock (each $p \leq 0.007$). The trigonal region (HYP=8.8 ± 2.6 mg/g) had significantly greater HYP than either other region (each $p < 0.001$).

D.3.3 Pullout Force and Hydroxyproline Fraction Correlation

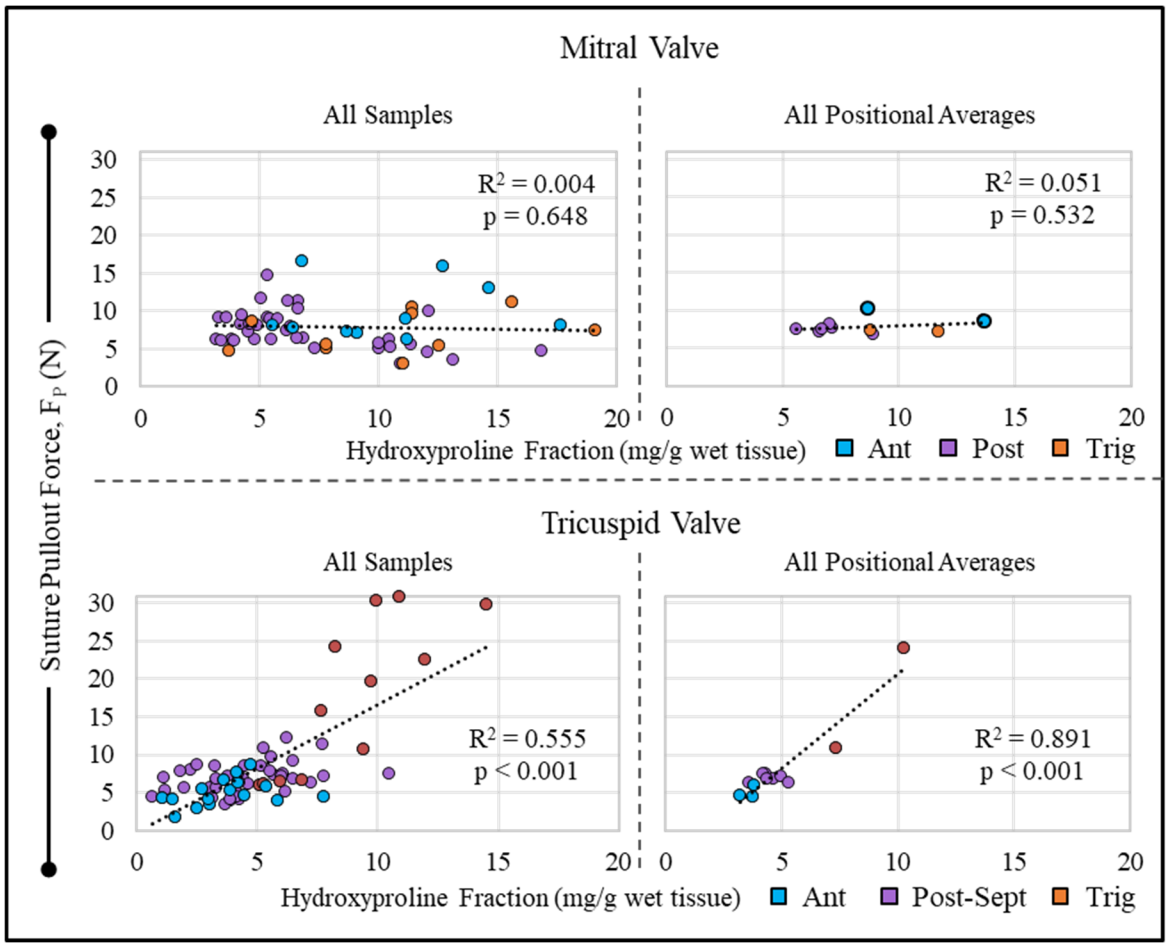

Figure D-5 Correlations of hydroxyproline fraction (a metric for collagen content) versus suture pullout force. Correlations are computed for each valve, both using *every* available data point and using *mean* data from each suture position.

As shown in Figure D-5 no correlation existed between HYP and F_P for the MV, however, a significant correlation existed for the TV. These findings were consistent whether accounting for all data points or mean values. It was also observed that data points from a given suture region tended to "cluster" together for the TV, but not for the MV.

D.4 Discussion

This investigation measured both suture pullout forces (F_P) and collagen content (in the form of hydroxyproline mass fraction, HYP) in mitral and tricuspid annuli from six donors age 60-79 with no history of heart disease. Both F_P and HYP were measured from each tissue sample. Numerous phenomena observed here mirrored those in the earlier SA1 and APPENDIX C studies, which utilized multiple cohorts of ovine hearts, and which quantified annular collagen via colorimetric analysis of fluoroscopic images. Across all MV studies, F_P was greatest for sutures placed in the anterior tissue, between the trigones. Across all TV studies, a strong F_P peak was consistently exhibited *approximately* near the septum. Also, it was found in all TV studies that F_P correlated strongly to collagen content. It is notable that, in the human tissue cohort, similar F_P vs. HYP correlations were observed whether accounting for all individual data points or positional means (Figure D-5). This observation adds validity to the correlations based on positional means in SA 1 and APPENDIX C.

Of equal importance, multiple findings from the present cohort differed from earlier findings obtained using ovine hearts. Firstly, although the human mitral annulus exhibited highest F_P between the trigones, differences in F_P were not significant among mitral suture positions or regions. In ovine tissue, the same trend was seen, but with statistical significance (Figure 6-11). Considering the similar physiologic surroundings for both the ovine and human inter-trigonal annulus (i.e. the cyclic rise and fall of the annular saddle, coupled to ventricular contraction and aortic root expansion), the lack of significance may reflect age-associated stiffening and/or calcification of these samples, which could impact F_P irrespective of collagen density (some such calcification was noted qualitatively,

especially along the posterior annulus, however it was not evaluated quantitatively). Alternatively, it may be a reflection of the limited sample size of the human tissue cohort. In either case, additional analyses in a larger cohort of human tissue would offer clarification.

Another distinct finding in the present data was the nature of the TV "spike" in F_P. In APPENDIX C, the strongest position in the ovine TV annulus had mean F_P=10.0 N, which was approximately 62% greater than all other positions (Figure C-3). In the human TV annulus, the strongest position had F_P = 24.0 N, which was approximately 257% greater than all other positions. Interestingly, this spike was located at 6 o'clock (above the mid-septal leaflet) in the ovine tissue, versus at the septal-anterior commissure in the human tissue. These positions were defined with respect to the leaflets and commissures. However, it is important to recognize that both of these positions were at or near the trigone. The shift in peak F_P location with respect to the commissures may reflect a difference in the anatomy of the two species: namely, the ovine septal leaflet occupies a larger portion of the annulus than does its human counterpart, placing the ovine trigone closer to 6 o'clock, as defined in this study. Rausch et al recently found that the septal leaflet occupied approximately 40-50% of the annulus in most ovine subjects.[211] Meanwhile, Kawada et al, found the same quantity averaged 31% in humans.[212] Regardless, the surprising strength of the human TV trigonal region adds further support to the notion that the heightened prevalence of tricuspid dehiscence from the septal annulus[175] owes to sub-optimal suture placement in that region as a means to avoid injury to the atrioventricular node.

Two unanticipated, likely related discrepancies were observed between the human mitral and tricuspid annuli. For the mitral annulus, collagen and F_P showed no relationship

(although collagen did correlate moderately with F_P and strongly with RS in ovine tissue; Figure D-5 and Figure 6-15). This is in contrast to the tricuspid annulus, where a strong correlation was observed in both species (Figure C-5). Meanwhile, although median TV F_P was within 11% of median MV F_P, median TV HYP was over 35% reduced versus median MV HYP. In other words, although tricuspid annular collagen was substantially reduced versus mitral annular collagen, this did not translate to an equal reduction in suture holding strength. Taken together, these two findings suggest that some discrepancy between mitral and tricuspid collagen must better enable the latter to withstand suture tension. Such differences could include collagen fiber alignment, which is well-known to impact directional material properties in valve leaflets.[213] In the setting of annular sutures, fiber alignment parallel to the suture path (i.e. circumferentially aligned) could inhibit the suture's ability to engage the fibers' load-bearing capacity, even if they are more densely packed. Another possible explanation is collagen sub-type. Strengths of different collagen sub-types are known to differ;[214] the hydroxyproline assay does not distinguish among them.

Both the limitations of this work, and its potential applications to device design and surgical practice, are as described earlier (see Sections 6.3.6 and C.4). In addition to the aforementioned follow-up studies that could shed further light collagen-suture holding strength relationships observed in this cohort of human valve annuli, further testing is warranted using larger cohorts of normal and diseased human tissue.

D.5 Conclusion

F_P and collagen distribution in mitral and tricuspid annuli from aged human donors largely paralleled those in ovine tissue, with two key exceptions. First, human mitral annular collagen showed no correlation to associated F_P. Second, the peak in tricuspid F_P near the trigone was far more pronounced in human tissue. These findings emphasize the importance of future anchor mechanics testing using larger cohorts of both normal and diseased human annuli. Also, tricuspid annular collagen content, although 35% less than mitral, correlated strongly with F_P, leading to F_P values only 11% less than mitral. These observations may be further explained through investigations into collagen type and/or alignment in either valve.

APPENDIX E. DATA TABLES FOR SPECIFIC AIM 1

E.1 Specific Aim 1.A Data

Table E-1 *In vivo* cyclic suture forces (N) using undersized Physio rings.

Animal ID		GTA2	GTA3	GTA6	GTA7	GTA11
Annulus Size		30	30	30	30	30
LVP_{max} = 100 mmHg	LT	4.16	3.88	2.26	1.48	3.51
	11 o'clock	1.97	2.12	1.66	1.97	1.52
	1 o'clock	2.58	2.79	0.63	0.38	1.79
	RT	3.38	4.37	1.53	5.61	2.24
	3 o'clock	1.15	1.36	5.30	1.20	2.00
	4 o'clock	0.17	2.69	2.68	1.62	1.43
	5 o'clock	1.35	1.99	0.78	1.50	1.17
	7 o'clock	0.81	0.26	1.13	1.48	0.97
	8 o'clock	0.85	1.58	0.57	2.26	1.26
	9 o'clock	2.66	2.76	0.33	1.14	1.76
LVP_{max} = 125 mmHg	LT	4.64	4.38	2.56	2.13	3.92
	11 o'clock	2.39	2.39	1.91	2.19	1.69
	1 o'clock	3.21	2.94	0.84	0.60	2.00
	RT	4.15	5.03	1.71	5.22	2.24
	3 o'clock	1.42	1.52	6.56	1.78	1.88
	4 o'clock	0.27	3.10	3.47	1.86	1.49
	5 o'clock	1.68	2.18	1.01	1.89	1.16
	7 o'clock	1.00	0.36	1.04	1.66	0.87
	8 o'clock	0.99	1.80	0.90	2.34	1.37
	9 o'clock	3.08	3.33	0.56	1.14	1.77
LVP_{max} = 150 mmHg	LT	4.81	4.86	2.73	2.34	4.52
	11 o'clock	2.80	2.75	2.17	2.79	1.92
	1 o'clock	3.28	3.00	0.90	0.65	2.16
	RT	4.78	5.65	1.79	5.22	2.40
	3 o'clock	1.43	1.72	7.25	2.00	2.37
	4 o'clock	0.19	2.07	3.94	2.45	1.71
	5 o'clock	1.90	2.45	1.07	2.16	1.36
	7 o'clock	0.81	0.55	1.11	2.27	0.98
	8 o'clock	1.06	2.12	0.91	2.31	1.62
	9 o'clock	3.57	3.94	0.62	1.39	1.74

Table E-2 *Ex vivo* suture pullout forces (N) from ovine mitral annuli. For italicized data points, terminal displacement was reached before pullout; *maximum* force recorded during trial is used.

Heart ID	Ov1	Ov2	Ov3	Ov4	Ov5	Ov6
LT	4.76	4.72	1.91	2.48	3.06	3.20
11 o'clock	2.55	*8.13*	8.77	9.79	2.44	6.53
1 o'clock	4.16	*10.70*	*7.72*	*12.03*	2.63	5.42
RT	*10.32*	5.11	3.80	*12.64*	2.45	2.68
3 o'clock	4.28	4.53	3.83	3.62	4.26	5.56
4 o'clock	2.93	5.87	3.92	2.98	5.32	3.26
5 o'clock	1.46	6.43	2.23	4.88	5.48	3.42
7 o'clock	2.28	5.46	3.67	2.42	1.73	4.91
8 o'clock	1.84	6.08	4.16	1.95	4.42	1.34
9 o'clock	3.51	9.27	4.78	3.61	6.93	1.71
Heart ID	Ov7	Ov8	Ov9	Ov10	Ov11	Ov12
LT	2.88	7.35	7.43	10.58	8.09	3.50
11 o'clock	4.76	6.38	6.09	6.21	12.38	4.86
1 o'clock	2.46	*13.52*	8.46	5.31	5.66	10.85
RT	3.76	*17.57*	5.42	6.57	3.16	5.00
3 o'clock	3.92	4.85	4.55	6.29	4.54	5.10
4 o'clock	3.17	2.09	5.29	3.97	4.23	2.47
5 o'clock	2.37	1.60	5.97	7.40	4.47	2.97
7 o'clock	2.83	4.18	2.03	3.68	3.03	1.36
8 o'clock	3.52	2.13	3.05	3.91	3.90	3.41
9 o'clock	4.20	3.76	5.25	7.00	2.86	1.68

Table E-3 Mean Pixel Intensity, before and after normalization, from microstructural imaging of ovine mitral annuli.

Heart ID			Ov13	Ov14	Ov15	Ov16	Ov17
Mean Pixel Intensity (MPI)	Collagen	LT	3.91	16.57	8.14	6.47	12.51
		12	21.16	31.54	30.56	10.55	20.54
		RT	12.91	10.89	7.47	10.22	10.96
		6	3.45	35.31	11.76	4.52	6.80
	Myocardium	LT	45.77	11.22	14.32	26.95	17.32
		12	30.27	10.78	9.14	41.87	65.96
		RT	49.00	11.50	16.22	55.07	17.79
		6	52.22	8.84	14.88	53.27	20.98
normalized Mean Pixel Intensity (nMPI)	Collagen	LT	0.38	0.70	0.56	0.81	0.98
		12	2.04	1.34	2.11	1.33	1.62
		RT	1.25	0.46	0.52	1.29	0.86
		6	0.33	1.50	0.81	0.57	0.54
	Myocardium	LT	1.03	1.06	1.05	0.61	0.57
		12	0.68	1.02	0.67	0.95	2.16
		RT	1.11	1.09	1.19	1.24	0.58
		6	1.18	0.83	1.09	1.20	0.69

E.2 Specific Aim 1.B Data

Note, in addition to the below, the data in Table E-1 was also used in Specific Aim 1.B. Also note, throughout the tables in Section E.2, missing F_C data was due to peri-operative failure of Suture Force Transducers. Missing $HWHM_{norm}$ data was due to low signal-to-noise ratio, which rendered half-max localization unreliable.

Table E-4 *In vivo* cyclic suture forces (N) using true-sized Physio rings.

Animal ID		GTA4	GTA5	GTA8	GTA9	GTA10
Annulus Size		26	32	28	30	28
LVP_{max} = 100 mmHg	LT	2.03	2.43	1.26	0.96	1.93
	11 o'clock	1.35	1.56	2.26	1.51	0.50
	1 o'clock	1.94	0.48	1.00	1.72	0.33
	RT	1.49	0.47	2.25	3.39	1.40
	3 o'clock	1.50	2.13	1.58	1.43	2.41
	4 o'clock	1.38	1.97	1.76	1.55	1.95
	5 o'clock	0.92	1.49	2.28	1.74	1.12
	7 o'clock	0.60	0.81	1.45	0.86	0.57
	8 o'clock	0.89	0.98	1.39	0.70	0.72
	9 o'clock	2.58	2.37	2.05	1.52	0.49
LVP_{max} = 125 mmHg	LT	2.37	2.87	1.87	1.29	2.11
	11 o'clock	1.60	1.82	1.78	2.10	0.45
	1 o'clock	2.42	0.53	1.41	2.08	0.29
	RT	1.70	0.62	3.12	4.23	1.61
	3 o'clock	1.59	3.17	2.56	1.77	2.94
	4 o'clock	1.76	2.40	2.48	1.88	2.27
	5 o'clock	1.19	1.73	2.12	2.17	1.36
	7 o'clock	0.87	0.88	1.59	1.15	0.67
	8 o'clock	1.22	1.13	1.90	0.83	0.75
	9 o'clock	2.94	2.79	1.48	1.68	0.48
LVP_{max} = 150 mmHg	LT	2.91	3.29	2.20	1.56	2.30
	11 o'clock	1.87	1.84	2.12	2.34	0.52
	1 o'clock	3.13	0.62	1.74	2.42	0.28
	RT	2.11	0.93	3.87	4.87	1.88
	3 o'clock	1.77	3.23	2.95	2.02	3.39
	4 o'clock	1.86	2.80	2.73	2.19	2.47
	5 o'clock	1.51	1.99	2.39	2.46	1.55
	7 o'clock	0.78	0.78	1.69	1.33	0.78
	8 o'clock	1.29	1.27	2.14	0.94	0.64
	9 o'clock	3.12	3.09	1.63	1.83	0.67

Table E-5 *In vivo* cyclic suture forces (N) using undersized Profile 3D rings.

Animal ID		GTA12	GTA18	GTA20	GTA26	GTA27	GTA28
Annulus Size		26	26	26	26	26	26
LVP_{max} = 100 mmHg	LT	0.75	0.66	2.48	1.45	3.39	1.25
	11 o'clock	1.81	1.07	2.04	1.75	0.65	1.50
	1 o'clock	1.77	2.87	3.97	2.21	1.65	2.43
	RT	4.27	1.16	2.69	2.90	1.08	2.09
	3 o'clock	1.93	1.99	1.54	3.52	1.53	1.37
	4 o'clock	2.05	1.35	1.45	3.34	0.90	0.58
	5 o'clock	3.04	1.17	1.64	3.13	0.95	0.91
	7 o'clock	1.72	1.36	1.68	1.59	1.69	1.10
	8 o'clock	1.34	2.41	1.48	2.13	1.99	0.48
	9 o'clock	2.10	1.14	0.62	2.52	0.32	0.64
LVP_{max} = 125 mmHg	LT	1.03	0.94	3.36	2.01	4.14	1.55
	11 o'clock	2.01	1.33	2.89	1.33	0.92	1.87
	1 o'clock	2.05	3.76	5.05	2.63	2.04	2.41
	RT	4.97	1.57	3.57	3.43	1.33	2.65
	3 o'clock	2.21	2.32	1.73	3.98	1.66	1.61
	4 o'clock	2.42	1.55	1.72	3.98	1.33	0.74
	5 o'clock	3.94	1.38	2.00	3.50	0.96	1.21
	7 o'clock	2.03	1.48	2.00	1.60	1.90	1.41
	8 o'clock	1.66	2.63	1.78	2.29	2.35	0.36
	9 o'clock	2.19	1.37	0.84	2.97	0.48	0.80
LVP_{max} = 150 mmHg	LT	1.23	1.15	4.44	2.40	4.38	1.84
	11 o'clock	2.39	1.50	2.82	2.31	0.99	2.91
	1 o'clock	2.34	4.68	5.22	3.39	2.39	2.96
	RT	5.14	1.86	4.01	3.83	1.63	3.80
	3 o'clock	2.17	2.49	1.71	4.24	1.71	1.66
	4 o'clock	2.75	1.87	1.87	4.14	1.14	0.71
	5 o'clock	4.21	1.71	2.40	4.49	1.02	1.26
	7 o'clock	2.06	1.62	2.32	1.99	1.80	1.40
	8 o'clock	1.80	2.94	1.97	2.81	2.49	0.28
	9 o'clock	2.52	1.51	1.13	2.90	0.67	0.85

Table E-6 *In vivo* cyclic suture forces (N) using true-sized Profile 3D rings.

Animal ID		GTA 19	GTA 21	GTA 22	GTA 23	GTA 25	GTA 29	GTA 30
Annulus Size		28	28	26	26	26	30	30
LVP_{max} = 100 mmHg	LT	0.39	3.59	2.16	2.47	2.03	3.77	1.80
	11 o'clock	0.41	0.51	1.19	0.32	0.42	2.27	1.59
	1 o'clock	0.52	2.56	1.61	0.59	2.42	3.27	1.06
	RT	1.33	2.54	1.71	1.97	3.78	2.43	3.04
	3 o'clock	0.26	1.45	2.96		2.84	1.35	1.01
	4 o'clock	0.93	1.28	2.59	1.28	1.63	1.31	1.77
	5 o'clock	0.51	2.46	1.88	1.25	1.66	1.46	1.05
	7 o'clock	3.26	2.40	2.42	1.01	0.18	2.82	2.55
	8 o'clock	1.88	1.26	2.79	2.04	3.16	1.56	1.06
	9 o'clock	0.30	0.41	1.53	1.75	0.66	0.40	1.02
LVP_{max} = 125 mmHg	LT	0.42	4.89	2.53	2.89	2.27	4.54	2.38
	11 o'clock	0.56	0.86	1.44	0.45	0.79	2.85	1.69
	1 o'clock	0.60	2.86	1.88	0.88	2.61	3.34	1.15
	RT	1.72	3.05	2.34	2.25	3.79	3.41	3.96
	3 o'clock	0.25	1.47	3.48		2.77	1.61	1.30
	4 o'clock	1.27	1.45	3.03	1.51	1.79	1.27	2.17
	5 o'clock	0.58	2.73	2.20	1.37	2.21	1.60	1.46
	7 o'clock	3.90	2.88	2.95	1.17	0.18	3.05	3.13
	8 o'clock	2.39	1.55	3.24	2.37	3.10	1.84	1.23
	9 o'clock	0.28	0.59	1.57	2.05	0.76	0.55	1.33
LVP_{max} = 150 mmHg	LT	0.54	4.99	2.93	3.69	3.17	5.13	2.84
	11 o'clock	0.74	0.91	2.08	0.95	2.02	3.39	1.98
	1 o'clock	0.74	2.39	1.97	1.47	2.84	3.77	1.65
	RT	1.72	2.35	3.18	2.61	4.58	3.62	4.99
	3 o'clock	0.25	2.17	3.49		2.93	1.97	1.41
	4 o'clock	1.27	1.68	2.95	1.14	2.39	1.70	2.39
	5 o'clock	0.58	2.47	2.04	1.10	2.61	1.99	1.56
	7 o'clock	3.90	3.08	2.83	1.39	0.19	3.41	3.21
	8 o'clock	2.39	1.58	3.03	2.70	3.03	2.14	1.01
	9 o'clock	0.28	0.57	1.75	2.25	0.95	0.65	0.93

Table E-7 *In vivo* cyclic suture forces (N) using undersized, rigid, Physio ring prototypes.

Animal ID		GTA34	GTA35	GTA36	GTA44	GTA45	GTA46
Annulus Size		32	34	32	32	32	32
	LT	1.10	4.21	0.58	2.26	0.73	0.77
	11 o'clock	1.30	2.04	2.86	2.85	2.12	0.44
	1 o'clock	0.17	1.41	1.36	3.78	2.21	0.68
	RT	1.98	2.28	3.96	2.74		
	3 o'clock	1.33	2.24	1.62	1.17	0.68	0.94
	4 o'clock	1.22	1.31	1.47		0.79	1.31
	5 o'clock	2.61	1.69	1.63		1.66	1.42
	7 o'clock	1.68	0.93	2.25	2.45	1.75	0.43
LVP_{max} = 100	8 o'clock	1.60	0.99	1.55	1.56	2.42	0.97
mmHg	9 o'clock	0.66	0.56	2.20	3.24	3.71	0.60
	LT	1.71	5.50	0.98	2.49	1.05	0.92
	11 o'clock	1.80	2.39	3.41	3.35	2.12	0.69
	1 o'clock	0.31	1.45	1.69	4.23	2.17	0.71
	RT	2.49	2.67	4.80	3.32		
	3 o'clock	1.96	3.31	2.10	1.17	0.69	1.11
	4 o'clock	1.97	1.81	2.29		0.91	1.80
	5 o'clock	3.83	2.43	2.58		1.86	2.26
	7 o'clock	2.50	1.21	3.32	3.01	2.03	0.62
LVP_{max} = 125	8 o'clock	3.41	1.32	1.91	1.83	2.58	1.22
mmHg	9 o'clock	0.89	0.91	3.39	3.81	4.97	0.79
	LT	1.91	6.49	1.15	2.68	1.01	0.88
	11 o'clock	1.41	2.62	3.47	3.98	2.07	0.77
	1 o'clock	0.28	1.61	2.05	4.38	2.32	0.86
	RT	2.82	3.29	5.38	3.83		
	3 o'clock	1.86	3.28	2.30	1.27	0.80	1.11
	4 o'clock	2.15	2.18	2.55		0.68	2.12
	5 o'clock	4.12	2.68	2.98		1.62	2.84
	7 o'clock	2.83	1.24	1.24	3.01	2.26	0.85
LVP_{max} = 150	8 o'clock	3.46	1.44	2.08	2.14	2.53	1.44
mmHg	9 o'clock	0.97	0.85	3.99	4.23	4.55	1.06

Table E-8 *In vivo* cyclic suture forces (N) using undersized, flexible, Physio ring prototypes.

Animal ID		GTA33	GTA37	GTA38	GTA39	GTA40
Annulus Size		30	34	34	32	32
LVP_{max} = 100 mmHg	LT	0.74	1.90	2.94	0.55	3.98
	11 o'clock	0.15	2.80	1.11	1.48	2.68
	1 o'clock	0.74	2.40	3.18	1.09	1.96
	RT	0.93	1.32	3.08	2.64	4.69
	3 o'clock	0.79	0.64	0.97	0.56	0.50
	4 o'clock	0.74	1.57	0.68	0.41	0.79
	5 o'clock	1.69	0.47	0.52	1.53	1.49
	7 o'clock	0.75	0.36	0.35	1.13	0.60
	8 o'clock	0.83	1.60	1.47	0.99	2.35
	9 o'clock	0.42	0.07	0.22	0.95	1.06
LVP_{max} = 125 mmHg	LT	0.79	2.05	3.35	0.71	4.67
	11 o'clock	0.26	3.20	1.62	1.91	2.78
	1 o'clock	1.04	2.37	3.58	1.29	2.85
	RT	0.87	1.20	3.65	2.83	5.85
	3 o'clock	0.98	0.66	1.36	1.08	0.60
	4 o'clock	0.80	1.73	0.82	0.48	0.99
	5 o'clock	1.99	0.51	0.73	1.78	1.57
	7 o'clock	0.91	0.46	0.36	1.37	0.79
	8 o'clock	0.98	1.53	1.81	1.22	2.68
	9 o'clock	0.31	0.11	0.18	1.27	1.11
LVP_{max} = 150 mmHg	LT	0.76	2.57	4.48	0.93	6.12
	11 o'clock	0.29	3.98	2.22	2.48	3.51
	1 o'clock	1.04	2.90	4.22	1.70	3.50
	RT	0.94	1.18	4.00	2.98	6.01
	3 o'clock	0.83	0.61	1.08	0.83	0.80
	4 o'clock	0.90	1.67	0.90	0.49	1.71
	5 o'clock	1.93	0.52	0.74	1.74	3.05
	7 o'clock	0.91	0.39	0.56	1.48	1.25
	8 o'clock	1.03	1.92	2.21	1.23	3.37
	9 o'clock	0.37	0.12	0.22	1.15	1.78

Table E-9 *In vivo* normalized half-width at half-maximum suture forces ($HWHM_{norm}$), using undersized, rigid Physio ring prototypes.

Animal ID		GTA34	GTA35	GTA36	GTA44	GTA45	GTA46
LVP_max = 100 mmHg	LT	0.19	0.06	0.20	0.07	0.05	0.18
	11 o'clock	0.14	0.06	0.10	0.06	0.06	0.21
	1 o'clock	0.12	0.07	0.10	0.06	0.06	0.09
	RT	0.10	0.06	0.10	0.09		
	3 o'clock	0.09	0.05	0.09	0.05	0.05	0.07
	4 o'clock	0.10	0.06	0.10		0.08	0.08
	5 o'clock	0.09	0.05	0.10		0.05	0.10
	7 o'clock	0.09	0.05	0.10	0.05	0.05	0.13
	8 o'clock	0.10	0.05	0.10	0.08	0.05	0.07
	9 o'clock	0.20	0.05	0.16	0.10	0.05	0.17
LVP_max = 125 mmHg	LT	0.15	0.06	0.16	0.08	0.18	0.16
	11 o'clock	0.09	0.06	0.10	0.10	0.06	0.12
	1 o'clock	0.08	0.07	0.11	0.06	0.06	0.23
	RT	0.11	0.07	0.11	0.10		
	3 o'clock	0.09	0.06	0.09	0.05	0.14	0.07
	4 o'clock	0.09	0.05	0.09		0.06	0.08
	5 o'clock	0.09	0.07	0.10		0.05	0.09
	7 o'clock	0.10	0.05	0.11	0.05	0.06	0.12
	8 o'clock	0.10	0.06	0.10	0.07	0.06	0.08
	9 o'clock	0.14	0.05	0.14	0.10	0.06	0.15
LVP_max = 150 mmHg	LT	0.13	0.07	0.15	0.07	0.43	0.12
	11 o'clock	0.38	0.07	0.10	0.06	0.28	0.07
	1 o'clock	0.07	0.15	0.11	0.07	0.15	0.32
	RT	0.10	0.08	0.12	0.10		
	3 o'clock	0.09	0.06	0.09	0.06	0.27	0.07
	4 o'clock	0.09	0.06	0.09		0.06	0.08
	5 o'clock	0.09	0.07	0.09		0.05	0.09
	7 o'clock	0.10	0.06	0.10	0.05	0.06	0.11
	8 o'clock	0.10	0.06	0.11	0.06	0.06	0.09
	9 o'clock	0.11	0.05	0.12	0.08	0.06	0.12

Table E-10 *In vivo* normalized half-width at half-maximum suture forces ($HWHM_{norm}$), using undersized (commercial, semi-rigid) Physio rings.

Animal ID		GTA2	GTA3	GTA6	GTA7	GTA11
LVP_max = 100 mmHg	LT	0.06	0.08	0.11	0.49	0.11
	11 o'clock	0.07	0.09	0.11	0.07	0.14
	1 o'clock	0.07	0.13	0.09	0.06	0.12
	RT	0.06	0.07	0.27	0.07	0.10
	3 o'clock	0.06	0.07	0.09	0.06	0.10
	4 o'clock	0.04	0.07	0.09	0.06	0.07
	5 o'clock	0.05	0.06	0.07	0.06	
	7 o'clock	0.05	0.05	0.07	0.08	
	8 o'clock	0.05	0.06	0.08	0.08	0.08
	9 o'clock	0.07	0.15	0.10	0.16	0.11
LVP_max = 125 mmHg	LT	0.07	0.08	0.10	0.50	0.11
	11 o'clock	0.07	0.08	0.10	0.08	0.11
	1 o'clock	0.09	0.08	0.09	0.07	0.11
	RT	0.08	0.08	0.28	0.08	0.10
	3 o'clock	0.06	0.07	0.10	0.07	0.09
	4 o'clock	0.06	0.07	0.09	0.07	0.06
	5 o'clock	0.05	0.06	0.07	0.07	0.07
	7 o'clock	0.06	0.06	0.07	0.14	
	8 o'clock	0.05	0.06	0.08	0.08	0.08
	9 o'clock	0.08	0.13	0.09	0.11	0.11
LVP_max = 150 mmHg	LT	0.11	0.07	0.11	0.49	0.11
	11 o'clock	0.11	0.08	0.11	0.07	0.10
	1 o'clock	0.10	0.08	0.10	0.07	0.11
	RT	0.10	0.08	0.33	0.09	0.10
	3 o'clock	0.09	0.07	0.11	0.07	0.10
	4 o'clock	0.06	0.06	0.09	0.07	0.07
	5 o'clock	0.09	0.06	0.08	0.07	0.07
	7 o'clock	0.09	0.05	0.15	0.08	
	8 o'clock	0.08	0.06	0.09	0.08	0.08
	9 o'clock	0.13	0.11	0.10	0.09	0.13

Table E-11 *In vivo* normalized half-width at half-maximum suture forces ($HWHM_{norm}$), using undersized, flexible Physio ring prototypes.

Animal ID		GTA33	GTA37	GTA38	GTA39	GTA40
LVP_max = 100 mmHg	LT	0.11	0.08	0.08	0.18	0.07
	11 o'clock	0.17	0.08	0.07	0.26	0.07
	1 o'clock	0.19	0.07	0.08	0.26	0.07
	RT	0.12	0.07	0.07	0.08	0.07
	3 o'clock	0.08	0.05	0.15	0.17	0.05
	4 o'clock	0.08	0.07	0.09	0.05	0.06
	5 o'clock	0.10	0.05	0.06	0.11	0.06
	7 o'clock	0.09	0.10	0.17	0.08	0.09
	8 o'clock	0.12	0.07	0.07	0.09	0.07
	9 o'clock	0.52		0.19	0.25	0.08
LVP_max = 125 mmHg	LT	0.11	0.09	0.08	0.44	0.07
	11 o'clock	0.18	0.09	0.07	0.10	0.07
	1 o'clock	0.28	0.08	0.08	0.17	0.07
	RT	0.13	0.18	0.07	0.08	0.08
	3 o'clock	0.08	0.06	0.10	0.09	0.05
	4 o'clock	0.07	0.08	0.07	0.05	0.07
	5 o'clock	0.09	0.17	0.06	0.21	0.07
	7 o'clock	0.08	0.13	0.14	0.08	0.29
	8 o'clock	0.12	0.08	0.07	0.23	0.08
	9 o'clock	0.48		0.29	0.13	0.13
LVP_max = 150 mmHg	LT	0.12	0.11	0.09	0.30	0.09
	11 o'clock	0.10	0.09	0.07	0.14	0.08
	1 o'clock	0.13	0.09	0.08	0.13	0.09
	RT	0.12	0.20	0.08	0.10	0.08
	3 o'clock	0.07	0.06	0.08	0.18	0.57
	4 o'clock	0.29	0.08	0.07	0.06	0.05
	5 o'clock	0.09	0.44	0.06	0.18	0.07
	7 o'clock	0.09	0.13	0.10	0.11	0.09
	8 o'clock	0.12	0.09	0.08	0.11	0.09
	9 o'clock	0.44		0.11	0.23	0.09

E.3 Specific Aim 1.C Data

Note, in addition to the below, Table E-1, Table E-7, and Table E-8 were used in SA1.C.

Table E-12 *In vivo* cyclic suture forces (N) using prototype hybrid rings.

Animal ID		GTA47	GTA48	GTA49
Annulus Size		34	34	34
LVP_{max} = 100 mmHg	LT	0.59	1.73	2.09
	11 o'clock	3.03	2.25	1.65
	1 o'clock	2.44	2.96	4.52
	RT	1.00	1.20	0.98
	3 o'clock	0.94	1.35	0.45
	4 o'clock	0.20	0.94	2.77
	5 o'clock	0.39	1.41	2.01
	7 o'clock	1.90	2.03	0.20
	8 o'clock	1.16	2.12	0.64
	9 o'clock	1.22	1.69	0.83
LVP_{max} = 125 mmHg	LT	0.47	2.03	2.15
	11 o'clock	3.92	2.84	0.67
	1 o'clock	2.69	3.27	4.83
	RT	1.30	1.60	1.15
	3 o'clock	0.79	1.68	0.76
	4 o'clock	0.26	1.08	3.46
	5 o'clock	0.56	1.69	2.51
	7 o'clock	1.75	2.18	0.27
	8 o'clock	1.10	2.32	0.89
	9 o'clock	1.26	1.87	0.89
LVP_{max} = 150 mmHg	LT	0.49	2.48	2.09
	11 o'clock	4.72	3.58	0.48
	1 o'clock	2.77	3.64	4.66
	RT	1.60	1.74	1.30
	3 o'clock	1.06	1.77	1.03
	4 o'clock	0.31	1.17	4.18
	5 o'clock	0.90	1.80	2.77
	7 o'clock	2.09	2.34	0.40
	8 o'clock	1.34	2.58	0.78
	9 o'clock	1.58	2.03	1.28

APPENDIX F. DATA TABLES FOR SPECIFIC AIM 2

F.1 Specific Aim 2.A Data

Note, in three instances (Porc2 D+4, Porc3 D+6, Porc7 D+6) substantial variability was noticed between acquisitions, in real-time. In these cases a fourth acquisition was collected. Also, in four instances (Porc1 D+2, Porc1 C+4, Porc3 C+4, Porc5 C+4), positioning errors were noticed only during post-processing (evidenced by a sharp shift in pressure and leakage in the middle of the acquisition); these acquisitions were discarded.

Table F-1 Paravalvular Leakage (PVL) and trans-mitral pressure gradient (ΔP) data using eight mock TMV plugs.

Heart ID	Size	Circular		D-shape	
		ΔP (mmHg)	PVL (ml/sec)	ΔP (mmHg)	PVL (ml/sec)
		59.5	7.0	63.9	8.7
		97.6	17.1	73.9	9.7
		119.3	27.8	91.9	15.7
		145.0	35.8	122.3	26.0
		158.5	69.8	170.3	60.2
		61.7	8.7	61.5	6.0
		92.5	10.5	77.9	5.3
		120.0	18.8	90.7	20.8
		146.4	42.0	114.1	32.7
		166.0	65.9	157.6	73.9
		59.5	9.3	60.5	2.5
		71.3	11.7	95.4	7.0
		88.2	14.8	116.6	9.7
		116.5	36.1	133.0	23.7
	+0	157.4	72.1	191.6	47.0
		58.0	6.4		
		101.3	10.3		
		125.7	29.6		
		145.7	37.7		
		174.3	59.1		
		62.1	8.8	61.5	5.9
		89.8	8.4	96.9	7.9
		117.6	15.9	117.6	14.4
		151.5	60.2	135.0	43.6
		160.0	69.7	169.3	65.8
		61.7	9.7	61.6	2.9
		98.8	15.0	91.8	4.1
		126.7	14.9	122.0	18.7
		136.5	27.5	144.8	58.7
Porc1	+2	155.4	74.1	149.9	77.0

Table F-1 continued

Heart ID	Size	Circular		D-shape	
		ΔP (mmHg)	PVL (ml/sec)	ΔP (mmHg)	PVL (ml/sec)
				57.5	3.5
				79.1	1.3
				95.4	4.1
				120.4	22.5
				159.9	65.3
		63.8	6.4	52.5	2.6
		96.7	3.6	91.5	9.0
		120.2	13.1	127.1	21.1
		156.1	44.5	158.3	45.6
		177.3	53.7	171.8	62.5
		61.7	13.1	56.3	5.8
		89.3	22.2	80.9	7.6
		119.5	35.5	94.1	7.8
		142.5	46.7	116.2	13.5
	+4	164.5	64.0	134.3	43.2
		55.5	6.8	59.7	5.9
		95.3	9.1	87.9	6.9
		123.9	18.8	122.3	8.0
		148.9	38.5	143.4	26.6
		162.0	69.2	163.2	67.7
		66.2	6.8	57.7	4.5
		86.9	8.8	95.6	4.9
		118.3	16.4	129.6	4.7
		155.5	31.0	156.1	24.4
		168.0	65.5	179.2	57.3
		59.0	5.6	62.2	5.9
		86.8	8.8	94.4	6.2
		121.3	16.8	124.5	10.1
		129.0	37.9	156.5	25.0
Porc1	+6	155.1	50.5	168.8	64.3

Table F-1 continued

Heart ID	Size	Circular		D-shape	
		ΔP (mmHg)	PVL (ml/sec)	ΔP (mmHg)	PVL (ml/sec)
		59.6	3.6	63.3	6.6
		91.3	3.8	94.2	5.1
		119.4	5.9	124.5	3.7
		134.5	20.1	141.8	10.4
		172.3	64.2	184.4	55.5
		58.9	5.6	58.2	1.4
		93.8	9.2	93.6	3.7
		116.5	21.2	120.8	15.5
		140.3	63.0	145.0	51.6
		150.7	79.3	155.5	76.7
		60.1	5.3	57.1	1.0
		91.3	4.8	92.0	5.7
		121.9	15.5	123.5	6.4
		145.1	24.5	142.8	10.9
	+0	175.0	64.9	191.7	45.8
		60.5	2.1	60.9	1.6
		91.2	2.5	93.9	4.1
		119.7	4.7	126.4	5.0
		145.0	8.8	146.5	9.7
		190.7	44.7	189.1	43.7
		58.8	1.3	63.6	1.7
		88.7	5.8	95.4	9.9
		120.6	13.2	118.9	10.8
		141.4	20.1	142.6	14.9
		189.8	42.7	195.4	31.3
		62.1	3.3	62.5	4.4
		87.4	9.2	90.1	8.8
		120.3	13.3	124.3	10.1
		137.3	22.0	146.4	9.1
Porc2	+2	187.8	44.7	191.5	40.9

Table F-1 continued

Heart ID	Size	Circular		D-shape	
		ΔP (mmHg)	PVL (ml/sec)	ΔP (mmHg)	PVL (ml/sec)
				60.1	8.1
				89.7	7.3
				120.9	7.0
				144.7	7.3
				201.6	21.3
		61.3	3.6	59.9	6.2
		93.3	10.5	94.1	8.0
		118.6	18.1	117.4	8.5
		141.4	30.8	146.3	6.9
		171.4	64.6	197.0	31.1
		63.2	5.6	60.1	2.2
		89.8	13.4	91.3	12.6
		116.3	31.2	121.0	32.3
		134.7	70.8	137.9	70.8
		141.6	86.0	143.3	88.1
		62.8	3.8	58.4	5.0
		91.8	12.0	92.6	9.2
		119.8	19.9	121.3	8.0
		145.7	57.0	141.8	12.3
	+4	160.2	75.1	186.2	53.7
		59.9	3.9	62.2	1.0
		88.4	12.3	90.1	9.6
		119.4	33.0	120.3	10.5
		143.8	51.6	138.8	20.5
		152.3	81.7	150.8	86.1
		61.5	5.6	60.5	2.9
		93.5	9.4	89.9	11.2
		118.3	10.3	119.3	10.2
		142.1	22.2	142.1	16.8
		176.2	64.2	184.2	56.3
		60.6	7.8	60.4	1.2
		93.5	9.6	87.9	7.2
		123.5	10.2	118.0	11.3
		147.0	16.2	138.4	28.6
Porc2	+6	188.5	52.5	161.1	79.7

Table F-1 continued

Heart ID	Size	Circular		D-shape	
		ΔP (mmHg)	PVL (ml/sec)	ΔP (mmHg)	PVL (ml/sec)
		58.8	3.8	57.8	4.2
		92.3	2.8	94.9	6.8
		117.0	7.3	120.4	3.4
		151.2	32.4	150.6	5.3
		179.1	66.5	202.7	43.2
		58.3	1.7	63.2	3.5
		90.9	9.5	93.5	2.1
		120.4	16.7	123.0	6.1
		148.0	47.5	153.2	9.5
		166.5	80.9	207.6	31.4
		61.0	7.0	59.7	7.1
		92.4	11.3	94.1	7.8
		122.1	22.4	119.7	9.9
		151.3	48.9	150.3	16.8
	+0	173.5	76.8	193.2	52.0
		63.9	1.1	60.0	8.8
		90.1	3.0	90.6	8.1
		118.4	8.4	120.6	10.9
		149.2	21.4	148.7	23.2
		180.1	68.6	194.7	48.8
		58.5	2.8	65.5	3.5
		92.1	6.4	88.7	3.4
		125.9	34.7	116.0	10.3
		146.5	69.3	148.3	37.1
		165.8	82.3	174.6	73.1
		59.6	3.0	56.3	6.8
		89.2	2.7	96.5	8.2
		128.1	9.2	116.0	9.0
		153.6	42.6	154.6	35.7
Porc3	+2	179.7	71.4	182.5	65.7

Table F-1 continued

Heart ID	Size	Circular		D-shape	
		ΔP (mmHg)	PVL (ml/sec)	ΔP (mmHg)	PVL (ml/sec)
				57.1	3.9
				90.2	5.7
				116.8	9.8
				157.6	17.1
				194.9	52.3
		58.8	3.0	62.3	3.3
		93.4	3.9	93.6	2.0
		123.0	9.8	133.2	10.6
		148.2	55.7	151.3	44.1
		169.9	79.6	170.9	78.3
		59.0	3.0	57.9	2.2
		93.3	4.1	95.1	4.1
		119.8	6.0	121.9	16.7
		147.7	20.0	148.0	56.3
	+4	191.8	54.8	177.7	71.8
				59.0	1.0
				92.8	2.4
				122.7	9.2
				145.7	21.0
				180.9	69.3
		59.7	3.7	63.5	7.4
		92.6	7.9	88.9	6.2
		121.9	7.7	121.4	3.0
		149.8	10.2	152.0	10.1
		207.6	34.7	197.8	46.3
		57.9	1.9	60.4	7.0
		92.7	3.9	93.6	8.0
		122.7	2.9	121.8	6.0
		148.2	9.5	154.1	7.8
		208.7	30.7	193.4	49.0
		58.9	4.6	56.9	8.7
		93.0	9.7	92.5	8.3
		123.6	11.4	122.8	14.3
		150.3	25.4	149.4	17.6
Porc3	+6	197.8	45.1	187.3	56.3

Table F-1 continued

Heart ID	Size	Circular		D-shape	
		ΔP (mmHg)	PVL (ml/sec)	ΔP (mmHg)	PVL (ml/sec)
		62.4	13.1	60.0	11.6
		92.6	17.4	92.0	19.1
		115.9	28.0	115.0	28.3
		147.2	54.6	143.0	43.7
		161.7	80.2	175.5	68.4
		59.6	18.1	59.2	13.1
		94.6	29.4	93.2	15.9
		120.7	40.9	117.0	24.8
		148.2	61.8	151.5	65.2
		161.1	79.3	168.8	74.9
		62.4	17.4	63.4	1.0
		92.8	22.1	91.4	13.2
		120.4	30.2	120.1	30.4
		146.8	54.6	148.9	59.5
	+0	167.6	72.8	169.0	71.8
		62.8	8.7	63.6	8.6
		95.0	11.7	92.9	19.0
		116.1	18.1	121.6	29.5
		149.7	21.1	145.7	51.6
		181.4	64.2	168.1	76.6
		60.7	7.8	60.5	6.0
		94.3	8.2	92.4	14.3
		117.9	11.7	120.0	25.7
		142.4	42.3	148.8	54.1
		165.7	77.0	173.4	67.8
		61.3	8.9	57.9	4.8
		91.2	16.1	97.0	8.0
		120.0	48.7	121.5	7.8
		150.7	83.8	147.8	12.8
Porc4	+2	155.9	82.0	204.4	36.9

Table F-1 continued

Heart ID	Size	Circular		D-shape	
		ΔP (mmHg)	PVL (ml/sec)	ΔP (mmHg)	PVL (ml/sec)
		58.3	5.7	60.6	5.1
		92.5	5.8	92.2	6.3
		119.0	18.6	118.6	3.5
		149.1	50.2	151.2	6.9
		167.3	75.3	196.7	48.0
		60.9	6.7	59.0	15.2
		92.2	13.3	92.0	12.2
		118.0	30.5	123.6	10.4
		148.3	55.7	150.1	11.6
		165.3	72.1	200.4	40.6
		59.8	3.1	59.9	8.3
		93.7	8.7	93.1	5.1
		123.3	14.4	122.4	4.5
		147.2	20.6	150.4	20.8
	+4	189.6	53.8	179.0	64.1
		62.3	1.3	61.1	6.9
		94.1	7.9	93.2	3.0
		123.7	14.8	122.2	8.7
		147.2	28.3	149.6	21.5
		172.2	68.3	183.9	59.8
		59.2	7.9	59.0	7.1
		92.6	10.6	93.4	6.0
		123.6	17.9	119.8	11.4
		146.2	60.6	147.3	27.9
		159.1	83.2	176.9	68.3
		62.9	6.2	60.6	6.3
		91.8	4.3	92.3	4.5
		123.6	3.4	120.7	14.2
		150.9	13.2	148.8	34.6
Porc4	+6	185.1	60.7	182.0	60.4

Table F-1 continued

Heart ID	Size	Circular		D-shape	
		ΔP (mmHg)	PVL (ml/sec)	ΔP (mmHg)	PVL (ml/sec)
		65.3	7.3	63.2	4.7
		93.7	16.7	95.0	1.8
		124.3	31.9	124.3	4.5
		153.0	46.6	154.6	9.3
		176.0	68.6	205.6	29.8
		62.1	6.4	63.9	11.5
		93.1	17.0	97.7	13.2
		124.4	39.5	125.1	25.9
		150.9	64.8	148.7	36.7
		169.9	73.2	181.1	64.3
		63.7	10.1	64.8	7.3
		93.7	12.4	95.2	8.9
		122.5	30.9	123.1	12.9
		151.5	46.7	152.9	26.9
	+0	173.9	70.1	196.5	48.8
		66.9	9.8	64.1	11.6
		95.6	15.1	97.1	23.1
		127.4	34.5	124.4	35.4
		151.3	58.8	150.3	54.8
		167.7	74.5	180.0	64.9
		64.0	11.9	66.7	9.4
		91.1	16.0	92.4	16.3
		121.0	23.5	127.8	31.2
		149.2	34.2	153.2	48.5
		185.9	60.5	173.5	71.9
		66.1	10.7	65.7	7.5
		96.3	21.1	91.1	5.0
		124.3	53.4	123.3	10.8
		152.9	66.2	151.1	20.0
Porc5	+2	166.2	76.7	197.5	45.2

Table F-1 continued

Heart ID	Size	Circular		D-shape	
		ΔP (mmHg)	PVL (ml/sec)	ΔP (mmHg)	PVL (ml/sec)
				62.8	3.2
				94.9	6.7
				121.2	10.0
				153.0	37.3
				181.7	64.2
		62.3	7.1	62.8	4.4
		95.7	21.0	91.8	10.5
		121.6	40.5	120.8	30.4
		147.2	59.2	152.7	57.9
		164.4	77.2	170.6	71.5
		62.9	2.7	62.9	3.5
		93.4	7.1	96.1	3.2
		122.0	26.2	124.8	11.1
		149.2	65.5	149.2	21.5
	+4	175.3	66.6	171.6	68.6
		62.5	7.8	66.1	4.9
		92.1	23.6	92.6	9.0
		122.4	41.4	125.7	19.7
		156.4	66.9	148.1	31.4
		164.3	75.6	177.1	62.7
		62.5	1.6	64.9	3.1
		94.8	6.9	93.8	6.3
		119.8	23.7	122.5	14.0
		148.4	63.4	152.4	32.1
		162.2	76.5	175.4	66.3
		64.9	1.1	63.0	1.2
		95.8	4.6	94.5	1.3
		123.8	21.2	123.5	1.0
		148.9	38.5	148.3	9.0
Porc5	+6	172.8	68.9	179.3	60.9

Table F-1 continued

Heart ID	Size	Circular		D-shape	
		ΔP (mmHg)	PVL (ml/sec)	ΔP (mmHg)	PVL (ml/sec)
		62.5	6.7	61.8	1.5
		93.0	9.9	90.6	4.7
		122.3	18.0	120.5	9.4
		148.4	31.9	149.3	18.8
		189.6	53.9	202.2	38.3
		62.2	8.1	61.1	6.8
		93.2	13.9	91.1	10.1
		121.8	20.3	119.2	11.1
		146.5	31.5	150.2	17.9
		185.8	56.6	202.6	38.0
		60.5	9.5	60.8	6.7
		92.2	19.1	92.3	9.6
		119.8	28.9	120.0	14.4
		151.4	49.2	149.9	21.9
	+0	172.2	68.6	192.1	49.5
		61.2	9.8	60.8	10.3
		93.1	20.5	94.0	17.7
		119.9	50.3	122.4	29.2
		153.6	68.2	150.5	35.7
		161.2	80.2	185.6	57.9
		65.0	10.3	62.5	7.8
		93.0	12.1	97.6	12.0
		115.3	13.2	124.9	21.1
		141.7	22.1	148.3	33.0
		195.7	44.9	196.3	50.3
		56.7	13.1	61.6	11.3
		92.1	15.8	89.9	12.4
		116.7	21.2	124.8	19.8
		142.7	30.7	146.3	31.0
Porc6	+2	180.2	63.5	182.6	63.3

Table F-1 continued

Heart ID	Size	Circular		D-shape	
		ΔP (mmHg)	PVL (ml/sec)	ΔP (mmHg)	PVL (ml/sec)
		53.2	10.3	56.2	8.0
		94.8	12.3	93.8	14.8
		124.9	13.9	113.6	24.2
		148.7	26.0	154.4	50.0
		183.2	61.9	180.5	64.8
		59.9	9.7	60.8	6.0
		88.2	12.3	89.9	10.4
		120.2	22.7	125.1	14.1
		149.3	51.3	148.7	26.0
		172.7	72.3	180.6	64.6
		53.9	6.2	65.0	7.7
		88.1	10.1	95.0	11.0
		121.1	16.5	120.5	12.4
		151.2	35.1	149.8	31.4
	+4	182.3	60.4	174.7	69.2
		62.8	5.0	56.9	7.3
		89.8	5.5	94.3	8.7
		119.5	7.3	121.4	8.9
		154.3	14.7	144.7	22.3
		197.0	45.9	191.7	52.1
		55.4	7.9	60.2	1.7
		96.5	9.9	94.0	5.4
		121.2	10.2	121.3	13.9
		151.4	24.1	153.6	32.2
		182.1	60.7	183.4	58.8
		58.8	7.0	59.0	3.2
		92.6	8.5	95.9	1.0
		127.2	7.9	123.0	3.8
		154.3	17.4	149.7	14.3
Porc6	+6	180.6	59.9	191.0	50.1

Table F-1 continued

Heart ID	Size	Circular		D-shape	
		ΔP (mmHg)	PVL (ml/sec)	ΔP (mmHg)	PVL (ml/sec)
		61.5	3.3	61.9	8.1
		94.3	4.6	94.5	11.5
		123.0	17.9	118.8	30.4
		152.5	38.2	145.7	58.8
		180.6	64.6	161.3	81.6
		63.9	3.4	62.3	3.2
		90.5	7.8	91.3	4.5
		119.7	23.3	120.4	10.8
		148.0	44.3	151.9	44.0
		174.8	70.7	174.6	69.4
		63.5	3.8	60.8	4.3
		92.3	10.6	92.5	3.5
		122.1	25.4	120.4	11.1
		149.2	39.2	148.2	32.5
	+0	166.0	75.2	169.0	69.4
		64.4	7.5	62.0	9.2
		91.7	21.0	92.2	15.4
		118.9	40.3	120.3	26.1
		149.6	62.4	148.0	71.2
		161.0	79.9	161.9	79.0
		62.9	4.1	59.3	3.6
		96.4	13.4	91.3	7.7
		119.0	18.3	121.6	16.8
		148.2	41.3	146.0	47.2
		177.7	61.1	162.2	78.3
		62.1	2.2	60.8	3.1
		89.4	11.9	94.8	4.9
		122.2	35.3	119.5	13.4
		149.1	54.0	150.9	40.7
Porc7	+2	165.1	75.5	167.9	73.1

Table F-1 continued

Heart ID	Size	Circular		D-shape	
		ΔP (mmHg)	PVL (ml/sec)	ΔP (mmHg)	PVL (ml/sec)
		61.2	4.9	62.7	1.0
		89.9	13.5	91.8	2.0
		121.8	38.8	120.2	6.2
		147.0	65.0	149.9	26.3
		162.8	77.0	186.7	55.7
		59.6	7.0	60.9	3.5
		95.2	11.0	94.2	6.6
		118.8	30.7	117.3	14.4
		151.4	73.1	145.8	45.5
		152.1	86.2	171.3	67.1
		62.0	4.0	65.3	5.6
		91.3	4.9	94.5	7.0
		123.6	9.1	126.6	24.6
		145.7	36.9	147.8	61.9
	+4	171.0	72.0	158.4	78.9
				61.9	4.6
				91.0	3.8
				122.5	7.5
				151.6	21.9
				190.4	50.6
		60.3	2.0	61.3	1.0
		92.6	2.3	92.0	3.5
		117.6	17.2	126.8	5.4
		145.5	60.8	151.3	24.7
		160.4	78.5	180.0	59.7
		60.6	4.4	61.8	4.1
		90.1	10.8	92.4	5.2
		120.1	37.0	119.2	16.1
		149.1	69.7	148.7	64.7
		160.2	79.2	159.3	77.9
		63.0	8.5	59.2	3.3
		92.3	10.9	91.9	9.5
		122.4	24.9	125.5	32.1
		146.1	51.9	146.5	65.6
Porc7	+6	163.5	76.2	166.9	73.6

F.2 Specific Aim 2.B Data

Note, in some instances aortic pressure errors (i.e., outside of the 110-130 mmHg range) were identified only during post-processing; these acquisitions were discarded.

Table F-2 Septal-lateral force (F_{SL}) and inter-commissural force (F_{IC}) data using the Circular and D-shaped Radial Expansion Force Transducers (C-REFT and D-REFT).

Heart ID	Size	Circular		Heart ID	Size	Circular	
		F_{SL} (N)	F_{IC} (N)			F_{SL} (N)	F_{IC} (N)
		9.9	8.4				
		13.6	11.3				
		13.4	10.1			29.0	36.9
		14.1	10.9			24.6	35.1
		12.3	10.6			18.3	35.5
		13.8	10.8			15.8	35.2
		12.5	8.2			13.6	35.3
	+2	12.2	11.0		+2	15.1	31.2
		26.7	21.9				
		20.4	19.9				
		22.2	19.1				
		24.4	21.8				
		24.6	16.7			11.0	46.5
		26.8	20.8			11.9	43.4
		22.9	16.5			17.0	47.0
	+4	21.9	19.3		+4	10.7	30.9
		30.2	35.5				
		30.7	34.0				
		29.8	33.5				
		29.7	29.1				
		24.0	28.1				
		27.8	28.4				
		28.8	33.4				
Porc8	+6	27.9	28.3	Porc9	+6		

Table F-2 continued

Heart ID	Size	Circular		Heart ID	Size	Circular	
		F_{SL} (N)	F_{IC} (N)			F_{SL} (N)	F_{IC} (N)
		26.9	21.2			21.0	33.6
		19.9	29.3			18.8	31.8
		7.7	13.0			16.2	30.6
		9.0	19.6			18.9	34.1
		16.3	25.8			21.2	30.5
		10.4	14.1			20.7	31.1
		13.9	22.6			19.0	29.1
	+2	9.1	12.9		+2	17.9	33.7
		12.2	26.8				
		32.6	41.7				
		33.8	41.4			28.3	53.9
		35.2	44.3			25.3	47.9
		24.3	29.9			27.9	45.0
		31.1	36.8			24.1	36.9
		33.2	44.4			22.5	48.2
	+4	29.4	34.3		+4	20.3	47.6
		33.8	52.2			24.8	47.8
		34.7	45.9			24.3	41.3
		39.2	43.2			27.5	40.5
		35.3	40.3			23.0	36.3
		26.9	35.4			22.6	42.4
		33.3	42.0			19.9	37.1
		37.0	43.8			20.6	37.8
Porc10	+6	35.8	41.0	Porc11	+6	21.4	33.2

Table F-2 continued

Heart ID	Size	Circular		Heart ID	Size	Circular	
		F_{SL} (N)	F_{IC} (N)			F_{SL} (N)	F_{IC} (N)
		20.4	25.1			15.2	29.8
		16.4	22.0			15.5	26.7
		19.6	18.0			11.7	30.1
		17.5	20.8			9.9	20.8
		17.2	17.8			14.9	34.8
		15.8	20.5			14.5	28.4
		18.8	22.6			7.5	14.8
	+2	12.1	16.3		+2	14.3	30.2
		20.7	38.6			17.9	39.8
		11.6	32.8			21.6	51.6
		17.4	32.4			16.8	36.8
		12.3	26.1			20.5	47.1
		16.2	23.5			14.6	28.7
		17.3	29.9			20.0	43.7
		11.9	30.3			20.1	42.8
	+4	20.5	31.9		+4	18.4	40.0
		8.3	36.1			17.9	41.5
		10.7	30.1			19.1	43.9
		16.1	29.5			15.4	37.8
		17.3	27.5			17.1	38.7
		8.7	29.5			15.7	38.4
		10.7	29.7			17.8	39.4
		6.8	30.9			15.0	42.2
Porc12	+6	12.9	29.5	Porc13	+6	15.2	41.3

Table F-2 continued

Heart ID	Size	D-shape F_{SL} (N)	D-shape F_{IC} (N)	Heart ID	Size	D-shape F_{SL} (N)	D-shape F_{IC} (N)
		12.4	19.0				
		5.8	18.9				
		13.6	29.3				
		10.4	22.0				
		10.3	19.9				
	+2	7.0	19.3		+2	17.0	35.8
		11.4	31.5			29.4	55.4
		13.8	29.3			17.2	21.2
		8.0	29.4			30.7	52.1
		9.2	28.7			30.8	53.8
		9.6	28.4			29.7	53.8
		8.9	21.2			18.2	35.2
		5.4	29.5			30.2	54.2
	+4	8.0	26.7		+4	14.6	26.0
		9.0	42.8			43.3	67.0
		8.2	37.5			39.2	66.8
		8.8	40.3			36.4	63.1
		11.2	38.5			36.1	64.8
		11.0	37.6			35.4	64.1
		12.4	39.6			35.2	65.9
		9.6	38.4			36.8	66.8
Porc14	+6	10.5	36.6	Porc15	+6	32.8	64.6

Table F-2 continued

Heart ID	Size	D-shape		Heart ID	Size	D-shape	
		F_{SL} (N)	F_{IC} (N)			F_{SL} (N)	F_{IC} (N)
		5.6	13.6				
		5.3	26.8			12.7	28.0
		5.4	13.3			4.0	15.1
		3.1	13.2			5.8	9.6
		3.6	29.2			3.6	12.9
		4.5	14.4			5.0	16.2
		4.6	19.7			8.5	7.8
	+2	4.0	22.5		+2	8.3	24.2
		16.0	35.7			18.2	13.3
		13.8	35.6			17.3	22.9
		13.5	32.5			15.4	24.6
		13.3	29.4			19.6	30.5
		8.1	31.9			21.5	32.9
		12.8	28.5			15.9	18.7
		12.1	39.3			15.6	11.9
	+4	9.2	29.3		+4	18.7	28.2
		21.7	46.6			29.0	44.8
		17.7	46.5			27.8	41.5
		19.6	44.2			25.2	42.2
		17.4	43.3			23.9	44.1
		17.4	41.0			23.0	43.8
		16.1	36.6			20.0	27.9
		14.2	48.0			22.4	42.7
Porc16	+6	16.7	38.2	Porc17	+6	21.7	43.1

Table F-2 continued

Heart ID	Size	D-shape		Heart ID	Size	D-shape	
		F_{SL} (N)	F_{IC} (N)			F_{SL} (N)	F_{IC} (N)
		20.1	23.8			12.8	27.3
		20.2	33.2			6.3	21.4
		19.1	28.0			7.8	22.2
		11.8	29.5			6.3	22.1
		18.2	25.2			8.2	22.7
		5.1	16.8			9.9	20.0
		14.2	28.1			1.9	24.4
	+2	18.3	28.7		+2	2.4	20.2
		15.4	40.8			12.3	41.2
		30.5	43.7			17.3	30.8
		30.2	40.5			17.2	43.5
		25.5	22.0			14.4	32.5
		26.0	24.0			6.8	24.7
		40.6	53.9			6.2	38.7
		26.7	36.9			11.4	42.3
	+4	27.5	47.3		+4	10.9	37.5
		34.1	69.7			7.8	47.2
		40.4	64.6			10.7	51.3
		44.3	64.2			11.9	49.8
		45.0	69.5			29.1	58.8
		31.2	72.8			17.1	62.4
		30.2	75.8			17.5	58.7
		42.1	69.3			21.3	56.8
Porc18	+6	48.3	64.1	Porc19	+6	14.0	60.9

APPENDIX G. DATA TABLES FOR APPENDICES A-D

Table G-1 *In vivo* suture tie-down forces (N) using Physio and Profile 3D rings.

Animal ID	GTA5	GTA6	GTA7	GTA11	GTA12	GTA18
Sizing	true	under	under	under	under	under
Surgeon	other	other	other	other	other	1
Ring	Ph	Ph	Ph	Ph	3D	3D
LT	4.47	0.57	0.00	2.21	2.66	0.54
11 o'clock	4.37	5.56	5.70	1.42	2.35	0.88
1 o'clock	3.03	1.61	1.51	2.02	2.40	4.59
RT	2.99	2.38	3.09	0.83	2.54	3.37
3 o'clock	4.57	2.54	6.68	2.32	0.73	2.71
4 o'clock	2.33	7.24	5.93	2.37	1.19	3.49
5 o'clock	1.78	2.53	2.09	1.36	2.18	1.41
7 o'clock	1.81	0.22	1.20	3.02	3.56	2.30
8 o'clock	2.65	1.17	2.54	2.15	2.41	1.47
9 o'clock	3.15	3.47	4.41	2.92	1.64	2.08
Animal ID	GTA19	GTA20	GTA21	GTA22	GTA23	GTA25
Sizing	true	under	true	true	true	true
Surgeon	2	1	2	1	2	2
Ring	3D	3D	3D	3D	3D	3D
LT	2.60	1.74	3.48	2.95	1.98	3.51
11 o'clock	2.74	1.45	1.40	2.03	3.73	3.05
1 o'clock	1.16	1.96	0.84	1.84	2.90	5.09
RT	2.62	4.13	3.91	4.83	3.83	3.84
3 o'clock	1.12	3.50	3.93	0.24		4.23
4 o'clock	0.76	2.82	2.86	3.67	2.95	2.74
5 o'clock	0.09	1.72	3.11	0.77	2.17	2.36
7 o'clock	2.39	1.32	1.82	2.05	3.55	5.72
8 o'clock	2.74	0.95	1.82	2.12	4.48	5.17
9 o'clock	3.54	0.42	5.71	1.49	3.10	4.50

Table G-1 continued

Animal ID	GTA26	GTA27	GTA28	GTA29	GTA30
Sizing	under	under	under	true	true
Surgeon	2	1	other	2	1
Ring	3D	3D	3D	3D	3D
LT	2.97	0.45	0.00	2.23	0.21
11 o'clock	1.83	1.86	7.98	2.92	1.35
1 o'clock	1.02	1.27	5.73	2.45	6.79
RT	2.50	3.02	4.93	3.50	3.94
3 o'clock	1.99	4.07	3.26	3.67	3.82
4 o'clock	3.08	3.87	3.56	3.04	1.43
5 o'clock	2.67	1.16	1.48	2.56	2.85
7 o'clock	3.00	2.40	2.03	1.85	2.92
8 o'clock	3.19	1.65	6.27	2.59	2.11
9 o'clock	4.10	0.98	3.04	2.27	1.46

Note, in Table G-1, one missing data point was caused by temporary, peri-operative malfunction of the Suture Force Transducer.

Table G-2 *Ex vivo* suture pullout forces (N) from ovine tricuspid annuli.

Heart ID	Ov18	Ov19	Ov20	Ov21	Ov22	Ov23	Ov24	Ov25
1 o'clock	4.55	4.40	4.16	3.37	2.14	3.91	3.50	3.17
2 o'clock	5.83	6.62	3.85	6.44	2.01	3.70	6.52	2.86
3 o'clock	5.56	7.14	6.87	2.38	4.08	8.54	6.43	3.31
PSC	4.92	4.94	6.64	4.59	5.12	9.33	5.31	4.11
5 o'clock	7.22	3.98	13.99	7.87	8.69	9.86	9.85	5.48
6 o'clock	16.32	6.11	4.57	5.78	13.63	17.01	9.50	7.42
7 o'clock	9.29	3.95	7.25	6.05	3.61	3.36	9.24	10.47
SAC	7.57	3.29	3.84	4.00	1.88	4.28	4.54	9.85
9 o'clock	6.93	9.28	4.14	6.37	2.39	3.97	6.92	4.94
10 o'clock	6.70	7.62	6.78	8.38	3.96	7.60	5.87	4.87
11 o'clock	10.764	3.77	5.721	5.363	6.086	6.424	4.678	5.315
APC	3.683	10.088	2.478	2.088	2.864	5.971	3.445	4.41

Heart ID	Ov26	Ov27	Ov28	Ov29	Ov30	Ov31	Ov32
1 o'clock	2.30	6.31	5.48	4.83	6.47	5.94	4.57
2 o'clock	5.16	7.63	5.19	7.05	3.99	3.50	7.08
3 o'clock	9.62	*7.27*	5.84	6.02	7.00	8.72	8.22
PSC	5.26	*4.88*	8.64	6.99	9.19	6.01	7.82
5 o'clock	9.74	6.69	9.55	15.58	10.13	8.46	10.25
6 o'clock	7.95	10.73	8.40	6.13	14.92	8.26	13.30
7 o'clock	10.89	4.81	6.24	5.70	8.39	6.19	8.83
SAC	7.25	8.30	8.28	5.90	3.06	5.82	7.50
9 o'clock	6.79	6.46	8.45	6.27	5.71	6.90	5.47
10 o'clock	8.16	4.92	8.42	8.18	7.21	5.46	3.19
11 o'clock	8.26	5.83	4.92	4.18	6.80	5.10	5.78
APC	6.93	5.33	7.75	3.37	5.01	5.59	4.29

Table G-3 Mean Pixel Intensity, before and after normalization, from microstructural imaging of ovine tricuspid annuli.

Heart ID			Ov33	Ov34	Ov35	Ov36	Ov37	Ov38	Ov39
Mean Pixel Intensity (MPI)	Collagen	PL	2.98	2.84	1.05	2.93	3.24	7.68	6.39
		PSC	3.26	3.59	1.35	4.32	3.30	7.96	10.17
		SL	3.65	4.24	1.69	6.08	5.62	7.84	12.44
		SAC	4.22	3.62	1.94	2.44	6.06	7.84	4.78
		AL	4.23	2.83	1.28	4.90	4.11	8.10	5.85
		APC	3.33	3.31	1.15	4.20	3.64	6.17	8.93
	Myocard-ium	PL	19.48	13.60	4.44	8.05	15.48	39.60	31.21
		PSC	25.48	37.51	4.19	14.95	8.74	22.28	33.10
		SL	22.56	14.94	2.71	24.15	15.36	30.35	20.50
		SAC	10.28	12.48	5.57	5.27	14.38	26.61	17.78
		AL	20.04	13.13	5.03	15.72	25.84	29.62	17.72
		APC	17.32	24.05	6.10	6.62	18.55	33.74	36.98
normalized Mean Pixel Intensity (nMPI)	Collagen	PL	0.83	0.83	0.75	0.71	0.75	1.01	0.79
		PSC	0.90	1.05	0.95	1.04	0.76	1.05	1.26
		SL	1.01	1.24	1.20	1.47	1.30	1.03	1.54
		SAC	1.17	1.06	1.37	0.59	1.40	1.03	0.59
		AL	1.17	0.83	0.91	1.18	0.95	1.07	0.72
		APC	0.92	0.97	0.82	1.01	0.84	0.81	1.10
	Myocard-ium	PL	1.02	0.71	0.95	0.65	0.94	1.30	1.19
		PSC	1.33	1.95	0.90	1.20	0.53	0.73	1.26
		SL	1.18	0.77	0.58	1.94	0.94	1.00	0.78
		SAC	0.54	0.65	1.19	0.42	0.88	0.88	0.68
		AL	1.04	0.68	1.08	1.26	1.58	0.98	0.68
		APC	0.90	1.25	1.31	0.53	1.13	1.11	1.41

Table G-4 Summary data and *ex vivo* suture pullout forces (N) from human mitral and tricuspid annuli.

Heart ID		Hu1	Hu2	Hu3	Hu4	Hu5	Hu6
Gender		F	F	F	M	M	M
Body Mass Index		16.72	27.46	24.63	28.58	20.09	17.79
Age		79	68	60	73	74	70
Post-mortem interval		8	7	6	4	3	6
	LT	7.42	10.43	5.34	5.02	9.59	5.53
	11 o'clock	16.63	6.19	7.09	15.94	8.12	7.78
	1 o'clock	12.96		7.17	8.15	6.29	8.90
	RT	11.15		4.65	2.99	9.21	8.64
	3 o'clock	6.47	6.24	6.16	6.03	11.62	8.28
	4 o'clock	5.62	2.95	9.03	8.00	11.26	8.88
	5 o'clock	6.19	4.96	5.69	7.46	9.48	9.13
	7 o'clock	4.51	5.23	8.19	7.23	9.04	14.61
	8 o'clock	4.75	3.44	6.16	7.86	8.94	10.35
Mitral	9 o'clock	6.29	9.92	5.06	6.37	6.01	11.32
	APC	6.61	7.95	7.33	8.64	7.33	7.17
	1 o'clock	4.67	10.93	7.07	5.57	8.48	7.45
	2 o'clock	3.96	8.47	6.77	4.45	9.72	7.16
	3 o'clock	4.00	6.01	6.82	5.61	11.38	8.55
	PSC	4.04	12.26	5.17	4.46	6.74	7.76
	5 o'clock	5.30	9.15	6.07	6.92	3.48	6.32
	6 o'clock	7.41	6.32	4.92	7.86	7.47	4.13
	7 o'clock	5.96	6.54	19.74	6.05	15.81	10.70
	SAC	29.85	6.49	30.75	30.28	24.25	22.60
	9 o'clock	4.00	6.89		2.83	4.11	5.45
	10 o'clock	5.27	4.43	1.72	4.25	6.55	4.66
Tricuspid	11 o'clock	6.28	5.86	3.48	4.01	8.67	7.60

Table G-5 Hydroxyproline content (mg/g wet weight) in human mitral and tricuspid annuli.

Heart ID		Hu1	Hu2	Hu3	Hu4	Hu5	Hu6
	LT	19.09	11.44	12.55	7.83	11.41	7.85
	11 o'clock	6.79	11.19	9.13	12.70	5.55	6.41
	1 o'clock	14.64	16.08	8.68	17.63		11.16
	RT	15.64		3.73	11.06		4.73
	3 o'clock	6.87	10.47	3.23	3.42	5.07	4.60
	4 o'clock	11.35	10.93	3.30	4.92	6.63	5.80
	5 o'clock	5.53	10.01	10.03	6.15	4.27	3.61
	7 o'clock	12.08	10.52	4.24	4.52	5.34	5.35
	8 o'clock	16.87	13.15	4.82	6.35	5.44	6.63
Mitral	9 o'clock	3.85	12.13	7.36	6.58	3.95	6.24
	APC	3.31	2.25	4.21	2.54	5.69	7.76
	1 o'clock	2.78	5.50	3.80	2.01	5.17	6.07
	2 o'clock	3.54	4.72	4.41	4.14	5.58	6.03
	3 o'clock	3.91	4.67	6.48	3.29	7.69	3.25
	PSC	4.27	6.17	6.19	0.68	3.32	5.54
	5 o'clock	1.20	6.23	4.66	1.14	3.71	4.26
	6 o'clock	10.48	7.20	4.15	1.80	4.21	3.89
	7 o'clock	5.10	7.22	9.73	5.28	7.67	9.42
	SAC	14.52	5.96	10.92	9.96	8.23	11.95
	9 o'clock	5.85		1.86	2.52	3.02	2.73
	10 o'clock	3.89	7.78	1.63	1.07	3.66	4.47
Tricuspid	11 o'clock	4.21	5.38	3.06	1.49	4.73	4.17

Note, in Table G-4 and Table G-5, missing data was due to experimental error and/or thin boundary between mitral and tricuspid annuli making it impossible to fully separate them for testing. Also note, the tricuspid leaflets in Hu1 and Hu2 were highly non-uniform in size. In order to maintain 12 total sutures in these cases, 2 sutures were placed in the shortest segment (i.e., Hu1 tricuspid posterior, Hu2 tricuspid septal) and 4 in the longest (i.e., Hu1 tricuspid anterior, Hu2 tricuspid posterior). Whether 2, 3, or 4 sutures were

placed in a given annular segment, their spacing was uniform. To enable positional comparison, when 2 or 4 sutures were placed, a three-suture arrangement was approximated by averaging values from the two adjacent positions. For example, in Hu1, the final 1 o'clock values were derived from the average of the anterior-most posterior suture and the SAC, 2 o'clock was derived from the average of the two posterior sutures, etc.

APPENDIX H. GUIDE TO SUPPLEMENTARY COMPUTER AIDED DESIGN FILES

Attached to this thesis, a set of supplementary files has been uploaded within SMARTech (the Georgia Tech repository for theses and other scholarly works). All supplementary files are Computed Aided Design (CAD) files for components and assemblies that were used in this thesis. All files were produced in Solidworks 2016 or earlier (Dassault Systemes, Waltham, MA). For every .sldprt file except for 2_P41_D-profileForPlugsAndREFT.sldprt, a duplicate file has been provided in .stl format. The .stl format is more readily suited for 3D printing, and may prove easier to read in the future, in the event the .sldprt format becomes obsolete. In addition to an accompanying README file, the interested reader may refer to the following table for a description of these files.

Table H-1 Description of supplementary CAD files.

File Name	Used in Aim	Manufac. Method	Manufac. Material	Comment
1_P1_SutureForceTxducerSpringElement.sldprt	1	3D printing (20 um)	316L Stainless Steel	-
1_P2_SuturePulloutsBase.sldprt	1.A	Mill	Aluminum sheet	-
1_P3_SuturePulloutsMiddle.sldprt	1.A	Mill	Aluminum sheet	-
1_P4_SuturePulloutsTop.sldprt	1.A	Mill	Aluminum sheet	-

File Name	Used in Aim	Manufac. Method	Manufac. Material	Comment
1_P5_SuturePullouts Tippytop.sldprt	1.A	Laser Cutter	Acrylic sheet	Suture pullout test plate, top acrylic layer for rubber sheet attachment
1_A1_SuturePullouts System.sldasm	1.A	-	-	-
2_P1_Funnel.sldprt	2.A	3D printing (250 um) + vapor polish	ABS	final step: thread with 3/8-16 die
2_P2_TMVPlugC0.sldprt	2.A	3D printing (250 um) + vapor polish	ABS	final step: thread with 3/8-16 tap
2_P3_TMVPlugC2.sldprt	2.A	3D printing (250 um) + vapor polish	ABS	final step: thread with 3/8-16 tap
2_P4_TMVPlugC4.sldprt	2.A	3D printing (250 um) + vapor polish	ABS	final step: thread with 3/8-16 tap
2_P5_TMVPlugC6.sldprt	2.A	3D printing (250 um) + vapor polish	ABS	final step: thread with 3/8-16 tap
2_P6_TMVPlugD0.sldprt	2.A	3D printing (250 um) + vapor polish	ABS	final step: thread with 3/8-16 tap
2_P7_TMVPlugD2.sldprt	2.A	3D printing (250 um) + vapor polish	ABS	final step: thread with 3/8-16 tap
2_P8_TMVPlugD4.sldprt	2.A	3D printing (250 um) + vapor polish	ABS	final step: thread with 3/8-16 tap
2_P9_TMVPlugD6.sldprt	2.A	3D printing (250 um) + vapor polish	ABS	final step: thread with 3/8-16 tap

File Name	Used in Aim	Manufac. Method	Manufac. Material	Comment
2_P10_LVApicalPort Inner.sldprt	2.A	3D printing (250 um) + vapor polish	ABS	final step: thread with 1/2-20 die
2_P11_LVApicalPort Outer.sldprt	2.A	3D printing (250 um) + vapor polish	ABS	final step: thread with 1/2-20 tap
2_P12_C-REFTArm.sldprt	2.B	3D printing (25 um)	FormLabs Clear Resin	for 12, 3, 6, and 9 oclock
2_P13_C-REFTHub.sldprt	2.B	3D printing (25 um)	FormLabs Clear Resin	-
2_P14_C-REFTCap.sldprt	2.B	3D printing (25 um)	FormLabs Clear Resin	-
2_P15_C-REFTPistonWedge.sldprt	2.B	3D printing (25 um)	FormLabs Clear Resin	-
2_P16_C-REFTPistonRod.sldprt	2.B	Water jet	Steel Sheet	bonded to wedge after machining
2_P17_D-REFTArm12.sldprt	2.B	3D printing (25 um)	FormLabs Clear Resin	for 12 oclock only
2_P18_D-REFTArm3.sldprt	2.B	3D printing (25 um)	FormLabs Clear Resin	for 3 oclock only
2_P19_D-REFTArm6.sldprt	2.B	3D printing (25 um)	FormLabs Clear Resin	for 6 oclock only
2_P20_D-REFTArm9.sldprt	2.B	3D printing (25 um)	FormLabs Clear Resin	for 9 oclock only

File Name	Used in Aim	Manufac. Method	Manufac. Material	Comment
2_P21_D-REFTHub.sldprt	2.B	3D printing (25 um)	FormLabs Clear Resin	-
2_P22_D-REFTCap.sldprt	2.B	3D printing (25 um)	FormLabs Clear Resin	-
2_P23_D-REFTPistonWedge.sldprt	2.B	3D printing (25 um)	FormLabs Clear Resin	-
2_P24_D-REFTPistonRod.sldprt	2.B	Water jet	Steel Sheet	bonded to wedge after machining
2_P25_REFTHubScrew.sldprt	2.B	Lathe	Threaded Aluminum Rod	hollowed out threaded rod, bonded to either hub after machining
2_P26_C-REFTCalModulePusherPad.sldprt	2.B	3D printing	ABS	for 12, 3, 6, and 9 oclock
2_P27_C-REFTCalBase.sldprt	2.B	Mill	Acrylic sheet	-
2_P28_D-REFTCalModulePusherPad12.sldprt	2.B	3D printing	ABS	for 12 oclock only
2_P29_D-REFTCalModulePusherPad3.sldprt	2.B	3D printing	ABS	for 3 oclock only
2_P30_D-REFTCalModulePusherPad6.sldprt	2.B	3D printing	ABS	for 6 oclock only
2_P31_D-REFTCalModulePusherPad9.sldprt	2.B	3D printing	ABS	for 9 oclock only

File Name	Used in Aim	Manufac. Method	Manufac. Material	Comment
2_P32_D-REFTCalBase.sldprt	2.B	Mill	Acrylic sheet	-
2_P33_REFTCalModuleHousing.sldprt	2.B	Mill	Acrylic bar	-
2_P34_REFTCalModulePiston.sldprt	2.B	Lathe	Aluminum Rod	-
2_P35_REFTCalModuleSpring.sldprt	2.B	OEM	OEM	OD 0.36", 0.042" wire, 7/16" free length, 49 lb. spring rating
2_P36_REFTCalModulePusherShaft.sldprt	2.B	Lathe	Aluminum Rod	-
2_P37_REFTCalLargeScrew.sldprt	2.B	OEM	OEM	1-1/4" 6-40 socket cap screw
2_P38_REFTCalLargeNut.sldprt	2.B	OEM	OEM	for 6-40 screw
2_P39_REFTCalSmallScrew.sldprt	2.B	OEM	OEM	1/2" 3-48 socket cap screw
2_P40_REFTCalSmallNut.sldprt	2.B	OEM	OEM	for 3-48 screw
2_P41_D-profileForPlugsAndREFT.sldprt	2	N/A	N/A	2-D sketch only. An included equation called "Scale Factor" allows user to generate all sizes based on perimeters only.
2_A1_LVApicalPort.sldasm	2.A	-	-	-
2_A2_C-REFT.sldasm	2.B	-	-	-
2_A3_D-REFT.sldasm	2.B	-	-	-

File Name	Used in Aim	Manufac. Method	Manufac. Material	Comment
2_A4_REFTCalModule.sldasm	2.B	-	-	-
2_A5_C-REFTCal.sldasm	2.B	-	-	-
2_A6_D-REFTCal.sldasm	2.B	-	-	-

APPENDIX I. MATLAB CODES

The following MATLAB codes (MathWorks, Natick, MA) are included:

- multiway_anova.m - a generic code used for all ANOVA models in both Specific Aims.
- Fc_processing_part1.m - enabled selection of 10-cardiac cycle periods for subsequent computation of cyclic force (F_C) in *in vivo* studies throughout SA 1.
- Fc_processing_part2.m - computed F_C throughout SA 1.
- HWHM.m - computed normalized half-width at half maximum force data ($HWHM_{norm}$) for SA 1.B.
- Ftd_processing.m - produced a graph for subsequent, manual extraction of tie-down force (F_{TD}) in APPENDIX A.
- annular_measurements.m - computed all photogrammetry-based annular dimensions throughout SA 2.
- PVL_processing_part1.m - computed the PCHIP curves representing incidental leakage rates through apical, aortic, or other connections, as a function of ΔP, in SA 2.A.
- PVL_processing_part2.m - computed the ΔP and PVL values from each acquisition in SA 2.A.
- REFT_processing.m - computed forces measured on each REFT arm in SA 2.B.

I.1 multiway_anova.m

```
%multiway_anova.m

%Description: This code runs a one-way or multi-way ANOVA, followed by
%Tukey's post-hoc. This was used for many different data sets but is shown
%with a two-way ANOVA sample from SA 1 (ANOVA model 9). It is meant to be
%run one section at a time. This way, the model can first be tested without
%interactions (for main effects), and then with interaction.

close all; clear all; clc

%% Initialize
%All input data has been previously put in .mat format
load stiffness_apratio.mat

apratio = stiffness_apratio(:,1);
stiffness = stiffness_apratio(:,2);
LVP = stiffness_apratio(:,3);

%% Run without interaction
[p tab stats terms] = anovan(apratio, {stiffness, LVP}a,...
    'varnames', {'stiffness','LVP'},...
    'model','linear');
for i=1:2
    figure;
    [comps{i} mean_se{i} h gnames] = multcompare(stats,'dimension',i);
end

%% Run with interaction
[p tab stats terms] = anovan(apratio, {stiffness, LVP},...
    'varnames', {'stiffness','LVP'},...
    'model','interaction');
for i=1:2
    for j=2:2
        if i==j
        elseif i>j
        else
            figure;
            [comps{i,j} mean_se{i,j} h gnames] =
multcompare(stats,'dimension',[i j]); %this is doing Tukey's
        end
    end
end
```

I.2 Fc_processing_part1.m

```
%Fc_processing_part1.m

%This code reads in the recorded forces, then prompts the use to select a
%start and and end point. These two points were always chosen for 10
%consecutive cardiac cycles. Based on an average from the ten cycles, heart
%rate and peak left ventricular pressure are computed. Output files are
%produced, which are force and LVP data over the chosen range.
```

```
close all; clear all; clc

%% User input section
%these inputs cover where the files are located, and how the outputs will
%be named.
hdir = 'C:\Users\epierce7\Dropbox\Documents\Lab\Research - Thesis\1 - Aim 1-2 -
Gorman NIH Grant\Animal Raw and Processed Data\';
Expt = 'GTA52'; %pulls data from this folder and applies this prefix to output
files
Acquisition = '31'; %pulls data from this folder and applies this prefix to
output files
Event = 'LVP100'; %applies this prefix to output files


%% Analyze data to identify cycles of interest
cd(strcat(hdir,Expt,'\',Expt,' Processed\',Acquisition))

%Read in data files
for i=1:10
    ch(i)=dlmread(strcat('ch',num2str(i-1),'.txt'));
end
LVP=dlmread('LVP.txt');

%Plot all of the data
x=1:length(ch(:,1));
figure(1)
for i=1:10
    hold on
    plot(x,ch(i))
end
legend('0','1','2','3','4','5','6','7','8','9')
xlabel('indexed time')
ylabel('Force [N]')

%prompt user for the start and endpoints
pause=0;
while pause==0
    hold off
    figure(2)
    set(gcf,'units','normalized','outerposition',[0 0 1 1])
    plot(x,LVP)
    xlabel('indexed time')
    ylabel('LVP [mmHg]')
    start=input('what would you like the start point to be?');
    disp('')
    finish=input('what would you like the end point to be?');

    %%
    [pks,locs] = findpeaks(LVP(start:finish), 'minpeakdistance', 400,
'minpeakheight', 80);

    %Calculate Heart Rate
    for i=2:length(locs)
        HR(i-1)=locs(i)-locs(i-1);
    end
    HR=60./(HR/1613);
    MeanPeakLVP=mean(pks);
    StdDevPeakLVP=std(pks);
    MeanHeartRate=mean(HR);
    StdDevHeartRate=std(HR);
```

```
    close Figure 2
    figure(2)
    plot(x(start:finish),LVP(start:finish))
    hold on
    plot(x(locs)+start,pks+5,'k^','markerfacecolor',[1 0 0]);
    title(strcat(['LVP = ' num2str(MeanPeakLVP) ' +/- ' num2str(StdDevPeakLVP)
...
        '; HR = ' num2str(MeanHeartRate) ' +/- ' num2str(StdDevHeartRate)]));

    figure(3)
    set(gcf,'units','normalized','outerposition',[0 0 1 1])
    hold off
    for i=1:10
        subplot(2,5,i); plot(x(start:finish),ch(start:finish,i))
    end

    pause=input('LVP and HR OK? (0=redo, 1=OK)')
end

%% Export selected data
%store the selected data into a matrix A
for i=1:10
    A(1:finish-start+1,i)=ch(start:finish,i);
end
B(1:finish-start+1,1)=LVP(start:finish);

%write and move data files for further analyses
cd(strcat(hdir,Expt,'\',Expt,' Processed'))
File1 =
strcat(Expt,'_Acq',Acquisition,'_',Event,'_','CyclicForcesToBeEvaluated.txt');
File2 = strcat(Expt,'_Acq',Acquisition,'_',Event,'_','LVPtoBeEvaluated.txt');
dlmwrite(File1,A);
dlmwrite(File2,B);

cd(hdir)
```

I.3 Fc_processing_part2.m

```
%Fc_processing_part2.m

%This code extracts cyclic forces from the cycles selected in part 1. The
%code first attempts to identify min and max forces automatically. The user
%determines whether to keep these values or redo the identification
%manually.

clear all
close all
clc

%% User input section
%these inputs cover where the files are located, and how the outputs will
%be named.
hdir = 'C:\Users\epierce7\Dropbox\Documents\Lab\Research - Thesis\1 - Aim 1-2 -
Gorman NIH Grant\Animal Raw and Processed Data\';
```

```
Expt = 'GTA52'; %applies this prefix to output files
Acquisition = '31'; %applies this prefix to output files
Event = 'LVP100'; %applies this prefix to output files

%% Import data
cd(strcat(hdir,Expt,'\',Expt,' Processed\'))
disp('  ')%spacer
disp('reading in txt file of the forces.....')
disp('  ') %spacer
Force=dlmread(strcat(Expt,'_Acq',Acquisition,'_',Event,'_','CyclicForcesToBeEva
luated.txt'));
[M N]=size(Force);%calculates the size of the column vector1
x=1:M;

%% Analyze data
for w=1:N
    Signal=Force(:,w);

    fifty=prctile(Signal,70);
    [pks,locs] = findpeaks(Signal, 'minpeakheight', fifty,
'minpeakdistance',400);
    SignalInverted=Signal*-1;
    fiftyInverted=prctile(SignalInverted,70);
    [pks2,locs2] = findpeaks(SignalInverted, 'minpeakheight', fiftyInverted,
'minpeakdistance',400);
    pks2=pks2*-1;
    if length(pks2)>10
        pks2(11)=[];
        locs2(11)=[];
    end

    plot(x,Signal); hold on;
    plot(x(locs),pks+0.05,'k^','markerfacecolor',[1 0 0]);
    plot(x(locs2),pks2-0.05,'k^','markerfacecolor',[1 0 0]);
    hold off
    set(gcf, 'Position', get(0,'Screensize'));
    title('Invert forces? (keep=1, flip=2)', 'fontsize', 16)
    answer1=input('Invert forces? (keep=1, flip=2)');

    if answer1==1
    elseif answer1==2
        Signal=Signal.*-1;
        clear('pks','pks2','locs','locs2');
        fifty=prctile(Signal,70);
        [pks,locs] = findpeaks(Signal, 'minpeakheight', fifty,
'minpeakdistance',400);
        SignalInverted=Signal*-1;
        fiftyInverted=prctile(SignalInverted,70);
        [pks2,locs2] = findpeaks(SignalInverted, 'minpeakheight',
fiftyInverted, 'minpeakdistance',400);
        pks2=pks2*-1;
        if length(pks2)>10
            pks2(11)=[];
            locs2(11)=[];
        end
        plot(x,Signal,x,LVP./10,'r'); hold on;
        plot(x(locs),pks+0.05,'k^','markerfacecolor',[1 0 0]);
        plot(x(locs2),pks2-0.05,'k^','markerfacecolor',[1 0 0]);
        hold off
        set(gcf, 'Position', get(0,'Screensize'));

    end
```

```
    title('Did you find all the peaks you wanted? (yes=1, no=2)','fontsize',16)
    answer2=input('did you find all the peaks you wanted? (yes=1, no=2)');

    if answer2==1
        AbsoluteLow(:,w)=pks2;
        AbsolutePeaks(:,w)=pks;
        PeakValues(:,w)=pks-pks2;
        MeanValue(w,1)=mean(PeakValues(:,w));
        StandardDeviation(w,1)=std(PeakValues(:,w));
        PercentageOfMean(w,1)=100*StandardDeviation(w,1)/MeanValue(w,1);
    end

    if answer2==2
        title('pick points on graph (min, max, min, max...etc), click enter key
when all have been selected','fontsize',14)
        [a b]=ginput;
        a=round(a);
        %Values=Signal(a);
        k=100;
        j=1;
        for i=1:2:length(a)-1
            if a(i)<k
                low(j)=min(Signal(1:a(i)+k));
            else
                low(j)=min(Signal(a(i)-k:a(i)+k));
            end
            j=j+1;
        end

        j=1;
        for i=2:2:length(a)
            if a(i)+k>length(Signal)
                high(j)=max(Signal(a(i)-k:end));
            else
                high(j)=max(Signal(a(i)-k:a(i)+k));
            end
            j=j+1;
        end

        AbsoluteLow(:,w)=low;
        AbsolutePeaks(:,w)=high;
        PeakValues(:,w)=high-low;
        MeanValue(w,1)=mean(PeakValues(:,w));
        StandardDeviation(w,1)=std(PeakValues(:,w));
        PercentageOfMean(w,1)=100*StandardDeviation(w,1)/MeanValue(w,1);

    end
    close all
end

%% Export data
xlswrite(strcat('Acq',Acquisition,'_',Event,'_','absolutelows.xls'),AbsoluteLow
);
xlswrite(strcat('Acq',Acquisition,'_',Event,'_','absolutepeaks.xls'),AbsolutePe
aks);

cd(hdir)
```

I.4 HWHM.m

```
%HWHM.m

%Description: This code produces normalized HWHM values from SA 1.B.

clear all
close all
clc

%% USER INPUT SECTION
%these inputs cover where the files are located
hdir = 'C:\Users\Eric\Dropbox\Documents\Lab\Research - Thesis\1 - Aim 1-2 -
Gorman NIH Grant\Animal Raw and Processed Data\';
Expt = 'GTA11'; %applies this prefix to output files
Acquisition = '11'; %applies this prefix to output files
Event = 'LVP100'; %applies this prefix to output files

%% Read in the Force File
cd(strcat(hdir,Expt,'\',Expt,' Processed\'))
force=dlmread(strcat(Expt,'_Acq',Acquisition,'_',Event,'_','CyclicForcesToBeEva
luated.txt'));

%% Plot each file and identify maxes
major_count=1; %necessary in case there were any busted transducers and some
channels must be skipped
for channel=[1:10]
    close all
    if channel==110%|channel==5
        check=1;
    else
        %auto-find peaks
        height_cutoff=prctile(force(:,channel),70);
        [max_force{major_count},max_t{major_count}] =
findpeaks(force(:,channel), 'minpeakheight', height_cutoff,
'minpeakdistance',550);
        [min_force{major_count},min_t{major_count}] =
findpeaks(force(:,channel).*-1, 'minpeakheight', height_cutoff*-1,
'minpeakdistance',550);
        min_force{major_count}=min_force{major_count}.*-1;

        %clean up list of found peaks
        if min_t{major_count}(1)>max_t{major_count}(1)
            max_t{major_count} = max_t{major_count}(2:end);
            max_force{major_count} = max_force{major_count}(2:end);
        end
        if length(max_force{major_count})>10
            max_force{major_count} = max_force{major_count}(1:10);
            max_t{major_count} = max_t{major_count}(1:10);
        end
        if length(min_force{major_count})>10
            min_force{major_count} = min_force{major_count}(1:10);
            min_t{major_count} = min_t{major_count}(1:10);
        end
        if length(max_force{major_count})>length(min_force{major_count})
            max_force{major_count} =
max_force{major_count}(1:length(min_force{major_count}));
        end
        if length(max_force{major_count})<length(min_force{major_count})
            min_force{major_count} =
min_force{major_count}(1:length(max_force{major_count}));
```

```
        end

        for i = 1:size(max_force{major_count},1) %find half-width locations
            subset = force(min_t{major_count}(i):max_t{major_count}(i),
channel);
            targetHW = (subset(1)+subset(end))/2;

            [resid,HW_t{major_count}(i)]=min(abs(subset-targetHW));
            HW_force{major_count}(i) = subset(HW_t{major_count}(i));
            HW_t{major_count}(i) = HW_t{major_count}(i)+ min_t{major_count}(i);
        end

        plot(force(:,channel)); hold on;
        set(gcf, 'Position', get(0,'Screensize'));
        scatter(max_t{major_count}, max_force{major_count}, 'kv',
'markerfacecolor', 'r');
        scatter(min_t{major_count}, min_force{major_count}, 'k^',
'markerfacecolor', 'r');
        scatter(HW_t{major_count}, HW_force{major_count}, 'ko',
'markerfacecolor', 'g');

        title('Manual Correction Required?? Press enter to proceed; type 1 to
correct manually')
        check=input('Press enter to proceed; type 1 to correct manually');
    end
    while check==1
        close all
        clear a b
        min_t{major_count}=[];
        max_t{major_count}=[];
        min_force{major_count}=[];
        max_force{major_count}=[];
        HW_t{major_count}=[];
        HW_force{major_count}=[];

        plot(force(:,channel)); hold on;
        set(gcf, 'Position', get(0,'Screensize'));
        title('pick min/max/min/max/etc. on graph, then click
enter','fontsize',14)

        [a,b]=ginput;
        a=round(a);
        minor_count=1;
        for i=1:2:length(a)-1
            [min_force{major_count}(minor_count),
min_t{major_count}(minor_count)] = min(force(a(i)-25:a(i)+25, channel));

min_t{major_count}(minor_count)=min_t{major_count}(minor_count)+a(i)-25;
            minor_count=minor_count+1;
        end
        minor_count=1;
        for i=2:2:length(a)
            [max_force{major_count}(minor_count),
max_t{major_count}(minor_count)] = max(force(a(i)-25:a(i)+25, channel));
            max_t{major_count}(minor_count) =
max_t{major_count}(minor_count)+a(i)-25;
            minor_count=minor_count+1;
        end

        for i = 1:length(max_force{major_count}) %find half-width locations
            subset=force(min_t{major_count}(i):max_t{major_count}(i),channel);
            targetHW = (subset(1)+subset(end))/2;
```

```
            [resid,HW_t{major_count}(i)]=min(abs(subset-targetHW));
            HW_force{major_count}(i) = subset(HW_t{major_count}(i));
            HW_t{major_count}(i) = HW_t{major_count}(i)+ min_t{major_count}(i);
        end

        scatter(max_t{major_count}, max_force{major_count}, 'kv',
'markerfacecolor','r');
        scatter(min_t{major_count}, min_force{major_count}, 'k^',
'markerfacecolor','r');
        scatter(HW_t{major_count}, HW_force{major_count}, 'ko',
'markerfacecolor','g');
        title('Redo Required?? Press enter to proceed; type 1 to redo')
        check=input('Press enter to proceed; type 1 to redo');
    end

    for k=1:length(max_t{major_count})-1
        cyc_len{major_count}(k) = (max_t{major_count}(k+1)-
max_t{major_count}(k))./1613;
    end
    for k=1:length(max_t{major_count})
        finalHW{major_count}(k) = (max_t{major_count}(k)-
HW_t{major_count}(k))./1613;
    end
    major_count=major_count+1;
end
major_count=major_count-1;

% get the mean length of every cycle, averaged across each suture's
% recording (this is redundant but whatever)
for i=1:major_count
    avg_cyc_len(i)=mean(cyc_len{i});
end
avg_cyc_len=mean(avg_cyc_len);

% express the half-width interval in normalized time, then average across
% cycles for each suture
for i=1:major_count
    finalHW_norm{i}=finalHW{i}./avg_cyc_len;
    mean_finalHW_norm(i) = mean(finalHW_norm{i});
end

mean_finalHW_norm=mean_finalHW_norm'

cd(hdir)
```

I.5 Ftd_processing.m

```
%Ftd_processing.m

%This code generates a large plot of all ten force channels, ranging from
%before tie-down began to after it completed. The user then manually
%selects time points before and after each suture's tie-down, and computes
%the force differential. Note, for proper color visualization as used
%below, the published function rgb.m should be downloaded.

clear all; close all; clc
```

```
%% User input section
expt='GTA46';

PositionMap={'1'
    '5'
    'RT'
    '4'
    'LT'
    '8'
    '7'
    '9'
    '3'
    '11'  }; %each row corresponds to the channel, ie row1=ch0, etc.

acqstart = 1; %the acq when tie-down began
acqfinish = 4; %the acq when tie-down ended
%% Initial info
TiedownOrder={'LT','RT','11','1','3','4','5','7','8','9'};
%Get channel(+1) of ith suture that was tied down
for i=1:10; ch_loc(i)=find(strcmp(TiedownOrder{i},PositionMap)); end

datadir=strcat(['C:\Users\Eric\Dropbox\Documents\Lab\Research - Thesis\1 - Aim
1-2 - Gorman NIH Grant\Animal Raw and Processed Data\' expt '\' expt '
Processed\']);
hdir=cd;
%% Load ALL data, concatenate into long runs
for h=acqstart:acqfinish
% for h=[2 4]
    cd(strcat(datadir,num2str(h)))
    for i=1:10;
        ch(:,i)=load(strcat('ch',num2str(i-1),'.txt'));
    end
    if exist('Whole_ChOrder')==0
        Whole_ChOrder=ch;
    else
        Whole_ChOrder=vertcat(Whole_ChOrder,ch);
    end
%     acqsize(h-TiedownTimes(1,1)+1)=size(ch,1);
    clear ch
end

%Re-order all data to be in order of tie-down instead of channel
for i=1:10
    Whole_TieOrder(:,i)=Whole_ChOrder(:,ch_loc(i));
end

%% Offset and plot data
for i=1:10
    Whole_TieOrder(:,i)=Whole_TieOrder(:,i)-5*(i-1);
%     Whole_TieOrder(:,i)=Whole_TieOrder(:,i)-min(Whole_TieOrder(:,i));
end

x=(1:size(Whole_TieOrder,1))./1613;
ColorOrder = {'OrangeRed';'Black';'ForestGreen';'FireBrick';'RoyalBlue';...
    'Purple';'Brown';'DarkKhaki';'Sienna';'HotPink';...
    'DimGray';'YellowGreen;';'DeepSkyBlue';'Indigo';'MediumOrchid';};

cd(hdir)
figure(1)
set(gcf, 'Position', get(0,'Screensize'));
set(gca,'fontsize',14)
for i=1:10
    hold on
```

```
    plot(x,Whole_TieOrder(:,i),'color',rgb(ColorOrder{i}),'linewidth',1.25)

    set(gca,'fontsize',14)
    if i<10
         set(gca, 'XTick', [])
    end
end

xlabel('Time (sec)')
```

I.6 annular_measurements.m

```
% AnnularMeasurements.m

%This code will first measure annular perimeter and area, defined as
%follows: perimeter is measured with arclength.m, a publicly available
%function (fits spline through selected points). Area is measured using
%polyarea (fits polygon through selected points). Next, it will measure SL
%and CC diameters, defined as follows: The two trigones are defined. Then,
%a perpendicular from their mid-point to the posterior annulus defines SL.
%Then, based on the SL diameter, a perpendicular passing through its
%midpoint to the annulus (which is roughly at the commisures) defines the
%CC diamter.

clear all; close all; clc

%% User input data

file = 'IMAGE.jpg';

CalDist = 50; %distance you will select for calibration scale, in units
outlined below
unit = 'mm';

CalibrateFlag = 1; %1 if yes, 0 if no (no is unlikely)
getPerimAreaFlag = 1; %1 if yes, 0 if no
getDiametersFlag = 1; %1 if yes, 0 if no

%% Calibrate
if CalibrateFlag == 1

    M = imread(file); %import photo
    imshow(M); %show photo
    set(gcf, 'Position', get(0,'Screensize')); %set image to full-screen
    title('Set zoom for calibrating and measuring, then press ENTER.',
'fontsize',16)
    input('Press enter when zoom complete.')

    % calibrate the image
    title(['Select two calibration points equal to ' num2str(CalDist) ' ' unit
'.'], 'fontsize',16)
    cal = ginput(2); %select two points
    CalDist_Pixel = sqrt( (cal(2,1)-cal(1,1))^2 + (cal(2,2)-cal(1,2))^2 );
%find # pixels between points
    ScaleFac = CalDist/CalDist_Pixel;
```

```
end
%% Get area and perimeter
if getPerimAreaFlag ==1

    title('Select ~30 points around annulus then press enter (start and end on
same spot).', 'fontsize',16)
    [p_x, p_y] = ginput(); % select points for perimeter
    hold on
    scatter (p_x,p_y, 'go', 'filled')

    [pixelPerim,seglen] = arclength(p_x,p_y,'spline');
    realPerim=pixelPerim*ScaleFac;
    disp(['Perimeter is ' num2str(realPerim) ' ' unit])

    pixelArea = polyarea(p_x,p_y);
    realArea = pixelArea*ScaleFac^2;
    disp(['Area is ' num2str(realArea) ' ' unit '^2'])

end
%% Get SL and CC diameters
if getDiametersFlag == 1

    %find trigones
    title('Select LT and RT.', 'fontsize',16)
    [tt_x, tt_y] = ginput(2); % select points for trigones
    SLAnt_x=mean(tt_x);
    SLAnt_y=mean(tt_y);
    hold on
    scatter (tt_x, tt_y, 'ro', 'filled')
    scatter(SLAnt_x,SLAnt_y,'co','filled')
    plot(tt_x,tt_y,'r','LineWidth',1.5)

    %find 6 o'clock and SL diameter
    slope_trig = (tt_y(2)-tt_y(1))/(tt_x(2)-tt_x(1));
    slope_SL = -1/slope_trig;
    SL_yint = SLAnt_y-slope_SL*SLAnt_x; %use known slope and TT midpoint to
define b in y=mx+b

    SLAxis_arb_x = SLAnt_x + SLAnt_x/3;
    SLAxis_arb_y = slope_SL*SLAxis_arb_x + SL_yint;
    SLAxis_arb_x(2) = SLAnt_x - SLAnt_x/3;
    SLAxis_arb_y(2) = slope_SL*SLAxis_arb_x(2) + SL_yint;
    scatter(SLAxis_arb_x,SLAxis_arb_y,'co')

    plot(SLAxis_arb_x,SLAxis_arb_y,'c','LineWidth',1.5)
    title('Select the point where the SL axis crosses the posterior
annulus.','fontsize',16)
    [SLPost_x, SLPost_y] = ginput(1);
    PixelSLDist = sqrt((SLAnt_x-SLPost_x)^2 + (SLAnt_y-SLPost_y)^2);
    RealSLDist = PixelSLDist * ScaleFac;
    disp(['SL Diameter is ' num2str(RealSLDist) ' ' unit])

    %find CC diameter
    scatter(SLPost_x,SLPost_y,'co','filled')
    SLMid = [mean([SLAnt_x SLPost_x]) mean([SLAnt_y SLPost_y])];
    scatter(SLMid(1),SLMid(2),'yo')

    %find 3 and 9 oclock
    CC_yint = SLMid(2)-slope_trig*SLMid(1); %use known slope and TT midpoint to
define b in y=mx+b
```

```
    CCAxis_arb_x = SLMid(1) + SLMid(1);
    CCAxis_arb_y = slope_trig*CCAxis_arb_x + CC_yint;
    CCAxis_arb_x(2) = SLMid(1) - SLMid(1);
    CCAxis_arb_y(2) = slope_trig*CCAxis_arb_x(2) +CC_yint;
    scatter(CCAxis_arb_x,CCAxis_arb_y,'yo')

    plot(CCAxis_arb_x,CCAxis_arb_y,'y','LineWidth',1.5)
    title('Select the points where the CC axis crosses the
annulus.','fontsize',16)
    [CC_x, CC_y] = ginput(2);
    scatter(CC_x,CC_y,'yo','filled')
    PixelCCDist = sqrt((CC_y(2)-CC_y(1))^2 + (CC_x(2)-CC_x(1))^2);
    RealCCDist = PixelCCDist * ScaleFac;
    disp(['CC Diameter is ' num2str(RealCCDist) ' ' unit])

end

output=[RealSLDist RealCCDist];
```

I.7 PVL_processing_part1.m

```
%PVL_processing_part1.m

%This code computes PCHIP curves representing the incidental leakage across
%the full pressure range, at every timepoint for which incidental leakage
%data was acquired throughout a single experiment. Each acquisition is
%imported, the user selects a set pressure-leakage pairs, and the
%coefficients and constants describing each PCHIP are stored in a .mat
%file for use in PVL_processing_part2.m.

clear all; close all; clc

%% User input section
%these inputs cover where the files are located.
Path = 'C:\Users\Eric\Dropbox\Documents\Lab\Research - Thesis\2 - Aim 3 -
TMVR\PVL Testing\Data\Expt 7\19-07-2017\'; %file path
Prefix = 'Expt7'; %from file names
Date = '19-07-2017'; %from file names
WinSize = 5; %number of seconds upstream of the final pressure instant to be
used in average; default is 4

FiltFlag = 1; %set to 1 if you want to apply low-pass filter, 2 if not
FiltCutoff = 4; %low-pass filter cutoff to use if filtering; default is 4
DwnsmpFac = 8; %downsample factor to use if filtering; ignore this otherwise;
default is 8

BaseFileNumbers = [3
9
21
26
33
37
41
46
50
```

```
53
]; %baseline (false leakage) files to be read

%% Initialization
if FiltFlag==2; DwnsmpFac=1; end
SampleFreq = round(1613/DwnsmpFac);
addpath(Path);

%% Read in, massage, and filter data
for i=1:length(BaseFileNumbers)
    FileNames{i} =
strcat(Prefix,'_',num2str(BaseFileNumbers(i)),'_',Date,'.lvm');
end

Data = cell(length(FileNames),1); %create empty cell
for i=1:length(FileNames)
    Path_File = strcat(Path, FileNames{i});
    Data{i} = textread(Path_File,'',-1,'delimiter',' ','headerlines',18); %read
in file

    if FiltFlag==1
        %downsample data to support low-pass filter
        for j=1:size(Data{i},1)/DwnsmpFac
            Data_Dwn(j,:)=mean(Data{i}(DwnsmpFac*(j-1)+1:DwnsmpFac*j,:),1);
        end

        %design and apply filter to downsampled data
        conv_filter = fir1(floor(size(Data_Dwn,1)/3)-
1,FiltCutoff/SampleFreq,'low');
        Data_Filt=filtfilt(conv_filter,1,Data_Dwn);

        %replace data with downsampled/filtered data
        Data{i} = [];
        Data{i} = Data_Filt;
        clear Data_Dwn Data_Filt
    end

    Data{i} = [Data{i}(:,4) Data{i}(:,5)-Data{i}(:,6)]; %discard all LVP and
Flow; subtract AoFlow from ApFlow to get PVL
    Data{i} = [linspace(0,size(Data{i},1)/SampleFreq,size(Data{i},1))'
Data{i}(:,1:2)]; %add a new 1st column for time
end

PtsSumm = []; %set up to populate later
for i = 1:length(FileNames)

    proceed = 2; %enables while loop
    while proceed==2;
        close all
        clear MeanData

        %% Plot data
        figure(1)
        set(gcf,'units','normalized','outerposition',[0 0 1 1])
        hAx = plotyy(Data{i}(:,1), Data{i}(:,2),...
            Data{i}(:,1), Data{i}(:,3));
        xlabel('time [sec]')
        ylabel(hAx(1),'LVP (mmHg)') % left y-axis
        ylim(hAx(1), [0 1.05*max(Data{i}(:,2))])
        set(hAx(1), 'YTick', 0:25:200)
        ylabel(hAx(2),'PVL (ml/sec)') % right y-axis
        ylim(hAx(2), [-20 1.05*max(Data{i}(:,3))])
```

```
        title('LVP and PVL vs. time. Select FINAL points for each pressure.
Code will average over 5 seconds prior. Press enter when done!')

        figure(2)
        plot(Data{i}(:,2),Data{i}(:,3))
        xlabel ('LVP (mmHg)')
        ylabel ('PVL (ml/sec)')
        title ('PVL vs. LVP')

        %% Take measurements
        figure(1)
        Endpoints=ginput(); %select terminal point of each pressure level
        Endpoints_IndexedTime=round(Endpoints.*SampleFreq); %convert to indexed
time

        for h=1:size(Endpoints,1)
            if Endpoints_IndexedTime(h,1)-SampleFreq*WinSize<1
                MeanData(h,1) = mean(Data{i}(1:Endpoints_IndexedTime(h,1),2));
                MeanData(h,2) = mean(Data{i}(1:Endpoints_IndexedTime(h,1),3));
            else
                MeanData(h,1) = mean(Data{i}(Endpoints_IndexedTime(h,1)-
SampleFreq*WinSize:Endpoints_IndexedTime(h,1),2));
                MeanData(h,2) = mean(Data{i}(Endpoints_IndexedTime(h,1)-
SampleFreq*WinSize:Endpoints_IndexedTime(h,1),3));
            end
            %plot means on top of raw data; get confirmation to proceed
            figure(1)
            hold(hAx(1), 'on')
            plot([Endpoints(h,1)-WinSize Endpoints(h,1)],[MeanData(h,1)
MeanData(h,1)],'g','linewidth',2)
            hold(hAx(2), 'on')
            plot([Endpoints(h,1)-WinSize Endpoints(h,1)],[MeanData(h,2)
MeanData(h,2)],'k','linewidth',2,'Parent',hAx(2))
            title('Proceed? (Enter 1 to proceed, 2 to repeat selections.)')
        end

        %%  PCHIP fit
        MeanData=sortrows(MeanData); %curve fit requires sequential x-coords
        int=linspace(MeanData(1,1),MeanData(end,1),2000);
        curve=pchip(MeanData(:,1),MeanData(:,2),int);
        figure(3)
        plot(MeanData(:,1),MeanData(:,2),'ob'); hold on
        plot(int,curve,'r') %review this looks reasonable

        proceed=input('Proceed? (Enter 1 to proceed, 2 to repeat
selections.)');
    end

    %% Summarize selected points and pchip equations
    for h=1:size(Endpoints,1)
        TempSumm = [BaseFileNumbers(i) Endpoints_IndexedTime(h,1)-
SampleFreq*WinSize...
            Endpoints_IndexedTime(h,1) MeanData(h,:)]; %.lvm#, start pt, end
pt, LVP, leak
        PtsSumm = vertcat(PtsSumm, TempSumm); %stick the selected point at the
bottom of the aggregate list
    end

    BaseSumm{i} = pchip(MeanData(:,1),MeanData(:,2));
    %     PtsSumm = vertcat(PtsSumm, Summ);
end
```

```
save(strcat([Prefix '_Baseline.mat']),'BaseSumm') %write data to a .mat file
that can be called in next script
```

I.8 PVL_processing_part2.m

```
%PVL_processing_part2.m

%This code generates PVL and trans-mitral delta_P values for each
%acquisition. Uses the .mat file produced by PVL_processing_part1.m. The
%variable AcqFileNumbers (i.e., the set of files to be analyzed) must only
%include files acquired between two consecutive incidental leak files. In
%other words, all acquisitions should have the same two incidental leak
%files as their before and after points. All data is output as two
%matrices, ProcessedDataLeft and ProcessedDataRight, which can then be
%stored in an Excel spreadsheet.

clear all; close all; clc

%% User input: DO NOT EDIT BELOW THIS SECTION
%these inputs cover where the files are located.
Path = 'C:\Users\Eric\Dropbox\Documents\Lab\Research - Thesis\2 - Aim 3 -
TMVR\PVL Testing\Data\Expt 6\10-07-2017\'; %file path
Prefix = 'Expt6'; %from file names
Date = '10-07-2017'; %from file names

WinSize = 4; %number of seconds upstream of the final pressure instant to be
used in average; default is 4
FiltFlag = 1; %set to 1 if you want to apply low-pass filter, 2 if not
FiltCutoff = 4; %low-pass filter cutoff to use if filtering; default is 4
DwnsmpFac = 8; %downsample factor to use if filtering; ignore this otherwise;
default is 8

BaseFileNumbers = [7
11
16
20
24
28
32
37
41]; %baseline (incidental leakage) files to be read

AcqFileNumbers = [21 22 23]; %acquisition files to be read

%% Initialization
if FiltFlag==2; DwnsmpFac=1; end
SampleFreq = round(1613/DwnsmpFac);
addpath(Path);

%% Read in and massage all data
FileNames=cell(length(AcqFileNumbers),1); %create empty cell
%then populate it with full File Names
for i=1:length(FileNames)
    FileNames{i} =
strcat(Prefix,'_',num2str(AcqFileNumbers(i)),'_',Date,'.lvm');
end
```

```
Data = cell(length(FileNames),1); %create empty cell
for i=1:length(FileNames)
    Path_File = strcat(Path, FileNames{i});
    Data{i} = textread(Path_File,'',-1,'delimiter',' ','headerlines',18); %read
in file

    if FiltFlag==1
        %downsample data to support low-pass filter
        for j=1:size(Data{i},1)/DwnsmpFac
            Data_Dwn(j,:)=mean(Data{i}(DwnsmpFac*(j-1)+1:DwnsmpFac*j,:),1);
        end

        %design and apply filter to downsampled data
        conv_filter = fir1(floor(size(Data_Dwn,1)/3)-
1,FiltCutoff/SampleFreq,'low');
        Data_Filt=filtfilt(conv_filter,1,Data_Dwn);

        %replace data with downsampled/filtered data
        Data{i} = [];
        Data{i} = Data_Filt;
        clear Data_Dwn Data_Filt
    end

    Data{i} = [Data{i}(:,4) Data{i}(:,5)-Data{i}(:,6)]; %discard all LVP and
Flow; subtract AoFlow from ApFlow to get PVL
    Data{i} = [linspace(0,size(Data{i},1)/SampleFreq,size(Data{i},1))'
Data{i}(:,1:2)]; %add a new 1st column for time
end

load(strcat([Prefix '_Baseline.mat'])); %loads baseline data as BaseSumm, a
cell of structures

%% Plot and analyze data
colors=['r','g','b','c','k'];

for i = 1:length(FileNames)

    proceed = 2;
    while proceed==2;
        close(figure(1),figure(2))

        %plot data
        figure(1)
        set(gcf,'units','normalized','outerposition',[0 0 1 1])
        hAx = plotyy(Data{i}(:,1), Data{i}(:,2),...
            Data{i}(:,1), Data{i}(:,3));
        xlabel('time [sec]')
        ylabel(hAx(1),'LVP (mmHg)') % left y-axis
        ylim(hAx(1), [0 1.05*max(Data{i}(:,2))])
        set(hAx(1), 'YTick', 0:25:200)
        ylabel(hAx(2),'PVL (ml/sec)') % right y-axis
        ylim(hAx(2), [-5 1.05*max(Data{i}(:,3))])
        title('LVP and PVL vs. time. Select FINAL points for each pressure.
Code will average over 5 seconds prior. Press enter when done!')

        figure(2)
        plot(Data{i}(:,2),Data{i}(:,3))
        xlabel ('LVP (mmHg)')
        ylabel ('PVL (ml/sec)')
        title ('PVL vs. LVP')

        %select spans of interest
        figure(1)
```

```
        Endpoints=ginput(); %select terminal point of each pressure level
        Endpoints_IndexedTime=round(Endpoints.*SampleFreq); %convert to indexed
time

        for h=1:size(Endpoints,1)
            %compute mean LVP's and PVL's
            meanLVP(h) = mean(Data{i}(Endpoints_IndexedTime(h,1)-
SampleFreq*WinSize:Endpoints_IndexedTime(h,1),2));
            meanPVL(h) = mean(Data{i}(Endpoints_IndexedTime(h,1)-
SampleFreq*WinSize:Endpoints_IndexedTime(h,1),3));

            %plot means on top of raw data
            figure(1)
            hold(hAx(1), 'on')
            plot([Endpoints(h,1)-WinSize Endpoints(h,1)],[meanLVP(h)
meanLVP(h)],'g','linewidth',2)
            hold(hAx(2), 'on')
            plot([Endpoints(h,1)-WinSize Endpoints(h,1)],[meanPVL(h)
meanPVL(h)],'k','linewidth',2,'Parent',hAx(2))
            title('Proceed? (Enter 1 to proceed, 2 to repeat selections.)')

            %% correct for incidental leakage
            %find file numbers and piecewise intervals of the correct
            %baseline leakage recording
            [x file_before] = min(abs(BaseFileNumbers-min(AcqFileNumbers)));
            [err bk_bef] = min(abs(BaseSumm{1,file_before}.breaks-meanLVP(h)));
            if BaseSumm{1,file_before}.breaks(bk_bef)>meanLVP(h)
                bk_bef=bk_bef-1;
            end

            [x file_after] = min(abs(BaseFileNumbers-max(AcqFileNumbers)));
            file_after = file_before + 1;
            [x bk_aft] = min(abs(BaseSumm{1,file_after}.breaks-meanLVP(h)));
            if BaseSumm{1,file_after}.breaks(bk_aft)>meanLVP(h)
                bk_aft=bk_aft-1;
            end

            %find incidental leakage at meanLVP(h) based on before/after
            %baseline recordings
            offset_before(h) = ...
                BaseSumm{1,file_before}.coefs(bk_bef,1)*(meanLVP(h)-
BaseSumm{1,file_before}.breaks(bk_bef))^3 +...
                BaseSumm{1,file_before}.coefs(bk_bef,2)*(meanLVP(h)-
BaseSumm{1,file_before}.breaks(bk_bef))^2 +...
                BaseSumm{1,file_before}.coefs(bk_bef,3)*(meanLVP(h)-
BaseSumm{1,file_before}.breaks(bk_bef)) +...
                BaseSumm{1,file_before}.coefs(bk_bef,4);

            offset_after(h) = ...
                BaseSumm{1,file_after}.coefs(bk_aft,1)*(meanLVP(h)-
BaseSumm{1,file_after}.breaks(bk_aft))^3 +...
                BaseSumm{1,file_after}.coefs(bk_aft,2)*(meanLVP(h)-
BaseSumm{1,file_after}.breaks(bk_aft))^2 +...
                BaseSumm{1,file_after}.coefs(bk_aft,3)*(meanLVP(h)-
BaseSumm{1,file_after}.breaks(bk_aft)) +...
                BaseSumm{1,file_after}.coefs(bk_aft,4);

            offset(h)=fudge*mean([offset_before(h) offset_after(h)]);

            %correct for incidental leakage
            meanPVL(h) = meanPVL(h) - offset(h);

            %populate summary data
```

```
            ProcessedDataLeft(5*(i-1)+h,:) = [AcqFileNumbers(i)
Endpoints_IndexedTime(h,1)-SampleFreq*WinSize Endpoints_IndexedTime(h,1)
offset(h)];
            ProcessedDataRight(5*(i-1)+h,:) = [i meanLVP(h) meanPVL(h)];
        end

        %visualize baseline offset values
        figure(3)
        hold on
        scatter(meanLVP,offset_before,colors(i),'x')
        scatter(meanLVP,offset_after,colors(i),'o')
        scatter(meanLVP,offset,colors(i),'^','filled')

        %confirm OK to proceed
        proceed=input('Proceed? (Enter 1 to proceed, 2 to repeat
selections.)');
        if proceed == 2
            close(figure(3))
        end
    end
end

%% VERIFY CORRECT OFFSET WAS USED
figure(3)
hold on
for k=1:length(BaseSumm{1,file_before}.breaks)-1

a=linspace(BaseSumm{1,file_before}.breaks(k),BaseSumm{1,file_before}.breaks(k+1
),100);
    plot(a,...
        BaseSumm{1,file_before}.coefs(k,1).*(a-
BaseSumm{1,file_before}.breaks(k)).^3 +...
        BaseSumm{1,file_before}.coefs(k,2).*(a-
BaseSumm{1,file_before}.breaks(k)).^2 +...
        BaseSumm{1,file_before}.coefs(k,3).*(a-
BaseSumm{1,file_before}.breaks(k)) +...
        BaseSumm{1,file_before}.coefs(k,4));
end

for k=1:length(BaseSumm{1,file_after}.breaks)-1

a=linspace(BaseSumm{1,file_after}.breaks(k),BaseSumm{1,file_after}.breaks(k+1),
100);
    plot(a,...
        BaseSumm{1,file_after}.coefs(k,1).*(a-
BaseSumm{1,file_after}.breaks(k)).^3 +...
        BaseSumm{1,file_after}.coefs(k,2).*(a-
BaseSumm{1,file_after}.breaks(k)).^2 +...
        BaseSumm{1,file_after}.coefs(k,3).*(a-BaseSumm{1,file_after}.breaks(k))
+...
        BaseSumm{1,file_after}.coefs(k,4));
end

%% done
disp('Success! Get outputs from ProcessedDataLeft and ProcessedDataRight!')
```

I.9 REFT_processing.m

```
%REFT_processing.m

%This code imports a set of REFT acquisitions, enables the user to select
%time points of interest, and outputs the forces on each arm associated
%with the each REFT acquisition. All data is output as finaloutput, which
%can then be stored in an Excel spreadsheet.

clear all; close all; clc

%% User input section
%these inputs cover where the files are located.
RootPath = 'C:\Users\Eric\Dropbox\Documents\Lab\Research - Thesis\2 - Aim 3 -
TMVR\REFT Testing\Data\'; %file path
Expt = 'C6';
Prefix = 'plus2'    ; %from file names
Date = '24-01-2018'; %from file names

AcqFileNumbers = [1
    2
    3
    4
    5
    6
    7
    8];

calfac = [-160076.3146
    -167705.9941
    -152129.8866
    -182690.8505];%calibration factors for each arm
%% Import and prep data
TCR = 5; %total channels recorded. INDEX FROM 1.
SampleFreq = 1613;

Path = (strcat(RootPath,Expt,'\',Date,'\'));

FileNames=cell(length(AcqFileNumbers),1); %create empty cell
%then populate it with full File Names
for i=1:length(FileNames)
    FileNames{i} =
strcat(Prefix,'_',num2str(AcqFileNumbers(i)),'_',Date,'.lvm');
end

data = cell(length(FileNames),1); %create empty cell
for i=1:length(FileNames)
    Path_File = strcat(Path, FileNames{i});
    data{i} = textread(Path_File,'',-1,'delimiter',' ','headerlines',26); %read
in file
    time = linspace(0,size(data{i},1)/SampleFreq,size(data{i},1));
    filtereddata{i} = data{i}(:,TCR+1:end);

    %% Plot data
    proceed = 2;
    while proceed==2;
        hold off
        figure(1);
        set(gcf,'units','normalized','outerposition',[0 0 1 1])
        subplot(2,1,2);
        plot(time,filtereddata{i}(:,5))
```

```
        hold on
        plot([0 time(end)],[115 115],'r--',[0 time(end)],[125 125],'r--')
        set(gca,'position',[0.07 0.1 0.88 0.33])
        xlim([0,time(end)])
        ylim([100,140])
        xlabel ('Time (sec)')
        ylabel ('Aortic Pressure (mmHg)')

        colororder=['k','r','y','b'];

        subplot(2,1,1);
        for j=1:4
            plot(time,filtereddata{i}(:,j).*calfac(j),colororder(j))
            hold on
        end
        legend('12','3','6','9')
        xlim([0,time(end)])
        ylabel('Strain')
        set(gca,'XTick',[])
        set(gca,'position',[0.07 0.45 0.88 0.5])

        %% select points, review selections
        title(strcat(['TRIAL ' num2str(i) '. Select endpoints for 1) before, 2)
during, and 3) after deployment.']))
        Endpoints = ginput(3);
        Endpoints_IndexedTime=round(Endpoints.*SampleFreq); %convert to indexed
time

        WinSize = 1.5; %number of secs beforethe final instant to be averaged

        %compute mean AoPs and Forces
        for j = 1:3
            meanAoP(j) = mean(filtereddata{i}(Endpoints_IndexedTime(j,1)-
SampleFreq*WinSize:Endpoints_IndexedTime(j,1),5));
            for k = 1:4
                meanStrain(j,k) =
mean(filtereddata{i}(Endpoints_IndexedTime(j,1)-
SampleFreq*WinSize:Endpoints_IndexedTime(j,1),k));
                plot([Endpoints(j,1)-WinSize Endpoints(j,1)],[meanStrain(j,k)
meanStrain(j,k)],'g','linewidth',2)
            end
        end
        title(strcat(['TRIAL ' num2str(i) 'Proceed? (Enter 1 to proceed, 2 to
repeat selections.)']))

        %confirm OK to proceed
        proceed=input('Proceed? (Enter 1 to proceed, 2 to repeat
selections.)');
        if proceed == 2
            close(figure(1))
        end
    end

    %get final force and pressures from that trial
    finaloutput(i,1:6) = [AcqFileNumbers(i) Endpoints_IndexedTime(:,1)' WinSize
mean(meanAoP)];
    for k = 1:4
        finaloutput(i,6+k) = meanStrain(2,k) - mean(meanStrain(3,k)-
meanStrain(1,k));
        finaloutput(i,6+k) = meanStrain(2,k) - mean(meanStrain(3,k)-
meanStrain(1,k));
    end
end
```

REFERENCES

1. Nkomo VT, Gardin JM, Skelton TN, Gottdiener JS, Scott CG, Enriquez-Sarano M. Burden of valvular heart diseases: a population-based study. *The Lancet.* 2006;368:1005-1011.

2. Pate G, Webb J, Thompson C, et al. Percutaneous closure of a complex prosthetic mitral paravalvular leak using transesophageal echocardiographic guidance. *The Canadian journal of cardiology.* 2004;20:452-455.

3. Edmunds LH. Thrombotic and bleeding complications of prosthetic heart valves. *The Annals of thoracic surgery.* 1987;44:430-445.

4. Grapsa J, Cabrita IZ, Jakaj G, et al. Strain balance of papillary muscles as a prerequisite for successful mitral valve repair in patients with mitral valve prolapse due to fibroelastic deficiency. *European Heart Journal-Cardiovascular Imaging.* 2015;16:53-61.

5. Acker MA, Parides MK, Perrault LP, et al. Mitral-valve repair versus replacement for severe ischemic mitral regurgitation. *New England Journal of Medicine.* 2014;370:23-32.

6. Potter DD, Sundt TM, Zehr KJ, et al. Risk of repeat mitral valve replacement for failed mitral valve prostheses. *The Annals of thoracic surgery.* 2004;78:67-72.

7. Jones-Haywood M-M, Combs C, Pu M, Gandhi SK, Dhawan R, Tempe DK. Percutaneous closure of mitral paravalvular leak. *Journal of cardiothoracic and vascular anesthesia.* 2013;27:168-177.

8. Guerrero M, Wang DD, Himbert D, et al. Short-term results of alcohol septal ablation as a bail-out strategy to treat severe left ventricular outflow tract obstruction after transcatheter mitral valve replacement in patients with severe mitral annular calcification. *Catheterization and Cardiovascular Interventions.* 2017.

9. Kim H-J, Ahn SJ, Park SW, et al. Cardiopulmonary exercise testing before and one year after mitral valve repair for severe mitral regurgitation. *The American journal of cardiology.* 2004;93:1187-1189.

10. Singh JP, Evans JC, Levy D, et al. Prevalence and clinical determinants of mitral, tricuspid, and aortic regurgitation (the Framingham Heart Study). *The American journal of cardiology.* 1999;83:897-902.

11. Mirabel M, Iung B, Baron G, et al. What are the characteristics of patients with severe, symptomatic, mitral regurgitation who are denied surgery? *European heart journal.* 2007;28:1358-1365.

12. Anyanwu AC, Adams DH. Transcatheter Mitral Valve Replacement: The Next Revolution?∗. *Journal of the American College of Cardiology.* 2014;64:1820-1824.

13. De Backer O, Piazza N, Banai S, et al. Percutaneous Transcatheter Mitral Valve Replacement An Overview of Devices in Preclinical and Early Clinical Evaluation. *Circulation: Cardiovascular Interventions.* 2014;7:400-409.

14. Preston-Maher GL, Torii R, Burriesci G. A Technical Review of Minimally Invasive Mitral Valve Replacements. *Cardiovascular engineering and technology.* 2014;6:174-184.

15. Carrel T. Transcatheter mitral valve replacement: still a long way to go! *Annals of Translational Medicine.* 2017.

16. Chiam PT, Ruiz CE. Percutaneous transcatheter mitral valve repair: a classification of the technology. *JACC: Cardiovascular Interventions.* 2011;4:1-13.

17. Rabbah J-PM, Saikrishnan N, Siefert AW, Santhanakrishnan A, Yoganathan AP. Mechanics of healthy and functionally diseased mitral valves: a critical review. *Journal of biomechanical engineering.* 2013;135:021007.

18. Siefert AW, Siskey RL. Bench Models for Assessing the Mechanics of Mitral Valve Repair and Percutaneous Surgery. *Cardiovascular engineering and technology.* 2015;6:193-207.

19. Cerfolio RJ, Orszulak TA, Pluth JR, Harmsen WS, Schaff HV. Reoperation after valve repair for mitral regurgitation: early and intermediate results. *The Journal of thoracic and cardiovascular surgery.* 1996;111:1177-1184.

20. Gillinov AM, Cosgrove DM, Lytle BW, et al. Reoperation for failure of mitral valve repair. *The Journal of Thoracic and Cardiovascular Surgery.* 1997;113:467-475.

21. Dumont E, Gillinov AM, Blackstone EH, et al. Reoperation after mitral valve repair for degenerative disease. *The Annals of thoracic surgery.* 2007;84:444-450.

22. Wong VM, Wenk JF, Zhang Z, et al. The effect of mitral annuloplasty shape in ischemic mitral regurgitation: a finite element simulation. *The Annals of thoracic surgery.* 2012;93:776-782.

23. Spratt JR, Spratt JA, Beachley V, Kang Q. Strength comparison of mitral annuloplasty ring and suturing combinations: an in-vitro study. *The Journal of heart valve disease.* 2012;21:286-292.

24. Siefert AW, Pierce EL, Lee M, et al. Suture forces in undersized mitral annuloplasty: novel device and measurements. *The Annals of thoracic surgery.* 2014;98:305-309.

25. Khamooshian A, Buijsrogge MP, de Heer F, Gründeman PF. Mitral valve annuloplasty rings: review of literature and comparison of functional outcome and ventricular dimensions. *Innovations: Technology and Techniques in Cardiothoracic and Vascular Surgery.* 2014;9:399-415.

26. Duncan A, Daqa A, Yeh J, et al. Transcatheter mitral valve replacement: long-term outcomes of first-in-man experience with an apically tethered device-a case series from a single centre. *EuroIntervention: journal of EuroPCR in collaboration with the Working Group on Interventional Cardiology of the European Society of Cardiology.* 2017;13:e1047-e1057.

27. Jeevan RR, Murari BM. Engineering challenges and the future prospects of transcatheter mitral valve replacement technologies: a comprehensive review of case studies. *Expert Review of Medical Devices.* 2017;14:297-307.

28. Ma L, Tozzi P, Huber CH, Taub S, Gerelle G, von Segesser LK. Double-crowned valved stents for off-pump mitral valve replacement. *European Journal of Cardio-Thoracic Surgery.* 2005;28:194-199.

29. Sondergaard L, Brooks M, Ihlemann N, et al. Transcatheter mitral valve implantation via transapical approach: an early experience. *European Journal of Cardio-Thoracic Surgery.* 2015:ezu546.

30. Søndergaard L, De Backer O, Franzen OW, et al. First-in-Human Case of Transfemoral CardiAQ Mitral Valve Implantation. *Circulation: Cardiovascular Interventions.* 2015;8:e002135.

31. Kodali SK, Williams MR, Smith CR, et al. Two-year outcomes after transcatheter or surgical aortic-valve replacement. *New England Journal of Medicine.* 2012;366:1686-1695.

32. Cho IJ, Moon J, Shim CY, et al. Different clinical outcome of paravalvular leakage after aortic or mitral valve replacement. *The American journal of cardiology.* 2011;107:280-284.

33. Ruiz CE, Hahn RT, Berrebi A, et al. Clinical trial principles and endpoint definitions for paravalvular leaks in surgical prosthesis: an expert statement. *European heart journal.* 2017:ehx211.

34. Pozzoli A, Alfieri O, Maisano F, Taramasso M. Surgical Aspects of Paravalvular Leak. *Transcatheter Paravalvular Leak Closure*: Springer; 2017:1-11.

35. Binder RK, Webb JG. Percutaneous mitral and aortic paravalvular leak repair: indications, current application, and future directions. *Current cardiology reports.* 2013;15:342.

36. Hall JE. *Guyton and Hall Textbook of Medical Physiology E-Book*: Elsevier Health Sciences; 2015.

37. Carpentier A, Adams DH, Filsoufi F. *Carpentier's reconstructive valve surgery*: Elsevier Health Sciences; 2011.

38. Brazile B, Wang B, Wang G, et al. On the bending properties of porcine mitral, tricuspid, aortic, and pulmonary valve leaflets. *Journal of long-term effects of medical implants.* 2015;25.

39. Toma M, Bloodworth CH, Pierce EL, et al. Fluid-structure interaction analysis of ruptured mitral chordae tendineae. *Annals of biomedical engineering.* 2017;45:619-631.

40. Khalighi AH, Drach A, Bloodworth CH, et al. Mitral valve chordae tendineae: topological and geometrical characterization. *Annals of biomedical engineering.* 2017;45:378-393.

41. Angelini A, Ho S, Anderson R, Davies M, Becker A. A histological study of the atrioventricular junction in hearts with normal and prolapsed leaflets of the mitral valve. *Heart.* 1988;59:712-716.

42. Stephens EH, Fahrenholtz MM, Connell PS, et al. Cellular and Extracellular Matrix Basis for Heterogeneity in Mitral Annular Contraction. *Cardiovascular engineering and technology.* 2015;6:151-159.

43. Gunning GM, Murphy BP. Determination of the tensile mechanical properties of the segmented mitral valve annulus. *Journal of biomechanics.* 2014;47:334-340.

44. Gorman JH, Gupta KB, Streicher JT, et al. Dynamic three-dimensional imaging of the mitral valve and left ventricle by rapid sonomicrometry array localization. *The Journal of thoracic and cardiovascular surgery.* 1996;112:712-724.

45. Jimenez JH, Soerensen DD, He Z, He S, Yoganathan AP. Effects of a saddle shaped annulus on mitral valve function and chordal force distribution: an in vitro study. *Annals of biomedical engineering.* 2003;31:1171-1181.

46. Rausch MK, Bothe W, Kvitting J-PE, et al. Characterization of mitral valve annular dynamics in the beating heart. *Annals of biomedical engineering.* 2011;39:1690-1702.

47. Komoda T, Hetzer R, Oellinger J, et al. Mitral annular flexibility. *Journal of cardiac surgery.* 1997;12:102-109.

48. Kaplan SR, Bashein G, Sheehan FH, et al. Three-dimensional echocardiographic assessment of annular shape changes in the normal and regurgitant mitral valve. *American heart journal.* 2000;139:378-387.

49. Itoh A, Ennis DB, Bothe W, et al. Mitral annular hinge motion contribution to changes in mitral septal–lateral dimension and annular area. *The Journal of thoracic and cardiovascular surgery.* 2009;138:1090-1099.

50. Grigioni F, Avierinos J-F, Ling LH, et al. Atrial fibrillation complicating the course of degenerative mitral regurgitation: determinants and long-term outcome. *Journal of the American College of Cardiology.* 2002;40:84-92.

51. Anyanwu AC, Adams DH. Etiologic classification of degenerative mitral valve disease: Barlow's disease and fibroelastic deficiency. *Seminars in thoracic and cardiovascular surgery.* Vol 19: Elsevier; 2007:90-96.

52. Flameng W, Meuris B, Herijgers P, Herregods M-C. Durability of mitral valve repair in Barlow disease versus fibroelastic deficiency. *The Journal of thoracic and cardiovascular surgery.* 2008;135:274-282.

53. Grewal J, Suri R, Mankad S, et al. Mitral annular dynamics in myxomatous valve disease new insights with real-time 3-dimensional echocardiography. *Circulation.* 2010;121:1423-1431.

54. Enriquez-Sarano M, Akins CW, Vahanian A. Mitral regurgitation. *The Lancet.* 2009;373:1382-1394.

55. Mauri L, Foster E, Glower DD, et al. 4-year results of a randomized controlled trial of percutaneous repair versus surgery for mitral regurgitation. *Journal of the American College of Cardiology.* 2013;62:317-328.

56. Stewart WJ, Currie PJ, Salcedo EE, et al. Intraoperative Doppler color flow mapping for decision-making in valve repair for mitral regurgitation. Technique and results in 100 patients. *Circulation.* 1990;81:556-566.

57. Nishimura RA, Otto CM, Bonow RO, et al. 2014 AHA/ACC guideline for the management of patients with valvular heart disease: a report of the American College of Cardiology/American Heart Association Task Force on Practice Guidelines. *Journal of the American College of Cardiology.* 2014;63:e57-e185.

58. Borger MA, Alam A, Murphy PM, Doenst T, David TE. Chronic ischemic mitral regurgitation: repair, replace or rethink? *The Annals of thoracic surgery.* 2006;81:1153-1161.

59. McGee EC, Gillinov AM, Blackstone EH, et al. Recurrent mitral regurgitation after annuloplasty for functional ischemic mitral regurgitation. *The Journal of thoracic and cardiovascular surgery.* 2004;128:916-924.

60. Yun KL, Sintek CF, Miller DC, et al. Randomized trial comparing partial versus complete chordal-sparing mitral valve replacement: effects on left ventricular volume and function. *The Journal of Thoracic and Cardiovascular Surgery.* 2002;123:707-714.

61. Kaneko T, Aranki S, Javed Q, et al. Mechanical versus bioprosthetic mitral valve replacement in patients< 65 years old. *The Journal of thoracic and cardiovascular surgery.* 2014;147:117-126.

62. Chiang YP, Chikwe J, Moskowitz AJ, Itagaki S, Adams DH, Egorova NN. Survival and long-term outcomes following bioprosthetic vs mechanical aortic valve replacement in patients aged 50 to 69 years. *JAMA.* 2014;312:1323-1329.

63. Braun J, Klautz RJ. Mitral valve surgery in low ejection fraction, severe ischemic mitral regurgitation patients: should we repair them all? *Current opinion in cardiology.* 2012;27:111-117.

64. Gillinov A, Cosgrove D. Mitral valve repair for degenerative disease. *The Journal of heart valve disease.* 2002;11:S15-20.

65. Kron IL, Green GR, Cope JT. Surgical relocation of the posterior papillary muscle in chronic ischemic mitral regurgitation. *The Annals of thoracic surgery.* 2002;74:600-601.

66. Salvador L, Mirone S, Bianchini R, et al. A 20-year experience with mitral valve repair with artificial chordae in 608 patients. *The Journal of Thoracic and Cardiovascular Surgery.* 2008;135:1280-1287. e1281.

67. Adams DH, Rosenhek R, Falk V. Degenerative mitral valve regurgitation: best practice revolution. *European heart journal.* 2010;31:1958-1966.

68. Ngaage D, Schaff H. Mitral valve surgery in non-ischemic cardiomyopathy. *Journal of Cardiovascular Surgery.* 2004;45:477.

69. Bothe W, Miller DC, Doenst T. Sizing for mitral annuloplasty: where does science stop and voodoo begin? *The Annals of thoracic surgery.* 2013;95:1475-1483.

70. Bothe W, Kvitting J-PE, Swanson JC, Hartnett S, Ingels NB, Miller DC. Effects of different annuloplasty rings on anterior mitral leaflet dimensions. *The Journal of thoracic and cardiovascular surgery.* 2010;139:1114-1122.

71. Okada Y, Shomura T, Yamaura Y, Yoshikawa J. Comparison of the Carpentier and Duran prosthetic rings used in mitral reconstruction. *The Annals of thoracic surgery.* 1995;59:658-663.

72. Silberman S, Klutstein MW, Sabag T, et al. Repair of ischemic mitral regurgitation: comparison between flexible and rigid annuloplasty rings. *The Annals of thoracic surgery.* 2009;87:1721-1727.

73. Nelson JS, Bolling SF. Who is doing mitral valve surgery in the United States? *Seminars in thoracic and cardiovascular surgery.* Vol 24: Elsevier; 2012:1-4.

74. Feldman T, Foster E, Glower DD, et al. Percutaneous repair or surgery for mitral regurgitation. *New England Journal of Medicine.* 2011;364:1395-1406.

75. Smith PK, Puskas JD, Ascheim DD, et al. Surgical treatment of moderate ischemic mitral regurgitation. *New England Journal of Medicine.* 2014;371:2178-2188.

76. Bolling SF, Li S, O'Brien SM, Brennan JM, Prager RL, Gammie JS. Predictors of mitral valve repair: clinical and surgeon factors. *The Annals of thoracic surgery.* 2010;90:1904-1912.

77. Whitlow PL, Feldman T, Pedersen WR, et al. Acute and 12-month results with catheter-based mitral valve leaflet repair: the EVEREST II (Endovascular Valve Edge-to-Edge Repair) High Risk Study. *Journal of the American College of Cardiology.* 2012;59:130-139.

78. Cockburn J, Fragkou P, Hildick-Smith D. Development of mitral stenosis after single MitraClip insertion for severe mitral regurgitation. *Catheterization and Cardiovascular Interventions.* 2014;83:297-302.

79. Feldman T, Guerrero M. Assessing the Balance Between Less Mitral Regurgitation and More Residual Transmitral Pressure Gradient After MitraClip. *JACC: Cardiovascular Interventions.* 2017;10:940-941.

80. Feldman T, Kar S, Elmariah S, et al. Randomized comparison of percutaneous repair and surgery for mitral regurgitation: 5-year results of EVEREST II. *Journal of the American College of Cardiology.* 2015;66:2844-2854.

81. Maisano F, Taramasso M, Nickenig G, et al. Cardioband, a transcatheter surgical-like direct mitral valve annuloplasty system: early results of the feasibility trial. *European heart journal.* 2015;37:817-825.

82. Osnabrugge RL, Mylotte D, Head SJ, et al. Aortic stenosis in the elderly: disease prevalence and number of candidates for transcatheter aortic valve replacement: a meta-analysis and modeling study. *Journal of the American College of Cardiology.* 2013;62:1002-1012.

83. Leon MB, Smith CR, Mack MJ, et al. Transcatheter or surgical aortic-valve replacement in intermediate-risk patients. *N Engl J Med.* 2016;2016:1609-1620.

84. Guerrero M, Dvir D, Himbert D, et al. Transcatheter mitral valve replacement in native mitral valve disease with severe mitral annular calcification: results from the first multicenter global registry. *JACC: Cardiovascular Interventions.* 2016;9:1361-1371.

85. Descoutures F, Himbert D, Maisano F, et al. Transcatheter valve-in-ring implantation after failure of surgical mitral repair. *European Journal of Cardio-Thoracic Surgery.* 2013;44:e8-e15.

86. Eleid MF, Whisenant BK, Cabalka AK, et al. Early outcomes of percutaneous transvenous transseptal transcatheter valve implantation in failed bioprosthetic mitral valves, ring annuloplasty, and severe mitral annular calcification. *JACC: Cardiovascular Interventions.* 2017;10:1932-1942.

87. Stephens EH, Fahrenholtz MM, Connell PS, et al. Cellular and Extracellular Matrix Basis for Heterogeneity in Mitral Annular Contraction. *Cardiovascular Engineering and Technology.* 2015;6:151-159.

88. Schiros C, Ahmed M, McGiffin D, et al. Mitral Annular Kinetics, Left Atrial and Left Ventricular Diastolic Function Post Mitral Valve Repair in Degenerative Mitral Regurgitation. *Frontiers in Cardiovascular Medicine.* 2015;2:31.

89. Chitwood WR, Rodriguez E, Chu MW, et al. Robotic mitral valve repairs in 300 patients: a single-center experience. *The Journal of Thoracic and Cardiovascular Surgery.* 2008;136:436-441.

90. Kronzon I, Sugeng L, Perk G, et al. Real-time 3-dimensional transesophageal echocardiography in the evaluation of post-operative mitral annuloplasty ring and prosthetic valve dehiscence. *Journal of the American College of Cardiology.* 2009;53:1543-1547.

91. Ramakrishna H. Incidental TOE finding-Carpentier mitral annuloplasty ring dehiscence during heart transplantation. *Annals of cardiac anaesthesia.* 2008;11:49.

92. Shapira AR, Stoddard MF, Dawn B. Dehiscence of mitral annuloplasty ring. *Circulation.* 2005;112:e305-e305.

93. Levack MM, Vergnat M, Cheung AT, Acker MA, Gorman RC, Gorman III JH. Annuloplasty ring dehiscence in ischemic mitral regurgitation. *The Annals of thoracic surgery.* 2012;94:2132.

94. Tsang W, Wu G, Rozenberg D, Mosko J, Leong-Poi H. Early mitral annuloplasty ring dehiscence with migration to the descending aorta. *Journal of the American College of Cardiology.* 2009;54:1629-1629.

95. Piatkowski R, Janusz K, Scislo P, Opolski G. Usefulness of Live/Real Time Three-Dimensional Transesophageal Echocardiography in the Assessment of Severe Mitral Annuloplasty Ring Dehiscence. *Echocardiography.* 2012;29:E80-E81.

96. Aggarwal G, Schlosshan D, Mathur G, Wolfenden H, Cranney G. Recurrent ischaemic mitral regurgitation post mitral annuloplasty due to suture dehiscence evaluated using real time three dimensional transoesophageal echocardiography. *Heart, Lung and Circulation.* 2012;21:844-846.

97. Swaans MJ, Braam RL, Heijmen RH, Plokker HW, Jaarsma W. Three-Dimensional Transesophageal Echocardiography in a Patient With Early Failure of Mitral Valve Repair. *Circulation: Cardiovascular Imaging.* 2008;1:282-283.

98. Ghadimi K, Gosalia AR, Troianos CA. Intraoperative Delineation of Mitral Annuloplasty Dehiscence Using Three-Dimensional Transesophageal Echocardiography. *Anesthesia & Analgesia.* 2011;113:1013-1015.

99. Ciobanu AO, Griffin SC, Bennett S, Vinereanu D. Catastrophic mitral prosthesis dehiscence diagnosed by three-dimensional transesophageal echocardiography. *Journal of Clinical Ultrasound.* 2014;42:249-251.

100. Derkx S, Nguyen V, Cimadevilla C, et al. Anatomical features of acute mitral valve repair dysfunction: Additional value of three-dimensional echocardiography. *Archives of Cardiovascular Diseases.* 2017.

101. Genoni M, Franzen D, Tavakoli R, et al. Does the morphology of mitral paravalvular leaks influence symptoms and hemolysis? *The Journal of heart valve disease.* 2001;10:426-430.

102. Sadeghian H, Savand-Roomi Z. Paravalvular Leak of Prosthetic Valves. *3D Echocardiography of Structural Heart Disease*: Springer; 2017:369-392.

103. Détaint D, Lepage L, Himbert D, et al. Determinants of significant paravalvular regurgitation after transcatheter aortic valve implantation: impact of device and annulus discongruence. *JACC: Cardiovascular Interventions.* 2009;2:821-827.

104. Sherif MA, Abdel-Wahab M, Stöcker B, et al. Anatomic and procedural predictors of paravalvular aortic regurgitation after implantation of the Medtronic CoreValve bioprosthesis. *Journal of the American College of Cardiology.* 2010;56:1623-1629.

105. Haensig M, Lehmkuhl L, Rastan AJ, et al. Aortic valve calcium scoring is a predictor of significant paravalvular aortic insufficiency in transapical-aortic valve implantation. *European Journal of Cardio-Thoracic Surgery.* 2012;41:1234-1241.

106. Siefert AW, Jimenez JH, Koomalsingh KJ, et al. Contractile mitral annular forces are reduced with ischemic mitral regurgitation. *The Journal of thoracic and cardiovascular surgery.* 2013;146:422-428.

107. Siefert AW, Jimenez JH, Koomalsingh KJ, et al. Dynamic assessment of mitral annular force profile in an ovine model. *The Annals of thoracic surgery.* 2012;94:59-65.

108. Rabbah J-PM, Siefert AW, Bolling SF, Yoganathan AP. Mitral valve annuloplasty and anterior leaflet augmentation for functional ischemic mitral regurgitation: quantitative comparison of coaptation and subvalvular tethering. *The Journal of thoracic and cardiovascular surgery.* 2014;148:1688-1693.

109. Khoiy KA, Biswas D, Decker TN, Asgarian KT, Loth F, Amini R. Surface strains of porcine tricuspid valve septal leaflets measured in ex vivo beating hearts. *Journal of biomechanical engineering.* 2016;138:111006.

110. Leopaldi A, Vismara R, Lemma M, et al. In vitro hemodynamics and valve imaging in passive beating hearts. *Journal of biomechanics.* 2012;45:1133-1139.

111. Maisano F, Alfieri O, Banai S, et al. The future of transcatheter mitral valve interventions: competitive or complementary role of repair vs. replacement? *European heart journal.* 2015:ehv123.

112. International Organization for Standardization. 5840: Cardiovascular implants - cardiac valve prostheses. Part 3: Heart valve substitutes implanted by transcatheter techniques. 2013.

113. Services USDoHaH. Guidance for Annuloplasty Rings 510(k) Submissions; Final Guidance for Industry and FDA Staff. Maryland: Food and Drug Administration; 2001.

114. Wu Y, Butchart EG, Borer JS, Yoganathan A, Grunkemeier GL. Clinical evaluation of new heart valve prostheses: update of objective performance criteria. *The Annals of thoracic surgery.* 2014;98:1865-1874.

115. Généreux P, Head SJ, Hahn R, et al. Paravalvular leak after transcatheter aortic valve replacement: the new Achilles' heel? A comprehensive review of the literature. *Journal of the American College of Cardiology.* 2013;61:1125-1136.

116. DiVincenti J, Westcott R, Lee C. Sheep (Ovis aries) as a model for cardiovascular surgery and management before, during, and after cardiopulmonary bypass. *Journal of the American Association for Laboratory Animal Science.* 2014;53:439-448.

117. Siefert AW, Rabbah JPM, Koomalsingh KJ, et al. In vitro mitral valve simulator mimics systolic valvular function of chronic ischemic mitral regurgitation ovine model. *The Annals of thoracic surgery.* 2013;95:825-830.

118. Bhattacharya S, Pham T, He Z, Sun W. Tension to passively cinch the mitral annulus through coronary sinus access: an ex vivo study in ovine model. *Journal of biomechanics.* 2014;47:1382-1388.

119. Bendall J. Postmortem changes in muscle. *The structure and function of muscle.* 1973;2:244-309.

120. Vanderwee MA, Humphrey SM, Gavin JB, Armiger LC. Changes in the contractile state, fine structure and metabolism of cardiac muscle cells during the development of rigor mortis. *Virchows Archiv B.* 1980;35:159-167.

121. Hearse DJ, Garlick PB, Humphrey SM. Ischemic contracture of the myocardium: mechanisms and prevention. *The American journal of cardiology.* 1977;39:986-993.

122. Jensen MO, Jensen H, Levine RA, et al. Saddle-shaped mitral valve annuloplasty rings improve leaflet coaptation geometry. *The Journal of thoracic and cardiovascular surgery.* 2011;142:697-703.

123. Ryan LP, Jackson BM, Hamamoto H, et al. The influence of annuloplasty ring geometry on mitral leaflet curvature. *The Annals of thoracic surgery.* 2008;86:749-760.

124. Vergnat M, Levack MM, Jassar AS, et al. The influence of saddle-shaped annuloplasty on leaflet curvature in patients with ischaemic mitral regurgitation. *European Journal of Cardio-Thoracic Surgery.* 2012;42:493-499.

125. Mahmood F, Gorman JH, Subramaniam B, et al. Changes in mitral valve annular geometry after repair: saddle-shaped versus flat annuloplasty rings. *The Annals of thoracic surgery.* 2010;90:1212-1220.

126. Padala M, Hutchison RA, Croft LR, et al. Saddle shape of the mitral annulus reduces systolic strains on the P2 segment of the posterior mitral leaflet. *The Annals of thoracic surgery.* 2009;88:1499-1504.

127. Jimenez JH, Liou SW, Padala M, et al. A saddle-shaped annulus reduces systolic strain on the central region of the mitral valve anterior leaflet. *The Journal of thoracic and cardiovascular surgery.* 2007;134:1562-1568.

128. Jensen MO, Jensen H, Smerup M, et al. Saddle-shaped mitral valve annuloplasty rings experience lower forces compared with flat rings. *Circulation.* 2008;118:S250-S255.

129. Cuéllar H, Roque A, Pineda V, Rodríguez J. Cardiac computed tomography for valve disease. *Radiología (English Edition).* 2013;55:24-36.

130. Kwon GP, Schroeder JL, Amar MJ, Remaley AT, Balaban RS. Contribution of macromolecular structure to the retention of low-density lipoprotein at arterial branch points. *Circulation.* 2008;117:2919-2927.

131. Neilan TG, Coelho-Filho OR, Danik SB, et al. CMR quantification of myocardial scar provides additive prognostic information in nonischemic cardiomyopathy. *Journal of the American College of Cardiology: Cardiovascular Imaging.* 2013;6:944-954.

132. Pain HJ, Rankin P. *Introduction to vibrations and waves*. West Sussex, United Kingdom: John Wiley & Sons; 2015.

133. Campbell I, Fauchet PM. The effects of microcrystal size and shape on the one phonon Raman spectra of crystalline semiconductors. *Solid State Communications.* 1986;58:739-741.

134. Cronenwett SM, Oosterkamp TH, Kouwenhoven LP. A tunable Kondo effect in quantum dots. *Science.* 1998;281:540-544.

135. Vidakovic B. *Statistics for bioengineering sciences: with MATLAB and WinBUGS support*: Springer Science & Business Media; 2011.

136. Mak GJ, Blanke P, Ong K, et al. Three-Dimensional Echocardiography Compared With Computed Tomography to Determine Mitral Annulus Size Before Transcatheter Mitral Valve ImplantationCLINICAL PERSPECTIVE. *Circulation: Cardiovascular Imaging.* 2016;9:e004176.

137. Blanke P, Dvir D, Cheung A, et al. Mitral annular evaluation with CT in the context of transcatheter mitral valve replacement. *JACC: Cardiovascular Imaging.* 2015;8:612-615.

138. In-Service Guide: Profile 3D Annuloplasty System for Mitral Repair2008.

139. Lane RM, Nyuli CA. Transcatheter mitral valve prosthesis. *U.S. Patent 8,579,964.* 2013.

140. Banai S, Verheye S, Cheung A, et al. Transapical mitral implantation of the Tiara bioprosthesis: pre-clinical results. *JACC: Cardiovascular Interventions.* 2014;7:154-162.

141. Young M, Erdemir A, Stucke S, Klatte R, Davis B, Navia JL. Simulation based design and evaluation of a transcatheter mitral heart valve frame. *Journal of medical devices.* 2012;6:031005.

142. Pierce EL, Bloodworth CH, Naran A, Easley TF, Jensen MO, Yoganathan AP. Novel method to track soft tissue deformation by micro-computed tomography: application to the mitral valve. *Annals of biomedical engineering.* 2016;44:2273-2281.

143. Moler CB. *Numerical Computing with MATLAB: Revised Reprint*: Siam; 2008.

144. Blanke P, Dvir D, Cheung A, et al. A simplified D-shaped model of the mitral annulus to facilitate CT-based sizing before transcatheter mitral valve implantation. *Journal of cardiovascular computed tomography.* 2014;8:459-467.

145. Naoum C, Leipsic J, Cheung A, et al. Mitral annular dimensions and geometry in patients with functional mitral regurgitation and mitral valve prolapse: implications for transcatheter mitral valve implantation. *JACC: Cardiovascular Imaging.* 2016;9:269-280.

146. Vik P. *Regression, ANOVA, and the general linear model: A statistics primer*: SAGE Publications; 2013.

147. Osborne JW. *Best practices in quantitative methods*: Sage; 2008.

148. He Z, Bhattacharya S. Papillary muscle and annulus size effect on anterior and posterior annulus tension of the mitral valve: an insight into annulus dilatation. *Journal of biomechanics.* 2008;41:2524-2532.

149. US Department of Health and Human Services. Guidance for annuloplasty rings 510(k) submissions; final guidance for industry and FDA staff. Maryland: Food and Drug Administration. 2001.

150. Maisano F, Alfieri O, Banai S, et al. The future of transcatheter mitral valve interventions: competitive or complementary role of repair vs. replacement? *European heart journal.* 2015;36:1651-1659.

151. Edwards M-B, Draper ER, Hand JW, Taylor KM, Young IR. Mechanical testing of human cardiac tissue: some implications for MRI safety. *Journal of Cardiovascular Magnetic Resonance.* 2005;7:835-840.

152. Alavi SH, Ruiz V, Krasieva T, Botvinick EL, Kheradvar A. Characterizing the collagen fiber orientation in pericardial leaflets under mechanical loading conditions. *Annals of biomedical engineering.* 2013;41:547-561.

153. Rankin JS, Arentzen CE, McHale PA, Ling D, Anderson RW. Viscoelastic properties of the diastolic left ventricle in the conscious dog. *Circulation research.* 1977;41:37-45.

154. Sanjeevi R, Somanathan N, Ramaswamy D. A viscoelastic model for collagen fibres. *Journal of biomechanics.* 1982;15:181-183.

155. McCarthy PM. A chain is only as strong as its weakest link. *The Journal of thoracic and cardiovascular surgery.* 2016;152:e19-e20.

156. Lawrie GM, Earle EA, Earle N. Intermediate-term results of a nonresectional dynamic repair technique in 662 patients with mitral valve prolapse and mitral regurgitation. *The Journal of Thoracic and Cardiovascular Surgery.* 2011;141:368-376.

157. McCarthy PM. Invited Commentary. *The Journal of thoracic and cardiovascular surgery.* 2017;104:826.

158. Spratt JR, Spratt JA, Lawrie GM. Mitral annuloplasty ring dehiscence: optimal force distribution with flexible rings. *The Journal of thoracic and cardiovascular surgery.* 2016;152:1639.

159. MacArthur JW, Boyd J. The Tip of the Iceberg, Evaluating the Mechanism behind Dehiscence of Mitral Annuloplasty Ring. *the Journal of thoracic and cardiovascular surgery.* 2017:e-pub ahead of print.

160. Calhoon J. Cardiac Surgeons: Are we too tight? *The Journal of thoracic and cardiovascular surgery.* 2017, e-pub ahead of print.

161. Bolling SF. Invited Commentary. *The Annals of Thoracic Surgery.* 2016;102:526.

162. Morrisson TM. Using Modeling and Simulation for Medical Device Innovation: Virtual Patients for Regulatory Decision Making. *Food and Drug Administration Science Writers Symposium*. Silver Spring, MD2015.

163. Reporting of Computational Modeling Studies in Medical Device Submissions: Guidance for Industry and Food and Drug Administration Staff.2014.

164. Nishimura RA, Otto CM, Bonow RO, et al. 2014 AHA/ACC guideline for the management of patients with valvular heart disease. *Circulation.* 2014:CIR. 0000000000000031.

165. Loger K, Pokorny S, Schaller T, Haben I, Frank D, Lutter G. Novel stent design for transcatheter mitral valve implantation. *Interactive CardioVascular and Thoracic Surgery.* 2017;26:190-195.

166. Meredith I, Bapat V, Morriss J, McLean M, Prendergast B. Intrepid transcatheter mitral valve replacement system: technical and product description. *EuroIntervention: journal of EuroPCR in collaboration with the Working Group on Interventional Cardiology of the European Society of Cardiology.* 2016;12:Y78.

167. Regueiro A, Granada JF, Dagenais F, Rodés-Cabau J. Transcatheter mitral valve replacement: insights from early clinical experience and future challenges. *Journal of the American College of Cardiology.* 2017;69:2175-2192.

168. Muller DW, Farivar RS, Jansz P, et al. Transcatheter mitral valve replacement for patients with symptomatic mitral regurgitation: a global feasibility trial. *Journal of the American College of Cardiology.* 2017;69:381-391.

169. Gallegos RP, Nockel PJ, Rivard AL, Bianco RW. The current state of in-vivo pre-clinical animal models for heart valve evaluation. *Journal of Heart Valve Disease.* 2005;14:423-432.

170. Gillespie MJ, Aoki C, Takebayashi S, et al. Development of off-pump mitral valve replacement in a porcine model. *The Annals of thoracic surgery.* 2015;99:1408-1412.

171. Ter Keurs HE, Rijnsburger WH, Van Heuningen R, Nagelsmit MJ. Tension development and sarcomere length in rat cardiac trabeculae: evidence of length-dependent activation. *Cardiac dynamics*: Springer; 1980:25-36.

172. Rassier D, MacIntosh B, Herzog W. Length dependence of active force production in skeletal muscle. *Journal of Applied Physiology.* 1999;86:1445-1457.

173. Calhoon J. Cardiac surgeons: Are we too tight? *The Journal of thoracic and cardiovascular surgery.* 2018;155:142.

174. Zhu T-Y, Wang J-G, Meng X. Is a rigid tricuspid annuloplasty ring superior to a flexible band when correcting secondary tricuspid regurgitation? *Interactive cardiovascular and thoracic surgery.* 2013;17:1009-1014.

175. Pfannmüller B, Doenst T, Eberhardt K, Seeburger J, Borger MA, Mohr FW. Increased risk of dehiscence after tricuspid valve repair with rigid annuloplasty rings. *The Journal of thoracic and cardiovascular surgery.* 2012;143:1050-1055.

176. Rusy B, Komai H. Anesthetic depression of myocardial contractility: a review of possible mechanisms. *Anesthesiology.* 1987;67:745-766.

177. Matsunaga A, Duran CM. Progression of tricuspid regurgitation after repaired functional ischemic mitral regurgitation. *Circulation.* 2005;112:I453-457.

178. Rogers JH, Bolling SF. The tricuspid valve: current perspective and evolving management of tricuspid regurgitation. *Circulation.* 2009;119:2718-2725.

179. Teman NR, Huffman LC, Krajacic M, Pagani FD, Haft JW, Bolling SF. "Prophylactic" Tricuspid Repair for Functional Tricuspid Regurgitation. *Annals of Thoracic Surgery.* 2014;97:1520-1524.

180. Braunwald NS, Ross J, Jr., Morrow AG. Conservative management of tricuspid regurgitation in patients undergoing mitral valve replacement. *Circulation.* 1967;35:I63-69.

181. Desai RR, Vargas Abello LM, Klein AL, et al. Tricuspid regurgitation and right ventricular function after mitral valve surgery with or without concomitant tricuspid valve procedure. *The Journal of thoracic and cardiovascular surgery.* 2013;146:1126-1132 e1110.

182. Bouleti C, Juliard JM, Himbert D, et al. Tricuspid valve and percutaneous approach: No longer the forgotten valve! *Arch Cardiovasc Dis.* 2016;109:55-66.

183. Nishimura RA, Otto CM, Bonow RO, et al. 2014 AHA/ACC Guideline for the Management of Patients With Valvular Heart Disease: a report of the American College of Cardiology/American Heart Association Task Force on Practice Guidelines. *Circulation.* 2014;129:e521-643.

184. Taramasso M, Pozzoli A, Guidotti A, et al. Percutaneous tricuspid valve therapies: the new frontier. *Eur Heart J.* 2016.

185. Rogers JH, Bolling SF. Surgical approach to functional tricuspid regurgitation: should we be more aggressive? *Curr Opin Cardiol.* 2014;29:133-139.

186. Schofer J, Bijuklic K, Tiburtius C, Hansen L, Groothuis A, Hahn RT. First-in-human transcatheter tricuspid valve repair in a patient with severely regurgitant tricuspid valve. *J Am Coll Cardiol.* 2015;65:1190-1195.

187. Huffman LC, Nelson JS, Lehman AN, Krajacic MC, Bolling SF. Identical tricuspid ring sizing in simultaneous functional tricuspid and mitral valve repair: A simple and effective strategy. *The Journal of thoracic and cardiovascular surgery.* 2014;147:611-614.

188. Mukherjee D, Nader S, Olano A, Garcia MJ, Griffin BP. Improvement in right ventricular systolic function after surgical correction of isolated tricuspid regurgitation. *J Am Soc Echocardiogr.* 2000;13:650-654.

189. Bertrand PB, Koppers G, Verbrugge FH, et al. Tricuspid annuloplasty concomitant with mitral valve surgery: effects on right ventricular remodeling. *The Journal of thoracic and cardiovascular surgery.* 2014;147:1256-1264.

190. Ghoreishi M, Brown JM, Stauffer CE, et al. Undersized tricuspid annuloplasty rings optimally treat functional tricuspid regurgitation. *The Annals of thoracic surgery.* 2011;92:89-95; discussion 96.

191. Marquis-Gravel G, Bouchard D, Perrault LP, et al. Retrospective cohort analysis of 926 tricuspid valve surgeries: clinical and hemodynamic outcomes with propensity score analysis. *American heart journal.* 2012;163:851-858 e851.

192. McCarthy PM, Bhudia SK, Rajeswaran J, et al. Tricuspid valve repair: durability and risk factors for failure. *J Thorac Cardiovasc Surg.* 2004;127:674-685.

193. Navia JL, Nowicki ER, Blackstone EH, et al. Surgical management of secondary tricuspid valve regurgitation: annulus, commissure, or leaflet procedure? *The Journal of thoracic and cardiovascular surgery.* 2010;139:1473-1482 e1475.

194. Zhu TY, Wang JG, Meng X. Is a rigid tricuspid annuloplasty ring superior to a flexible band when correcting secondary tricuspid regurgitation? *Interact Cardiovasc Thorac Surg.* 2013;17:1009-1014.

195. Pfannmuller B, Doenst T, Eberhardt K, Seeburger J, Borger MA, Mohr FW. Increased risk of dehiscence after tricuspid valve repair with rigid annuloplasty rings. *The Journal of thoracic and cardiovascular surgery.* 2012;143:1050-1055.

196. Aupperle H, Marz I, Thielebein J, Kiefer B, Dinges G, Schoon HA. Distribution of Extracellular Matrix Components in Normal and Degenerated Canine Tricuspid Valve Leaflets. *J Comp Pathol.* 2009;141:41-51.

197. Ring L, Rana BS, Kydd A, Boyd J, Parker K, Rusk RA. Dynamics of the tricuspid valve annulus in normal and dilated right hearts: a three-dimensional transoesophageal echocardiography study. *Eur Heart J-Card Img.* 2012;13:756-762.

198. Pfannmuller B, Davierwala P, Misfeld M, Borger MA, Garbade J, Mohr FW. Postoperative outcome of isolated tricuspid valve operation using arrested-heart or beating-heart technique. *The Annals of thoracic surgery.* 2012;94:1218-1222.

199. Pierce EL, Siefert AW, Paul DM, et al. How Local Annular Force and Collagen Density Govern Mitral Annuloplasty Ring Dehiscence Risk. *The Annals of Thoracic Surgery.*102:518-526.

200. Tei C, Pilgrim JP, Shah PM, Ormiston JA, Wong M. The Tricuspid-Valve Annulus - Study of Size and Motion in Normal Subjects and in Patients with Tricuspid Regurgitation. *Circulation.* 1982;66:665-671.

201. Miglioranza MH, Mihaila S, Muraru D, Cucchini U, Iliceto S, Badano LP. Dynamic Changes in Tricuspid Annular Diameter Measurement in Relation to the Echocardiographic View and Timing during the Cardiac Cycle. *J Am Soc Echocardiog.* 2015;28:226-235.

202. Nishi H, Toda K, Miyagawa S, et al. Tricuspid Annular Dynamics Before and After Tricuspid Annuloplasty - Three-Dimensional Transesophageal Echocardiography - . *Circ J.* 2015;79:873-879.

203. McCarthy PM. A Chain is only as Strong as its Weakest Link. *The Journal of Thoracic and Cardiovascular Surgery.*

204. Maghami S, Ghoreishi M, Foster N, et al. Undersized Rigid Nonplanar Annuloplasty: The Key to Effective and Durable Repair of Functional Tricuspid Regurgitation. *Ann Thorac Surg.* 2016.

205. Rogers JH. Functional tricuspid regurgitation: percutaneous therapies needed. *JACC Cardiovasc Interv.* 2015;8:492-494.

206. Pham T, Sun W. Material properties of aged human mitral valve leaflets. *Journal of Biomedical Materials Research Part A.* 2014;102:2692-2703.

207. Martin C, Sun W, Primiano C, McKay R, Elefteriades J. Age-dependent ascending aorta mechanics assessed through multiphase CT. *Annals of biomedical engineering.* 2013;41:2565-2574.

208. Connell PS, Azimuddin AF, Kim SE, et al. Regurgitation hemodynamics alone cause mitral valve remodeling characteristic of clinical disease states in vitro. *Annals of biomedical engineering.* 2016;44:954-967.

209. Gerson CJ, Goldstein S, Heacox AE. Retained structural integrity of collagen and elastin within cryopreserved human heart valve tissue as detected by two-photon laser scanning confocal microscopy. *Cryobiology.* 2009;59:171-179.

210. Bia D, Pessana F, Armentano R, et al. Cryopreservation procedure does not modify human carotid homografts mechanical properties: an isobaric and dynamic analysis. *Cell and Tissue Banking.* 2006;7:183-194.

211. Rausch MK, Malinowski M, Wilton P, Khaghani A, Timek TA. Engineering Analysis of Tricuspid Annular Dynamics in the Beating Ovine Heart. *Annals of biomedical engineering.* 2017:1-9.

212. Kawada N, Naganuma H, Muramatsu K, Ishibashi-Ueda H, Bando K, Hashimoto K. Redefinition of Tricuspid Valve Structures for Successful Ring Annuloplasty. *The Journal of Thoracic and Cardiovascular Surgery.* 2017.

213. Kunzelman KS, Cochran R. Stress/strain characteristics of porcine mitral valve tissue: parallel versus perpendicular collagen orientation. *Journal of cardiac surgery.* 1992;7:71-78.

214. Lodish H, Berk A, Zipursky S, Matsudaira P, Baltimore D, Darnell J. Collagen: the fibrous proteins of the matrix. *Molecular Cell Biology.* Vol 4. 2000.